Fault core and its geostatistical analysis: Insight into the fault core thickness and fault displacement

Thesis for Master degree

In Petroleum Geology/Structural Geology

Magnus Ueland Johannessen

Department of Earth Science

University of Bergen

June 2017

This thesis was written in cooperation with Uni Research

Centre for Integrated Petroleum Research

Abstract

Fault core is a high-strain zone of a fault, which accommodate intense deformation. Due to high strain, complex structures and intensely deformed fault rocks form in the fault core, which again affects the geometry and lateral variations in fault core thickness. From a reservoir perspective, the complexity and variations in fault core thickness may affect fluid flow across the faults. The sub-seismic size of the fault core makes it not detectable on seismic data, so a scaling relationship between the core thickness and displacement needs to be investigated, as well as the variations and complexity of the fault core, based on outcrop studies. This Master thesis documents and quantifies the lateral variations in fault core thickness along different levels of the fault height, and examines factors affecting the thickness variations. Measurements of the fault core thickness and displacement have been performed in siliciclastic rocks and carbonates, to study the lithological effects on the fault attributes. The collected dataset have further been univariately analyzed, and exceedence frequency plots have been constructed to recognize the distribution trends. Statistical analysis was then performed to investigate the fault core thickness-displacement relationship and state the scaling relationship between the two fault attributes. The relationship has been examined using measurements of the fault core thickness and displacement from the exact same levels along the fault height, and from average measurements.

One of the factors controlling the fault core thickness is lithology and the competency contrasts of the faulted lithologies. The competency contrast leads to significant variations in core thickness, and measurements from this project show that faults juxtaposing heterogeneous sequences display a much wider fault core, compared to faults juxtaposing homogeneous sequences. Another factor affecting the variation in core thickness are the type of fault rocks situated in the fault core. Host rock lenses incorporated in the fault core have been observed and measured to increase the fault core and the internal core complexity. The measurements in this thesis also show that minor faults in carbonates generally exposes a wider fault core, compared to fault cores in siliciclastic rocks. The variations in fault core thickness in different lithologies are controlled by an interplay of factors, such as fault geometry, interactions between the surrounding faults, tectonic regimes and competency contrasts.

Analysis of a global dataset, including new data gathered in this thesis and the results from previously published studies, shows that fault core thickness and displacement follow an overall power-law or-log-normal for univariate distribution. Bivariate analysis of the relationship for the global dataset, reveals a strong power-law relationship, with a correlation coefficient of 0.7390. However, when the global dataset is sorted based on the faulted lithology, a stronger relationship (with higher correlation coefficient) can be found. When measurements from this thesis are included in the lithological based dataset, the measurements contributes to a minor increase in the regression value. This suggests that when handling such data, we need to differentiate between rocks of different lithologies.

Acknowledgements

This Master thesis has been conducted with the involvement from the Uni Research Centre for Integrated Petroleum Research (CIPR) and the Department of Earth Science at the University of Bergen. This thesis was part of a project called "Fault geometric and seismic attributes" at Uni Research CIPR. The project was founded by the Research Council of Norway under NORRUS and Petromaks2 programs. Additional support for this Master project was provided by the Institute of Earth Science at the University of Bergen.

First and foremost, I would like to thank and express my sincere gratitude to my supervisor, Anita Torabi (Uni CIPR), for her guidance, support, and motivation during the last two years. Thank you for sharing your knowledge, always keeping me on the right track and most appreciated feedback during the work of this thesis. I would also like to thank my co-supervisors, Behzad Alaei (Earth Science Analytics AS) and Atle Rotevatn (University of Bergen), for their contributions and support during the work of this thesis.

Special thanks to my field partner, Tor Saltnes Skram Ellingsen, for excellent company, support, and discussions in the field and during the work of this thesis. In addition to Tor and Anita, I would like to thank Audun Libak and Runar Sherling Kristensen, for their assistance, contributions and great company during the fieldwork in Utah, USA.

I would like to thank the authorities of the Majella National Park for granting us the permission to work in Vallone di Santo Spirito and gather data from this area. I would also like to express my gratitude to Dr. Domenico Chiarella (Royal Holloway, University of London) for providing us with helpful information related to our work in the Majella Mountain.

I am also very grateful to Vilde Dimmen for her proofreading and comments on different parts of this thesis. I would also like to thank Christian Hauge Eide for comments on the geological setting/history regarding Utah, and for providing useful literature related to this subject.

To all my fellow geology students at the University of Bergen, thank you so much for all the memories we shared at field trips, at the University and other social gatherings. It has been five unforgettable years, I will never forget.

Last but not least, I want to thank my family and girlfriend, Ingrid Flørenæss, for endless encouragement, support, and motivation the last five years.

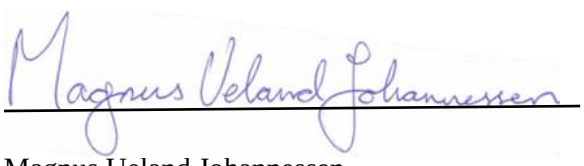

Magnus Ueland Johannessen Bergen, 1th of June 2017

Table of contents

1. Introduction 1

1.1. Background and rationale 1

1.2. Aims and objectives 2

1.3. Study areas 2

1.4. Definitions and explanations 4

1.4.1. Fault core 4

1.4.2. Fault rocks 5

1.4.3. Damage zone 8

1.4.4. Deformation bands 9

1.4.5. Pressure solution seams 11

1.4.6. Fault displacement and offset 11

1.5. State of the art on the scaling of fault core thickness and displacement 12

1.6. Methods 15

1.6.1. Field data 15

1.6.2. Measurements on outcrop pictures 17

1.6.3. Possible sources of error and uncertainties 18

1.6.4. Statistical treatment of data 18

2. Geological setting 21

2.1. The Colorado Plateau, southeastern Utah 21

2.1.1. Tectonic and structural evolution 23

2.1.2. Evolution of southeastern Utah and stratigraphic units 28

2.2. The Majella Mountain, eastern Italy 32

2.2.1. Tectonic and structural evolution 33

2.2.2. Evolution of the Majella platform and stratigraphic units 36

3. Results 41

3.1. R-191 Canyon, Utah 41

3.1.1. Structures and stratigraphic units 41

3.1.2. Fault core and fault descriptions 43

3.1.3. Statistical analysis of data 47

3.2. Hidden Canyon, Utah 50

3.2.1. Structures and stratigraphic units 50

3.2.2. Fault core and fault descriptions 51

3.2.3. Statistical analysis of data 53

3.3. Outside Arches National Park (ANP), Utah 55

3.3.1. Structures and stratigraphic units 55
3.3.2. Fault core and fault descriptions 57
3.3.3. Statistical analysis of data 63
3.4. Cache Valley, Utah 66
3.4.1. Structures and stratigraphic units 66
3.4.2. Fault core and fault descriptions 68
3.4.3. Statistical analysis of data 73
3.5. Humbug Flats, Utah 76
3.5.1. Structures and stratigraphic units 76
3.5.2. Fault core and fault descriptions 77
3.5.3. Statistical analysis of data 83
3.6. Vallone di Santo Spirito, Majella Mountain, Italy 85
3.6.1. Structures and stratigraphic units 85
3.6.2. Fault description 87
3.6.3. Fault core thickness and fault core descriptions 91
3.6.4. Statistical analysis of data 97
4. Discussion 99
4.1. Variation in fault core thickness 99
4.1.1. Variations caused by lithology 99
4.1.2. Variations caused by fault type 106
4.2. Displacement changes along faults 108
4.3. Discussion on statistical analysis of data 110
4.3.1. Univariate distributions of fault core and displacement data 110
4.3.2. Fault core thickness versus displacement 113
4.3.3. Comparison with previously published results 115
4.4. Implications for fault architecture and fault core structures 120
5. Conclusions and further work 121
5.1. Conclusions 121
5.2. Suggestions for further work 122
6. References 125

1. Introduction

1.1 Background and rationale

Faults and fault zones play a significant role in controlling fluid flow and fluid-rock interactions in the shallow parts of the crust. Faults can act both as barriers and conduits for fluid flow (e.g. Caine et al., 1996; Knipe et al., 1998; Fredman et al., 2007; Braathen et al., 2009; Childs et al., 2009). Thus, fault zones and fault geometric attributes have received significant attention the past decades (Walsh and Watterson, 1988; Evans, 1990; Shipton et al., 2006; Wibberley et al., 2008; Childs et al., 2009; Bastesen et al., 2013; among others). Fault geometric attributes include: fault displacement, length, damage zone width and fault core thickness (Torabi and Berg, 2011) and among these attributes, the fault core thickness is the most uncertain. In fault sealing analysis, the fault core thickness is considered as the key element for predicting the sealing potential of a fault zone (Fredman et al., 2007). This fault attribute also affects the petrophysical properties of rocks and hence influence the fluid flow within a fault zone, due to the accommodation of displacement and the resulting intense deformation. The fault core thickness is hard or impossible to capture on seismic data, because of the sub-seismic size of the attribute. Thus, details of fault core structure are usually captured through accessible vertical sections of faults in the outcrops. Fault core thickness measurements illustrate great lateral variation due to the variations in lithology and displacement, along the faults (Foxford et al., 1998; Shipton et al., 2006; Childs et al., 2009; Bastesen et al., 2013). The uncertainties related to the definition of fault core and variations observed in the fault core thickness have led to investigation and analysis of the scaling relationship between the fault core thickness and fault displacement (e.g. Robertson, 1983; Knott, 1994; Bastesen and Braathen, 2010; Bastesen et al., 2013).

The findings and information gained from the fault core thickness-fault displacement relationship could increase our overall understanding of fault behavior, and an estimate of this relationship could further be conducted on similar faults elsewhere or seismic data, to predict these attributes from each other (Shipton et al., 2006; Wibberley et al., 2008). This can increase our understanding of fault architecture and would be beneficial in reservoir modeling and well-planning, for better reservoir characterization and for developing more realistic fluid flow models. In fault sealing analysis, this relationship would improve the ongoing analysis, to better understand and predict the fault properties located in the subsurface. This would be of great interest and importance to the petroleum industry for hydrocarbon exploration, appraisal and development, when constructing geological models of faulted and deformed hydrocarbon reservoir. Furthermore, an understanding of the relationship would also be beneficial for CCS (Carbon Capture and Storage), for evaluation of the best suitable reservoir candidates to safely store CO_2 in the subsurface, as well as for other applications such as geothermal reservoirs.

1.2. Aims and objectives

The aim and objective of this study are to gain further understanding of fault architecture and internal structures, by studying the variations in fault core structure and thickness and investigating the relationship between the fault core thickness and fault displacement. This is conducted by field observations and statistical analysis of the collected data.

In this project, the fault core thickness and fault displacement data have been collected in siliciclastic rocks and carbonates from different fault types to study both the effect of lithology and fault type on the fault attributes.

The data and results achieved from this project can be further correlated and compared with previous published work and results (e.g. Evans, 1990; Foxford et al., 1998; Shipton et al., 2006; Bastesen and Braathen, 2010; Torabi and Berg, 2011) to improve the understanding of fault internal structures.

1.3. Study areas

This Master project is based on field works carried out in April 2016 on the Colorado Plateau, southeastern Utah, USA (Figure 1.3.1 A) and in September 2016, in Vallone di Santo Spirito, Majella Mountain, eastern Italy (Figure 1.3.1 B).

The study area located in southeastern Utah provides a unique opportunity to study and measure fault cores in minor to major normal faults situated in siliciclastic rocks. The study localities in Utah is located around the town of Moab and northwards towards the San Rafael Swell, where the Humbug Flats locality is located, close to Green River. The studied localities around Moab, are affected by the major 45 km long Moab Fault and the underlying salt-cored anticlines formed above the ancient Paradox Basin (Doelling, 1988; Foxford et al., 1996; Foxford et al., 1998). The development of these normal faults might be related to salt tectonics and salt migration, resulting in extensive uplift and folding of the overlying sedimentary strata (Doelling, 1988; Hintze and Kowallis, 2009; Trudgill, 2011). Northwards from the Moab study area, the Humbug Flats locality is situated on the northern edge of the San Rafael Swell. This locality is located outside the Paradox Basin and the studied normal faults is suggested to have developed due to the uplift of the major, dome-shaped, asymmetric anticline of San Rafael Swell, during the Laramide orogeny (75-45 Ma) (Davatzes et al., 2003; English and Johnston, 2004; Shipton et al., 2005; Ogata et al., 2014).

The second study area is located in eastern Italy, in Vallone di Santo Spirito on the eastern forelimb of the major, asymmetric Majella anticline. The anticline developed during the Apennenic fold-and-thrust belt during Oligocene-Pliocene (Eberli et al., 1993; Pizzi et al., 2010). The study area exposes a complex faulting system, consisting of normal-, reverse- and strike-slip faults, situated in a 2 km thick sequence of Late Cretaceous platform carbonates (Aydin et al., 2010; Festa et al., 2014; Rustichelli et al., 2016). The study area has been used as a great analog for a fractured- and faulted carbonate

reservoir (e.g. TaskForceMajella), due to the unique exposures of a complex, sub-seismic fault- and fracture network (Agosta et al., 2010a; Aydin et al., 2010). For this project, Vallone di Santo Spirito provides an excellent opportunity to study the differences in fault core thickness in different fault types in carbonates.

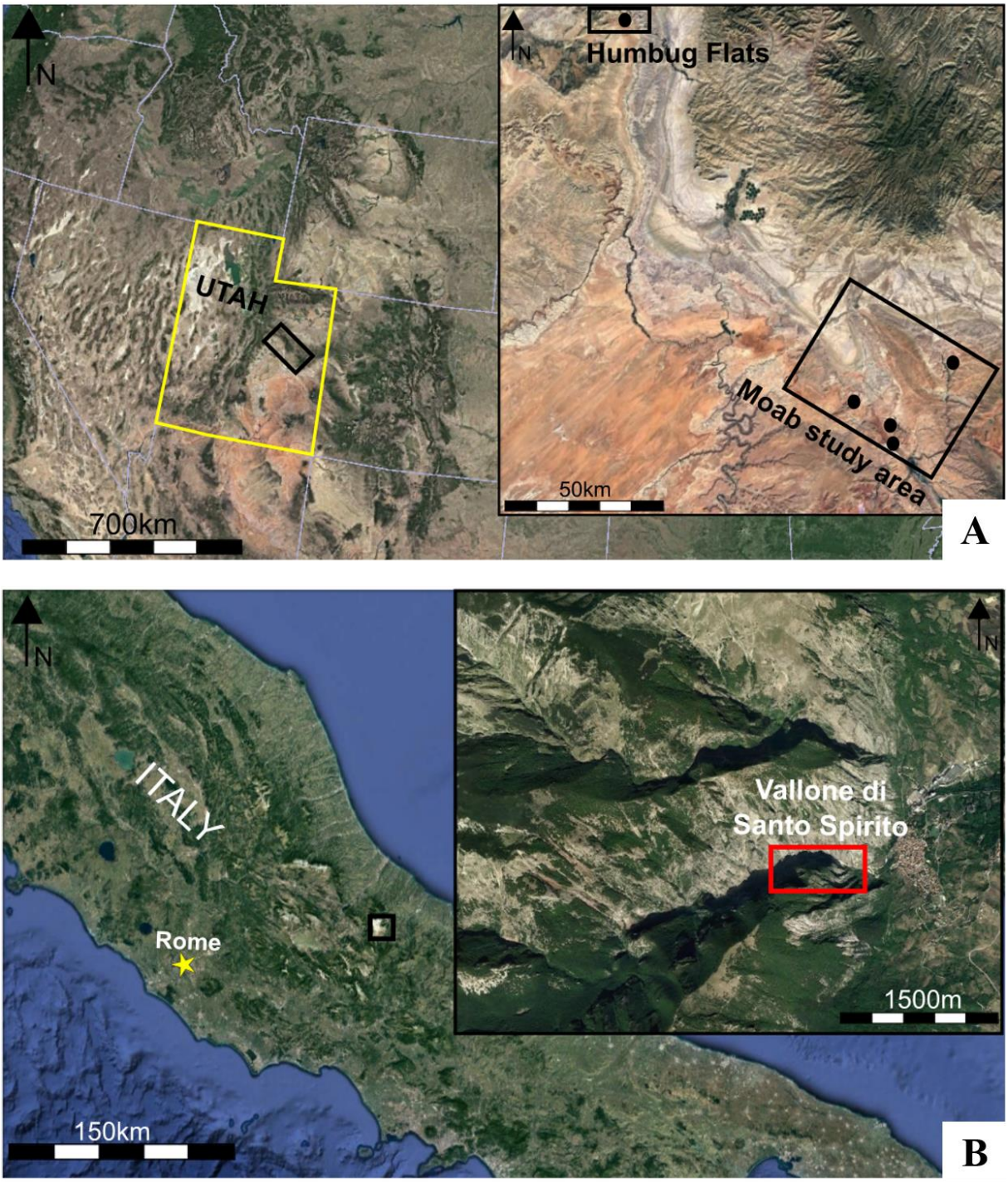

Figure 1.3.1: *Satellite photo of the study areas, acquired from Google Earth. (**A**) Satellite photo of the study area on the Colorado Plateau, in southeastern Utah, where the Moab study area and the Humbug Flats locality are illustrated. (**B**) Satellite photo of the study area in eastern Italy, where the Majella Mountain (Southern Apennines) and the Vallone di Santo Spirito are illustrated.*

1.4. Definitions and explanations

1.4.1. Fault core

Faults developed in the brittle regime deform and modify volumes of host rock in what is termed the fault zone (Figure 1.4.1), and this zone is often divided into a low-strain- and high-strain zone (Caine et al., 1996; Wibberley et al., 2008; Childs et al., 2009). The fault core represents the high-strain zone where most of the displacement and deformation is accommodated (Fredman et al., 2007; Schultz and Fossen, 2008; Braathen et al., 2009; Torabi and Berg, 2011; Bastesen et al., 2013). Consequently, the high degree of deformation and strain localization results in deformed and crushed rocks situated in the fault core, surrounding the main slip surface(s) (Torabi and Berg, 2011). These rocks are collectively referred to as fault rocks, and their texture and structure are usually altered compared to the original host rock (Sibson, 1977). The fault core could also include deformed or intact lenses derived from the wall rocks, interior slip surfaces, fractures or deformation bands, depending on the lithology of the faulted rocks. The fault core can vary from a millimeter thick core with one simple slip surface to a zone containing several slip surfaces and an intensely sheared, deformed core up to several meters thick, where only fragments of the original host rock are preserved.

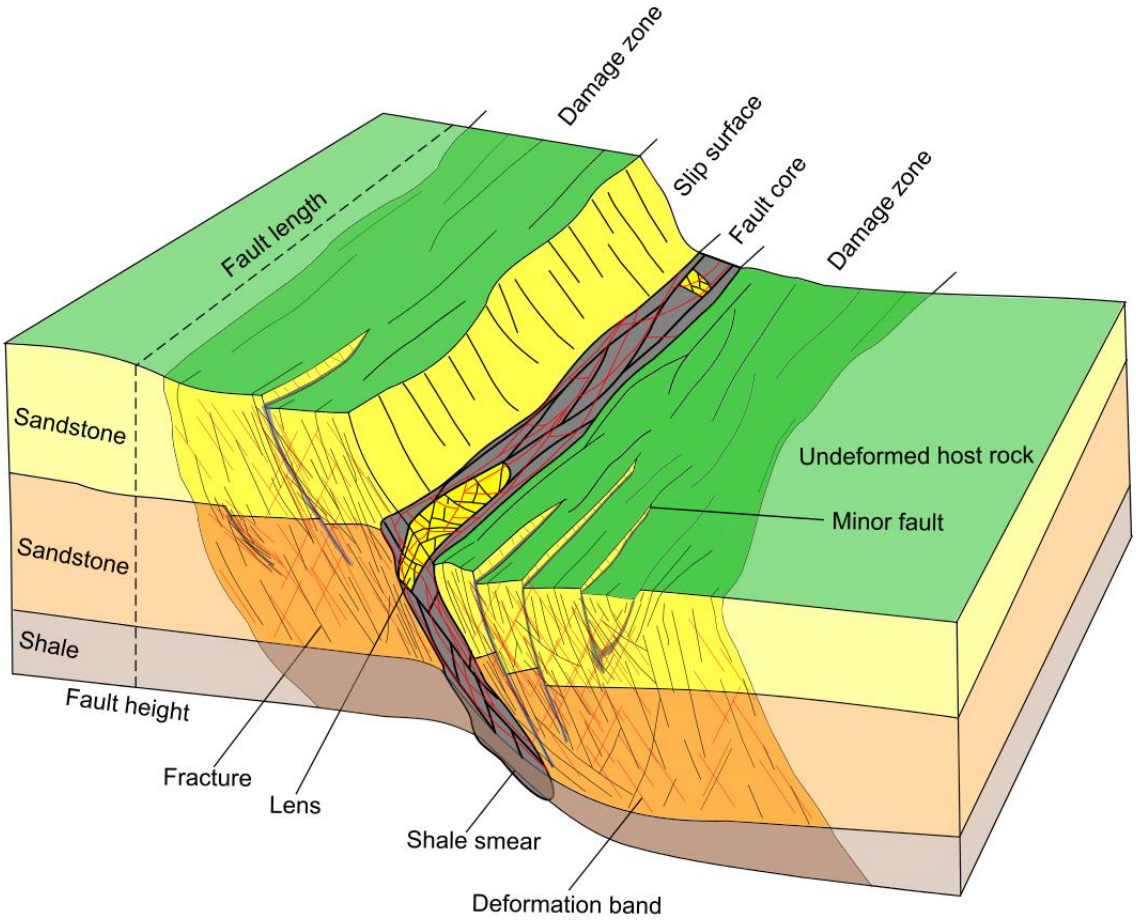

Figure 1.4.1: *Principal sketch of the fault zone architecture and elements encountered in fault zones. Note how the damage intensity and deformation structure density increases towards the main fault core and around the fault cores of the minor faults located in the damage zone of the main fault.*

1.4.2. Fault rocks

Fault rocks are deformed, altered rocks situated in the fault core, surrounding the principal slip surface(s). These fault rocks make up the architectural framework of the fault core. The type of fault rocks situated in the fault core are controlled by several factors such as host rock lithology, fault displacement, the strain rate, degree of reactivation, presence of fluids and the pressure-temperature conditions or burial depth (Sibson, 1977; Sperrevik et al., 2002; Shipton et al., 2006; Wibberley et al., 2008). Fault rocks in siliciclastic rocks and carbonates tend to present a barrier to fluid flows across faults, due to the reduction in porosity and permeability compared to the surrounding host rocks (Færseth et al., 2007; Wibberley et al., 2008). The changes in the petrophysical properties are caused due to deformation mechanisms such as pore collapse, grain size reduction and smearing of phyllosilicates and clay minerals (Sperrevik et al., 2002; Torabi et al., 2013). In addition, cementation and mineralization within the fault core often occur, and many fault rocks experience an increase in quartz or calcite cementation or grain-contact quartz dissolution following the deformation within faults (Sverdrup and Bjørlykke, 1997; Knipe et al., 1998; Sperrevik et al., 2002). In this project different fault rocks have been observed at the studied localities and the most common features are described and explained below.

Cataclasite or sandstone gouge (Figure 1.4.2 D) usually occurs in pure, porous sandstone faults and are a cohesive, fine-grained fault rock (Engelder, 1974; Schultz and Fossen, 2008). The original sandstone grains crushes due to friction mechanisms involving fractures and rigid-body rotation during the faulting (Engelder, 1974). Experiments done by Mandl et al. (1977) shows that cataclasites in faulted porous sandstone deforms first by pore collapse and then, given high effective stress, by grain breakage and crushing. In cataclasites, quartz cementation can occur with the right pressure-temperature condition, due to the compaction of grains and increasing grain-grain contact surfaces (Sverdrup and Bjørlykke, 1997; Bjørlykke et al., 2005).

Fault gouge occurs when fault rocks are further crushed and deformed, so much that the few original grains are almost entirely surrounded by a very fine-grained matrix of crushed grains (Engelder, 1974). This fine-grained and non-cohesive fault rock is often chemically altered compared to the original host rock and is a typical product of cataclasis at lower pressure and temperature regimes (Engelder, 1974; Fisher and Knipe, 1998). Fault gouge usually consists of more than 90 % fine-grained particles, but up to 10 % of the original grains can be located in the fine-grained matrix. Experimental studies performed by Engelder (1974) suggest that grain size and sorting of fault gouge decreases as fault displacement and confining pressure increases.

Shale smear forms usually when a shale or clay-rich sequence is ductilely rotated and sheared into the fault zone (Figure 1.4.1 and 1.4.2 C). Smears located in the fault core originate mainly from shales or clay layers, but coals, sands, and carbonates are also known to form smearing in the fault core

(Færseth, 2006). Sand smearing in the fault core appears to occur before consolidation and under low confining stresses (Bastesen et al., 2013). In fault sealing analysis in hydrocarbon exploration, the shale smear factor (SSF) is used to evaluate the sealing potential of faults and this method evaluates the relationship between the vertical thickness of the shale layer versus the fault displacement (Lindsay et al., 1993; Færseth et al., 2007). The membrane formed by shale smearing can create a barrier to fluid flow across the fault for a displacement that is as much as four times the thickness of the shale layer (SSF=4) (Færseth et al., 2007). For SSF values smaller or equal to 4, the smear is interpreted to be continuous for major faults and a barrier to fluid flow across the fault, but minor faults commonly have an SSF=7, which indicates that the smear is not continuous and hence not sealing (Færseth, 2006).

Fault core lenses are defined as lozenge-shaped rock bodies, oriented parallel to the main fault and bounded on all sides by slip surfaces (Lindanger et al., 2007; Braathen et al., 2009). The incorporation of lenses into the fault core is generally related to mechanisms such as fault splaying and asperity or tip-line bifurcation processes inside the fault core or in the surrounding damage zone (Lindanger et al., 2007; Childs et al., 2009). Typically lenses consist of deformed or intact host rock, derived either from the footwall or the hanging wall of the fault (Figure 1.4.1 and 1.4.2 A), but lenses derived from fault rocks and/or vein minerals are also common (Bastesen et al., 2013). Childs et al. (2009) suggest that breached relay ramps are a major source for host rock lenses in the fault core, as fault surface irregularities break off during the breaching and form areas of fault-bounded lenses. If host rock lenses are incorporated in the fault core, they represent an uncertainty in fault sealing analysis, since they may create a flow path for fluids across the fault within a faulted reservoir (Lindanger et al., 2007). Since lenses incorporated in the fault core could be relatively undeformed, the porosity and permeability of the lens could be approximately equal to the host rocks, and this will influence the fluid communication along and across the fault.

Fault breccia is a cohesive or non-cohesive fault rock (Figure 1.4.2 B), which consists of randomly oriented host rock fragments or clasts, which are incorporated in a fine-grained matrix. Post-fault cementation can occur due to fluid migration through the fault breccia, where the cement are infilled in void spaces or replaces the fine-grained matrix (Woodcock and Mort, 2008). Fault breccia can be classified based on the fabric and primary cohesion of the fault rock (Sibson, 1977) or by the clast size and clast proportion of the fault rock (Woodcock and Mort, 2008). Classification based on the clast size and proportion is probably preferable because it can be difficult to identify and distinguish primary versus secondary cohesion within the fault breccia.

Figure 1.4.2: *Different types of fault rocks observed in the fault core in sedimentary rocks. (**A**) A carbonate lens situated in the fault core of a right lateral strike-slip fault, Vallone di Santo Spirito, Italy. (**B**) Fault breccia, consisting of carbonate fragments incorporated in a beige, fine-grained matrix in the fault core of a right lateral strike-slip fault, Vallone di Santo Spirito, Italy. (**C**) Shale smearing and some minor sandstone breccias in the fault core of a normal fault, Outside Arches National Park, Utah. (**D**) Cataclasite situated in the fault core where two normal fault segments connect, Outside Arches National Park, Utah.*

1.4.3. Damage zone

The damage zone is the volume of brittle deformed rocks surrounding the fault core and are associated with fault initiation, propagation, interaction, as well as the evolution of the fault through the time, and have been used to understand fault evolution and growth (Cowie and Shipton, 1998; Shipton and Cowie, 2003; Kim et al., 2004; Childs et al., 2009; Choi et al., 2016). The density of deformation decreases outwards from the fault core and into the damage zone (Berg and Skar, 2005). In the damage zone, deformation structures such as fractures and minor subsidiary faults, antithetic and/or synthetic to the main fault, altered host rocks, stylolites or pressure solution seams and different types of deformation bands can be found depending on the lithology and initial porosity of the deformed rocks (Figure 1.4.1) (Shipton and Cowie, 2003; Berg and Skar, 2005; Wibberley et al., 2008; Viti et al., 2014). The damage zone width is constrained by a spatial distribution of deformation structures within the damage zone (Choi et al., 2016). Often the distribution of the damage zone around a fault is asymmetric, due to the different competency of the faulted rocks in the hanging wall and footwall. Figure 1.4.3 shows the Bartlett Fault, one of the Moab splay faults in Utah, and illustrates the asymmetry of the damage zone, due to different competency of the rocks surrounding the fault.

Figure 1.4.3: *In the aeolian sandstone units in the footwall, the damage zone width is relatively narrow, ranging from 43-70 m within the two members. The width was defined by measuring the density of deformation bands and fractures in the footwall (Berg and Skar, 2005). The Cedar Mountain Formation in the hanging wall consists of various fluvial sandstones, and the damage zone is affected by a fault-parallel syncline, creating drag folding (green dashed lines) which extends for several hundred meters towards the NE. Note the encircled car in the left corner for scale.*

1.4.4. Deformation bands

A deformation band is a millimeter-thick tabular zone of localized deformation that occurs in deformed porous sediments and rocks in a variety of depositional- and structural environments (Fossen et al., 2007). They do not show any continuous or mechanically weak fracture surfaces, although slip surfaces with displacement ranging from millimeter to centimeters, may develop in deformation band clusters (Figure 1.4.4 B), where eventually a fault can be initiated (Aydin and Johnson, 1978). The internal characteristics of deformation bands have the potential to change the petrophysical properties of reservoirs, e.g. reduce the permeability up to 3-4 orders of magnitude compared to undeformed host rock (Fossen and Bale, 2007). However, single deformation bands could display variations in both porosity and permeability along single bands (Torabi and Fossen, 2009).

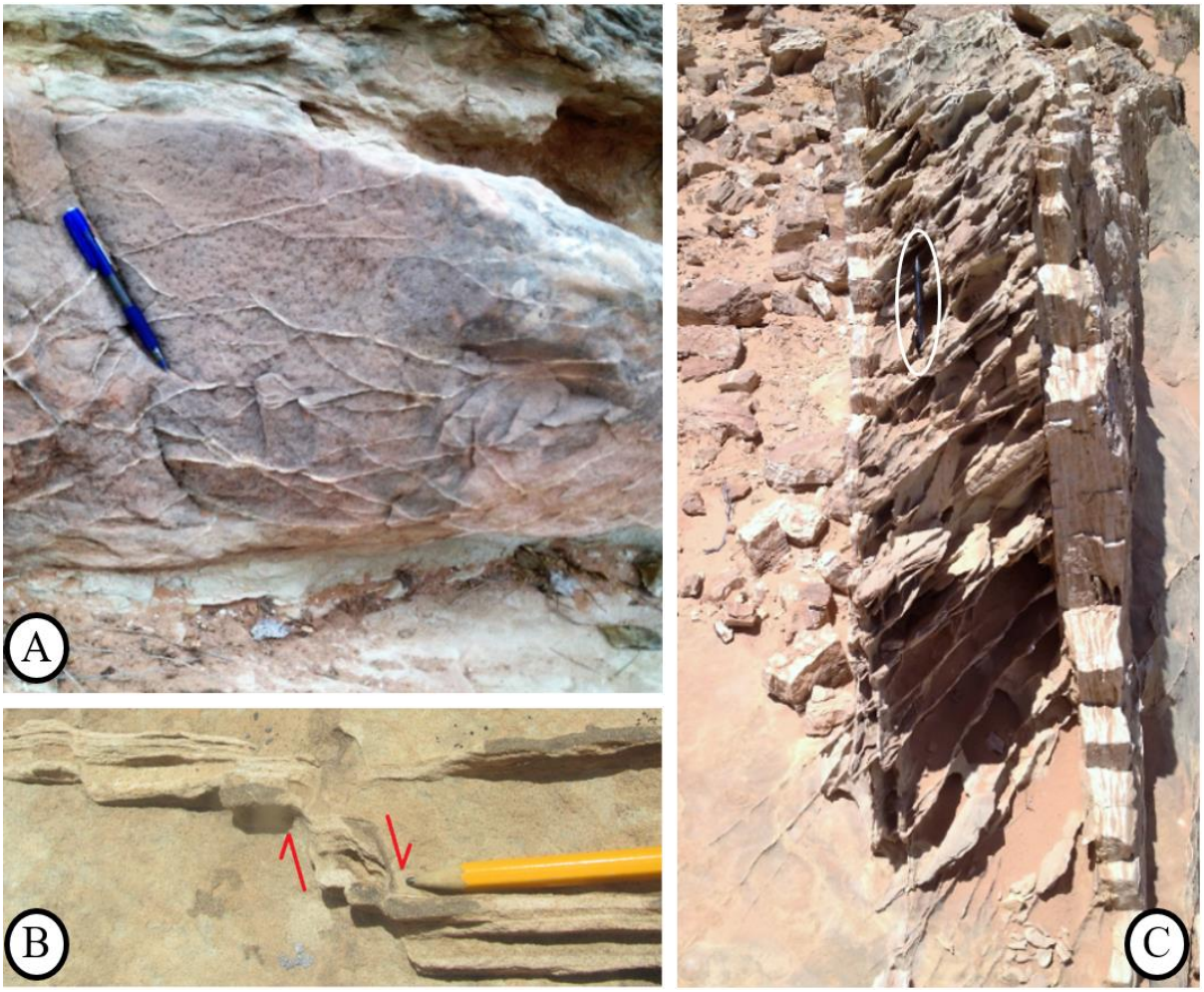

Figure 1.4.4: *Deformation bands observed in the field. (**A**) Connected cataclastic deformation bands, located in the damage zone of the Hidden Canyon Fault, Utah. (**B**) Deformation bands displaying a few centimeters of offset, San Rafael Desert, Utah. (**C**) Cataclastic deformation band cluster connected in a ladder pattern, located in the Entrada Sandstone, close to the "6-meter fault", Goblin Valley, Utah. Note the encircled pen for scale.*

Deformation bands can either be classified based on the kinematical mechanisms or the deformation mechanisms creating the band. The kinematics developing deformation bands (Figure 1.4.5) is either related to shearing (no pore volume changes) or compaction (decreasing pore volume) or dilation (increasing pore volume) or a combination of this three kinematics (Aydin et al., 2006; Fossen et al., 2007).

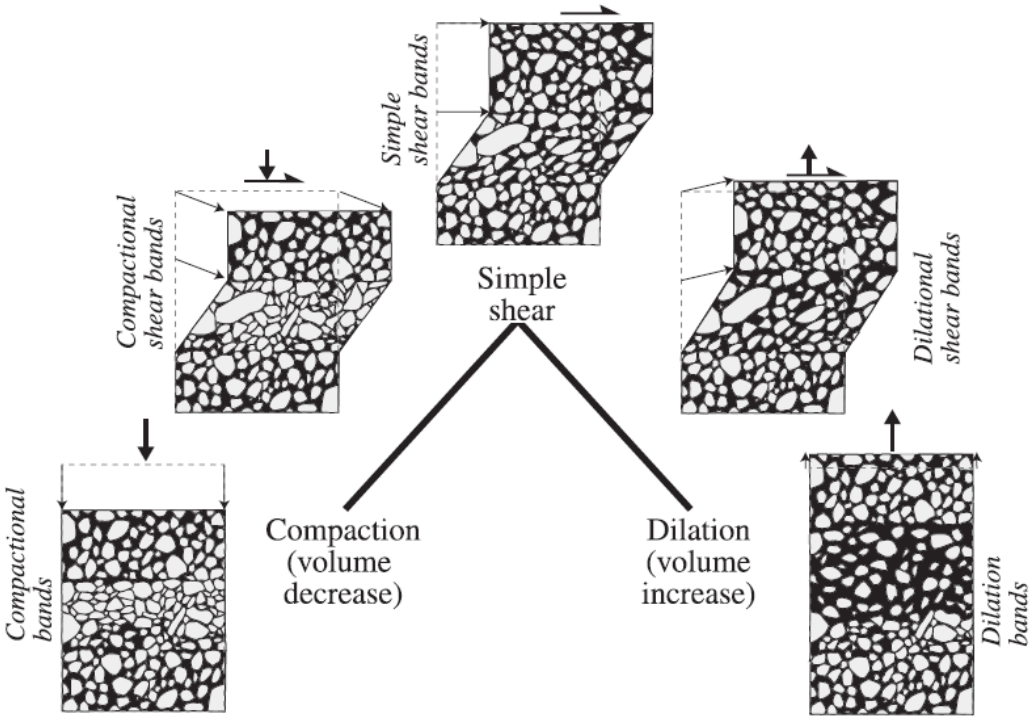

Figure 1.4.5: *Classification of deformation bands from the kinematic mechanisms creating the band. From Fossen et al. (2007).*

Classification based on the deformation mechanisms comprises three main types: disaggregation bands, cataclastic bands and cementation bands (Torabi, 2014). These deformation mechanisms are dependent on several physical factors such as confining pressure (burial depth), stress regime (tectonic environment), strain rate, pore fluid pressure, host rock lithology and host rock properties (Fossen et al., 2007; Torabi and Fossen, 2009). Deformation band formation is very sensitive to different host rock properties, such as mineralogy, cementation, porosity, grain size, grain sorting and grain shape (Fossen et al., 2007). Disaggregation bands develop by shear related disaggregation of grains, often found in poorly consolidated sandstones (Mandl et al., 1977; Fossen et al., 2007). Cataclastic bands form by grain fracturing, crushing, and abrasion (cataclasis), where porosity and the different grain properties play a significant role in the development. Dissolution and cementation of deformation bands occur during, or more commonly after deformation, and this process forms the cementation bands (Fossen et al., 2007).

1.4.5. Pressure solution seams

Pressure solution seams (PSS), also described as stylolites by Viti et al. (2014), are deformation structures associated with pressure solution processes, resulting in volume reduction in the rocks (Nenna and Aydin, 2011). PSS are closing mode structures of localized grain dissolution, which tend to form perpendicular to the maximum compressive stress direction, σ_1 (Nenna and Aydin, 2011). Viti et al. (2014) state that the formation of PSS can be divided into three main phases:

1) Dissolution and grain interpenetration at stressed grain contacts
2) Diffusion and removal of dissolved material through fluid flux in the spacing
3) Formation of PSS, through precipitation of soluble components in low-stress interfaces such as pores and/or cracks

The evolution and propagation of these structures is dependent on several factors such as the mineralogy of the host rock, the local stress conditions in the surrounding rocks, temperature-pressure conditions, presence of fluids on grain surfaces and micro-textures such as defects in the crystals and dislocation density (Meike and Wenk, 1988; Nenna and Aydin, 2011; Viti et al., 2014). In carbonate rocks, PSS play an important role during the deformation, where PSS can influence fault nucleation and growth (Willemse et al., 1997; Peacock et al., 1998). PSS have also been suggested to impact hydrocarbon migration, where Peacock et al. (1998) suggest that PSS within carbonate rocks can act as permeability barriers and restrict the flow within the reservoir.

1.4.6. Fault displacement and offset

The term displacement has several synonymous definitions, but in general for faults, displacement is the vector for the relative movement between two originally adjacent points on each side of the fault (Peacock et al., 2000). The maximum fault displacement is theoretically located in the central parts of a fault and will gradually decrease towards the fault tips (Barnett et al., 1987).

The displacement vector direction describes the relative movement of one side of the fault compared to the other side, while the magnitude of the vector gives the total offset for the two fault walls. Strike separation is the horizontal displacement measured along the strike direction of the fault and the dip separation is the vertical displacement measured along the dip direction. The dip separation can be sub-divided into a horizontal component (heave), which is the horizontal distance normal to the fault strike, and a vertical component (throw).

A similar term used to describe fault displacement is offset, addressed by Peacock et al. (2000) as the apparent displacement of a marker, like e.g. a layer or horizon. Another term also used is slip, but slip has been used to describe one seismic event (Cowie and Shipton, 1998; Shipton et al., 2006), while displacement specifies the complete fault history.

1.5. State of the art on the scaling of fault core thickness and displacement

Studies of statistical distribution of fault geometric attributes (fault displacement, length, damage zone width and fault core thickness) and scaling relationships between them has been in focus for many decades (e.g. Knott, 1994; Clark and Cox, 1996; Shipton et al., 2006; Schultz et al., 2008; Wibberley et al., 2008; Childs et al., 2009; Bastesen and Braathen, 2010; Torabi and Berg, 2011; Bastesen et al., 2013). Different fault attribute data have been interpreted and analyzed in order to predict the value and distribution of these attributes in geological models made for the subsurface.

Among the fault geometric attributes, the fault core thickness is the most uncertain fault attribute. Fault core thickness (*T*) is the thickness of fault rocks situated within the fault core, and the thickness can show rapid variations over short distances along the fault. Shipton et al. (2006) studied fault cores in different lithologies and observed how the fault core thickness could vary by a full order of magnitude along the faults. The great variations in fault core thickness over relatively short distances make it less predictable at fault jogs and when variations in lithology occur along a fault (Shipton et al., 2005; van der Zee et al., 2008; Torabi and Berg, 2011). However, there is no standard definition of fault core and its boundaries and measurements of the fault core thickness have often been subjective (Shipton et al., 2006; Childs et al., 2009; Torabi and Berg, 2011). Furthermore, in the literature an inconsistent use of terminology and definitions for describing the fault core. What some authors define or describe as the fault core (Caine et al., 1996; Davatzes et al., 2005; Shipton et al., 2006; Bastesen and Braathen, 2010; among others) other authors (e.g. Knott, 1994; Foxford et al., 1998; Wibberley et al., 2008; Childs et al., 2009) describe as the fault zone or fault zone thickness. The fault zone term is again used by other authors (e.g. Caine et al., 1996; Evans et al., 1997; Billi et al., 2003; Agosta and Aydin, 2006) to describe a fault containing a damage zone and a fault core, making the terminology more confusing. This uncertainty in definition and terminology of the fault core and its boundaries makes constraining the dimensions of this attribute challenging (Torabi and Berg, 2011).

A similar description of the fault core thickness is fault thickness, addressed by Peacock et al. (2000) as: " the extent of the deformation and grain size reduction in a fault zone, usually measured perpendicular to the fault". Another similar term used is gouge thickness, which is the thickness of crushed material incorporated between slip surfaces, defined by Byerlee and Summers (1976).

In this project, the fault core thickness is defined as the thickness of fault rocks or fault breccias, crushed material and lenses incorporated between slip surfaces in the fault core. This definition has been used for fault core thickness measurements in the field and on pictures.

Fault displacement is a general term used in fault terminology to describe the movement of two originally adjacent fault blocks along a fault plane, which can be measured in any specified direction (Walsh and Watterson, 1988; Peacock et al., 2000; Torabi and Berg, 2011). Fault displacement is

frequently used in scaling relationship, to examine the relationship with other fault attributes (e.g. Clark et al., 1999; Wibberley et al., 2008; Faulkner et al., 2011; Rotevatn and Fossen, 2012). The displacement data in the literature have been collected and measured in various ways, as cumulative displacement along fault segments, or as the maximum displacement theoretically located in the center of faults (Yielding et al., 1996; Torabi and Berg, 2011). Statistical analysis conducted by Torabi and Berg (2011), shows that displacement populations of faults, regardless of lithology and fault type, generally display a power-law scaling over 3-5 orders of magnitude and the power-law exponent (*n*-value) are in the range of 0.34-1.34. As faults propagate and interacts, the displacement becomes redistributed and transferred along the whole fault segment (Peacock and Sanderson, 1991; Torabi and Berg, 2011). This interaction and linkage of fault segments would eventually generate the formation of a relay structure between the fault segments, and the geometry of this structure could be related to the displacement gradients at the fault tips (Peacock and Sanderson, 1991). These fault segment linkage points generally expose a displacement minimum, and on the displacement profile a concave-up trend can be observed (Ellis and Dunlap, 1988; Peacock and Sanderson, 1991). The variations and changes in displacement profile would likely affect the displacement distribution of faults at their different phases of evolution in a fault system (Torabi and Berg, 2011).

Since the fault core thickness is the most uncertain attribute and hard or impossible to capture on seismic, the measurements are usually conducted on the outcrops. The correlation of fault core thickness with fault displacement involves some uncertainties as the definitions of fault core are often subjective and uncertain (Shipton et al., 2006; Childs et al., 2009; Torabi and Berg, 2011).

Otsuki (1978) presented the first data on the scaling relationship between the fault core thickness (*T*) and fault displacement (*D*) and he expressed the relationship with the equation:

$$\log D = a \log T + b \quad (1)$$

Where the constant *a*, is approximately 1 and suggest that growth mechanisms of the fault core thickness in nature are similar to the experiments conducted by Otsuki (1978). While the value *b* is nearly the same in different types of faults, in spite of the different rock strength (Otsuki, 1978). Evans (1990) used the data from Otsuki (1978) and Robertson (1983), and observed that there is at least two orders of magnitude scatter of the displacement and fault core thickness on a log-log scale. On a linear plot, the scatter was too great that no statistical relationship could be found.

A power-law relationship ($T=yD^n$) between the fault core thickness and fault displacement was reported by Knott et al. (1996) for normal faults measured at outcrops in western Sinai and northern Britain, but Knott et al. (1996) suggested that this relationship could be affected by lithology and layer thickness. Sperrevik et al. (2002) confirmed this lithological dependence of the fault core thickness, where their research demonstrated that for a given fault displacement, sandstone juxtaposed against sandstone will give a greater fault core thickness, than sandstone juxtaposed against shale.

A positive correlation between the fault displacement and fault core thickness was observed by Shipton et al. (2006), although the thickness can vary along the strike and dip of a fault (Evans, 1990; Foxford et al., 1998). Bastesen and Braathen (2010) found a power-law correlation with an *n*-exponent of approximately 0.6 which represented the general relationship between the fault displacement and fault core thickness in fine-grained carbonates. This trend line fits with similar datasets from Shipton et al. (2006) and Braathen et al. (2009)

Kolyukhin and Torabi (2012) analyzed several data sets of fault core thickness, damage zone widths and fault length versus fault displacement, using a statistical method called the Bayesian Information Criterion (BIC) and maximum likelihood. This statistical approach suggests that the fault core thickness and fault displacement relationship are scale dependent and that one single power-law equation is not sufficient for a range of displacements and could vary with fault type and lithology.

1.6. Methods

1.6.1 Field data

At the studied localities, a 50 m long scanline was conducted at the base of the outcrop, defining an area of the outcrop that should be investigated in this project. The scanline was used for positioning different faults at the outcrop, and the length of the scanline varied at each locality. In the field, two workers moved along the base of the outcrop, following the scanline. When a fault was observed, the position of the fault was recorded, and fault core thickness measurements were completed along the fault plane at different elevations or height (levels) every 60 or 30 cm, if great variations were observed along the fault core. The first fault core thickness measurement were completed at level 0, at the base of the outcrop and then at different levels along the fault core. The fault core thickness measurement was completed by placing a measuring tape perpendicular across the defined fault core, measuring thickness of the visible fault rocks situated in the fault core. The fault core boundary was defined by the location of fault rocks located in between synthetic slip surfaces (with the same dip direction and sense of displacement). The fault rocks are distinguished by the grain size reduction, internal deformation and alteration (color, physical or chemical) compared to the surrounding wall rocks. The fault core thickness measurements recorded were completed on isolated fault segments, overlapping and linked fault segments, capturing the lateral variations in fault core thickness. Figure 1.6.1 illustrates how the measurements were conducted in the field. The fault lenses that were situated in the fault core between slip surfaces were included in the thickness measurements. Other measurements recorded at the studied faults were fault orientation, fault displacement (if possible), type and description of fault rocks situated in the fault core.

The devices used to measure the fault core thickness, and fault displacement was a 2 m long carpenter's folding ruler and/or a 8 m long measuring tape, both with a metric scale. The smallest increment on the carpenter's folding ruler is 1 mm (0.001 m). Fault displacement was measured using displaced markers along the fault.

At two of the studied localities, Hidden Canyon Fault and R-191 Canyon, measurements of the fault core was performed at different intervals along the elevation (height or levels of the fault) because of the accessibility of the fault at higher levels in the vertical sections. Here a scanline was conducted along the faults and fault core thickness measurement was completed every 5 m (Hidden Canyon Fault) and 2 m (R-191 Canyon). This method also captured the lateral fault core thickness variations at both of the localities.

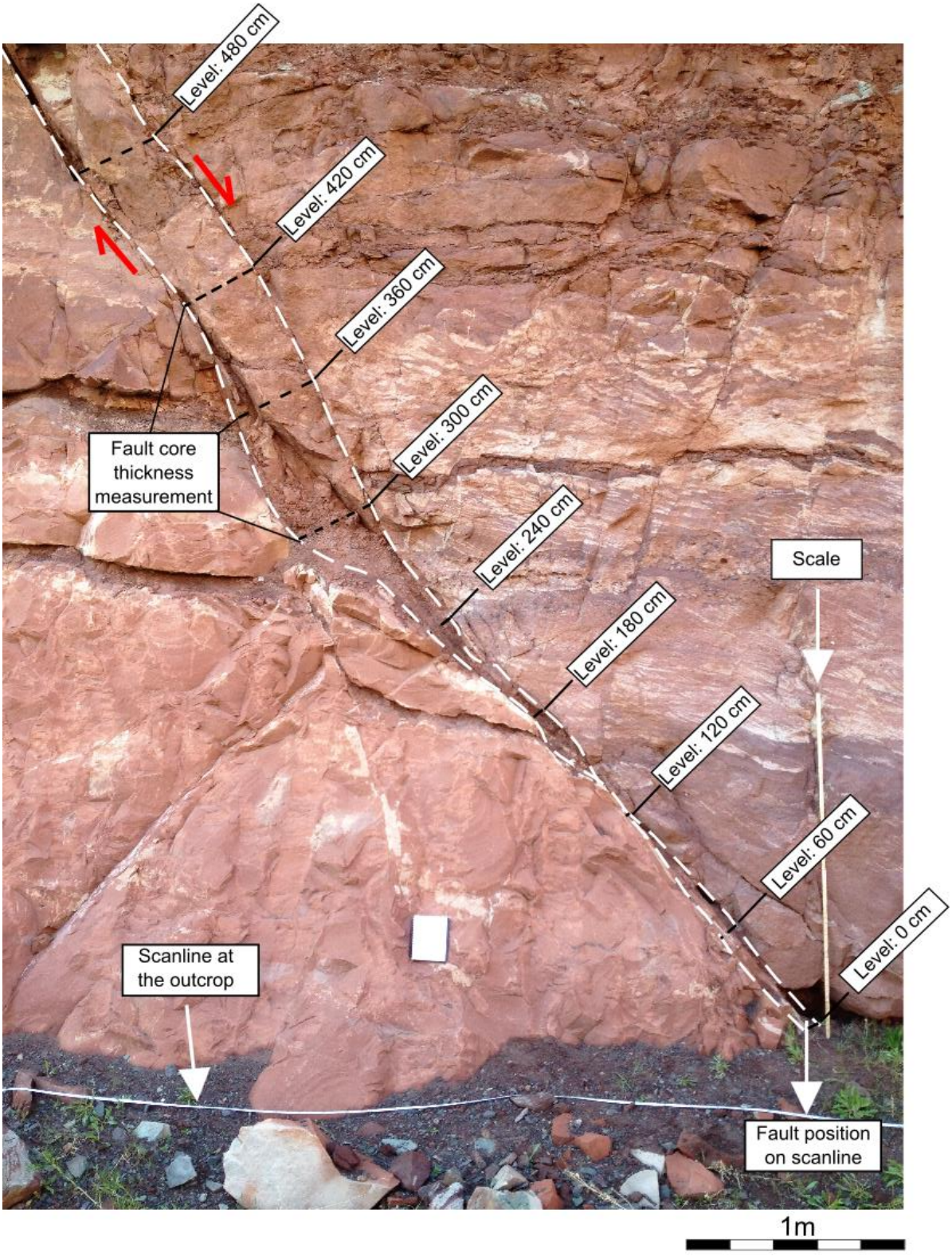

Figure 1.6.1**:** *Illustration of one of the measured faults in the field. The data collection started with recording the fault position on the scanline. Afterward, the fault core thickness (dashed black lines) was measured every 60 cm (level) along the fault height. The first measurement was performed at level 0 at the base of the outcrop, and then the fault core was measured at different levels along the fault, as illustrated in the figure. In the field, the measurements were limited to the lowermost 2-3 m, so picture measurements have been completed on the higher levels, not accessible in the field.*

1.6.2. Measurements on outcrop pictures

Pictures of the studied and measured faults were taken at the outcrops, and these pictures were used to verify and collect more fault core thickness and fault displacement measurements, in areas not accessible in the field. Because many of the outcrops were cliffs and/or steep exposures, the accessibility and data gathering in the field was generally limited to the lowermost 3-4 m. In the study area in Vallone di Santo Spirito, at some of the outcrops the base was covered by dense vegetation, reducing the accessibility in the field even more. Pictures of the faults were taken with a scale next to the faults and the completed measurements were done using the software Inkscape 0.91 and ImageJ. The fault core thickness measurements were completed at intervals similar to outcrop measurements or at points where fault displacement was measured. Figure 1.6.1 illustrates how the fault core thickness measurements were performed on the higher parts of the fault, using pictures. The picture measurements at lower levels were compared and correlated with the field measurements to verify the accuracy of the measurements. Then the comparison between the field and picture measurements for the lower parts was used to find the degree of fit (R^2), to verify the accuracy of the picture measurements completed in the higher parts of the outcrop. In southeastern Utah, a total of 145 picture measurements could be compared to the field measurements. The best fit is a linear trendline with the formula $y = 1.0211x + 0.9302$, and this gave a best of fit R^2 of 0.9641 (Figure 1.6.2 A). While for the picture measurements completed in Vallone di Santo Spirito, a total of 178 measurements could be compared to the field measurements. The best fit of these measurements was also a linear trendline with the formula $y = 0.8813x + 1.0842$ and this gave a best of fit R^2 of 0.9401 (Figure 1.6.2 B).

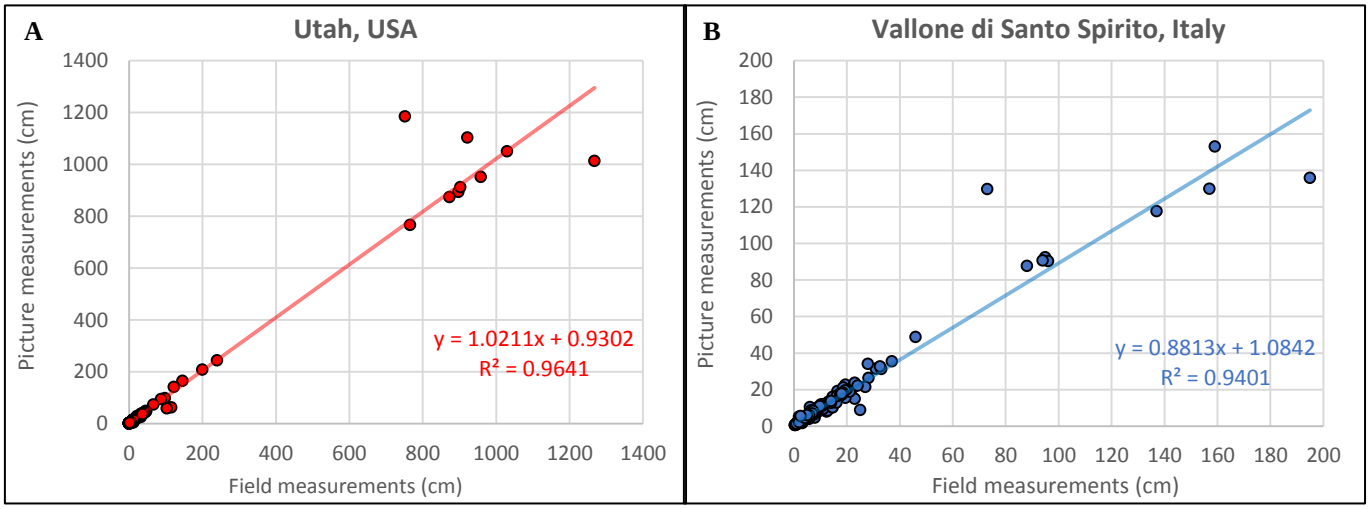

Figure 1.6.2: *Plots comparing the data collected in the field to data gathered from pictures, for the same faults. The comparison of measurements was used to verify the accuracy of the picture measurements completed. The regression found with the relationship indicates a positive correlation between data gathered in the field and data gathered from pictures. (**A**) Represents the Utah measurements in siliciclastic rocks. (**B**) Represents the Vallone di Santo Spirito measurements in carbonates.*

Many of the completed fault displacement measurements in this project have been carried out using picture measurements, since observable fault displacement at the outcrop was mainly in the higher parts, not accessible in the field.

1.6.3. Possible sources of error and uncertainties

Regarding the accuracy of the fault core thickness and displacement measurements from pictures, the best results from picture measurements are from pictures parallel to the strike of the fault and where the fault core was close to the center of the picture. However, due to topography around the studied faults, pictures at optimal angle displaying the fault core in the center was in some cases impossible. The most reliable measurements are the field measurements, and these were used to verify the accuracy of the picture measurements completed on levels not accessible in the field (Figure 1.6.2 A and B).

In the studied areas, the observed fault core shows great lateral variation in thickness at the different levels and this variation is represented in the completed measurements. Comparing the average fault core thickness measurements in the field to the picture measurements, different average values are generally displayed. The general lateral variation in fault core thickness was better investigated on pictures since the outcrop measurements covered mostly 3-4 meters of the accessible fault height.

1.6.4. Statistical treatment of data

For geologists, geostatistics involves the study of the distribution of sizes, thickness or accumulations (Matheron, 1963). The distribution of different data often reveals a recognizable pattern in nature, which could be investigated using statistical analysis. Applying univariate statistics, one variable is analyzed and investigated to determine how it is distributed. This variable may be fault core thickness or fault displacement, for a set of faults in a region. There are several ways to investigate and display the distribution of an attribute. Cumulative frequency plots and exceedence frequency (EF) plots are similar and can both be used to recognize the distribution type of the collected data. The exceedence frequency is calculated as the following:

$$EF_{Xi} = \frac{n-n_i}{n} \quad (2)$$

Where EF is the exceedence frequency for a given value on the X-axis, n is the total number of data used and n_i is the rank committed to the x-value after the data have been sorted. Recognizing a trend on the plotted data, a distribution type of the data can be determined. The most common types of parametric distribution are:

- Normal or Gaussian distribution
- Exponential or Poissonian distribution
- Logarithmic or lognormal distribution

- Power-law or hyperbolic distribution

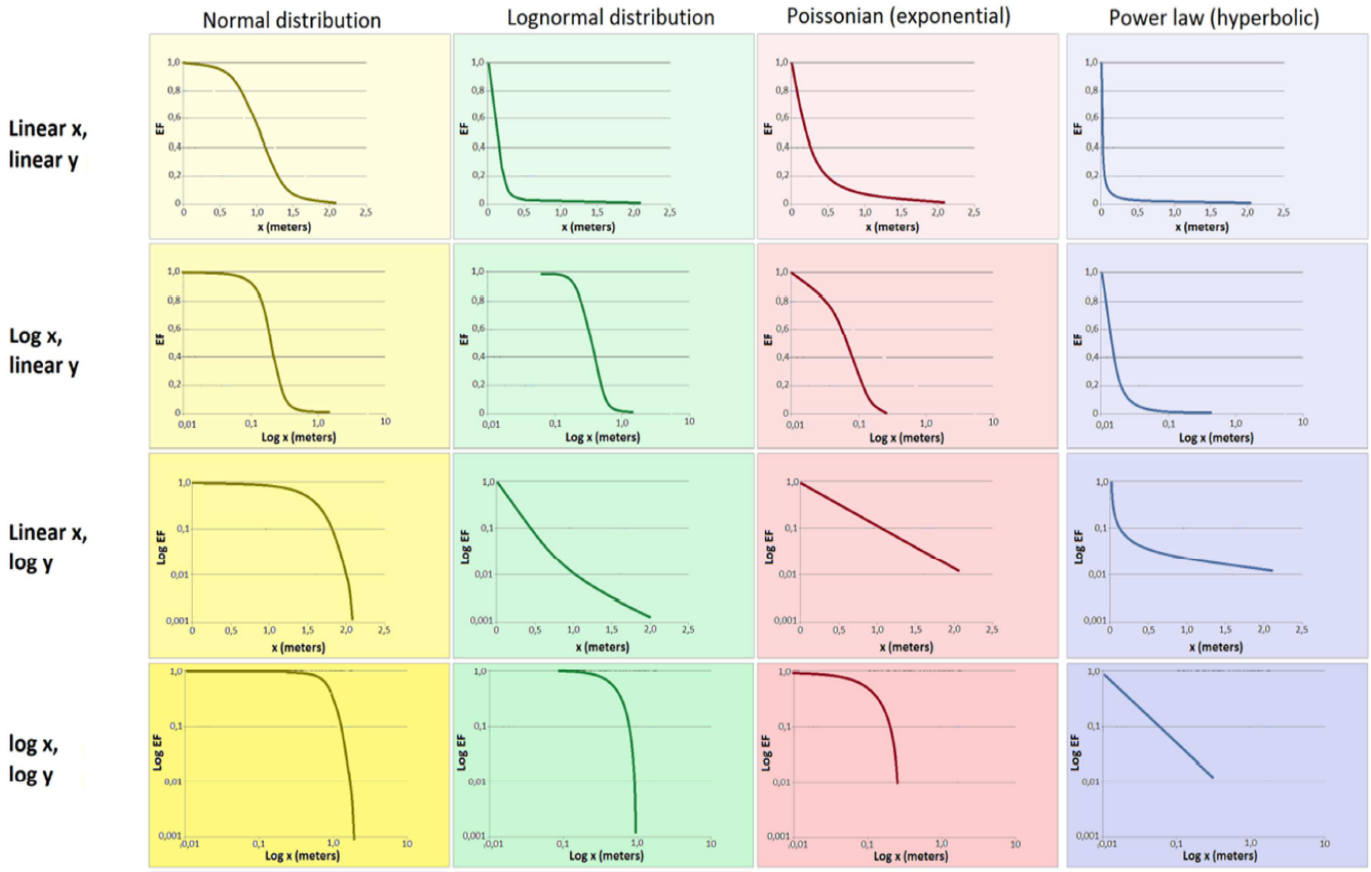

Figure 1.6.3: *EF plots used as a guide to determine the distribution trend/patterns of the collected data. Data which follows a trend may be parametric statistical analyzed. Plot from Seifried (2012), based on diagrams in Nemec (2011).*

Exponential or Poissonian distribution ($f(x) = a * \exp(x)$), the data is generally controlled by one dimension, such as distance or time. Characteristics for exponential distribution are the straight line of plotted data in log EF- linear X plot. The mean ($\bar{x}$) and variance (S_x^2) values are equal to one and another in Poissonian distribution.

Logarithmic or lognormal distribution ($f(x) = a * \log_a(x)$) are characterized by a slightly concave-up trend in the log EF-linear X plot and a concave down trend in the log EF-log X and EF-log X plot. The Y will show a normal distribution, regardless of the value based on.

Hyperbolic or power-law distribution ($f(x) = ax^b$) can be distinguished by investigating the element of self-similarity of the data, the property of a given object retains its ratios of dimension at any given scale (Clauset et al., 2009; Sornette, 2009). For a geometric object that shows self-similarity, it is called a fractal and the power-law forms a hyperbolic curve in a normal EF-plot when describing the fractal. Characteristics of a power-law distribution is the straight line of plotted data on a log EF-log X plot and the hyperbolic curve on the EF-X plot. Power-law distribution will typically involve

fluctuations towards the endmembers and a "tail" following a concave down pattern can be recognized, which make the distribution trend hard to detect (Torabi and Berg, 2011).

Trends and patterns in nature, don't follow perfect textbook examples, so the EF-plots need to be investigated and analyzed. In this project, EF-plots have been used as a guide to determine or recognize the distribution trends of the measured data (Figure 1.6.3) and to determine if parametric statistical analysis can be applied. EF-plots have been made using fault core thickness data from all the studied localities and fault displacement data from the outside Arches National Park (ANP) locality. The type of distribution is then used to determine how the collected data should be analyzed.

Bivariate statistics includes correlating two different variables, to investigate the relationship between the two variables. The aim of the analysis is to determine if a relationship between the two variables exist, and how they are related. This means that one variable (y-value) is dependent on the other variable (x-value).

Correlation of two different variables, a regression line's fit or goodness of fit (R^2), describes the scatter associated with the variables and are found by squaring the correlation coefficient. This regression line creates a formula that is the best fit for the relationship. The range of R^2 is between 0.0 (no relationship or random scatter) and 1.0 (one variable is completely determined by the other variable).

2. Geological setting

This chapter introduces the tectonic and structural evolution of the two study areas and gives an overview of the stratigraphic framework.

2.1. The Colorado Plateau, southeastern Utah

The first field site for this project is located in the southeastern part of Utah, on the Colorado Plateau. The geology of Utah can roughly be divided into western and eastern parts. The western part consists of the Basin and Range province, which have been and still being affected by considerable crustal thinning and extension. The eastern part consists of the Utah branches of the Rocky Mountains to the north (Hintze and Kowallis, 2009) and the Colorado Plateau provinces to the south, which are relatively unaffected by the extension and have been elevated relative to the Basin and Range province (Pederson et al., 2002).

The Colorado Plateau

The Colorado Plateau is a high standing crustal block which covers an area of approximately 360.000 km^2 within southern and eastern Utah, northern Arizona, northwestern New Mexico and western Colorado (Figure 2.1.1 A). The plateau is bounded to the north and east by the Rocky Mountains and the Basin and Range province to the west. Towards the north, the Colorado Plateau is also bounded by the Uinta Mountains, to the southeast by the Rio Grande Rift Valley and to the south by the Mogollon Rim. The elevation of the Colorado Plateau ranges from 0.9 km – 4.3 km, with an average elevation of 1.6 km (Foos, 1999). This high altitude and the fact that the Colorado Plateau is situated in the rain shadow of the Sierra Nevada Mountains, the region is characterized by an arid climate (average annual rainfall of 25 cm) and consists of high dessert, with some scattered areas of vegetation and forests. The plateau is also as mentioned elevated higher than the base level of the Basin and Range province to the west, which leads to high rate of erosion and rivers cutting through the rock formations, like the Colorado River and its tributaries, resulting in the famous scenery of deep canyons, mesas and buttes (Foos, 1999).

Although the Colorado Plateau is elevated on an average of 1.6 km, the plateau was situated at sea level by the end of Cretaceous, evidenced by the deposition of the extensive Mancos Shale and Blackhawk Formation (Foos, 1999; Pederson et al., 2002). The Mancos Shale was deposited in an open marine environment in the Western Interior Seaway, a continental sea that connected the Arctic Ocean to the Gulf of Mexico through the interior US. The Blackhawk Formation was deposited when the retreat of the Western Interior Seaway began.

Although the Colorado Plateau is bounded by the highly deformed Rocky Mountains and Basin and Range Province, the overall interior of the platform is relatively undeformed compared to its surroundings and show no tilting or folding of the sedimentary strata (Foos, 1999; Levander et al.,

2011). Some deformation within the Colorado Plateau have occurred, igneous laccoliths have intruded the sedimentary succession creating the La Sal Mountains and the Henry Mountains in southeastern Utah (Pederson et al., 2002). Areas have been uplifted across the Colorado Plateau, like the San Rafael Swell and the Uncompahgre Ridge (Barbeau, 2003; Bump and Davis, 2003). Different basins have also been formed due to buckling and subsidence on the plateau, like the Paradox Basin (Figure 2.1.1 B and 2.1.2) and the Unita Basin (Foxford et al., 1996; Trudgill, 2011).

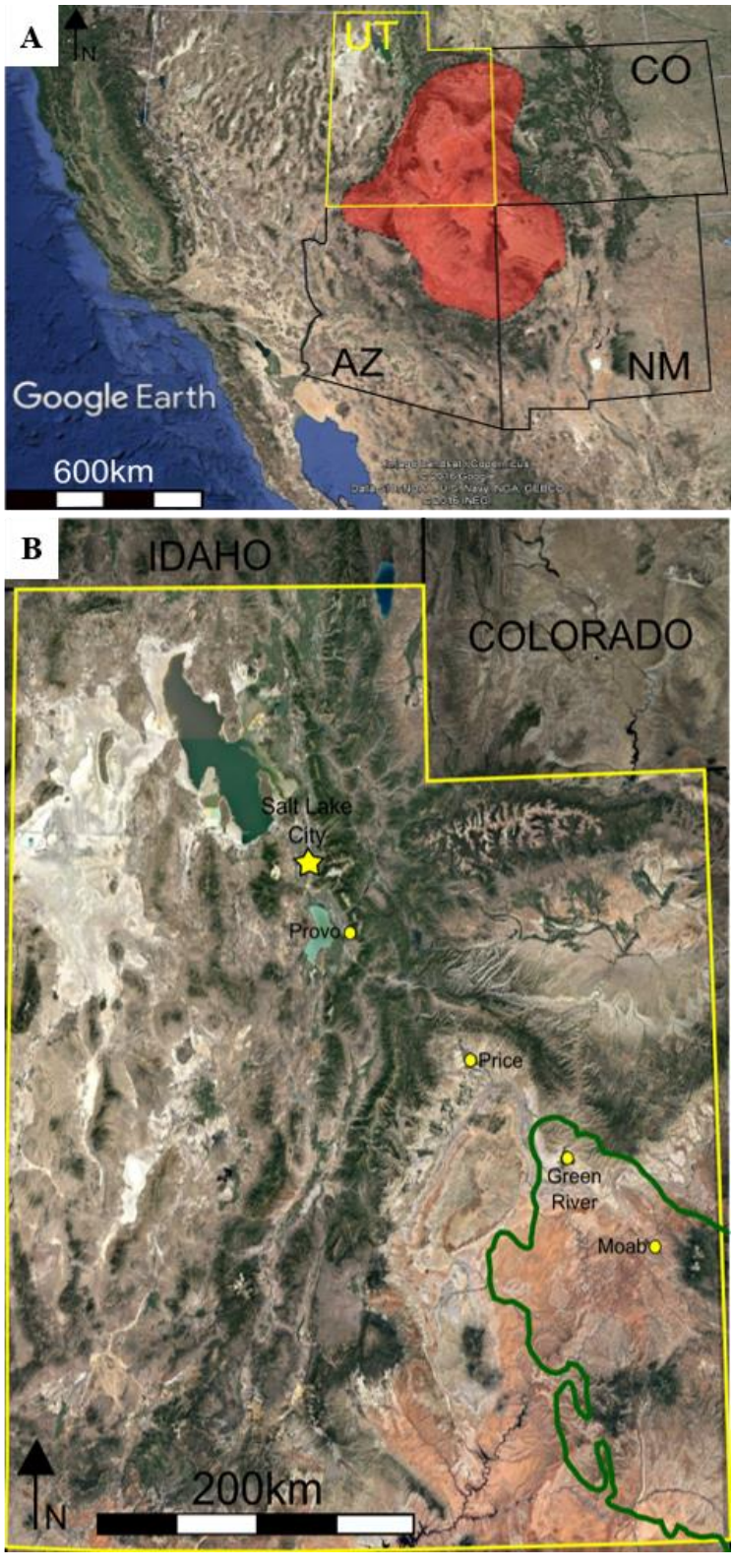

Figure 2.1.1: *Satellite photos over the study area (acquired from Google Earth). (**A**) Illustrating the western US, where the Colorado Plateau is highlighted in red and the state of Utah in yellow. (**B**) Satellite photo over the state of Utah. Encircled in dark green are the maximum extent of the Pennsylvanian Paradox Basin in southeastern Utah (after Trudgill (2011))*

2.1.1. Tectonic and structural evolution

The tectonic and structural evolution of the western US, Utah and the Colorado Plateau is rich and diverse, including several mountain building events, uplifts, subsidence of basins, erosion, and deposition of sediments. From the Cambrian and into the Paleogene the western margin of US has been bordered by subduction zones. In this time period, several collisions of island arc systems and micro-continents occurred, resulting in an extensive mountain belt occupying the entire length of the western US margin (Hintze and Kowallis, 2009).

The most important geological events that have the biggest impact on the studied areas occurred in the time interval between the Pennsylvanian (Late Carboniferous) and the Tertiary. During the Pennsylvanian-Permian, compressive forces from the collision between the supercontinents Laurentia and Gondwanaland (Trudgill, 2011), led to the formation of approximately 20 mountain ranges on the western interior of the US, collectively referred to as the Ancestral Rocky Mountain orogenic event (Smith and Miller, 1990; Barbeau, 2003; Hintze and Kowallis, 2009). This major continental collision, combined with the ongoing subduction on the western margin led to the major basement uplift of the Uncompahgre Uplift (Trudgill, 2011).

The Uncompahgre Uplift and Paradox Basin

The Uncompahgre Uplift formed in the Pennsylvanian as a major NW-SE trending basement-involved ridge and was located in present southeastern Utah and western Colorado (Figure 2.1.2) (Trudgill, 2011). The ridge was bounded to the southwest and northeast by a 200-300 km long fault zone, which was progressively buried by sediments (Barbeau, 2003). The major uplift of the Uncompahgre Uplift led to flexural subsidence on the southwestern edge, resulting in the formation of the Paradox Basin (Figure 2.1.2) (Hintze and Kowallis, 2009; Trudgill, 2011). The Paradox Basin is a large northwest-trending sedimentary foreland basin (190 km x 265 km) which developed along reactivated Precambrian basement faults, along the southwestern flank of the Uncompahgre Uplifts (Barbeau, 2003; Trudgill, 2011). The basin became isolated with a periodically restricted marine environment, due to the highlands in the north and east, and barriers to the west and south (Stokes, 1986; Doelling, 1988). In the Middle Pennsylvanian, rapid subsidence of the basin and repeated sea level changes, combined with high evaporation rates due to the geographical location, led to the formation of the Paradox Formation, which consists of up to 3 km thick accumulations of dolomites, black organic shales and evaporites (Barbeau, 2003; Trudgill, 2011). Approximately 1.8 km of Paradox Formation salt was deposited along the northeast margin of the basin (Stokes, 1986). Erosion and weathering of the Uncompahgre Uplift and the adjacent mountains led to deposition of sediments into the Paradox Basin throughout the entire Permian. The differential loading from sediments led to subsidence, and as the weight of accumulating sediments over the ductile evaporites increased, the salt started to flow or migrate northwestwards to areas of less confining pressure, creating the salt-cored anticlines in the

Paradox Basin, shown in Figure 2.1.2. The salt domes grew where the salt deposits were thickest and are located above or parallel to the basement faults (Hite and Lohman, 1973; Foxford et al., 1996). This migration of the salt deposits and the resulting salt anticlines led to later deformation of the northern part of Paradox Basin, creating the Paradox fault-and fold belt, among them the major Moab Fault zone (Foxford et al., 1996; Trudgill, 2011)

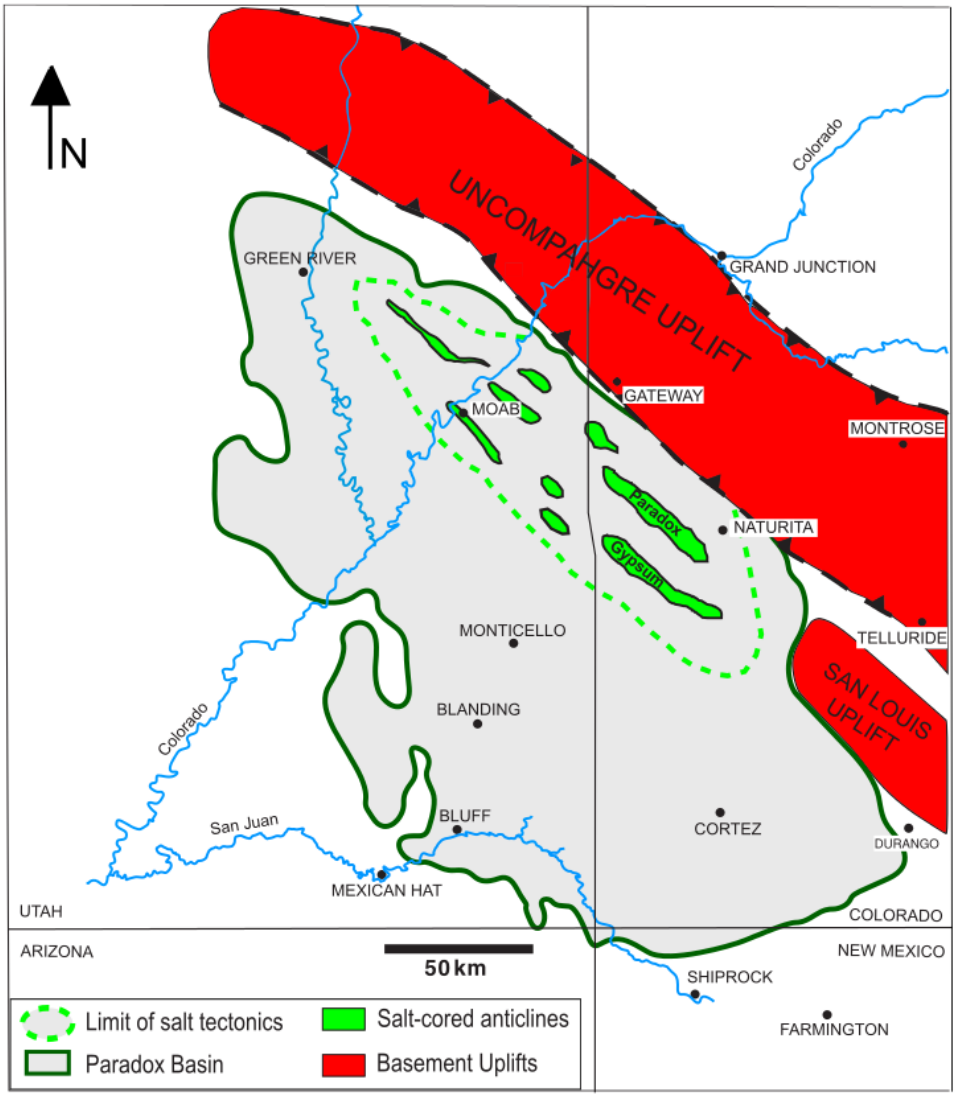

Figure 2.1.2: *Regional scale map and the location of the Paradox Basin and the associated Uncompahgre- and San Luis uplifts. Illustrating the approximate location of the salt anticlines, areal limit of salt tectonics and the depositional boundaries of evaporitic facies (modified from Trudgill (2011)).*

The Sevier and Laramide orogeny

At the beginning of the Mesozoic Era, an intense increase in mid-oceanic ridge activity led to the breakup of the supercontinent Pangea and initiation of global plate reorganization. The Farallon and Kula plates started to converge against the North American plate, and initial subduction-related deformation was concentrated along the western margin. This was the beginning of an extensive mountain-building phase called the Cordilleran orogenic belt, extending 6000 km along the western

coast of North America, from northern Mexico in the south to the northern Canada and Alaska in the north (DeCelles, 2004).

The Sevier orogeny or the Sevier phase, occurred in the Late Cretaceous to Eocene, with substantial shortening and westward compression of the upper crust (Figure 2.1.3) (DeCelles, 2004). The shortening of the crust resulted in a typical forearc thrust system with several thrust nappes stacked on top of each other with an eastward migration (Hintze and Kowallis, 2009). In front of the mountains, a foreland basin developed in eastern and central Utah, in response to the thrust sheets. Thick deposits of siliciclastic sediments were deposited in the basin, derived from the mountain chain to the west. Today these sediments are exposed along the famous Book Cliffs in eastern Utah and western Colorado.

During the Late Cretaceous, the subduction of the Farallon Plate continued, but the angle of the subducting slab decreased (Bird, 2002; DeCelles, 2004; English and Johnston, 2004). This forced the contractional deformation to reach further inland in the central parts of the western US, and this is referred to the Laramide orogeny or the Laramide phase of the Cordilleran orogeny (Figure 2.1.3). This mountain building event lasted from approximately 75-45 Ma (English and Johnston, 2004; Hintze and Kowallis, 2009) and extended from Canada to northern Mexico, with the easternmost extent represented by the Black Hills in South Dakota. This event led to a number of block uplifts and monoclines to develop, like the San Rafael Swell in eastern Utah, and these uplifts were eventually responsible for the retreat of the Western Interior Seaway. Compared to the thin-skinned Sevier orogeny tectonics, the Laramide uplifts were more deeply rooted, affecting rocks deeper into the crust (English and Johnston, 2004).

The uplift of the Colorado Plateau occurred during the last 65 million years, but there is much debate as to how and when the Colorado Plateau was uplifted (Pederson et al., 2002). Proposed mechanisms include isostatic response to the Laramide phase compression and crustal thickening or post-Laramide extension and crustal thinning, resulting in increased heat flux and mantle upwelling below the Plateau. Pederson et al. (2002) suggest that the uplift of the Colorado Plateau occurred in several stages from the tectonism of the Laramide orogeny and the Middle-Late Cenozoic changes in mantle buoyancy or dynamic asthenosphere. Levander et al. (2011) suggest that the Colorado Plateau was uplifted in the Pliocene, as a result of delamination caused by converging magmatism underneath the plateau from the rollback or collapse of the flat-subducting Farallon plate. This low-angle subduction weakened the Proterozoic mantle underneath the plateau and magmatism from Middle Cenozoic – present triggered the downwelling of the lithosphere, causing the delamination (Levander et al., 2011).

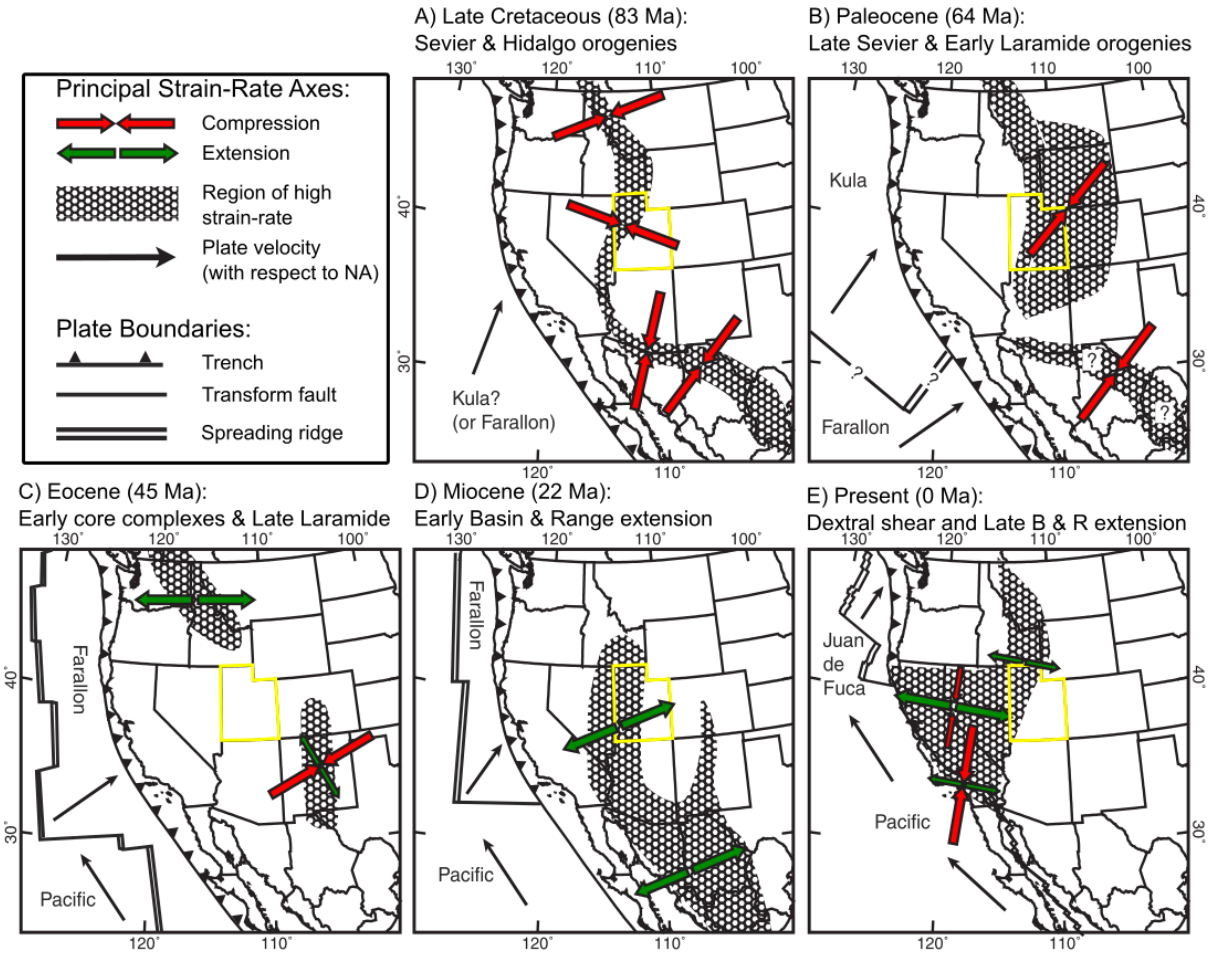

Figure 2.1.3: *The Sevier and Laramide orogeny development from Late Cretaceous to present. Highlighted in yellow are the state of Utah (modified from Bird (2002)). From the Late Cretaceous-Miocene, the Farallon and Kula plate converged against the North American plate. Today the Juan de Fuca and Pacific plate are converging against the North American plate.*

The Moab Fault

The Moab Fault is a 45 km long, salt-related normal fault located above the Paradox Basin in the northeastern Colorado Plateau. The fault zone is, with few exceptions, a defined brittle shear zone, 1-10 m wide, bounded by major slip surfaces were fault rocks is separated from relatively undeformed host rocks (Foxford et al., 1998). The fault trace extends north-westwards from the Moab-Spanish Valley salt anticline along the southwestern flank of the Courthouse syncline (Foxford et al., 1996). The fault offsets an approximately 5000 m thick sedimentary sequence from Pennsylvanian to Cretaceous, with a maximum surface dip-slip displacement of ~960 m (Foxford et al., 1998; Berg and Skar, 2005; Johansen et al., 2005), but displacement increases to 1800 m in the subsurface (Foxford et al., 1996). South of Moab-Spanish Valley the displacement of the fault is shifted to the Lisbon Fault, and to the north the fault splays out into several SE-NW trending faults which are hard-linked and is probably linked to the Tenmile Graben system further north (Figure 2.1.4) (Foxford et al., 1996; Olig et al., 1996; Berg and Skar, 2005; Johansen et al., 2005).

Foxford et al. (1996) suggest that the faulting and displacement history can be divided into two main phases; from Triassic-Middle Jurassic associated with salt migration and from Late Cretaceous-Early Paleogene related to tectonics from the Laramide orogeny, but the mechanisms responsible for the Moab Fault is controversial. Four possible mechanisms for the main activity of the Moab Fault are discussed in the literature:

1) Mesozoic-Cenozoic extension that initiated the salt migration (Foxford et al., 1998; Johansen et al., 2005; Solum et al., 2010)
2) Subsidence created by dissolution or collapse of the salt structures below the sedimentary strata of the Moab salt anticline (Berg and Skar, 2005; Trudgill, 2011)
3) Tertiary extension and reactivation of basement faults caused by relaxation of the Laramide orogeny (Foxford et al., 1996; Davatzes et al., 2005)
4) Late Tertiary, thin-skinned extension (Olig et al., 1996)

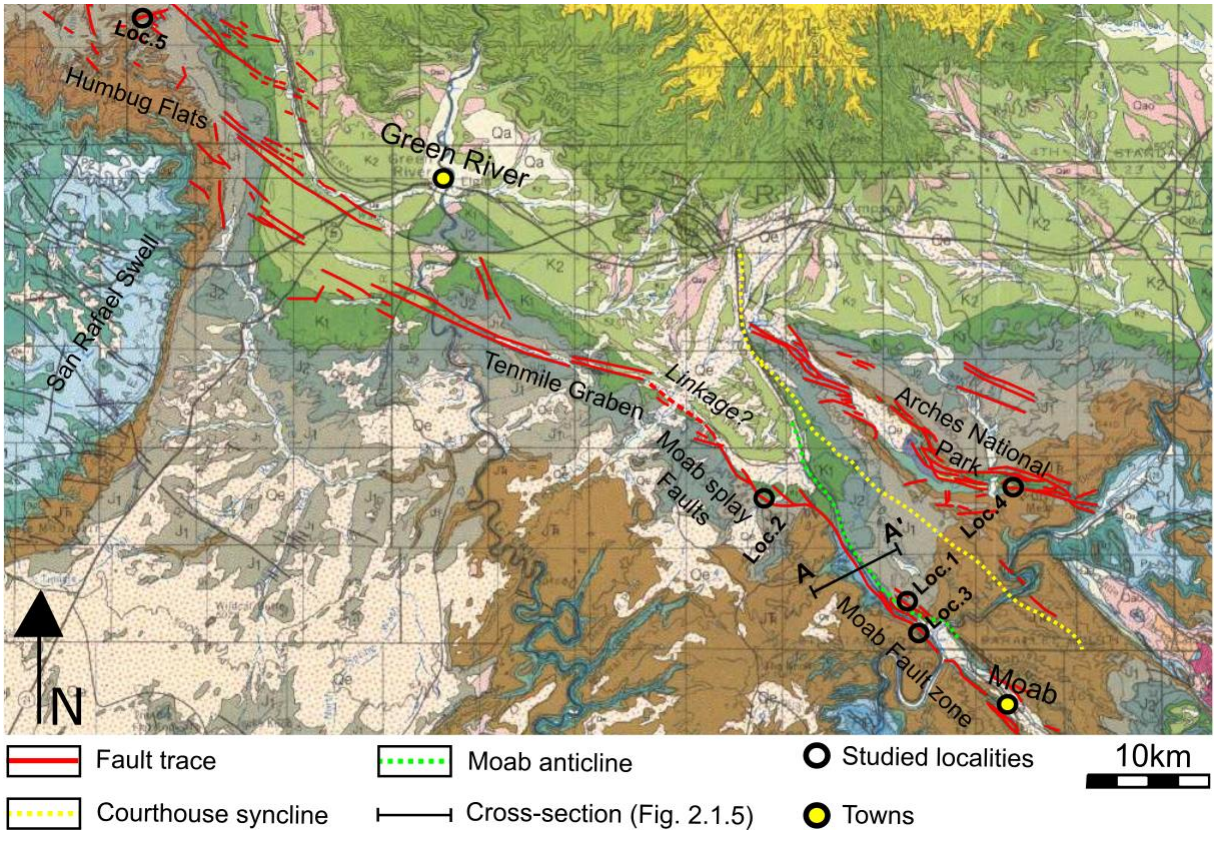

Figure 2.1.4: *Geological map over the northern Paradox Basin in southeastern Utah (acquired and modified from Utah Geological Survey). The map illustrates the geological features from Moab in the southeast to Humbug Flats in the northwest. The fault trace trending northwest around Moab represents the Moab Fault zone. Notice the possible linkage between the Moab Splay faults and the Tenmile Graben. A-A' represents a cross-section illustrated in Figure 2.1.5.*

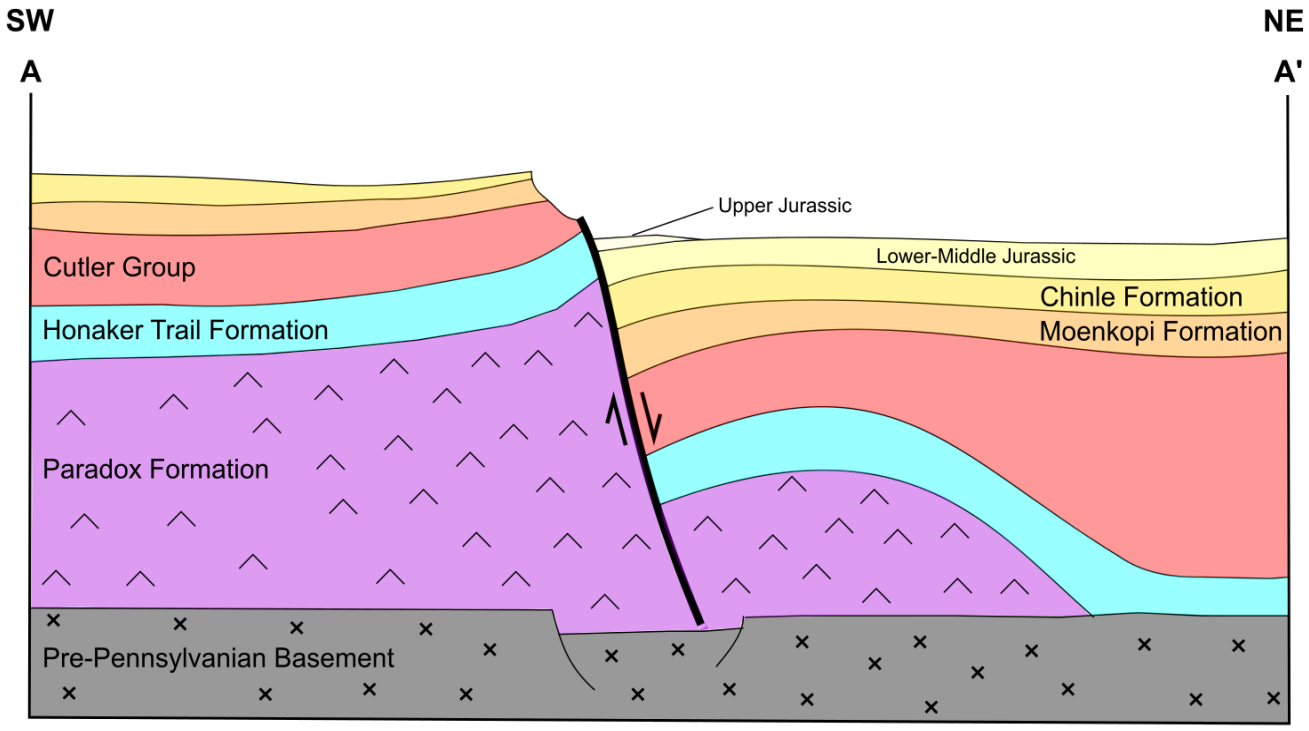

Figure 2.1.5: *Cross-section of the Moab Fault and the displaced stratigraphic units affected by the Moab Fault. The cross-section is modified after Foxford et al. (1996), derived from outcrop mapping and interpreted seismic data. The location of the cross-section is shown in Figure 2.1.4.*

2.1.2. Evolution of southeastern Utah and the stratigraphic units

The stratigraphic units encountered on the studied localities in southeastern Utah was deposited in a time span from Pennsylvanian-Cretaceous and consists of an approximately 5000 m thick sediment package. A general stratigraphic column of the sedimentary units is illustrated in Figure 2.1.6.

Pennsylvanian, 323-299 Ma

The Pennsylvanian was an tectonic active epoch, during this period the sediment deposition on the Colorado Plateau was influenced by the uplift of the Ancestral Rockies and the subsidence of basins. Warm, shallow seas covered Utah during this time period, with different basins developing, like the Paradox Basin. In this period the Hermosa Group was deposited, consisting of the Pinkerton Trail, Paradox and Honaker Trail Formations.

The lowermost Pinkerton Trail Formation was deposited in Early Pennsylvanian in a shallow warm sea, consisting of grey fossiliferous marine limestones and grey-black shales. The Paradox Formation was deposited in a periodically restricted shallow sea, consisting of an up to ~3 km thick mega sequence of 29 shale-dolomite-evaporite cycles, identified from well-logs (Barbeau, 2003). This mega sequence represents a fluctuating sea level, which led to this cyclic deposition and the shale beds in between each evaporite succession define each cycle (Doelling, 1985). During Upper Pennsylvanian,

the Paradox Basin became more stable and more connected to the open ocean through coastal channels, where limestones and dolomites in the Honaker Trail Formation were deposited (Doelling, 1985). The formation consists of cycles of shallow marine fossiliferous carbonates, shales and fluvial-aeolian sandstones (Trudgill, 2011).

Permian, 299-252 Ma

The Permian period is marked by a global climate change, due to the assembly of the vast supercontinent Pangea. In the Paradox Basin and adjacent areas the undivided Cutler Formation was deposited during this period and to the west the equivalent strata of Cutler Group (Barbeau, 2003). These sediments were eroded from the Uncompahgre Uplift and deposited into the Paradox Basin through alluvial fan systems and debris flows (Trudgill, 2011). Further to the west, the more marine influenced members of the Cutler Group, the Lower Cutler Beds, Cedar Mesa Sandstone, Organ Rock Formation and White Rim Sandstone were deposited (Barbeau, 2003; Trudgill, 2011).

Triassic, 252-201 Ma

In the Early Triassic shallow seas from the west extended across northern and western Utah, but these shallow seas got gradually replaced by a terrestrial environment (Trudgill, 2011). In the Triassic, the Moenkopi and Chinle Formations were deposited, which represents both the regression of the shallow seas and the terrestrial environment. The Moenkopi Formation was deposited in a marine-terrestrial environment along the shallow near-shore tidal flats and river flood plains (Doelling, 1988; Trudgill, 2011). Compared to the Moenkopi Formation, the Chinle Formation was deposited in a terrestrial alluvial plain system, consisting of a lacustrine, fluvial and aeolian environment.

Jurassic, 201-145 Ma

In Early Jurassic, the Colorado Plateau and Utah were dominated by an arid climate, and an extensive sandy desert covered most of the area, resulting in major aeolian sand dune deposits and some fluvial deposits. Towards the Middle Jurassic, shallow seaways from the north extend into Utah. Then in Late Jurassic, the area subsided and large lakes and shifting river systems dominated.

The Glen Canyon Group was deposited in an aeolian sand dune to interdune environment in Early Jurassic, where the Wingate Sandstone represents an aeolian dune and interdune deposits. The Kayenta Formation above represents a more sandy fluvial system (Trudgill, 2011). Above the Kayenta Formation, aeolian dune deposits dominate again, evidenced by the deposition of the Navajo Sandstone. The Navajo Sandstone was deposited in an extensive desert on the western portion of Pangea and could represent the largest recorded dune field in the Earth's history.

The Dewey Bridge and Entrada Sandstone, which make up the San Rafael Group, records the transgression and retreatment of shallow seaways that occupied the area in Middle Jurassic. The Dewey Bridge unit consists of a white sandstone overlain by a brown-red siltstone, but the

depositional environment is uncertain and has been interpreted to be either shallow marine, intertidal or a wet coastal sabkha system (Foxford et al., 1996; Trudgill, 2011). The Entrada Sandstone reflects the shift back to sand dominated deposition where the Slick Rock Member represents a sand dune to interdune deposits. Around the town of Moab, the Slick Rock Member is overlain by the Moab Tongue or Moab Member, which also is interpreted to be a sand dune deposit.

Towards the Late Jurassic, large lakes and river systems occupied the area and the depositional environment shifts into a mixed continental, lacustrine and fluvial systems (Trudgill, 2011). During this period the Morrison Formation were deposited. The Morrison Formation is famous for its abundant dinosaur fossils, which indicates dinosaurs roamed around these lakes and river systems during this period.

Cretaceous, 145-66 Ma

In the Cretaceous, the western Utah rises due to thrust faulting and folding from the Sevier orogeny, combined with globally sea level rise, results in the development of the Western Interior Seaway. In the study area, these deposits are known as the Cedar Mountain Formation, Dakota Sandstone, Mancos Shale, and the Blackhawk Formation.

The Cedar Mountain Formation display a gradual transition to a more sandy and fluvial dominated environment from the underlying Morrison Formation. The Dakota Sandstone was deposited in a braided fluvial system during the early development of a foreland basin in front of the Sevier Orogeny (Hintze and Kowallis, 2009). The unit can be divided into an upper and lower section, where the lower section was deposited on an extensive delta system and the upper section have been interpreted to be a shallow marine environment which grades into the Mancos Shale above. The extensive Mancos Shale consists of dark organic shale beds, mudstones, and siltstones, interpreted to be deposited in a deep marine to offshore environment. Overlying this formation, the Blackhawk Formation is located, and this formation shows a stepwise regression of the Western Interior Seaway. The formation has been interpreted to be deposited in a shallow marine to wave-river dominated delta system, where the sediments sourced from the Sevier orogeny and show a prograding delta front towards the retreating sea to the east (Hampson, 2010).

	Age		Formations & Members		Thickness (Meters)	Environment
	Cretaceous		Blackhawk Formation		15-120	Shallow marine to fluvial-tidal delta system
		Mancos Shale	*Blue Gate/Upper Shale Member*		152+	Marine-deep marine to offshore deposits
			Ferron Sandstone Member		15-35	
			Tununk/Tunbuck Shale Member		45-200	
			Dakota Sandstone		15-60	Braided fluvial system
			Cedar Mountain Formation		12-76	Mixed environments, continental, lacustrine and fluvial systems
145 Ma	Jurassic	*Morrison Formations*	*Brushy Basin Member*		80-105	
			Salt Wash Member		40-90	
			Tidwell Member		10-20	
			Summerville Formation		2-10	
		San Rafael Group	*Entrada Sst.*	*Moab Tongue/Member*	25-35	Aeolian dune and interdune
				Slick Rock Member	55-100	
			Upper Carmel	*Dewey Bridge*	12-50	Shallow marine, intertidal, wet sabkha?
			Lower Carmel			
		Glen Canyon Group	Navajo Sandstone		40-120	Aeolian dune and interdune
			Kayeta Formation		30-90	Sandy fluvial system
201 Ma			Wingate Sandstone		18-90	Aeolian dune and interdune
	Triassic		Chinle Formation		60-250	Alluvial plain system
			Moenkopi Formation		0-760	Marine-terrestrial, near shore, tidal flats, flood plain
252 Ma	Permian	*Cutler Group*	*White Rim Sandstone*		0-145	Coastal dune deposits
			Organ Rock Formation		0-500	Alluvial fan, interfingered with aeolian and shallow marine deposits
			Cedar Mesa Sst. Formation			
299 Ma			*Lower Cutler Beds*			
	Pennsylvanian	*Hermosa Group*	*Honaker Trail Formation*		300-750	Shallow marine shelf and nearshore
			Paradox Formation (mostly subsurface)	*Ismay (Cap Rock)*	600-2100	Periodically restricted shallow sea. Alluvial fan system towards the SW flank of the Uncompahgre Uplift
				Desert Creek		
				Akah		
				Barker Creek		
				Alkali Gulch		
323 Ma			*Pinkerton Trail Formation (subsurface only)*		60+	Shallow marine
	Mississippian-Cambrian		Leadville Formation + older formations (subsurface only)		500-600	Pre-foreland basin and platform

Figure 2.1.6: *A general stratigraphic column of the sedimentary units, thickness variations and depositional environments for the Moab Area and northern Paradox Basin from Pennsylvanian-Cretaceous (thickness measurements and depositional environments from Foxford et al. (1996), Barbeau (2003) and Trudgill (2011)).*

2.2. The Majella Mountain, eastern Italy

The second field site for this project is located, in the southern Apennines, eastern Italy, on the eastern edge of Majella Mountain, in Vallone di Santo Spirito (Figure 2.2.1 A and B). The Majella Mountain are located ~40 km westwards from the Adriatic coast and approximately 200 km east of Rome. The mountain is situated on the boundary between the provinces Chieti, Pescara, and L'Aquila in the Abruzzo region in eastern Italy. The mountain is characterized by steep valleys and gorges cut out by several rivers, such as the Orfento river and Foro river. Although the Majella Mountain is composed of platform-slope carbonates, the area is elevated high above sea level; Mount Amaro (2795 m) in the Majella unit is the second highest peak in the Italian Apennines chain (Masini et al., 2011).

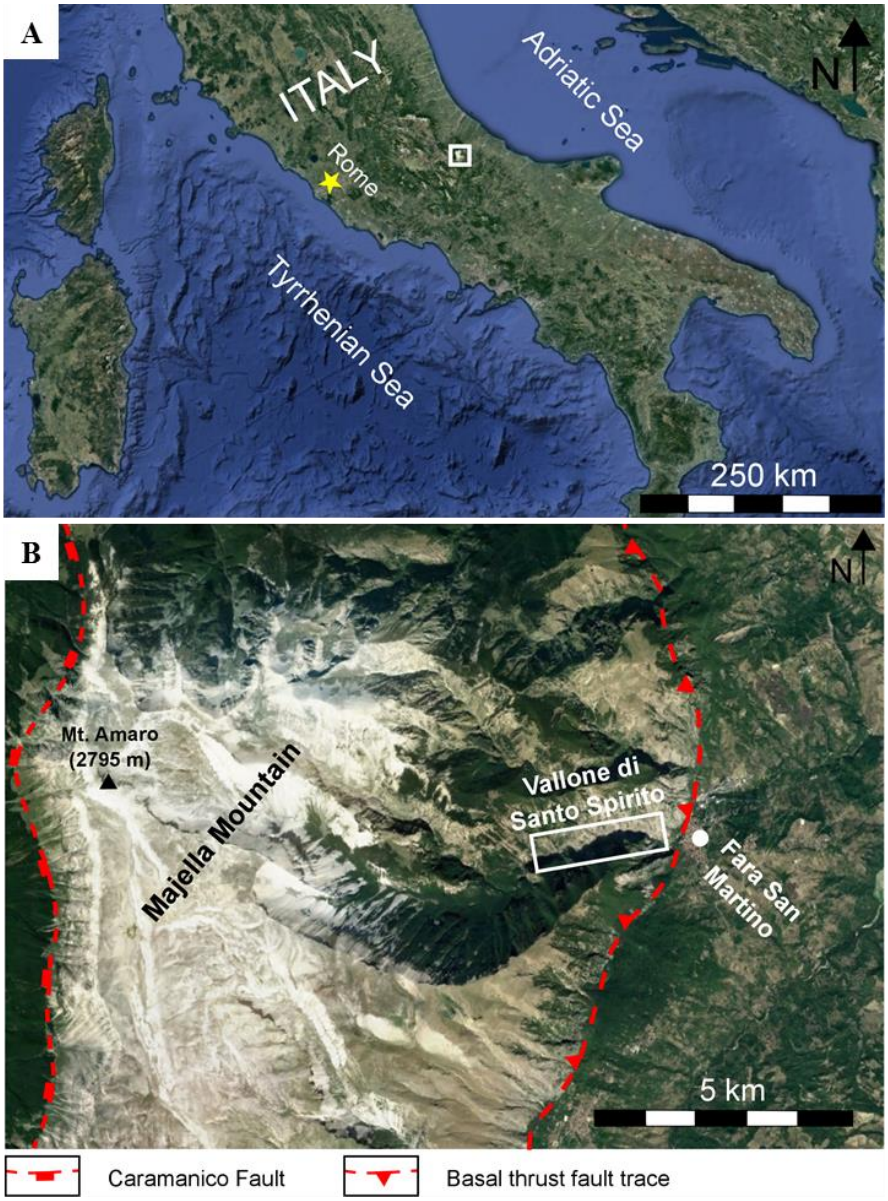

Figure 2.2.1: *(**A**) Satellite photo over Italy, pointing out the Majella Mountain. (**B**) Satellite photo, zooming in on the Majella Mountain and the study area in Vallone di Santo Spirito. The red dashed lines represents major faults in the area (position after Accotto et al., 2014; Festa et al., 2014; Rustichelli et al., 2016 and Geological Survey of Italy). Satellite photos acquired from Google Earth.*

Vallone di Santo Spirito

Vallone di Santo Spirito or the Valley of Holy Spirits is located approximately 3 km west of the small town of Fara San Martino in the Abruzzo region. The valley goes E-W for several kilometers through the eastern edge of Majella Mountain. The stratigraphic units located within the valley are the Early Cretaceous carbonate platform unit of Morrone di Pacentro Formation, and some Holocene-present post-orogenic talus deposits are scattered in the valley. To the north from the Vallone di Santo Spirito, the Late Cretaceous Cima delle Murelle Formation is located. Further northwards the carbonate slope-ramp and basin deposits of Valle dell' Inferno, Tre Grotte and Orfento Formations are located.

2.2.1. Tectonic and structural evolution

The Majella Mountain developed under the central Apenninic fold-and-thrust belt, which is one of several interconnected Mediterranean orogens that developed under the Late Cretaceous-Early Cenozoic closure of the Tethys Ocean (Festa et al., 2014). The Tethys Ocean developed in Early Triassic ~250 Ma, as a result of extensional tectonics along the northern continental shelf of southern Pangea (Gondwana). In Early Jurassic, two major carbonate platform systems developed in the Tethys Ocean, as a result of the extensional tectonics which had dissected the north African continental shelf, also called the Cimmerian terranes (Di Luzio et al., 2004; Di Cuia et al., 2009). The carbonate platforms include the Apulian Platform which developed to the east on Cimmerian crust, where the Majella area was situated on the northwestern edge, and the Apennenic Platform to the west on European crust, separated by oceanic crust (Eberli et al., 1993; Di Luzio et al., 2004; Di Cuia et al., 2009; Santantonio et al., 2013). The Early Jurassic extensional tectonics isolated the Apulian Platform from siliciclastic influence and produced the carbonate platform-pelagic basin differentiation on the platform margin. This margin which displays a listric geometry, probably related to flattening of normal faults within the Triassic evaporites (Santantonio et al., 2013). After a period of low tectonic activity, the Apulian Platform was affected by mild extensional tectonics in Late Jurassic-Early Cretaceous, probably through reactivation of pre-existing basement faults (Santantonio et al., 2013). Towards the end of Early Cretaceous, a steep tectonic escarpment developed, separating the Majella area to the south from basinal areas to the north and a carbonate ramp sequence developed (Eberli et al., 1993; Morsilli et al., 2002; Antonellini et al., 2008; Santantonio et al., 2013).

During the Cretaceous, major changes in relative plate motion were initiated, following the opening of the southern Atlantic and the sudden change in opening directions of the north and central Atlantic Ocean. This initiated the northward drifting of the African plate towards the European plate (Santantonio et al., 2013). Continental fragments of Gondwana- India, Arabia and Apulia started drifting northwards closing the Tethys Ocean in the Cenozoic Era when colliding with the European plate.

The Majella anticline

The oblique convergence between the European and African plate resulted in the formation of the Apenninic fold-and-thrust belt (Eberli et al., 1993; Casabianca et al., 2002; Festa et al., 2014), which incorporated different carbonate platform systems and allochthonous units onto the Italian mainland, developing the present day southern Apennines. One of these carbonate platforms was the Apulian Platform, where the Majella area was situated. The Majella Mountain is the easternmost major thrust sheet within the Apennine fold-and-thrust belt (Aydin et al., 2010). The thrusting and folding activity lasted from Oligocene-Pliocene, developing the Majella anticline, which had accommodated several kilometers of eastward movement and was overriding the Triassic Burano Evaporites (Eberli et al., 1993; Scisciani et al., 2002; Graham et al., 2003; Aydin et al., 2010). The Majella anticline is an approximately 30 km long, 10-15 km wide, kidney-shaped, east vergent, asymmetric anticline, with a steeply dipping eastern forelimb bounded by a underlying basal thrust fault (Figure 2.2.1 B) (Eberli et al., 1993; Graham et al., 2003; Aydin et al., 2010; Masini et al., 2011). Figure 2.2.2 A-C shows a structural map, a cross section of the Majella anticline and a simplified stratigraphic scheme of the carbonate platform margin. On the western backlimb, close to Mount Amaro, the Majella anticline is bounded by a major 30 km long, westward dipping, active normal fault system, the Caramanico Fault (Figure 2.2.1 B and 2.2.2 A and B) (Ghisetti and Vezzani, 2002; Graham et al., 2003; Pizzi et al., 2010; Rustichelli et al., 2016). This fault system has a maximum displacement of ~ 4 km, displacing the carbonate units in the Majella structure from the Early Pliocene clastic units interposed between the Morrone Unit (Ghisetti and Vezzani, 2002). There are different views about the main activity of the Carmanico Fault, some of them are: Miocene-Early Pliocene (Scisciani et al., 2002), Quaternary (Ghisetti and Vezzani, 2002) and pre-Quaternary (Pizzi et al., 2010). Pizzi et al. (2010) argue that most of the fault activity and displacement took place in pre-Quaternary. This is based on the facts that there is no extensional basin in the hanging wall from Quaternary and no geomorphic activity around the fault zone in the Quaternary.

The internal structure of the Majella anticline shows a complex distribution of fault and fracture network. The faulting within Majella anticline consist primarily of normal faults and strike-slip faults, but some reverse faults are also located (Marchegiani et al., 2006; Antonellini et al., 2008).These structures reflect four main tectonic/deformation stages recorded in the stratigraphy in the Majella anticline (Di Cuia et al., 2009):

1. ENE-WSW extensional syn-rifting tectonics in the Tethys Ocean until Late Cretaceous, evidenced by NNW-SSE striking normal faults in the Cretaceous strata (Casabianca et al., 2002).
2. Extension phase in the Late Miocene, approximately oriented NE-SW, related to the flexure of the westward subduction of the Apulian plate (Di Cuia et al., 2009).

3. E-W oriented folding and thrusting during the Pliocene Apennenic fold-and-thrust belt formation in the central Apennines related to the European-African continental collision, developing the Majella anticline and the majority of fault structures located along eastern forelimb (Scisciani et al., 2002; Di Cuia et al., 2009; Aydin et al., 2010; Pizzi et al., 2010).
4. Pleistocene strike-slip tectonics, evidenced by NE-SW to NW-SE fault system development (Casabianca et al., 2002; Di Cuia et al., 2009).

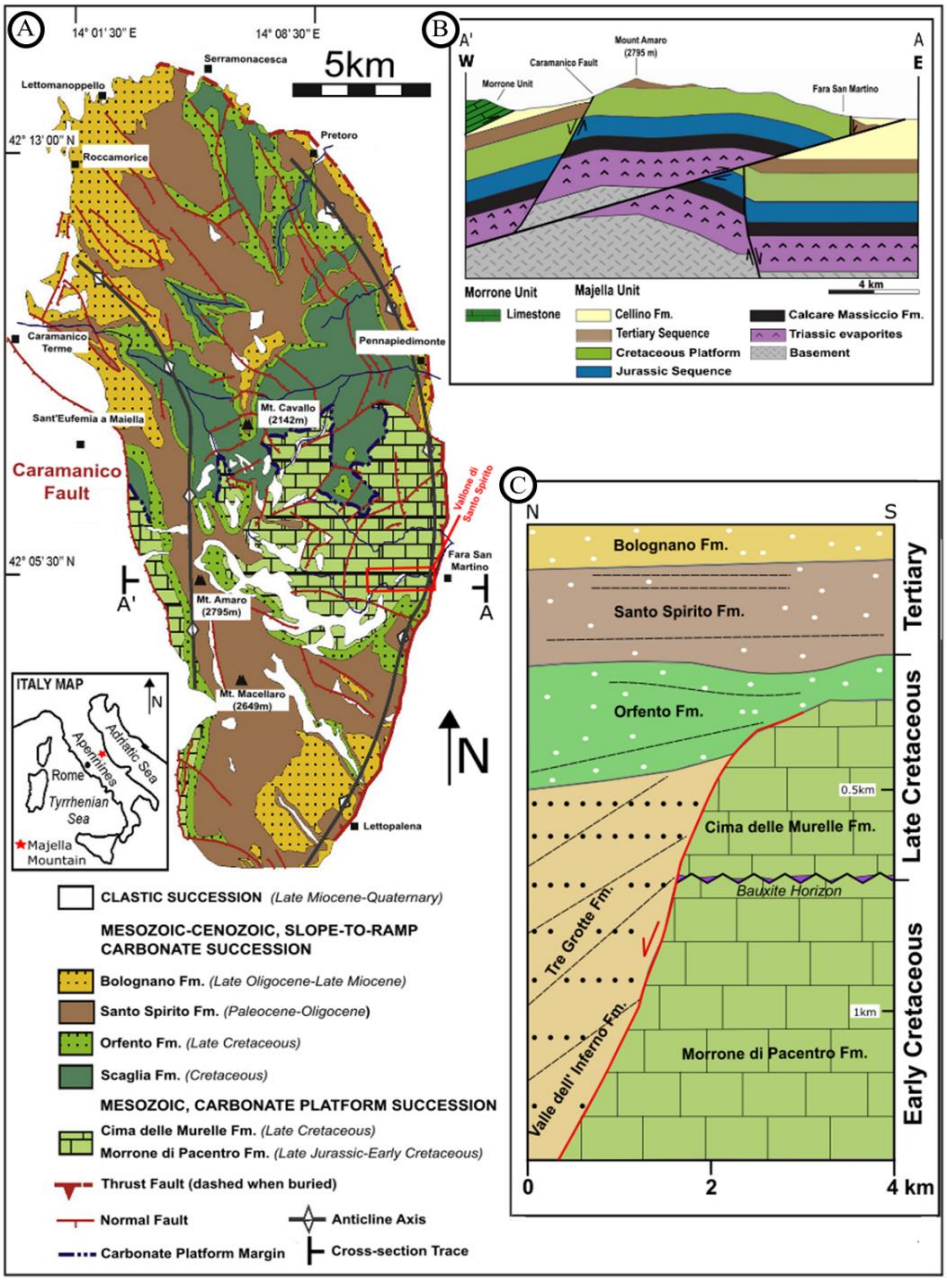

Figure 2.2.2: *(**A**) Geological map of Majella Mountain (modified after Ghisetti and Vezzani (2002); Rustichelli et al. (2016)).(**B**) Fara San Martino geological cross-section, from A-A' (modified from Masini et al. (2011)). Illustrating the structures of the Majella anticline and the main thrust fault overriding the Triassic Burano Evaporites. (**C**) Simplified stratigraphic scheme of the carbonate platform margin. Unconformity marked with a bauxite horizon in the transition Early Cretaceous-Late Cretaceous. The steep escarpment (red line) separates the platform system to the south from the basin setting towards the north.*

2.2.2. Evolution of the Majella platform and stratigraphic units

The Majella platform system consists of a 2 km thick carbonate succession from Early Cretaceous-Miocene times which has been accumulated within different marine settings in the Tethys Ocean (Antonellini et al., 2008; Agosta et al., 2010b; Rustichelli et al., 2016). A geological map of the main Mesozoic-Cenozoic tectono-stratigraphic and a chronostratigraphic scheme for the Majella Platform are illustrated in Figure 2.2.3 and 2.2.4, respectively. In the south, the Majella Platform consists of shallow water carbonates deposited on the Apulian Platform and to the north, a steep margin separates the platform carbonates from the slope and basin carbonates (Eberli et al., 1993; Morsilli et al., 2002; Di Cuia et al., 2009). The evolution of the Apulian Platform can be divided into two major stages: the aggradation stage, from Late Jurassic-Middle Cretaceous in the Albian, and the progradation stage, from the Albian to Late Cretaceous in Maastrichtian (Eberli et al., 1993; Mutti et al., 1996). The transition from the aggradation stage to the progradation stage is observed as an unconformity in the stratigraphic units.

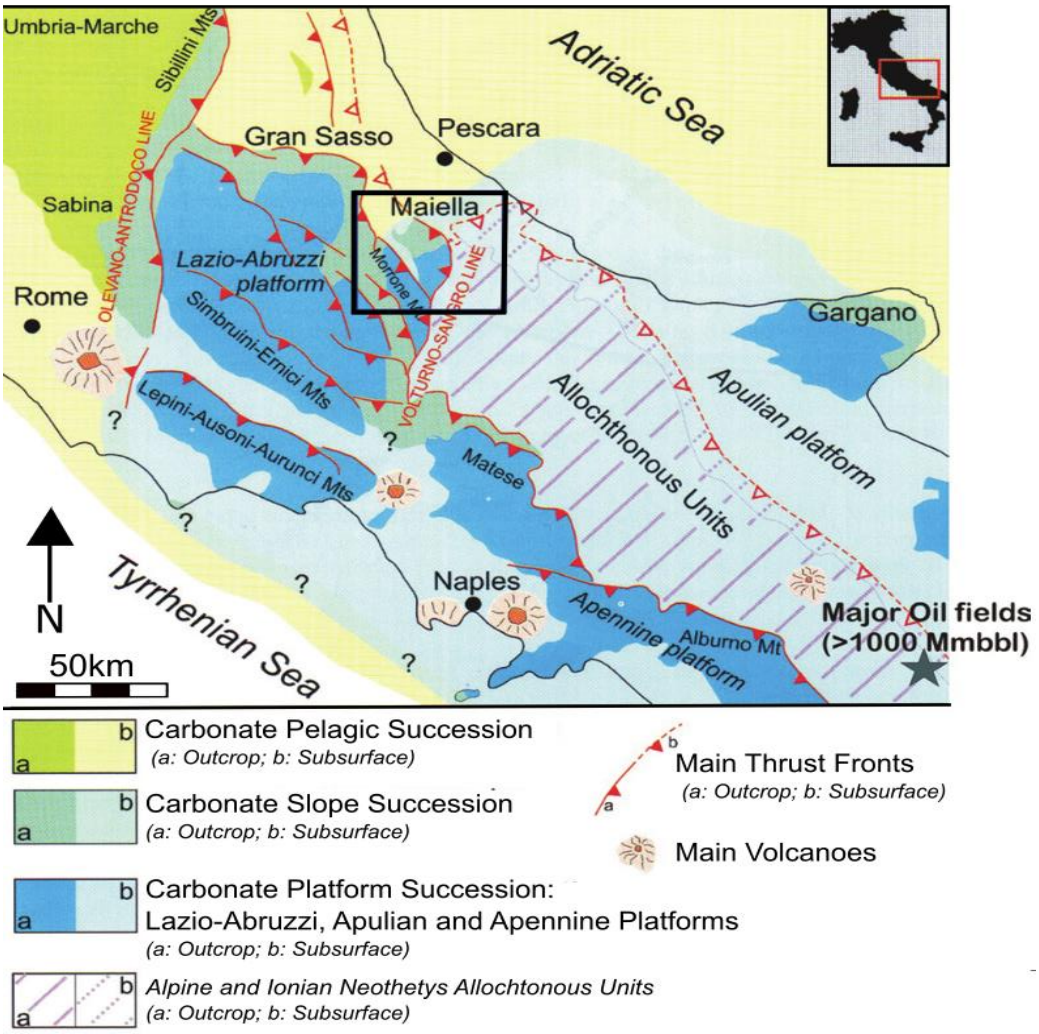

Figure 2.2.3: *Geological map of the main Mesozoic-Cenozoic tectono-stratigraphic units of the southern Apennines thrust belt. The Majella Mountain are highlighted in the black square on the figure (modified from Eberli et al. (1993); Di Cuia et al. (2009)).*

Early Cretaceous, 145-100 Ma

In Early Cretaceous, the Majella area was situated on the northwestern edge of the Apulian carbonate platform in the Tethys Ocean. This broad carbonate platform extended from present day southeastern Abruzzo region across Apulia and most likely to the Greek islands of Cephalonia and Zakynthos (Eberli et al., 1993).

In the Late Jurassic-Early Cretaceous, the Apulia-Adriatic domain was affected by tectonic extension and subsidence (Eberli et al., 1993; Santantonio et al., 2013). This made the Apulia Platform an isolated platform on the southern margin of the Tethys Ocean, sheltered from terrigenous influx by deeper troughs and plateaus (Eberli et al., 1993). At this time, the Apulia Platform system was located around the equatorial belt, surrounded by a warm, shallow water environment (Santantonio et al., 2013).

Towards the end of Early Cretaceous a steep escarpment approximately 1000 m high (Eberli et al., 1993; Mutti et al., 1996; Morsilli et al., 2002), separated the platform settings to the south from the basinal areas to the north. The escarpment had an average dip of 35^{o} and was modified by constructional and erosional process, which continuously re-shaped the escarpment (Eberli et al., 1993). In between the Apulia Platform and a pelagic carbonate platform, a narrow basin formed, which was infilled breccias, megabreccias, carbonate turbidites and bioclastics during the Early- and Late Cretaceous (Santantonio et al., 2013). In the same time period, the Apulian Platform was uplifted and subaerial exposed, due to the convergence between Africa and Europe (Eberli et al., 1993; Santantonio et al., 2013). This led to intense karstification, creating irregular surfaces and reworking of deposited sediments (Eberli et al., 1993). This subaerial exposure also resulted in a major unconformity, but the duration of the hiatus cannot be established in all locations due to the lack of suitable biomarkers. Hence, a duration from Late Albian-Middle Cenomanian is generally suggested (Eberli et al., 1993).

The stratigraphic unit deposited in the Early Cretaceous are the Morrone di Pacentro Formation, which is a massive micritic limestone, consisting of shallow marine platform boundstones (rudist biostromes), grainstones and wackestones (Di Cuia et al., 2009; Festa et al., 2014). In the formation, a 20 m thick shallowing upwards trend is localized, and the depositional environment is interpreted to be a peritidal environment (Eberli et al., 1993). At the top of the Morrone di Pacentro Formation an unconformity can be localized, due to the subaerial exposure, this is evidenced by breccia and speleothems filled karst holes, and bauxite deposits are locally preserved.

Late Cretaceous, 100-66 Ma

After the Early Cretaceous subaerial exposure and unconformity, the Apulian Platform reestablished shallow water conditions as the area was flooded in the Middle Cenomanian, in the Late Cretaceous

(Eberli et al., 1993; Morsilli et al., 2002). On top of the unconformity, thin shallowing upwards cycles of peritidal carbonates are located, but some subaerial exposure during the reinstallation of the platform occurred, evidenced by marls or black pebble conglomerates (Eberli et al., 1993). The steep escarpment prevented basinward progradation of the platform margins, so large amounts of bioclastic material (high productivity on the margin) were deposited basinward by-passing the slope (Morsilli et al., 2002). Onward in the Late Cretaceous, the burial of the escarpment was progressively ongoing, and the relative changes in sea level increasingly determined the deposition of sediments, facies distribution and the amount of erosion (Eberli et al., 1993). The escarpment was progressively buried by the Valle dell' Inferno Formation and the Tre Grotte Formation throughout the Late Cretaceous. During the burial process, deposits were shed basinward from the Apulian Platform edge over distances of 15 km as an average and distributed over an area at least 150 km^2 (Morsilli et al., 2002).

At the platform margin, two main parasequences are stacked in an aggradational and progradational order. Cross-laminated biosparite-oobiosparite overlies rudestones, and these sequences are repeated and in some areas they are topped by bioturbated grainstones and packstones, followed by limestones deposited in a restricted to supratidal environment (Eberli et al., 1993; Morsilli et al., 2002). These deposits are the first lithologies composed in the Cima delle Murelle Formation, which is the main carbonate platform formation in the Late Cretaceous. On the platform interior, a peritdal to lagoonal environment existed, where the sedimentation was cyclic less than 1 m thick, and compared to the marginal areas, the platform interior developed in a retrogradation order (Eberli et al., 1993).

In Maastrichtian time, end of Late Cretaceous, the escarpment was buried, and the platform started prograding basinward (Morsilli et al., 2002). A low angle slope or ramp-like margin developed on the Apulian Platform, which represents the Orfento Formation (Eberli et al., 1993; Di Cuia et al., 2009). The boundary between the Orfento Formation and the underlying Cima delle Murelle Formation is a gentle angular unconformity characterized by numerous erosional scours (Rustichelli et al., 2016). The carbonates situated in the Orfento Formation, have been interpreted to be accumulated from a distally steep carbonate ramp, under high hydrodynamic energy (Eberli et al., 1993; Mutti et al., 1996; Rustichelli et al., 2016). At the end of Late Maastrichtian, the sea level fell, and the platform progradation was terminated by subaerial exposure, which led to deep truncation on the platform (Eberli et al., 1993).

Paleocene-Miocene, 66-5 Ma

In Paleocene, the low sea level led to the development of small coralgal reefs, about 2 km north of the former platform margin (Eberli et al., 1993). However, the unstable sea level during this time period resulted in repeatedly flooding of the former Cretaceous platform. Shallow water biota and local reefs colonized the area, but when the sea level was lowered erosional forces dominated. Erosion of most of the Paleocene-Upper Eocene shallow water areas is observed as multiple incised channel fills towards

the platform margin and lithic breccias and carbonate turbidites on the lower slope (Eberli et al., 1993). Towards the Late Eocene-Oligocene, reefs developed over redeposited debris material, and prograded approximately 4 km towards the basin (Eberli et al., 1993).

Throughout the Cretaceous, thrusting activity from the African-European continental collision had been ongoing. In Oligocene-Pliocene the Majella area was thrusted and folded and became incorporated in the Apennenic fold-and-thrust belt and became part of the Italian mainland (Eberli et al., 1993; Aydin et al., 2005; Aydin et al., 2010; Pizzi et al., 2010; Rustichelli et al., 2016).

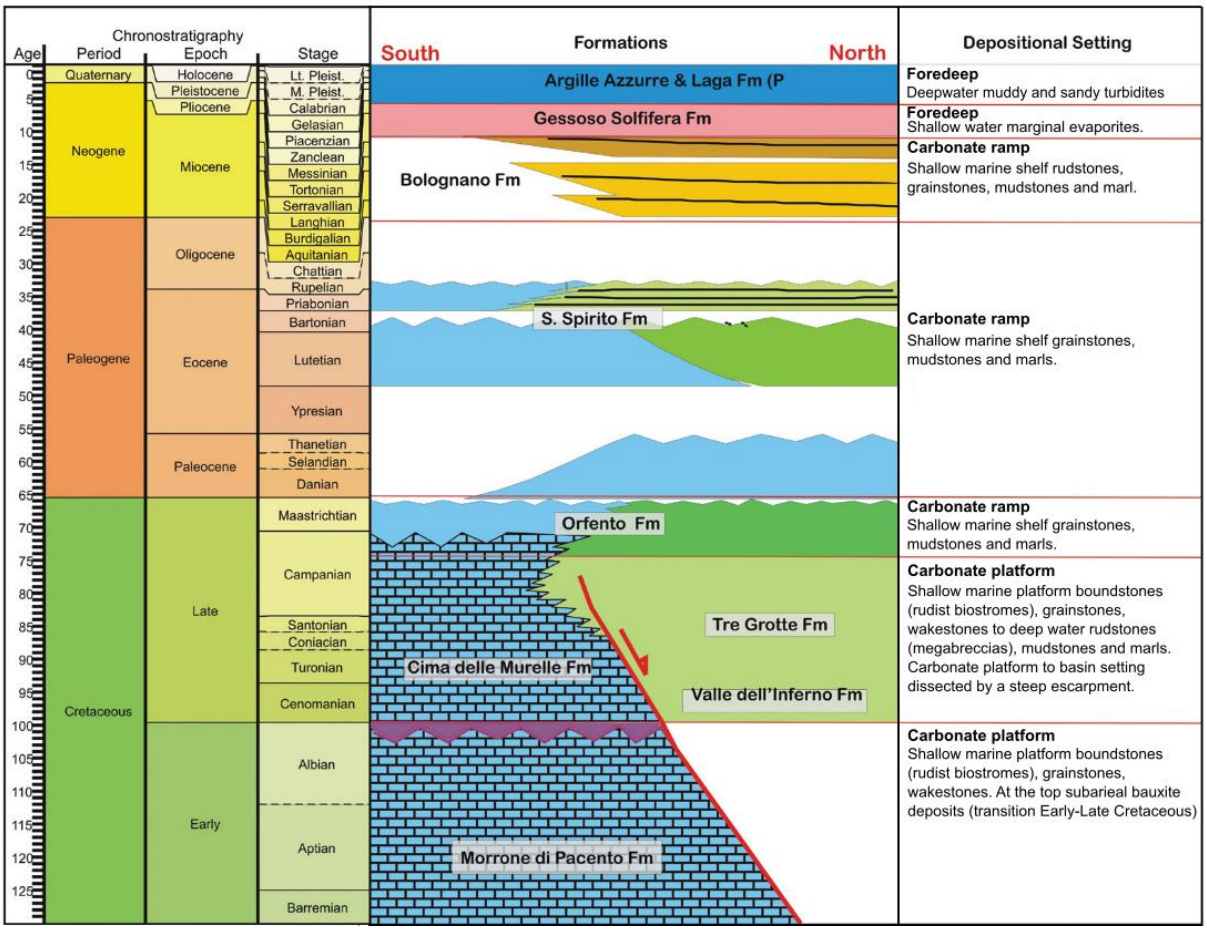

Figure 2.2.4: *Chronostratigraphic units from the Majella carbonate platform system from Early Cretaceous to Quaternary (from Di Cuia et al. (2009)). The platform units are situated in the south and are separated from basin carbonate units in the north by the steep escarpment, marked as the red line in the figure.*

3. Results

In this chapter, the field observations and measurements of fault core thickness, fault orientation and fault displacement from all of the studied localities will be presented. An overview of the structures and stratigraphy of the study area is first introduced, followed by the results and fault/fault core descriptions, presenting the measured fault core thickness for each studied locality. Afterward, a statistical analysis of the data will be presented. A different setup of the results is applied for the study area in Vallone di Santo Spirito, eastern Italy.

3.1. R-191 Canyon, Utah

3.1.1. Structures and stratigraphic units

The R-191 Canyon locality is situated along the Moab Canyon Pathway, about 600 m northeast of highway 191, Utah (Loc. 1 on Figure 2.1.4). At the locality, a 100 m scanline was conducted at the base of the outcrop where two normal faults (F1 and F2) were measured and documented along this scanline (Figure 3.1.2). The fault core at F2, with an estimated displacement of approximately 950 m (Foxford et al., 1996; Foxford et al., 1998), has accommodated much more displacement, compared to faults studied at the other localities. While the fault core at F1 has accommodated a displacement of ~60 m (Foxford et al., 1998). The two normal faults studied at the outcrop are part of the southern segment of the Moab Fault zone. F2 is oriented approximately parallel to the orientation of the Moab Fault, trending NW-SE with a dip of 44°NE, while F1 shows a different orientation, which better fits the splay or branch characterization by Foxford et al. (1998), trending E-W with a dip of 24°N (Figure 3.1.1).

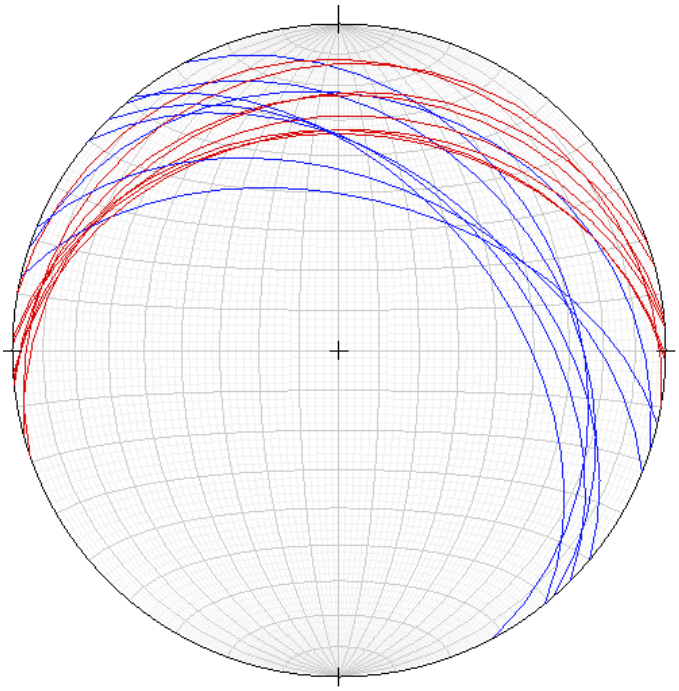

Figure 3.1.1: *Illustration of the orientation measurements of the studied faults at R-191. The red lines represent the orientation of F1, and the blue lines represent the orientation of F2.*

The Moab Fault segments can be studied at both the northern and southern side of the canyon at this locality. However, the southern exposure is much more accessible than the northern, so only the southern outcrop was studied and measured in detail for this project. There are approximately 40 m between the northern and southern exposure of the fault, but there are observable differences in fault core structures and fault architecture between the two sides. At the southern outcrop, a major sandstone lens from the Moab Member is juxtaposed in between the two studied faults (Figure 3.1.2). While on the northern exposure of the fault, the lens and two major slip surfaces are absent. This shows how lateral changes in fault structures and components could occur over relatively short distances (Foxford et al., 1998).

Figure 3.1.2: *Outcrop picture of the southern exposure of the Moab Fault at the R-191 Canyon. The two studied and measured faults are interpreted on the figure and located at 45.5 m and 65.7-69.1 m on the scanline, respectively. Juxtaposed in between the interpreted faults the massive Moab Member sandstone lens is situated. The R-191 highway is located to the right, towards the SW on the figure and where the stratigraphic units are presented in the steep cliffs of the Moab Canyon, on the footwall of the Moab Fault.*

3.1.2. Fault core and fault descriptions

Fault F1 is positioned at 45.5 m on the scanline and is juxtaposing the Salt Wash Member in the Morrison Formation towards the northeast, and the Moab Member sandstone lens to the southwest (Figure 3.1.3). In the field, a 20 m scanline was conducted along the fault core, and thickness measurements were completed every 2 m along the fault core. In the upper and middle part of the measured fault, a clear fault core boundary between the Salt Wash Member and the sandstone lens could be defined. Downwards, the boundary towards the lens is buried by debris. However, the boundary has been interpreted based on the fault trace, the presence of fault rocks and the upper boundary to the Salt Wash Member. This resulted in a total of 46 fault core thickness measurements to be completed in the field and on pictures, resulting in an average fault core thickness of 183.89 cm for the measured 20 m of the fault core.

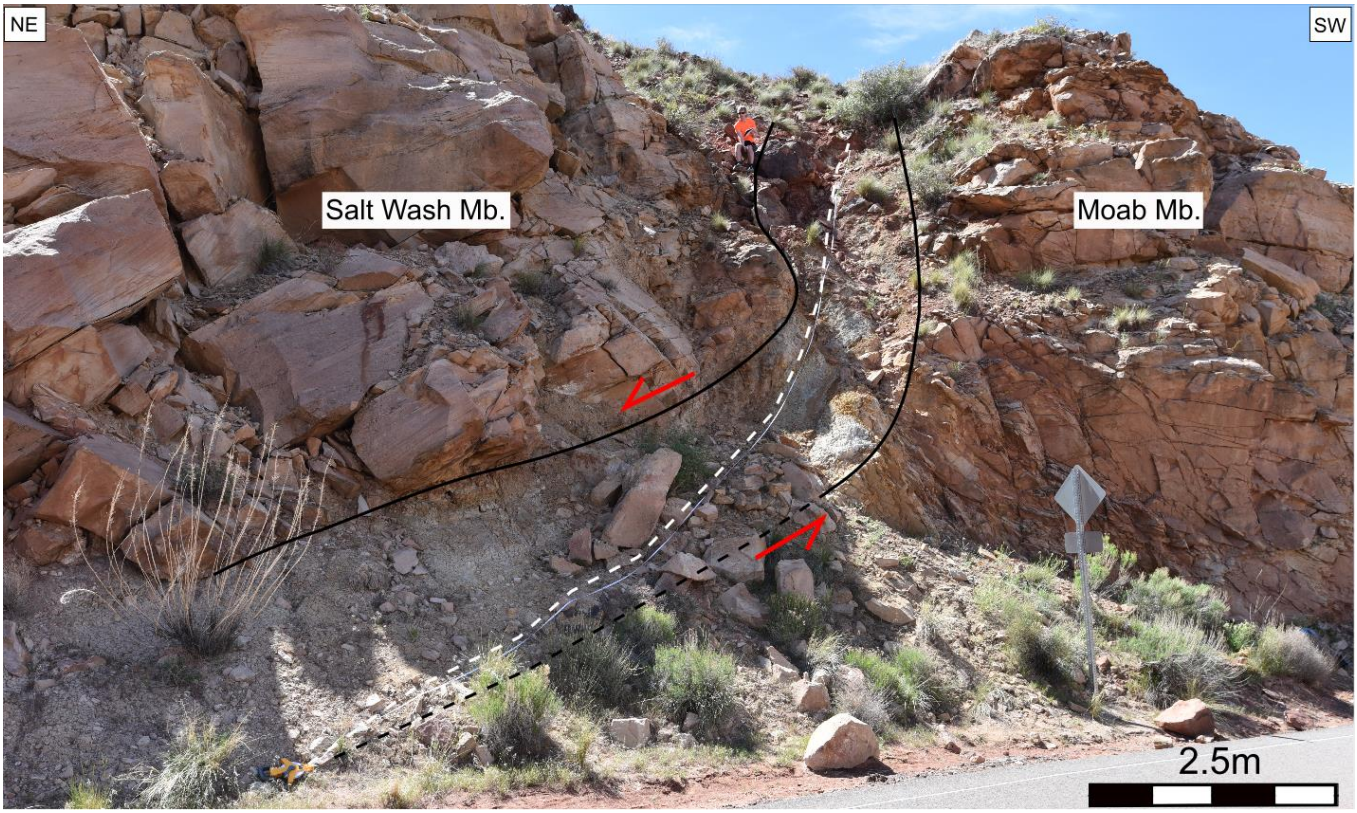

Figure 3.1.3: *Outcrop picture of F1 at the R-191 Canyon. In the upper and middle part of the fault, a clear fault core boundary between the Moab Member and Salt Wash Member can be established. Downwards along the fault, debris covers the lower boundary to the Moab Member and the black dashed lines represents the interpreted boundary. Note the 20 m scanline running parallel with the dashed white line within the fault core.*

The completed fault core thickness measurements show some lateral thickness variations at the different measured levels along the fault core (Figure 3.1.4). The lowermost 5 m of the thickness measurements show some small variations, and overall exposes a wide fault core, ranging from 224-237 cm in thickness. Upwards, the fault core shows greater variations and the minimum measured

value of 149.4 cm occurs at level 960 cm. A plot on Figure 3.1.4 shows the measured fault core thickness at the different levels along the fault, illustrating the variation in thickness.

The fault core consists of two main slip surfaces, bounding a zone of grey shaley fault gouge with some sandstone clasts incorporated. Foxford et al. (1998) interpret the shaley fault gouge to be derived from mudstones situated in the Brushy Basin Member in the Morrison Formation. The sandstone clasts incorporated in the fault core are most likely derived from either the Salt Wash Member or the Moab Member. The reddish-beige sandstone clasts are best observed in the upper parts of the fault core, with sizes ranging from cm to dm scale. At the upper part of the fault core, the present shaley fault gouge shows some color alteration, becoming more brown-rusty in color, which could represent iron oxide reduction in the gouge, which was also reported by Foxford et al. (1998). In the damage zone of the fault, both synthetic and antithetic fractures are observed.

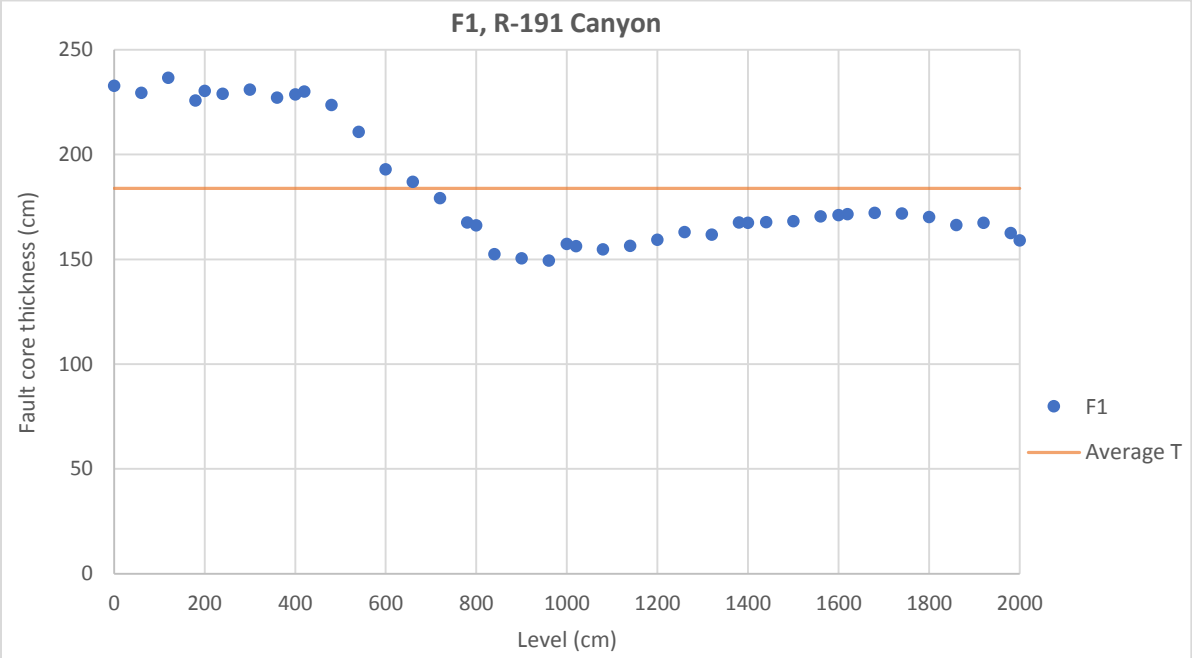

Figure 3.1.4: *Plot of the measured fault core thickness (T) along the different levels of the fault core, illustrating the lateral thickness variations.*

The Moab Member lens is located at 53.0-65.7 m on the scanline, followed by the lowermost fault (F2) from 65.7-69.1 m (Figure 3.1.2). The fault is juxtaposing the footwall rock of the Cutler Formation to the southwest and the Moab Member lens to the northeast (Figure 3.1.5). Underneath the Cutler Formation, the Late Pennsylvanian Honaker Trail Formation can be observed further to the southwest along the scanline (Figure 3.1.2). Four main slip surfaces can be observed in the fault core of F2 and suggested by Foxford et al. (1998) to have accommodated the principal displacement (~950 m). Two different types of fault rocks can be observed and distinguished in between the four slip surfaces, and are referred to as zone A and B for this project. The uppermost zone A, which is in contact with Moab Member lens, consists of beige- to light grey fault gouge, and some scattered

sections where cataclasite is observed. Within the Moab Member lens, intense fracturing is observed closest to zone A and the density of fractures decreases gradually away from the zone. The core thickness of zone A shows great lateral thickness variations along the different levels measured, as illustrated in Figure 3.1.5 and 3.1.6. The lowermost zone B, consists of a thick zone of reddish Cutler-derived smear, where some beige-reddish sandstone clasts are incorporated, interpreted to be derived from the pre-Wingate Sandstone by Foxford et al. (1998). Although some lateral thickness variations can be observed at the different levels of zone B, they are not as prominent as in zone A (Figure 3.1.6).

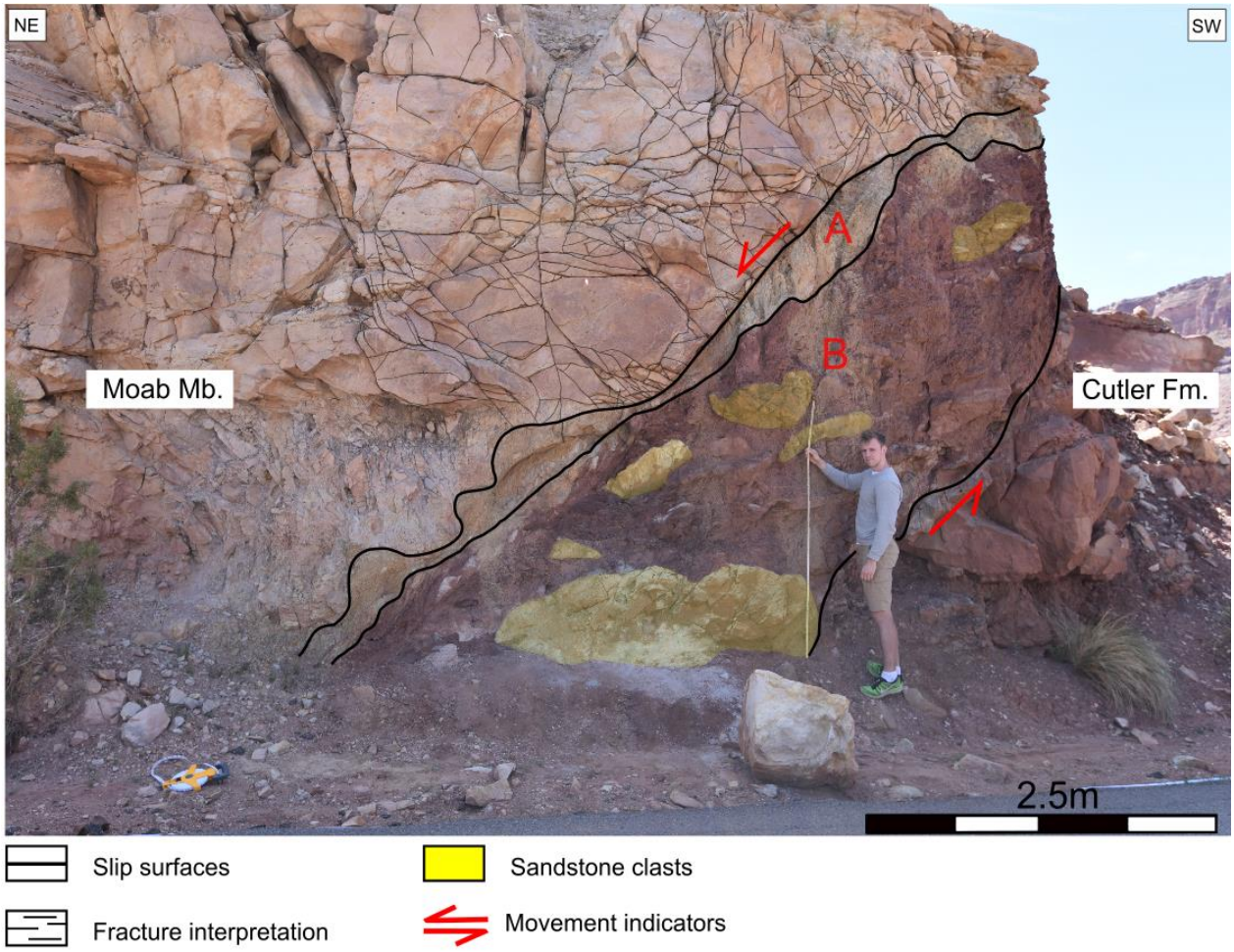

Figure 3.1.5: *Outcrop picture of fault F2 at the R-191 Canyon. The two different zones interpreted in the fault core exposes different fault rock lithologies and can easily be distinguished on the figure. In the Moab Member lens, intense fracturing has been interpreted, and the density of the fractures decreases gradually away from the fault.*

In the field, fault core thickness measurements were only completed for 4 m along the fault core, because of the accessibility of the outcrop in the field. However, picture measurements have been conducted every 60 or 30 cm along the fault core, because of major lateral thickness variations. For zone A, a total measured height of 14.4 m have been completed along the fault core, resulting in 35 fault core thickness measurements, which gives an average thickness of 29.43 cm. Due to debris material derived from the Moab Member, which buries parts of zone B, the measured height of this

zone is only 9.9 m, resulting in 23 thickness measurements along this zone and an average thickness of 162.66 cm. A plot of the measured fault core thickness, illustrating the thickness variations along zone A and B, is presented in Figure 3.1.6. On the figure, another plot is presented, combining the measured fault core thickness for the two zones at the same level. Since the two zones are situated in the same fault, only separated by slip surfaces, the total fault core thickness of F2 is equal to the sum of the thickness of both zones.

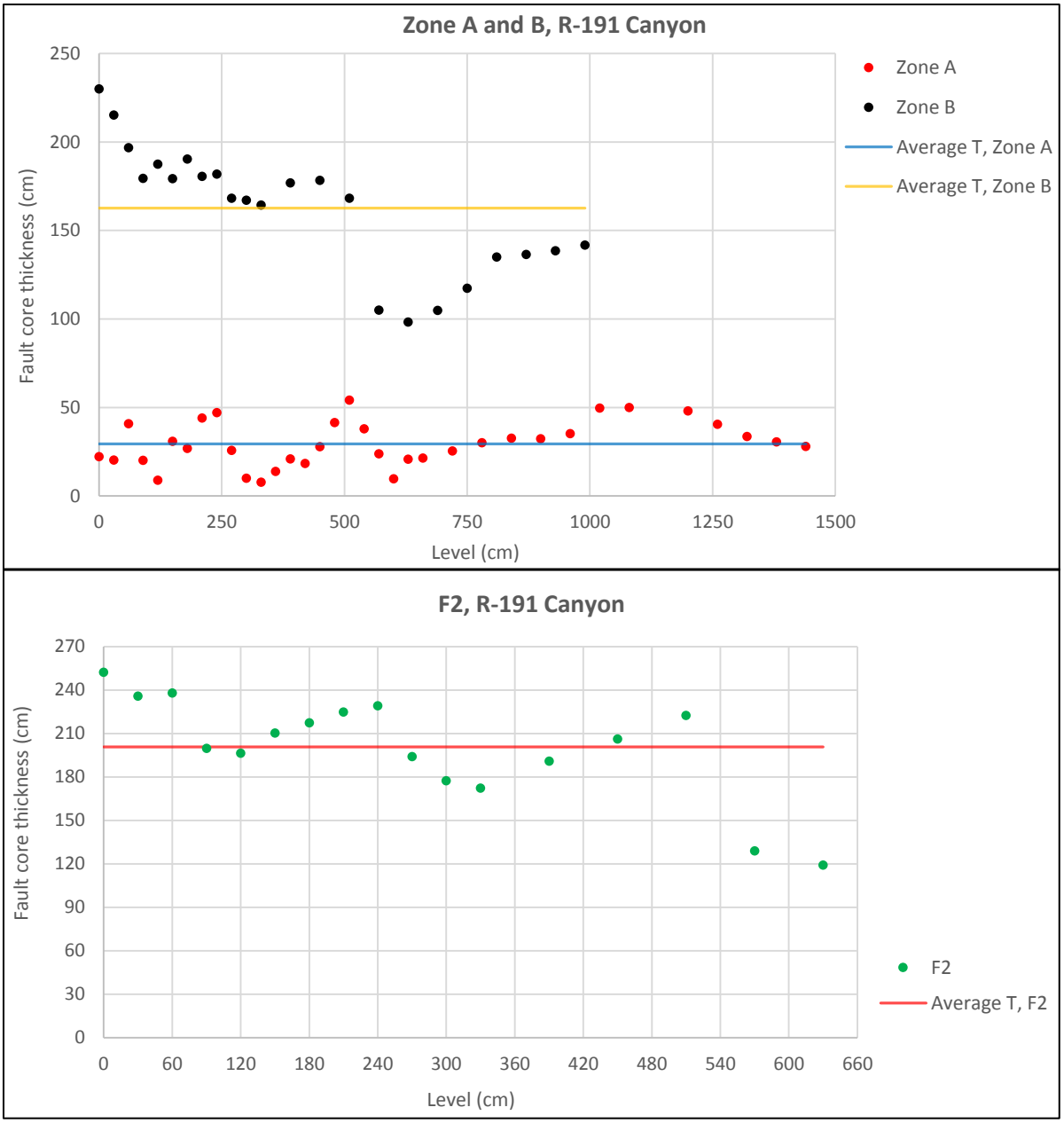

Figure 3.1.6: *Plots of the measured fault core thickness (T) of zone A and B, and the total thickness of A and B combined at the same level (F2). The average thickness of the measurements is also represented on both plots. Note how the thickness variations in zone A and B occur approximately at the same level.*

3.1.3. Statistical analysis of data

The fault core thickness measurements completed on fault F1 and F2, have been used to complete univariate analysis and construct exceedence frequency (EF) plots. Two EF-plots was constructed for each fault, EF-thickness and log EF-log thickness, and on the log-log plot, a trendline have been correlated to find the best fit for the data points.

The EF-plots regarding F1 are illustrated on Figure 3.1.7 A-B. When plotted in an EF-plot, the fault core thickness measurements from F1 can be divided into two segments that are separated by the thickness values from 1.7-2.25 m. At this interval, a change in curvature of the plot occurs, straightening the plot. This is visible on the EF-thickness plot (Figure 3.1.7 A), where a roughly straight interval can be observed (1.7-2.25 m), in between two approximately concave down trends. On the log EF-log thickness plot (Figure 3.1.7 B), the concave down trends become more steeply dipping, as well as the straight interval. The trend line with the best fit for the data points has been correlated to be a logarithmic function, with a regression of fit (R^2) of 0.8729. This could indicate that the two different segments form two log-normal distribution trends for each of the segments.

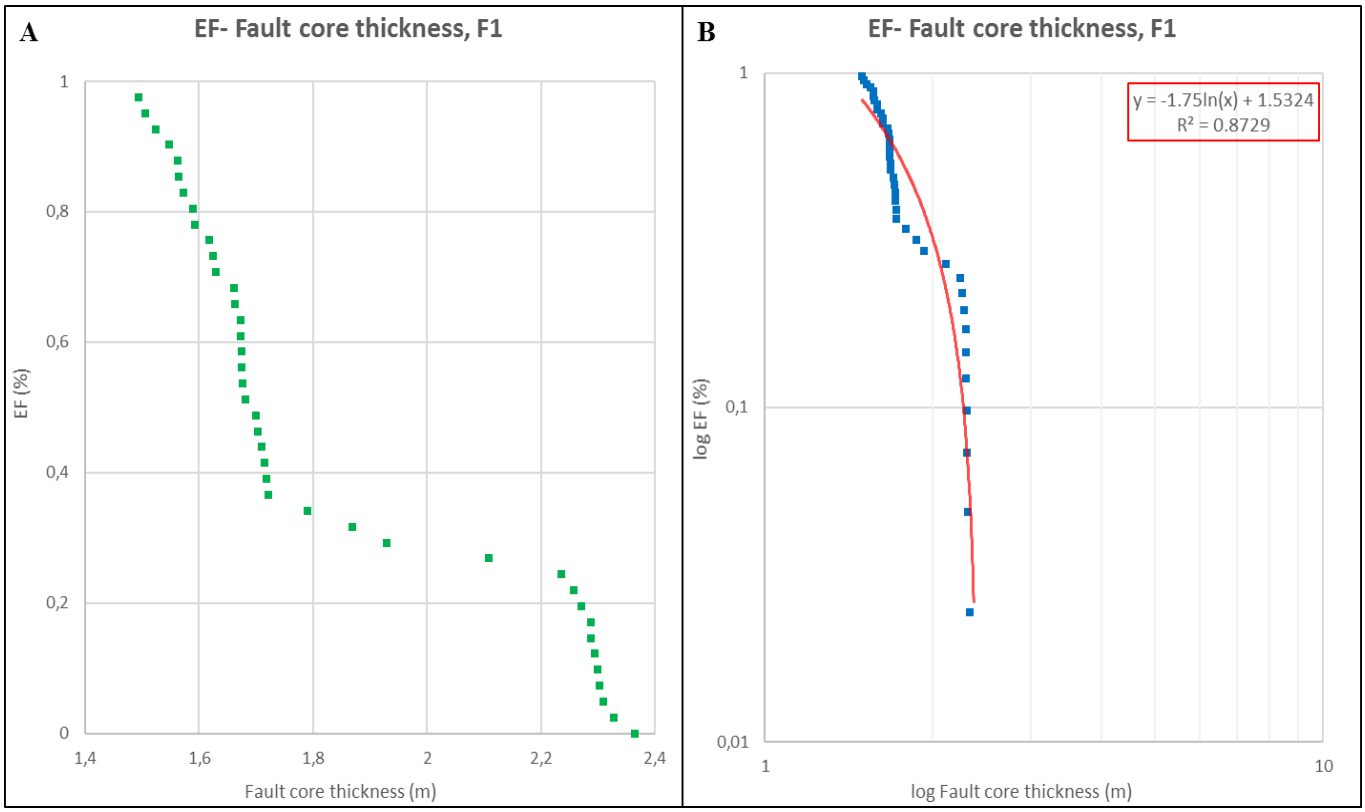

Figure 3.1.7: *EF-plots of the measured fault core thickness at fault F1 at R-191 Canyon. (**A**) Shows the EF in linear scale in relation to fault core thickness, also in linear scale. (**B**) Show the EF in logarithmic scale in relation to fault core thickness, also in logarithmic scale. The red line represents the correlated trend line fitted to the measurements. The correlated function and regression of fit are illustrated in the red square on the figure.*

On Figure 3.1.8 the EF-plots for the fault core thickness of zone A (A-B) and B (C-D) within F2 are illustrated. For the EF-thickness plots for the two zones (Figure 3.1.8 A and C), a roughly straight linear or concave down trend can be observed, but the plot for zone A (Figure 3.1.8 A), a straighter linear trend can be observed. While the log EF-log thickness plots (Figure 3.1.8 B and D), it appears that the measurements follow a concave down trend, characteristic for normal- or log-normal distribution. The EF-plots have been correlated to best fit a linear trend line, with a robust regression of fit value of 0.9769 for zone A and 0.931 for zone B, respectively. Based on the form of the plot and regression line fit, the general distribution trend supports a normal- or log-normal distribution of the thickness measurements.

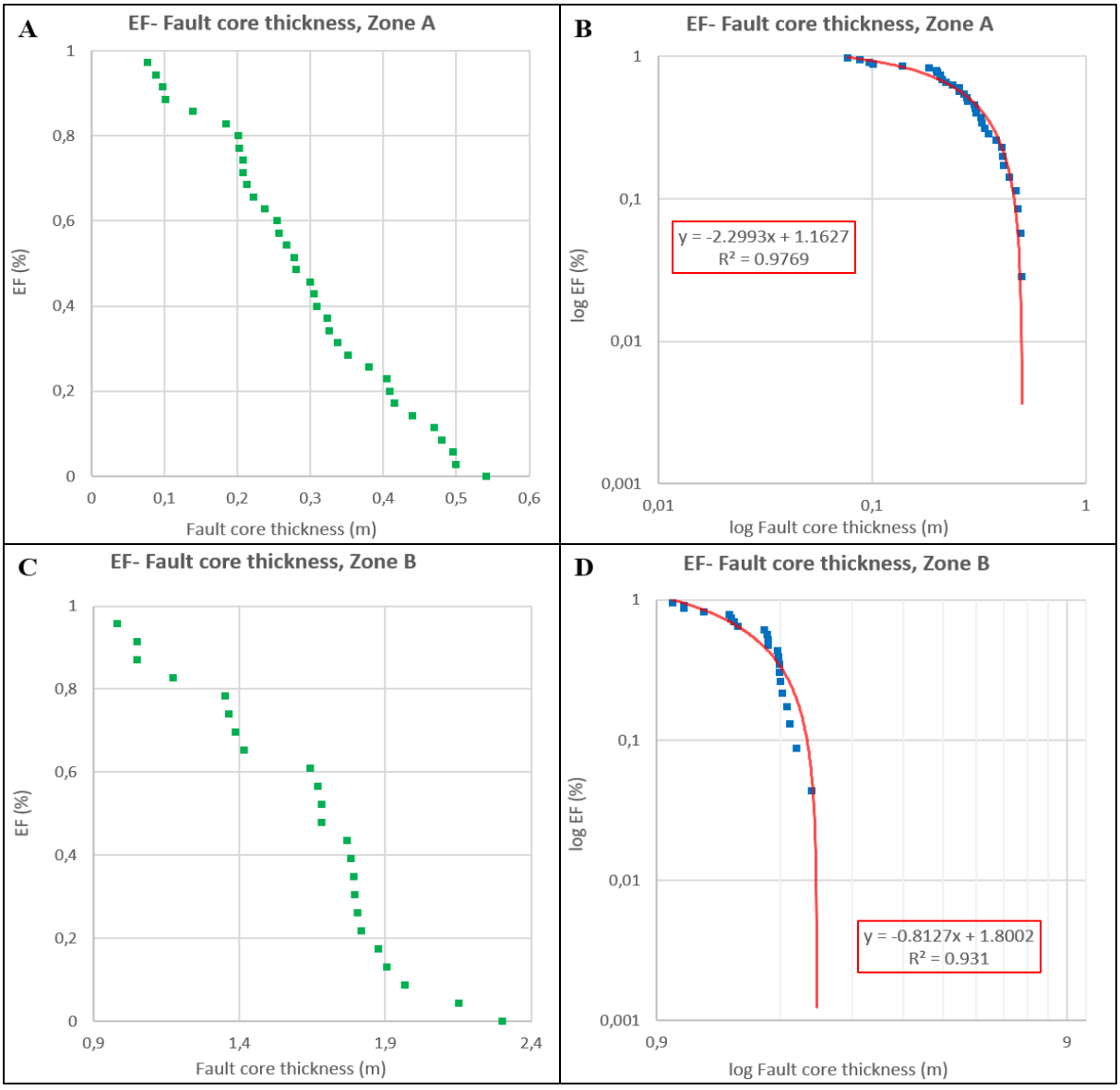

Figure 3.1.8: *EF-plots of the measured fault core thickness for zone A and B, F2 at R-191 Canyon. (**A** and **C**) Shows the EF in linear scale in relation to fault core thickness, also in linear scale. (**B** and **C**) Show the EF in logarithmic scale in relation to fault core thickness, also in logarithmic scale. The red line represents the correlated trend line fitted to the measurements. The correlated function and regression of fit are illustrated in the red square on the figure.*

Since zone A and B are situated within one fault, F2, only separated by slip surfaces, an EF-plot regarding the combined fault core thickness of zone A and B at the same level (representing total F2) are illustrated on Figure 3.1.9 A-B. The EF-thickness plot on Figure 3.1.9 A, show an overall linear or a slightly concave down trend from thickness values ranging from 1.5-2.5. For the two data points > 1.5 m, a concave up trend might be recognized. The log EF-log thickness plot (Figure 3.1.9 B), illustrates a similar concave down trend observed on the EF-plots for zone A and B (Figure 3.1.8 B and D). On this plot, a linear trend line has also been correlated to best fit the data points, with a regression of fit of 0.8831. This support a normal- or log-normal distribution of the core thickness measurements.

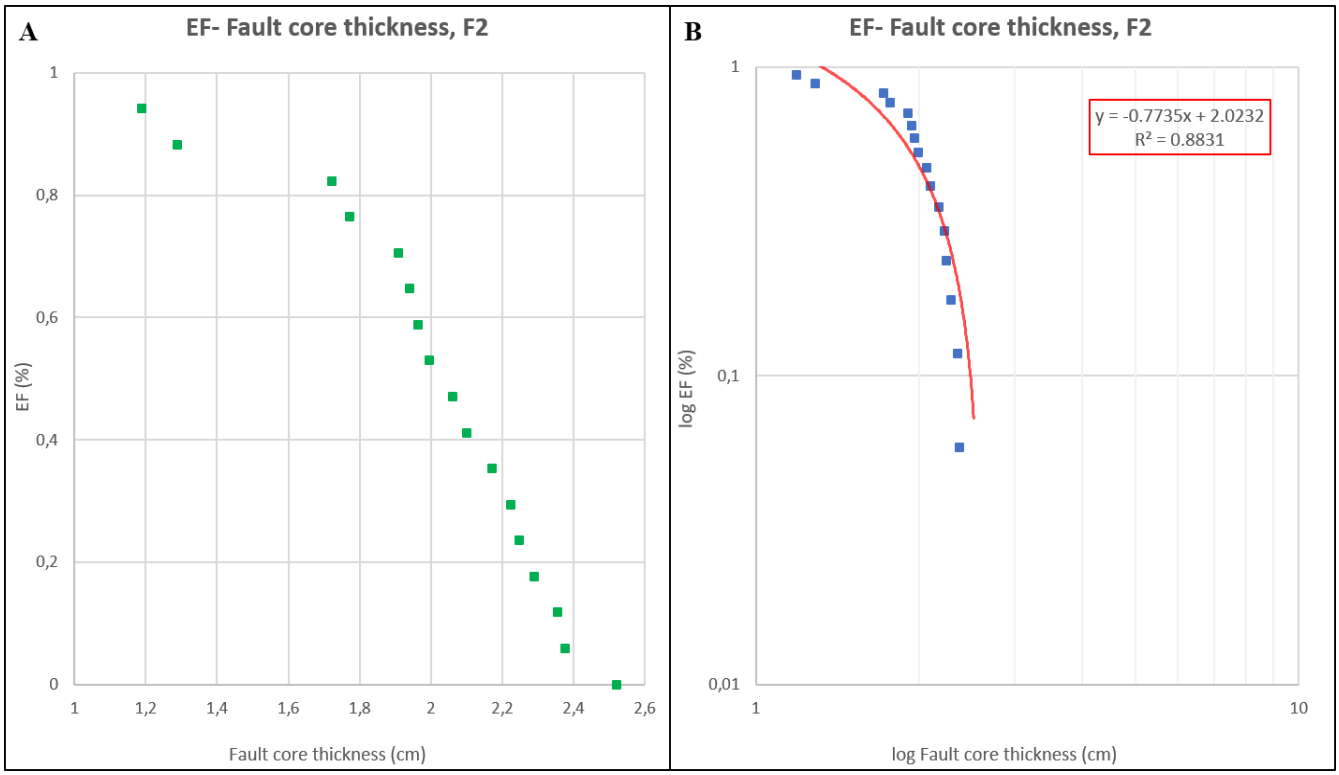

Figure 3.1.9: *EF-plots of the measured fault core thickness at fault F2 at R-191 Canyon. (**A**) Shows the EF in linear scale in relation to fault core thickness, also in linear scale. (**B**) Show the EF in logarithmic scale in relation to fault core thickness, also in logarithmic scale. The red line represents the correlated trend line fitted to the measurements. The correlated function and regression of fit are illustrated in the red square on the figure.*

3.2. Hidden Canyon, Utah

3.2.1. Structures and stratigraphic units

The Hidden Canyon Fault is a normal fault located ~25 km northwest of the town of Moab (Loc. 2 on Figure 2.1.4), within the Moab splay faults in the Bartlett Fault segment. The fault is located in one of several canyons that are oriented perpendicular to the strike of the Moab Fault. The displacement of the Hidden Canyon Fault is estimated to be about 200 m (Johansen and Fossen, 2008), while the displacement in the adjacent canyons of Bartlett Canyon and Waterfall Canyon ranges from 170 m to 300 m (Foxford et al., 1996). The orientation of the Hidden Canyon Fault is similar to the northern segments of the Moab Fault (Foxford et al., 1996), trending NW-SE with a dip of 63°NE (Figure 3.2.1).

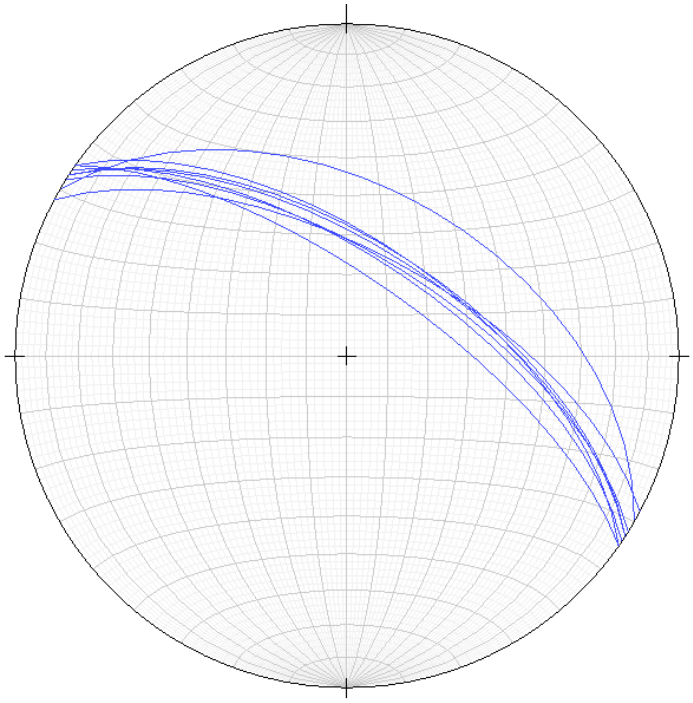

Figure 3.2.1: *Illustration of the completed orientation measurements on the Hidden Canyon Fault. The fault is trending NW-SE.*

The Hidden Canyon Fault is displacing the aeolian sandstone units of Moab Member and Slick Rock Member in the Entrada Sandstone in the hanging wall and the Cedar Mountain Formation, consisting of different fluvial sandstones and conglomerates in the footwall. On Figure 3.2.2 an outcrop picture of the Hidden Canyon Fault is shown, illustrating an interpretation of the fault core and the stratigraphic units in the wall rocks. The damage zone in the hanging wall includes a 200-300 m wide fault-parallel syncline, evidenced by drag folding and a complex rock- and fracture system within the Cedar Mountain Formation (Berg and Skar, 2005; Johansen and Fossen, 2008). The drag folding structures within the Cedar Mountain Formation has also been observed in the adjacent canyons, wherein Waterfall Canyon the drag structures were traced for 169 m, with intense fracturing. Indicating that the damage zone width in the hanging wall is minimum 169 m wide. The bedding of the aeolian sandstones in the footwall damage zone are oriented sub-horizontal, and fractures and

deformation bands (cataclastic- and disaggregation bands) are observed. Within the Moab Member, Berg and Skar (2005) observed some minor, subsidiary faults, oriented synthetic to the main Hidden Canyon Fault and the density of these subsidiary faults decreases away from the main fault core.

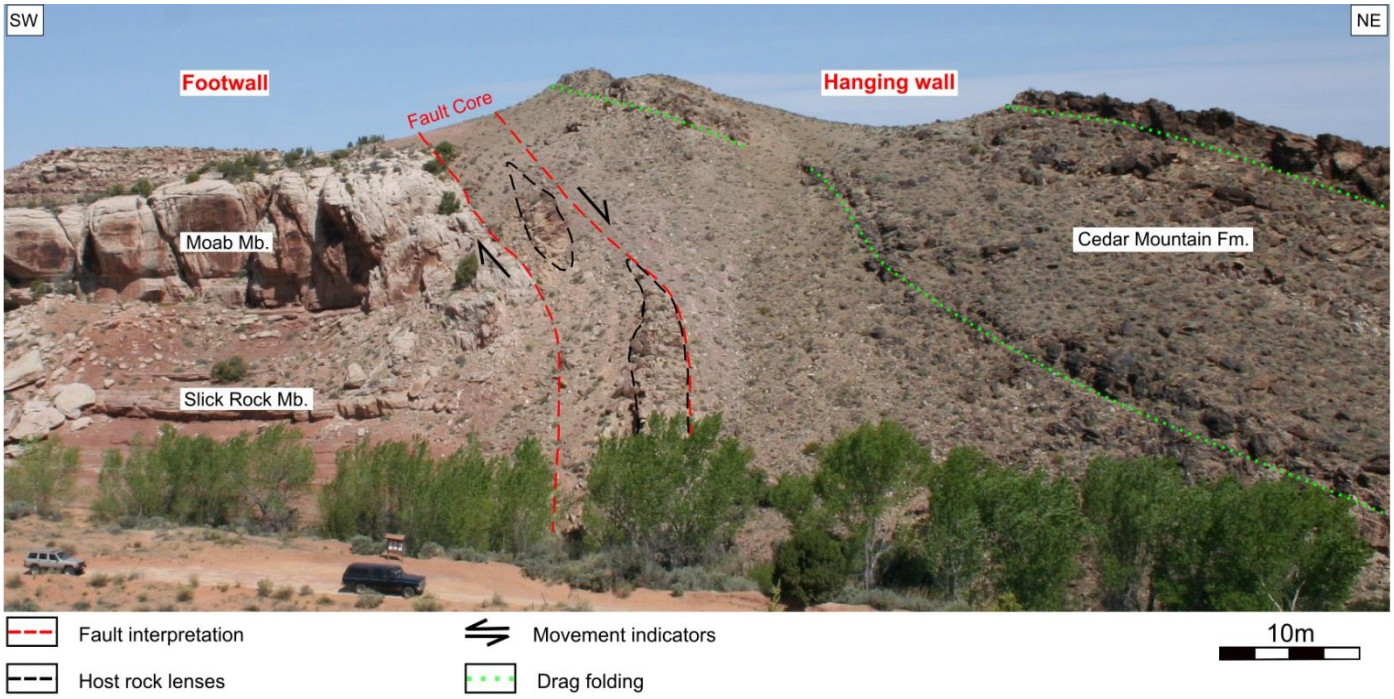

Figure 3.2.2: *Outcrop picture of the studied Hidden Canyon Fault, including fault interpretation and illustrating the stratigraphic units present in the wall rocks. The Hidden Canyon Fault show an irregular fault geometry and the measured fault core is wide. Situated within the fault core, two elongated sandstone host rock lenses derived from the Moab Member are present. Within the Cedar Mountain Formation in the hanging wall, drag folding related to the syncline have been interpreted with green dashed lines. Picture by Anita Torabi, 2009.*

3.2.2. Fault core and fault description

The Hidden Canyon Fault show an irregular fault core margin geometry at the outcrop (Figure 3.2.2), and this results in great lateral variation in the measured fault core thickness. The two Moab Member derived sandstone lenses incorporated in the fault core indicates major variation in strain intensity and deformation style during the faulting process (Berg and Skar, 2005). Cataclastic deformation bands, fractures, and slicken-lines are observed within these sandstone lenses. Measurements of the orientation completed on the slicken-lines indicated an N-S slip along the lenses. In the field, a 70 m scanline was conducted along the fault core, and thickness measurements of the fault core were completed every 5 m. The width of the present sandstone lenses was measured in the field, but the measurements are uncertain, due to the steep sides of the lenses reducing the accessibility to perform accurate measurements. To verify and support the measurements completed in the field, picture

measurements of the fault core thickness and the sandstone lens width was completed every 2.5 m. This resulted in a total of 27 fault core thickness measurements and 26 lens width measurements. The lowermost lens is located in the fault core from level 0-46.5 m, while the upper lens at 54.5-68 m from the base-scanline, respectively.

The fault rock documented in the fault core are a grey-beige fault gouge, but loads of debris buries major parts of the fault core. At the base of the outcrop, a clear fault core boundary between the Slick Rock Member and the lower sandstone lens can be identified (Figure 3.2.3). Following the boundary upwards, the boundary to the hanging wall rocks becomes buried by debris. However, the fault core boundary has been interpreted based on the fault trace and the fault core boundary at the lower- and upper parts of the fault.

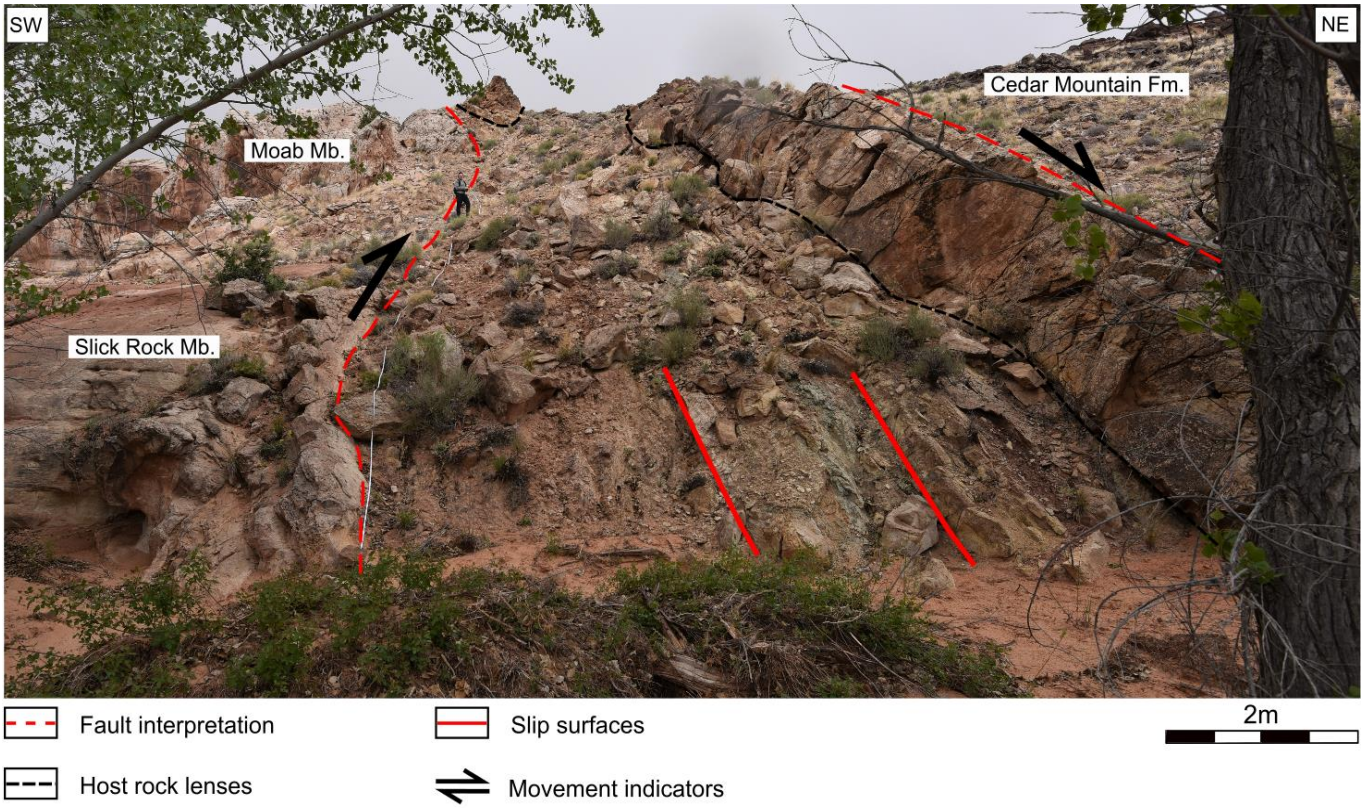

Figure 3.2.3: *Outcrop picture from the base-scanline of the Hidden Canyon Fault. In between the two interpreted slip surfaces a ~2.5 m wide zone of grey-beige fault gouge is located. The fault core boundary between the Slick Rock Member and the lowermost host rock lens can be observed. On the figure, the steep sides of the lowermost lens are visible, and this reduced the accessibility for accurate width measurements on the lenses in the field.*

From field observations and measurements completed on the Hidden Canyon Fault, the overall fault core thickness is wide, compared to the other fault cores studied and measured in this project. The fault core thickness measurements give an average thickness of 1090.79 cm, but if the lens widths are included in the thickness measurements, the average thickness increases to 1673.31 cm. This wide fault core could indicate several shaley fault gouge zones and slip surfaces present in the fault core,

where each gouge zone can vary in thickness from 1 cm to ~10 m (Foxford et al., 1998). Figure 3.2.4 shows a plot of the measured fault core thickness at the different levels along the fault core, both including and excluding the sandstone lenses width.

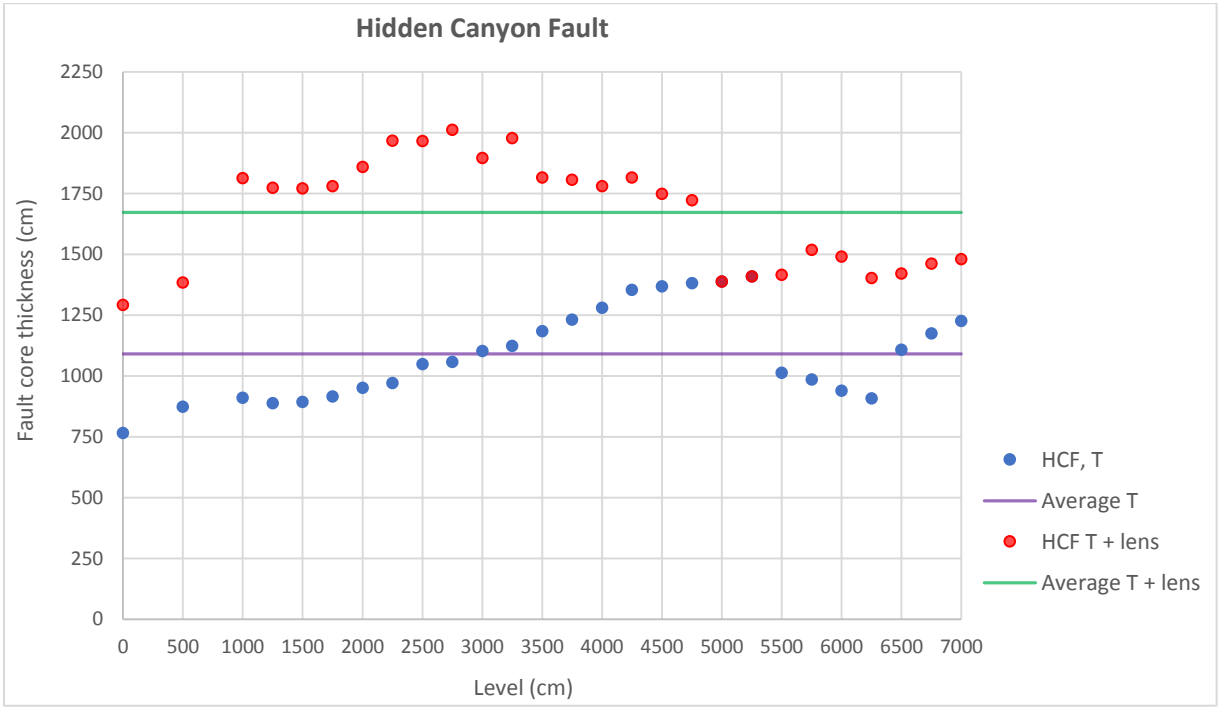

Figure 3.2.4: *Plot of the measured fault core thickness along the 70 m scanline, at the Hidden Canyon fault core. The width of the sandstone lenses is equal to the distance between the blue and red points on the plot. T; fault core thickness, HCF; Hidden Canyon Fault*

3.2.3. Statistical analysis of data

Two EF-plots have been constructed to recognize the distribution trend of the fault core thickness measurements from the Hidden Canyon Fault. The EF-plots are illustrated in Figure 3.2.5 A-B. The trend observed on the EF-thickness plot on Figure 3.2.5 A, appears to follow a roughly straight linear trend. On the log EF-log thickness plot (Figure 3.2.5 B), a concave down trend can be observed. The correlated function which best fit the data points show a logarithmic trend line with a strong R^2 of 0.9812. This indicates that the fault core thickness measurements appear to follow a log-normal distribution trend. However, based on the form of the data points in the EF-plots, an exponential distribution trend could also be an option.

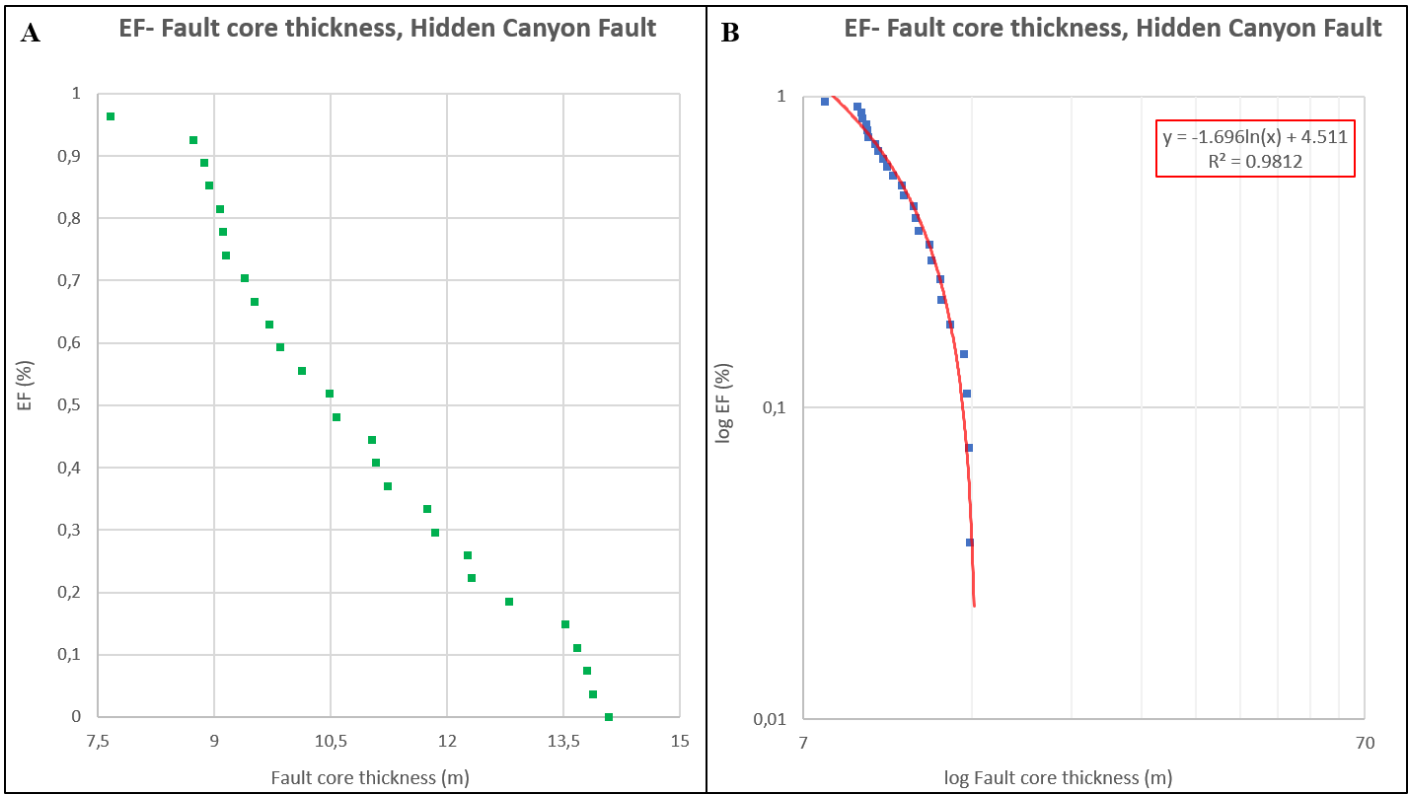

Figure 3.2.5: *EF-plots of the measured fault core thickness at the Hidden Canyon Fault. (**A**) Shows the EF in linear scale in relation to fault core thickness, also in linear scale. (**B**) Show the EF in logarithmic scale in relation to fault core thickness, also in logarithmic scale. The red line represents the trend line correlated to best fit the measurements. The correlated function and regression of fit are illustrated in the red square on the figure.*

3.3. Outside Arches National Park (ANP), Utah

3.3.1. Structures and stratigraphic units

The studied locality is located at a roadcut along highway 191, within sight of the Arches National Park (ANP) visitor center, about 7 km north of the town of Moab (Loc. 3 on Figure 2.1.4). At the locality, a 200 m long scanline was conducted along the base of the outcrop, and a total of 39 normal faults was documented and measured along the scanline (Figure 3.3.2). The normal faults located at the outcrop are part of the damage zone of the Moab Fault footwall, which forms the steep cliffs of the Moab Canyon. The orientation of the measured faults has a main NW-SE trend (Figure 3.3.1), running approximately parallel to the surrounding structures of the Moab anticline and the Moab Fault zone (Foxford et al., 1996). Within the orientation measurements, there appears to be a small N-S component, which cannot be convincingly explained. However, the NW-SE alignment of fault orientation indicates that the normal faults at the outcrop are either directly or indirectly controlled by the geometry of the surrounding deformation.

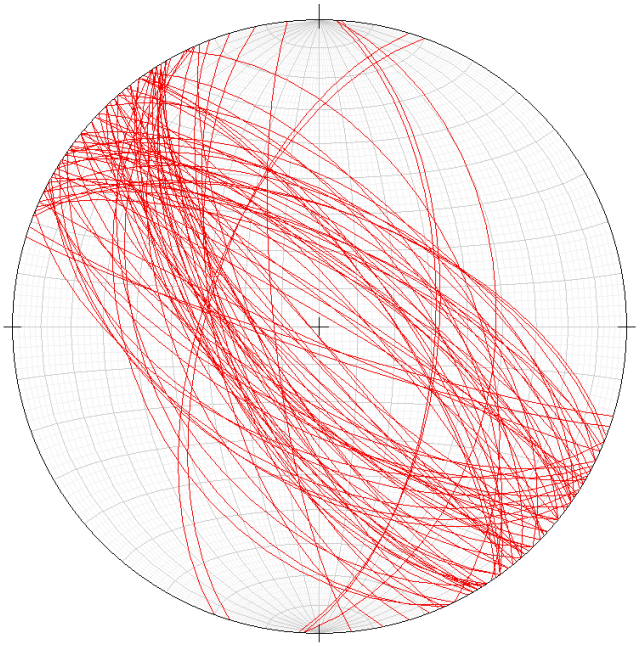

Figure 3.3.1: *Stereonet illustrating the total 96 fault orientation measurements completed on the 39 normal faults at the studied locality. For the general NW-SE trending faults, two different dip directions can be observed; one set dips on average 65°SW and the other dips on average 69°NE.*

The stratigraphic units exposed at the outcrop are the Honaker Trail Formation from the Upper Pennsylvanian, were different types of siliciclastic sedimentary rocks are observed. Although the Honaker Trail Formation are dominated by carbonates deposited in the Paradox Basin (Barbeau, 2003; Trudgill, 2011), the sedimentary rocks located at the outcrop includes both sandstones and shales, which could represent the proximal northeastern part of the basin, where accumulation of aeolian and fluvial deposits occurred (Nuccio and Condon, 1996). On Table 1, a short description of the different siliciclastic rocks found at the outcrop is presented. The boundaries between the rocks have been interpreted on Figure 3.3.2. These layer boundaries have been used as marker beds for displacement measurements of the different faults at the outcrop.

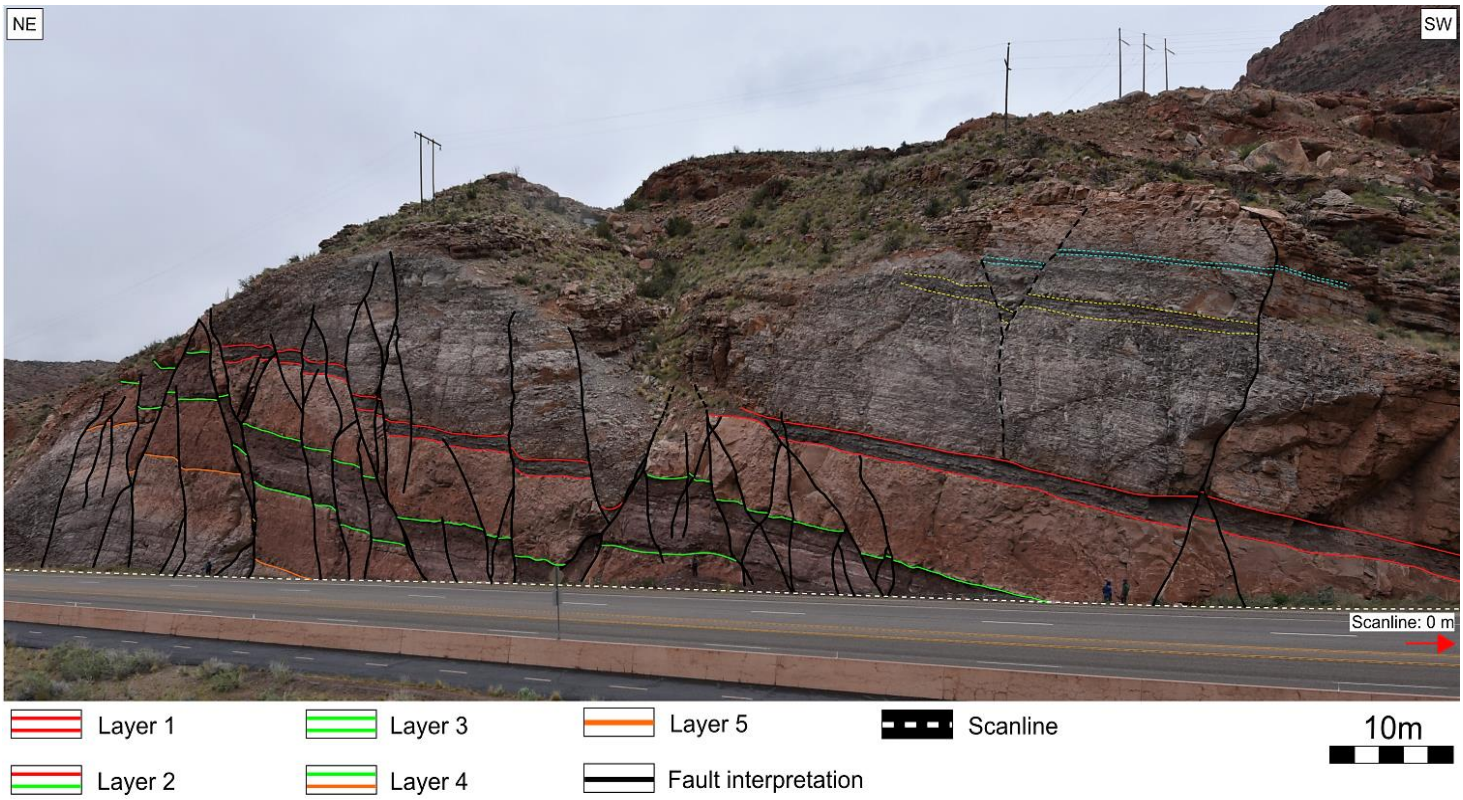

Figure 3.3.2: *Outcrop picture of the studied locality outside ANP. An interpretation of the studied normal faults is illustrated in the figure. Several of the faults display a complex fault geometry and conjugate fault sets, related to fault interactions and fault linkage. The figure also shows an interpretation of the stratigraphic boundaries between the different layers (1-5). A short description of each layer is presented in Table 1 below.*

Table 1: *A short description of the different layers exposed at the outcrop (Figure 3.3.2).*

Layer	Thickness (m)	Description
1	1.15 – 1.75	Grey-brown, friable, sandy shale layer. Within the shale layer, three 10-20 cm thick sandstone sequences are present, and each sequence is overlaid by a cm thick shale layer. Sharp boundary to layer 2.
2	6.10 – 8.00	Beige-orange, massive, well-sorted, very fine grained sandstone. Within the layer, low-angle eastward dipping cross-bedding are observed. Sharp planar boundary to layer 3.
3	4.00 – 5.65	Reddish-brown, fine-coarse grained, shaley sandstone. Top of the unit consists of a ~60 cm thick brown shale sequence, overlying a fine-coarse grained sandstone sequence. Sharp planar boundary to layer 4.
4	7.35 – 8.50	Brown-orange, massive, fine-grained sandstone. Some minor cross-bedding structures can be observed, otherwise no primary sedimentary structures visible within the layer. Sharp boundary towards layer 5.
5	> 10	Massive limestone layer, with no lower boundary visible at the outcrop. Crinoids and brachiopods fossils are observed in the layer. Intensely fractured around the faults, compared to the sandstones and shales.

3.3.2. Fault core and fault descriptions

At the studied locality, multiple fault core thickness and fault displacement measurements have been completed, both in the field and from pictures. Many of the displacement measurements have been carried out using pictures because at the outcrop the measurable displacement is displayed higher up on the outcrop, which was not accessible in the field. However, the displacement measured at one single fault show some variations in displacement. This can be related to lithological variations along the fault, or fault interactions and linkage which also can affect the displacement along the fault and displacement transfer between fault segments can occur (Peacock and Sanderson, 1991). The completed fault core thickness measurements also show great thickness variations among the measured faults. The general trend from the collected data indicates that faults with major displacements, usually have a wider fault core, compared to faults with smaller displacements. Another observation shows that lithology affects the fault core thickness. When faults juxtaposed against shale layers, the fault core widens, despite the amount of displacement. Figure 3.3.3 illustrates this observation, where the fault core widens dramatically when juxtaposed against the shale layer. The figure also shows the major lateral variations in fault core thickness and how it can occur over very short distances.

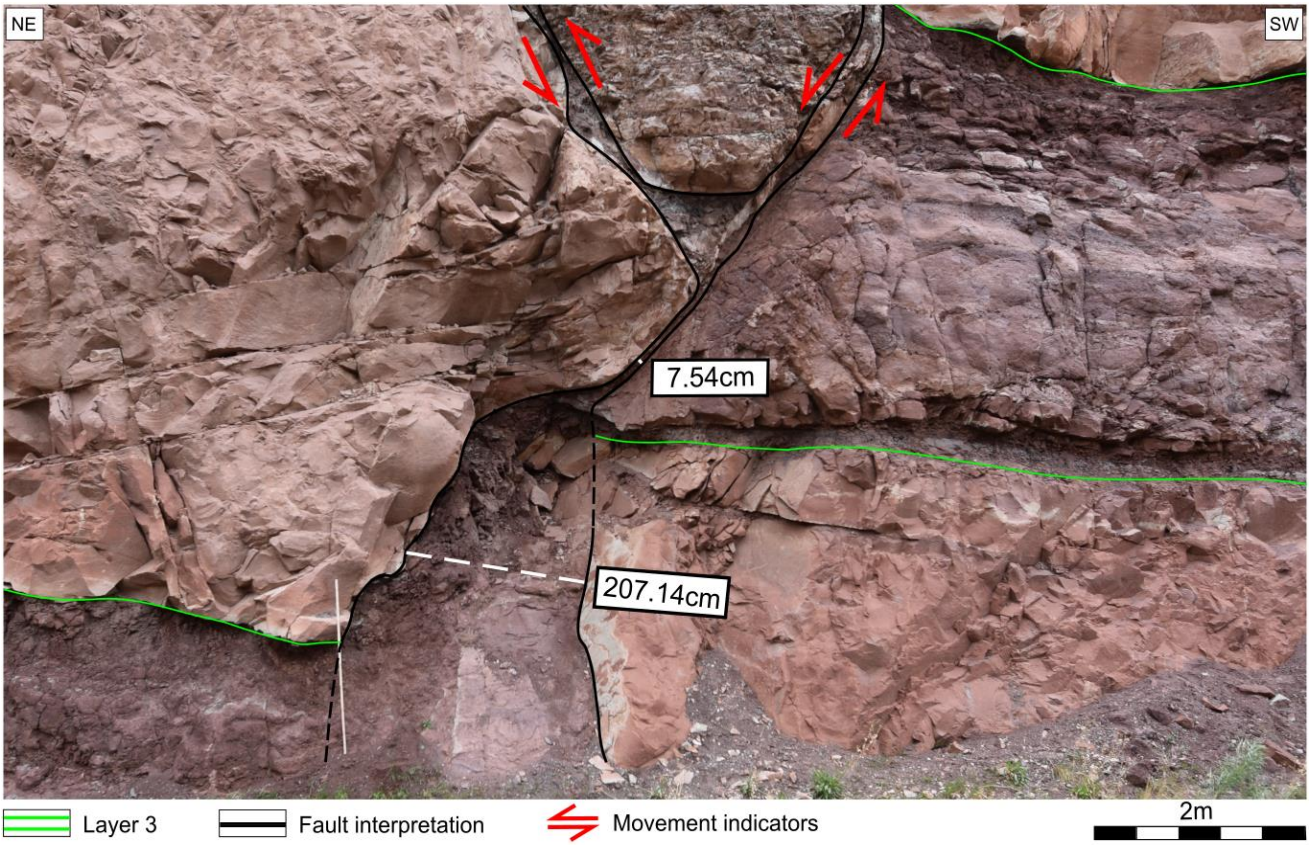

Figure 3.3.3: *Illustration of major lateral variation in fault core thickness at one of the measured faults at the ANP locality. The distance between the two measurements are 3.6 m, and the thickness varies by a factor of 27 over this relatively short distance. The shale layer is the top sequence of layer 3 at the outcrop and shows how the shale layer affects the fault core thickness.*

Similar lateral variations in fault core thickness related to lithology differences were observed in all the fault cores at the locality, but it is more remarkable in the fault illustrated in Figure 3.3.3. From the measured data, the general variation in fault core thickness ranges between a factor of 4-15, when comparing the core thickness of faults juxtaposed against sandstone and shale layers. The factor is found by dividing the average fault core thickness when displacing shale-sandstone, with the average fault core thickness when juxtaposing sandstone-sandstone. These observations show how the fault core thickness can vary due to changing lithologies along the fault and how these thickness variations can occur over relatively short distances.

Another factor affecting the lateral variations of fault core thickness is the occurrence of fault core lenses derived from the surrounding wall rocks. Generally, the fault core lenses were situated in major faults, with some exceptions. On Figure 3.3.4 a lens derived from layer 3 and 4 are situated in the fault core of a major fault at the outcrop. The lens on the figure are incorporated in between two slip surfaces and the figure also illustrate how the lens influence the fault core thickness.

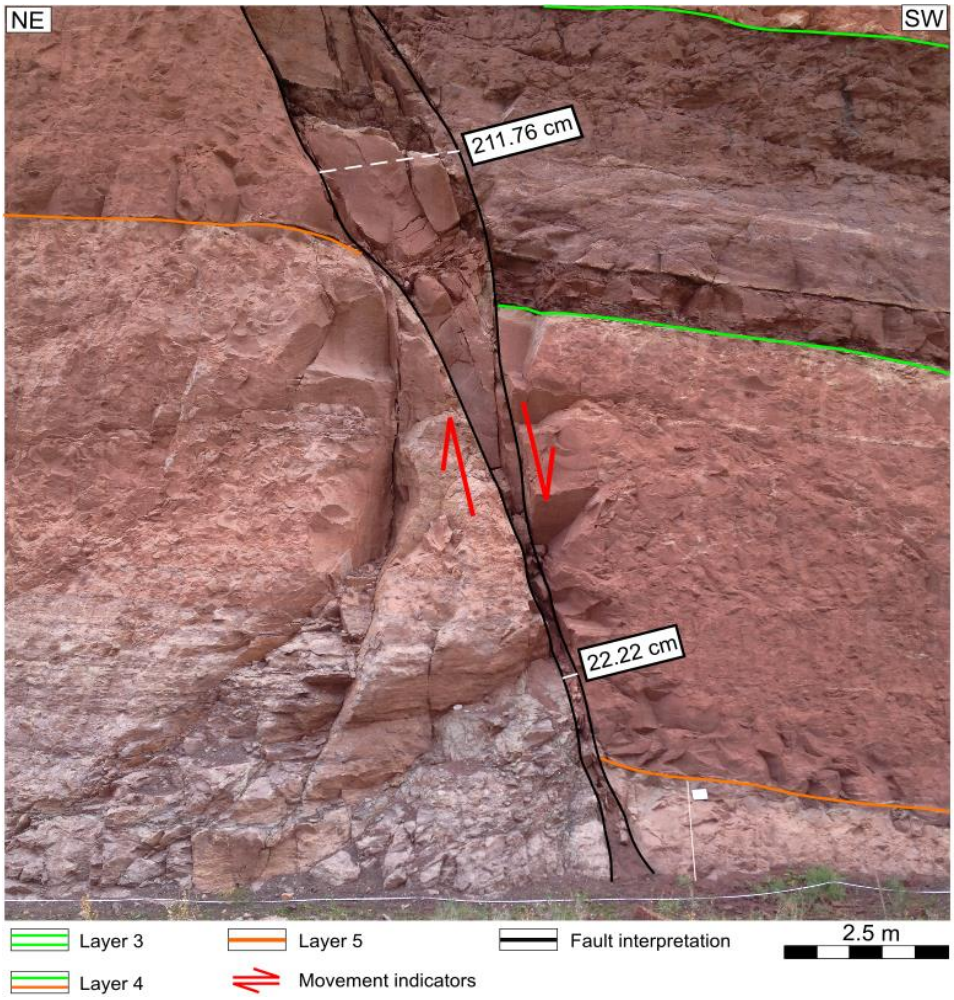

Figure 3.3.4: *A fault core lens derived from the wall rock, situated in the fault core of one of the major normal faults studied at the outcrop. The lens can be traced for 10.44 m along the fault core, and the average width of the lens is measured to 139.86 cm. The figure illustrates how the lens affects the fault core thickness along the fault.*

The density of faults at the outcrop varies along the scanline, but the most densely faulted area stretches from an interval of 69.4-136.6 m on the scanline, where 24 of the total 39 normal faults were measured and observed. In this interval, many of the measured faults are linked, or the faults are splaying towards the base of the outcrop, developing complex fault structures. Figure 3.3.5 illustrates a section from 110.2-130.8 m on the scanline, where a total of six faults are exposed. The faults on the figure have been interpreted and show linkage of fault segments, and how some of the faults are splaying towards the base of the outcrop.

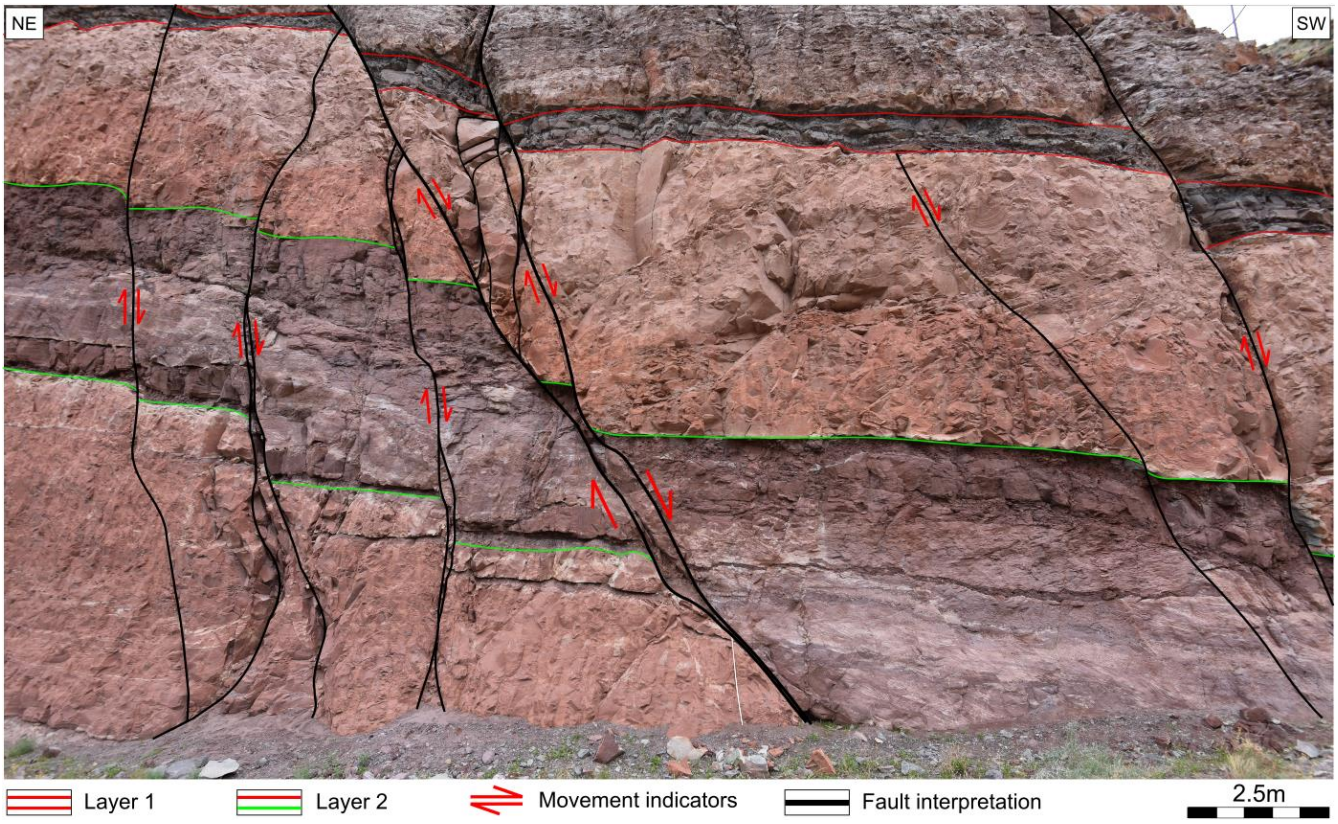

Figure 3.3.5: *Illustration and interpretation of the six normal faults located along the scanline section of 110.2-130.8 m. The interpreted faults show complex fault geometries and linkage of faults can be observed. The fault displacement of the different fault can easily be observed, due to the color differences between the layers and the sharp planar boundaries.*

Table 2 contains a summary of the measurements completed on the 39 normal faults studied at the ANP locality, including the total measured heights conducted in the field and from pictures. Since generally only the lowermost 3-4 m was accessible in the field, picture measurements have been completed, to strengthen the total fault core thickness measurements and to better examine the variations in thickness at the higher levels along the faults. A comparison of the average thickness from the picture- and field measurements are presented in the table. The table also presents the average displacement of the faults, collected both from the picture- and field measurements.

***Table 2**: Summary of the fault measurements completed on the 39 normal faults located along the scanline at ANP. H: height (or elevation), T; fault core thickness, D; displacement, Pic; measurements only possible or completed on pictures, X; no measurements*

Fault nr	Position on scanline (m)	Orientation	Measured *H* field (m)	Measured *H* picture (m)	Average *T* field (cm)	Average *T* picture (cm)	Average *D* (cm)
Fault 1	47.6	147/75	2.2	4.0	0.45	0.87	51.20
Fault 2	52.9	309/57	3.6	4.2	1.27	1.40	54.61
Fault 3	69.4	153/72	2.6	X	16.68	X	11.00
Fault 4	72.2	129/58	2.9	3.6	7.47	6.83	115.52
Fault 5	75.9	117/54	2.4	2.4	0.39	0.45	4.42
Fault 6.1	78.1	140/67	2.4	4.9	2.03	2.09	26.12
Fault 6.2	78.9	143/73	2.4	4.9	1.90	2.45	21.27
Fault 7.1	81.6	157/70	4.2	6.2	8.14	8.88	116.68
Fault 7.2	82.4	123/55	2.4	2.4	7.54	7.63	24.51
Fault 8.1	96.1	293/58	3.6	9.3	122.35	67.54	687.39
Fault 8.2	96.1	302/61	Pic	4.0	Pic	24.70	350.99
Fault 9.1	100.6	309/77	Pic	1.8	Pic	35.90	145.29
Fault 9.2	102.3	304/79	1.8	9.8	6.49	14.14	145.29
Fault 10	106.6	148/63	1.8	3.3	1.57	1.68	35.92
Fault 11	109.6	320/76	2.4	X	0.80	X	18.00
Fault 12	110.2	146/63	2.4	X	2.23	X	20.00
Fault 13	113.0	296/69	2.4	X	0.80	X	18.00
Fault 14.1	113.4	151/42	4.2	13.2	12.86	17.42	206.46

Fault 14.2	113.4	155/47	Pic	5.4	Pic	4.92	92.23
Fault 15	119.3	138/73	2.5	X	1.91	X	8.10
Fault 16.1	120.1	305/83	2.4	3.0	4.70	7.26	40.98
Fault 16.2	121.6	302/85	Pic	9.5	Pic	5.59	40.98
Fault 17.1	123.4	134/68	1.8	14.4	39.80	26.61	106.3
Fault 17.2	124.8	309/68	1.8	13.8	27.00	40.77	105.07
Fault 18	125.8	X	Pic	15.0	Pic	4.91	33.25
Fault 19	136.6	131/70	2.4	16.4	29.18	98.52	720.36
Fault 20	148.4	150/67	3.0	12.0	6.18	6.09	44.68
Fault 21	150.2	141/66	Pic	6.3	Pic	2.00	10.07
Fault 22	159.5	135/82	2.4	10.3	15.34	9.07	186.41
Fault 22.1	161.3	323/66	Pic	5.4	Pic	1.27	5.88
Fault 22.2	163.9	319/59	2.4	7.5	1.54	1.38	9.26
Fault 22.3	164.4	323/70	Pic	8.4	Pic	1.61	7.93
Fault 22.4	166.4	326/62	3.0	8.0	1.05	1.15	7.46
Fault 22.5	168.3	325/60	3.0	8.1	0.95	1.01	7.01
Fault 23	169.4	307/74	Pic	9.4	Pic	6.11	X
Fault 24	170.7	297/71	2.4	X	0.93	X	4.00
Fault 25	173.0	164/65	Pic	10.2	Pic	13.30	183.33
Fault 26	173.7	153/75	2.5	X	3.35	X	X
Fault 27	174.0	159/66	2.4	X	2.85	X	X

Two plots illustrating the average fault core thickness and displacement data in Table 2 are presented in Figure 3.3.6, allowing for comparison of the displacement and core thickness. The plots show the different faults position on the scanline. A general trend shows how the fault core thickness and fault displacement are connected. The plots show how fault core thickness typically increases with increasing displacement. This was also documented in the field, where faults with greater displacement had a wider fault core, compared to faults with smaller displacements. However, some exceptions are visible on the plots, and they are generally related to lithological variations along the different faults.

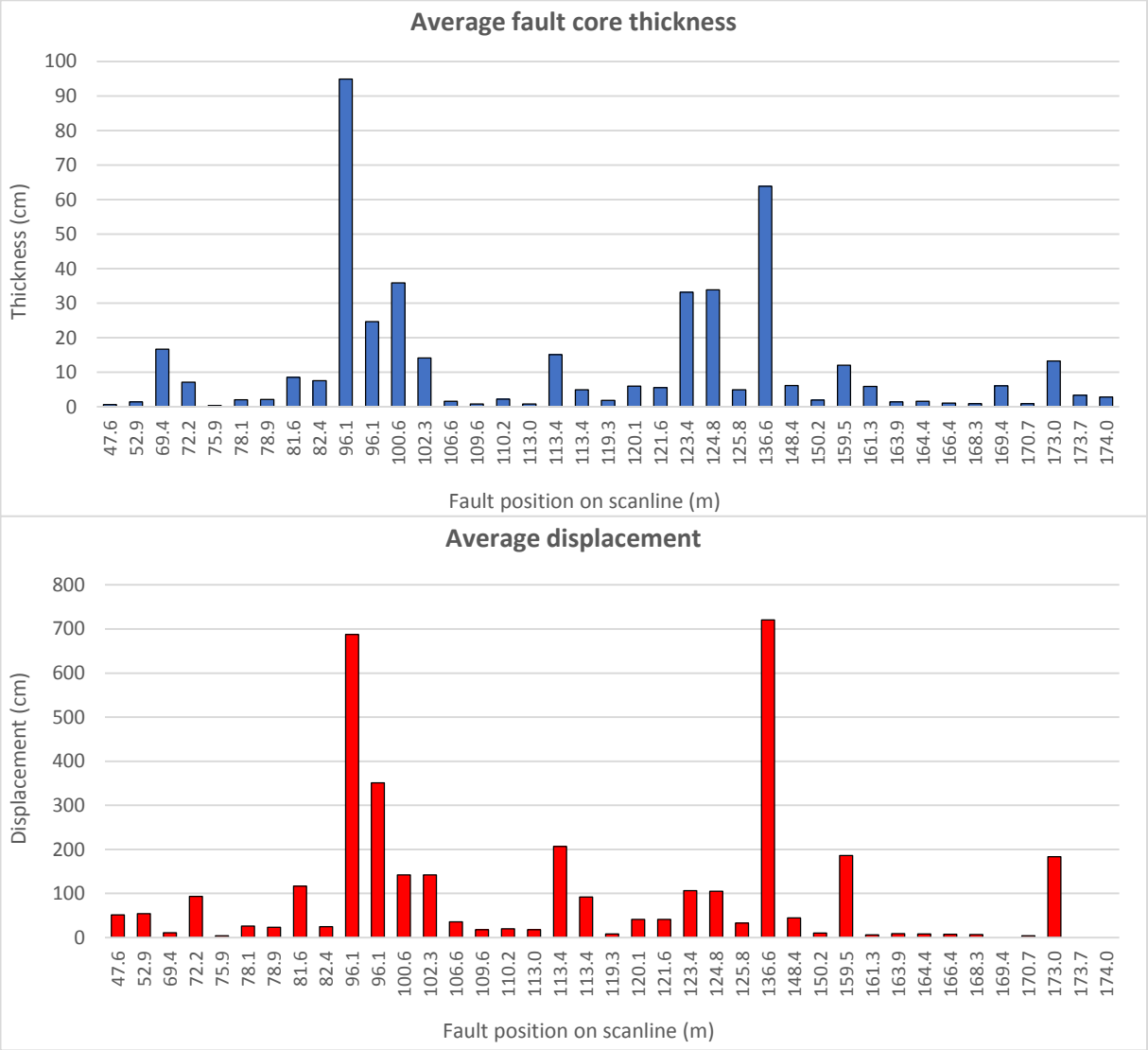

Figure 3.3.6: *Two plots illustrating the average fault core thickness and fault displacement of measured faults located along the scanline. The fault position on the scanline can be used to compare the fault core thickness and displacement for the different faults.*

3.3.3. Statistical analysis of data

The data collection completed at the ANP locality has resulted in a total of 571 fault core thickness- and 106 fault displacement measurements on the 39 studied faults. These measurements have been used to complete univariate analysis and to construct EF-plots for both the fault core thickness and fault displacement, to recognize the distribution type for these fault attributes. The EF-plots regarding the fault core thickness and fault displacement are illustrated on Figure 3.3.7 A-D. On the EF-thickness plot (Figure 3.3.7 A), the plot forms a hyperbolic shaped, concave down trend, characteristic for a power-law distribution. The same distribution trend can be observed on the EF-displacement plot on Figure 3.3.7 C. Although, on the log EF-log thickness and log EF-log displacement plots (Figure 3.3.7 B and D), a concave down trend forms and the "tails" can easily be observed (dashed black circle on the figure). For all the measurements, including the "tail" members, a log-normal distribution has been correlated to be the best fit for the dataset. However, if 10 % of the measurements are removed, a power-law distribution trend can be recognized on the log-log EF-plots, with characteristic distinct straight segments. On the log EF-log thickness plot (Figure 3.3.7 B), two straight segments can be observed, suggesting two power-law trends that intersect at ~0.25 m and EF=18 %. The two straight segments indicate that there is a power-law distribution for each of segment. The regression of fit for a power-law distribution trend is robust, with a correlated coefficient value above 0.93 for each trend. Based on the fitted trend lines and regression of fit values, the fault core thickness and displacement measurements appear to follow a power-law or log-normal distribution trend.

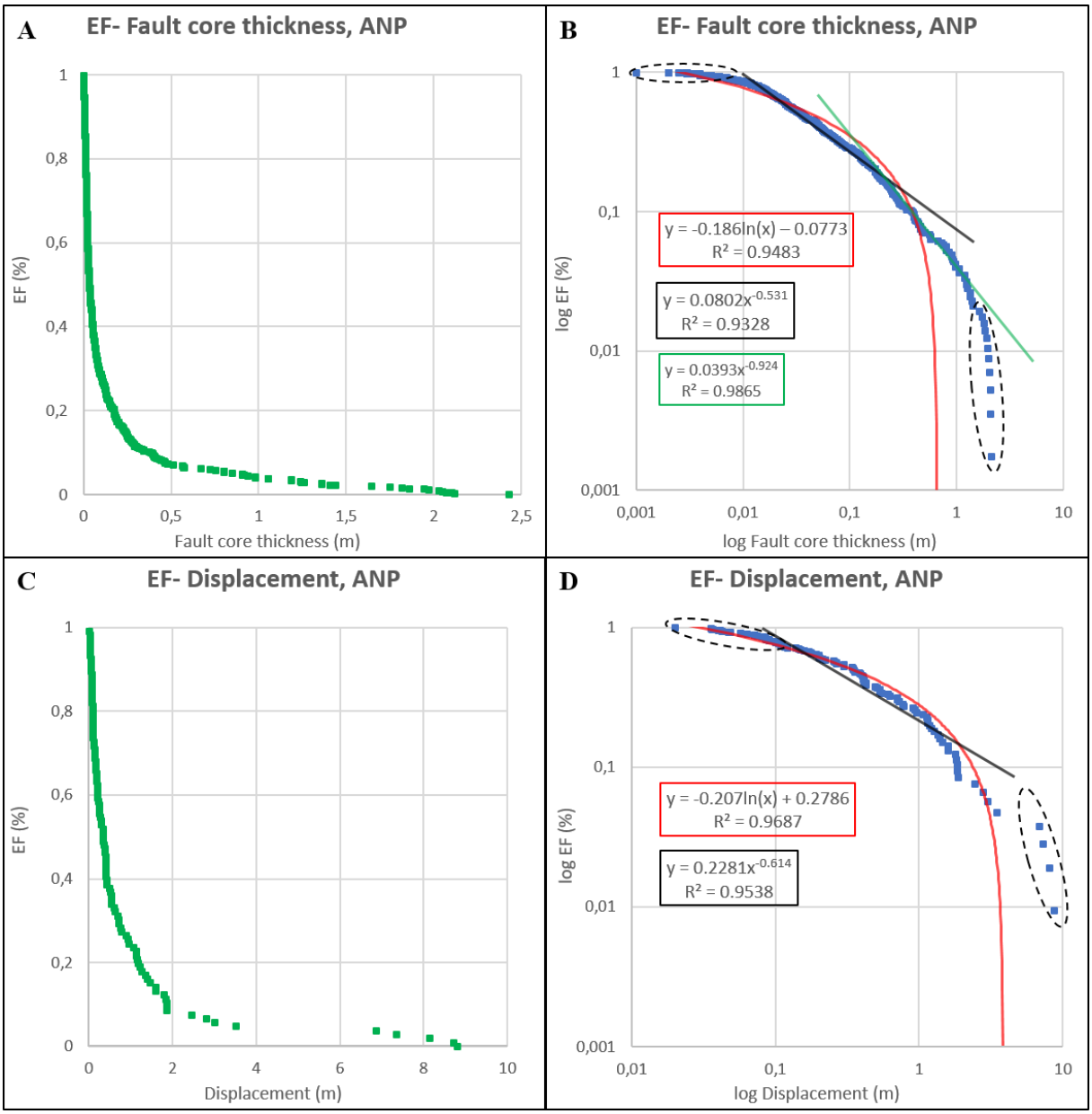

Figure 3.3.7: *EF-plots of the fault core thickness (A and B) and fault displacement (C and D) at the ANP locality. (**A**) Shows the EF in linear scale in relation to fault core thickness, also in linear scale. (**B**) Shows the EF in logarithmic scale in relation to fault core thickness, also in logarithmic scale. The red and black line represents the trend lines correlated to best fit the measurements. The correlated functions and R^2 values are presented in the squares on the figure, following the same color code as the trend lines. The dashed black circle represents the endmembers or "tail" members of the measurements. C-D follow the same order as A-B, using fault displacement data.*

Fault displacement was measured at different levels along the fault core, and where displacement measurements were conducted, the fault core thickness was measured at the exact same level. This was done to investigate and collect thickness measurements with known fault displacement. The measurements can further be examined to state if any relationship exists between the two fault attributes. Figure 3.3.8 illustrates a log-log plot of the measured fault core thickness and fault

displacement. The fault core thickness measurements are spread over four orders of magnitude, from 0.001 m up to 2.104 m, while the displacement measurements cover a range of three orders of magnitude from 0.02 to 8.716 m. From the EF-plots on Figure 3.3.7, the distribution of the measurements is following a power-law distribution. Using a power-law relationship, the measurements plotted show a core thickness-displacement relationship following the function $T = 0.0992D^{0.8151}$, with a regression of fit of 0.6146.

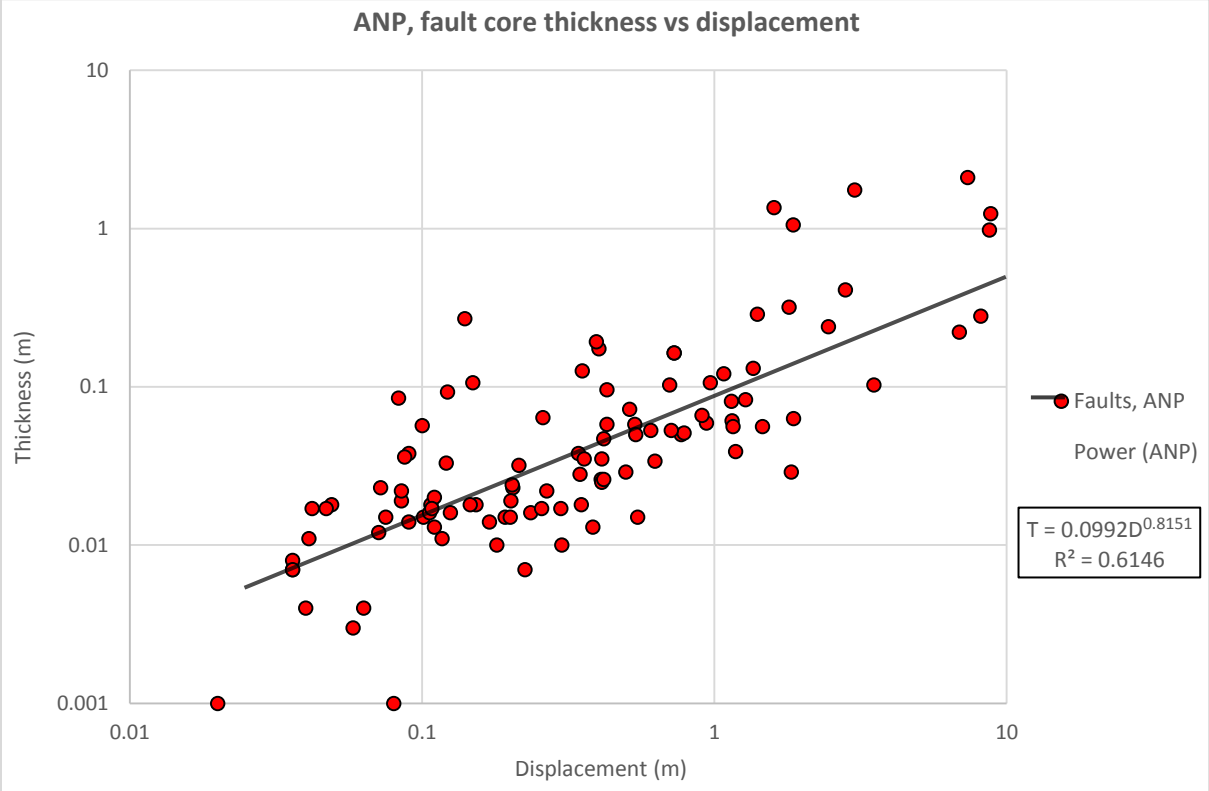

Figure 3.3.8: *Log-log plot of the fault core thickness versus fault displacement for the studied normal faults at ANP. The data plotted represents both field and picture measurements from the locality. The black line represents the power-law function, correlated to be the best fit of the dataset, giving a regression of fit (R^2) equal to 0.6146.*

3.4. Cache Valley, Arches National Park, Utah

3.4.1. Structures and stratigraphic units

Cache Valley is located along the eastern border of Arches National Park (Loc. 4 on Figure 2.1.4), and the studied outcrop is found approximately 1.4 km southeast from the famous Delicate Arch. The main fault at the studied outcrop is displacing the aeolian Navajo Sandstone in the footwall and the Entrada Sandstone and Dewey Bridge Member in the hanging wall. The fault is part of a large bounding normal fault system located in Cache Valley. A salt diapir developed underneath the valley during salt migration in the Pennsylvanian-Triassic, leading to the formation of a salt-cored anticline (Doelling, 1988; Davatzes and Aydin, 2003). The ongoing diapirism was probably responsible for the development of the bounding normal fault system during the Tertiary, and continuous dissolution of the underlying salt may have contributed to increased slip on these faults (Doelling, 1985; Davatzes and Aydin, 2003). The displacement of the main fault at the outcrop is estimated to be about 30 m, based on field observations by Braathen et al. (2012) and Alikarami et al. (2013).

Minor subsidiary normal faults have been observed and documented in the damage zone of the main fault, both in the hanging wall and footwall. These faults were observed along a 200 m scanline, conducted at the base of the footwall and hanging wall. Fault core thickness measurements have been carried out on the main fault, and on the five subsidiary faults in the hanging wall and one in the footwall. Orientation measurements completed on all the studied faults show that the minor subsidiary faults have an antithetic orientation compared to the main fault, illustrated in Figure 3.4.1. The main fault shows a steep dip of 71°SW and is trending NW-SE, which is sub-parallel to the axis of the Cache Valley salt-cored anticline (Doelling, 1988; Davatzes and Aydin, 2003).

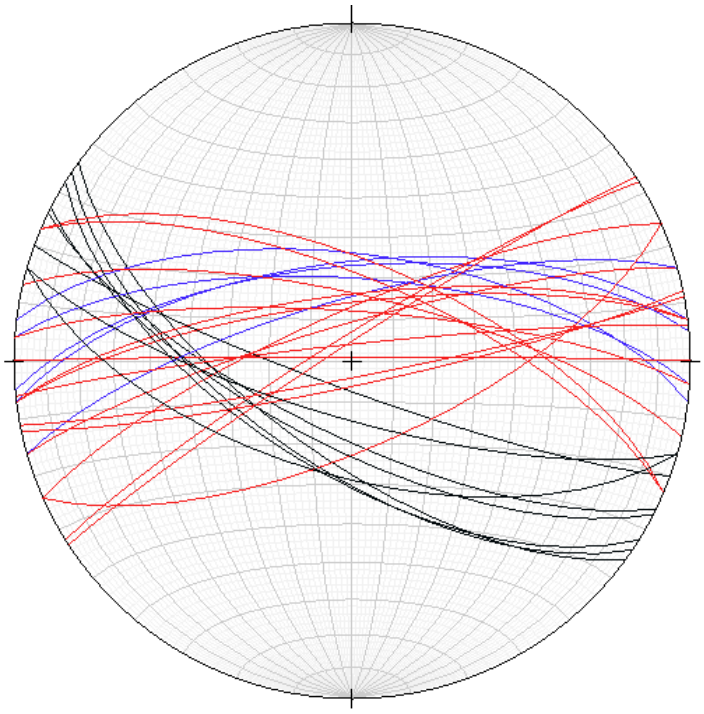

Figure 3.4.1: *Illustration of the orientation measurements on the studied faults in Cache Valley. The main fault orientation is represented by the black lines, while the orientation of the subsidiary faults situated in the hanging wall is illustrated with red lines and the footwall fault by the blue lines.*

In the footwall damage zone of the main fault, a swarm of deformation bands and deformation band clusters are observed. A distinct color alteration is observed in the sandstone unit, where the rocks have been affected by bleaching (removal of grain coating hematite), resulting from a reduced fluid migrating through the unit. Braathen et al. (2012) suggest that the fluid migrated through fracture systems located in the main fault core and migrated into the Navajo Sandstone (paleo-reservoir). Bleaching fingers are also observed in the Entrada Sandstone in the hanging wall, close to the main fault core. The boundaries of the bleaching are interpreted on Figure 3.4.2, illustrating the color alteration related to the bleaching in the sandstone units. The Dewey Bridge Member consists of a dense, fine-grained silty/muddy sandstone, with a low average permeability of 9 mD (Alikarami et al., 2013), and would act as an impermeable layer. This indicates that the main fault at one point acted as a conduit for fluid migration across the fault, and the fluids migrated into the most porous and permeable units at the outcrop. Another evidence for this hypothesis is the dense, cemented fault rocks documented and observed in the main fault core (Figure 3.4.3), which could result from reduced fluid migration and eventually cementation of the fault core.

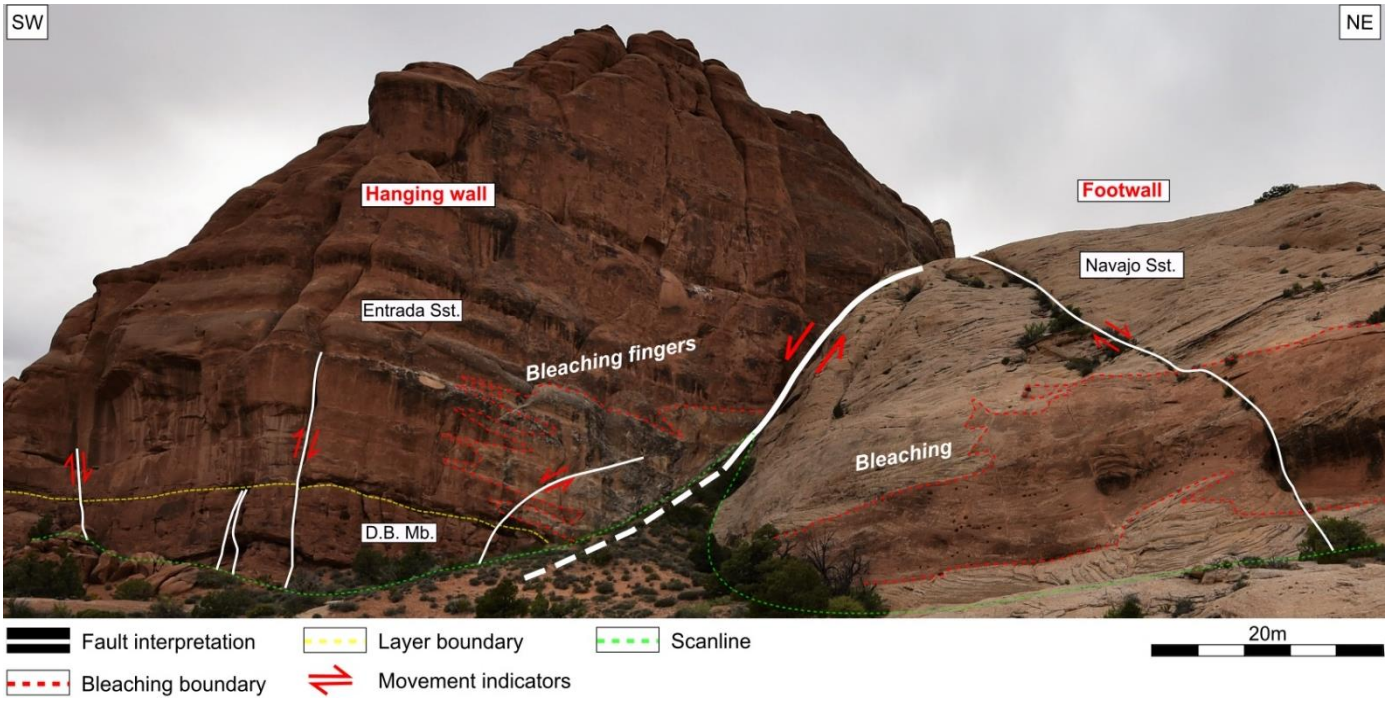

Figure 3.4.2: *Interpretation of the main fault in Cache Valley and the minor subsidiary normal faults situated in the hanging wall and footwall. The boundary of the bleaching has been interpreted in both the Navajo Sandstone and Entrada Sandstone. The bleaching effect in the Navajo Sandstone is easily observed, where the non-bleached intervals consist of grain coating hematite, developing a red-brown color. In the Entrada Sandstone, the bleaching appears as beige-grey fingers, compared to the otherwise red-brown color of the unit. A boundary to the underlying Dewey Bridge Member (D.B.Mb) is interpreted, in which no bleaching is observed.*

3.4.2. Fault core and fault descriptions

Fault core thickness measurements on the main fault were completed for 8.4 m along the fault in the field, but a clear fault core boundary could not be established for the lowermost 2.4 m of the measurements, due to vegetation and debris. A fault core boundary has been interpreted based on the fault trace in the upper parts of the fault, and therefore some uncertainties are related to these measurements. In the upper parts of the fault, a clear fault core boundary between the Navajo Sandstone and Entrada Sandstone can be defined. From level 600-840 cm the fault rock situated in the fault core are exposed, consisting of a dark/black, massive rock, which is hard to classify, due to the weathering and cementation effect (Figure 3.4.3).

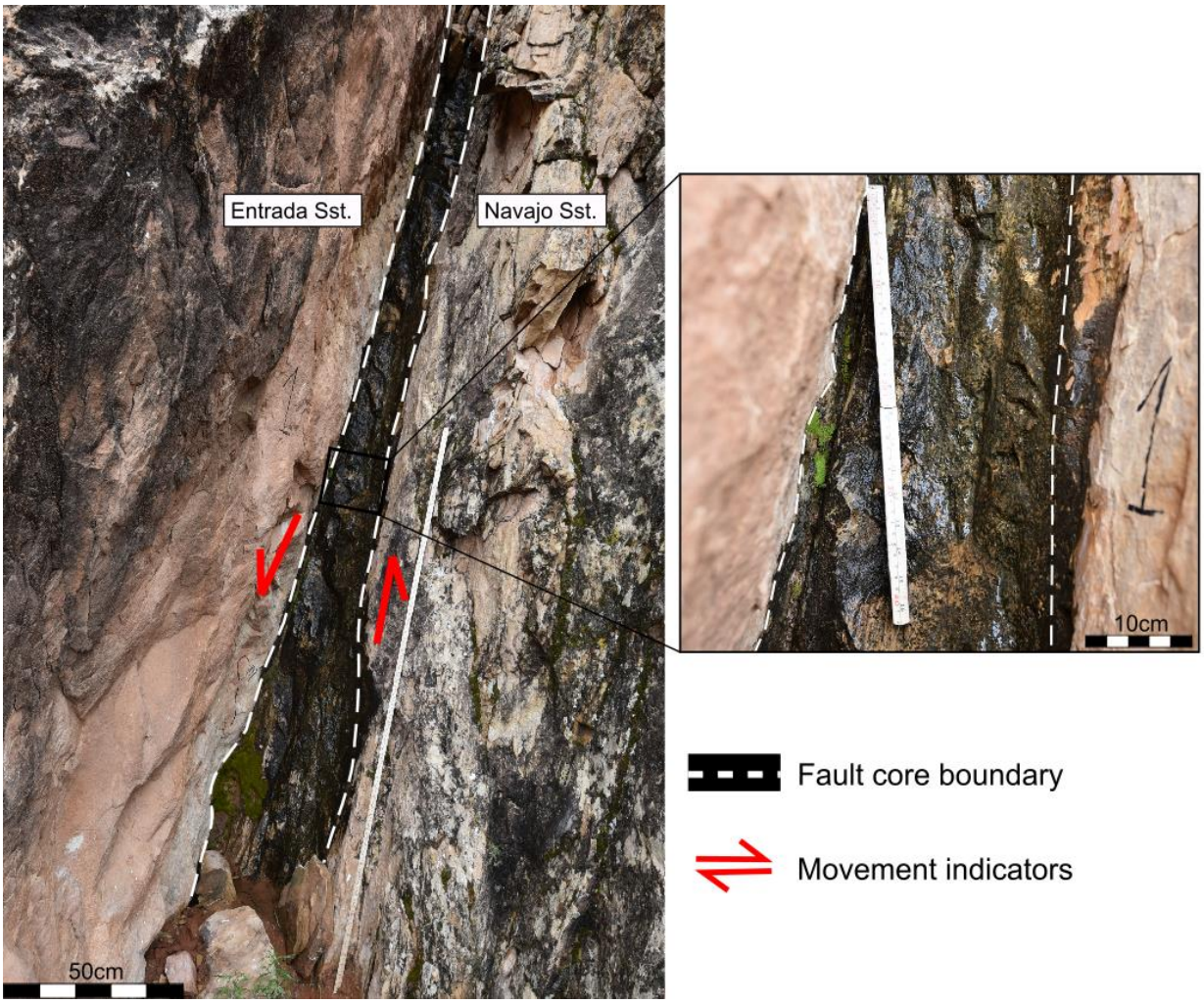

Figure 3.4.3: *Outcrop picture of the black, massive fault rock exposed in the upper parts of fault core of the main fault at the Cache Valley locality. The fault rocks are cemented, which supports the author's hypothesis that the main fault at one time was a conduit for fluid flow across the fault, but eventually got cemented by the fluid migration.*

A total of 15 fault core thickness measurements was performed in the field, covering 8.4 m of the fault core. In addition, picture measurements were conducted for a total height of 21 m along the fault core, resulting in 36 core thickness measurements. Correlation between the lowermost field- and picture measurements gives a high R^2 equal to 0.90, indicating the accuracy of the completed picture measurements. These measurements have resulted in an average fault core thickness of 36.97 cm. From the picture measurements, two sandstone lenses have been observed and documented in the fault core, and these were included in the thickness measurements since they are situated in between slip surfaces. A plot of the measured fault core thickness at the different levels are illustrated in Figure 3.4.4, and the sandstone lenses can be observed at level 1380-1620 cm and 1800-1920 cm, respectively.

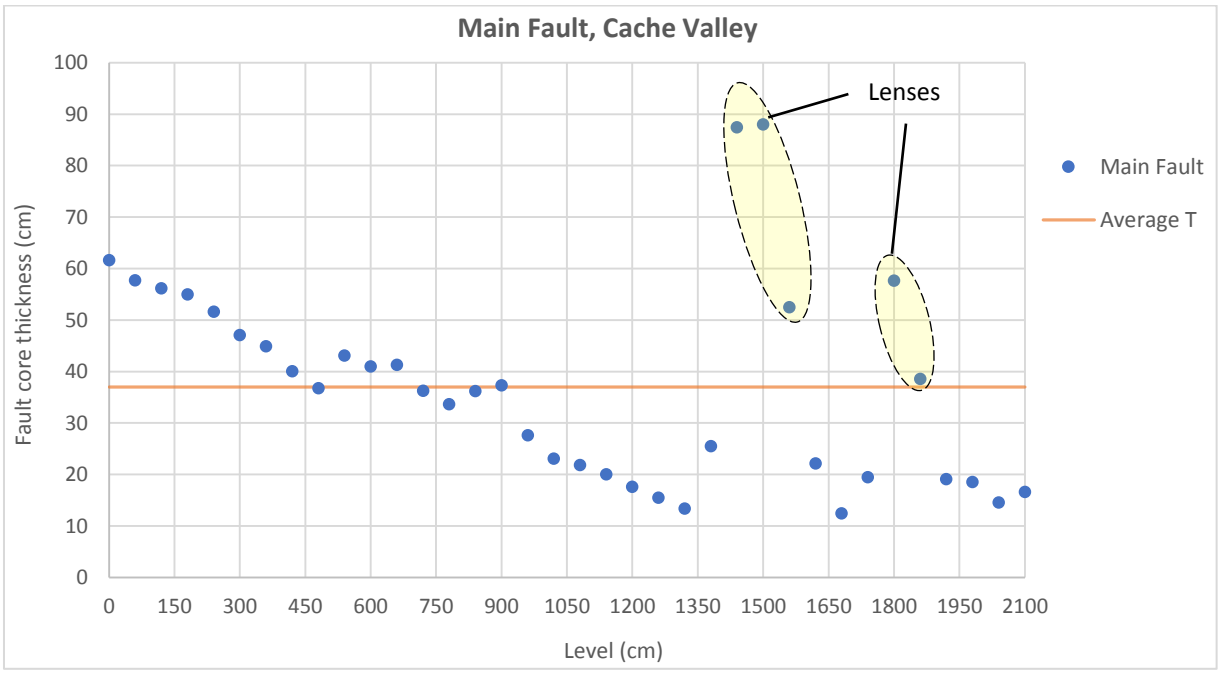

Figure 3.4.4: *Plot of the measured fault core thickness completed at different levels along the fault core. The sandstone lenses incorporated in the fault core can easily be distinguished in the plot, where the thickness suddenly increases and is illustrated with yellow shaded circles. T; fault core thickness.*

The five minor normal faults situated in the hanging wall, show different ranges of fault core thickness and fault displacement. Only two displacement measurements have been completed on the five fault due to the lack of good marker beds at the outcrop. A summary of the completed measurements on the five fault is presented in Table 3. The position of each fault can be observed in Figure 3.4.2 and the position along the scanline are presented in Table 3. The faults measured in the hanging wall all show approximately similar orientation, except Fault 5 (opposite dipping direction), and all the faults are oriented antithetic compared to the main fault, as illustrated in Figure 3.4.1.

Table 3: *Summary of the fault measurements completed on the minor subsidiary faults situated in the hanging wall. The fault position represents the location of the fault along the 100 m scanline at the base of the hanging wall. H; height (or elevation), T; fault core thickness, D; displacement, X; no measurements*

Fault nr	Position on scanline (m)	Orientation	Measured *H* field (m)	Measured *H* picture (m)	Average *T* field (cm)	Average *T* picture (cm)	Average *D* (cm)
Fault 2	34.2	260/77	4.2	8.3	1.86	1.98	X
Fault 3	57.2	250/84	4.2	9.3	1.96	2.77	24.13
Fault 4	64.2	275/79	3.0	4.2	0.59	0.74	X
Fault 5	65.9	067/74	3.0	4.2	0.68	0.81	X
Fault 6	84.4	284/69	3.0	4.2	3.99	4.53	6.40

The first fault located on the 100 m scanline running parallel with the base of the hanging wall is Fault 2. This fault shows a curving geometry towards the main fault at the outcrop and is the fault situated closest to the main fault. However, no linkage between Fault 2 and the main fault could be observed in the field. The core of the fault consists of beige-brown fault gouge and following the fault core towards the Entrada Sandstone, minor cataclasite in the fault gouge is observed.

Fault 3 is the next fault measured and documented along the scanline and this fault shows a vertical geometry in the outcrop. One set of displacement measurements has been completed at the stratigraphic boundary of the Entrada Sandstone and Dewey Bridge Member, where a measurable displacement of 24.13 cm was recorded. On Figure 3.4.5 A an interpretation of the fault is illustrated. The fault rock observed in the fault core is a beige shaley fault gouge.

Fault 4 and 5 are positioned right next to each other and the geometry of the faults are almost identical. The only observable difference of the faults is the dip direction, where Fault 4 is dipping 79°NE, and Fault 5 is dipping 74°SE. Upwards along the fault traces, it appears that both faults are dipping in the same direction, but when the fault encounters a denser, silty/shaley interval within the Dewey Bridge Member, they change their direction. The fault rocks documented in the fault core of the two faults are primarily brown fault gouge.

The last fault measured and documented in the hanging wall is Fault 6. An interpretation of the fault is illustrated in Figure 3.4.5 B. One displacement measurement has been completed, showing a displacement of 6.40 cm. Within the fault core, some brown-dark fault gouge is observed.

Fault core thickness measurements have been completed at different heights or levels for the five normal faults situated in the hanging wall. Figure 3.4.6 shows a plot of the recorded core thicknesses at different levels along the faults. The average fault core thickness measured at each fault is presented in Table 3. The plot illustrates the fault core thickness variations observed within each fault.

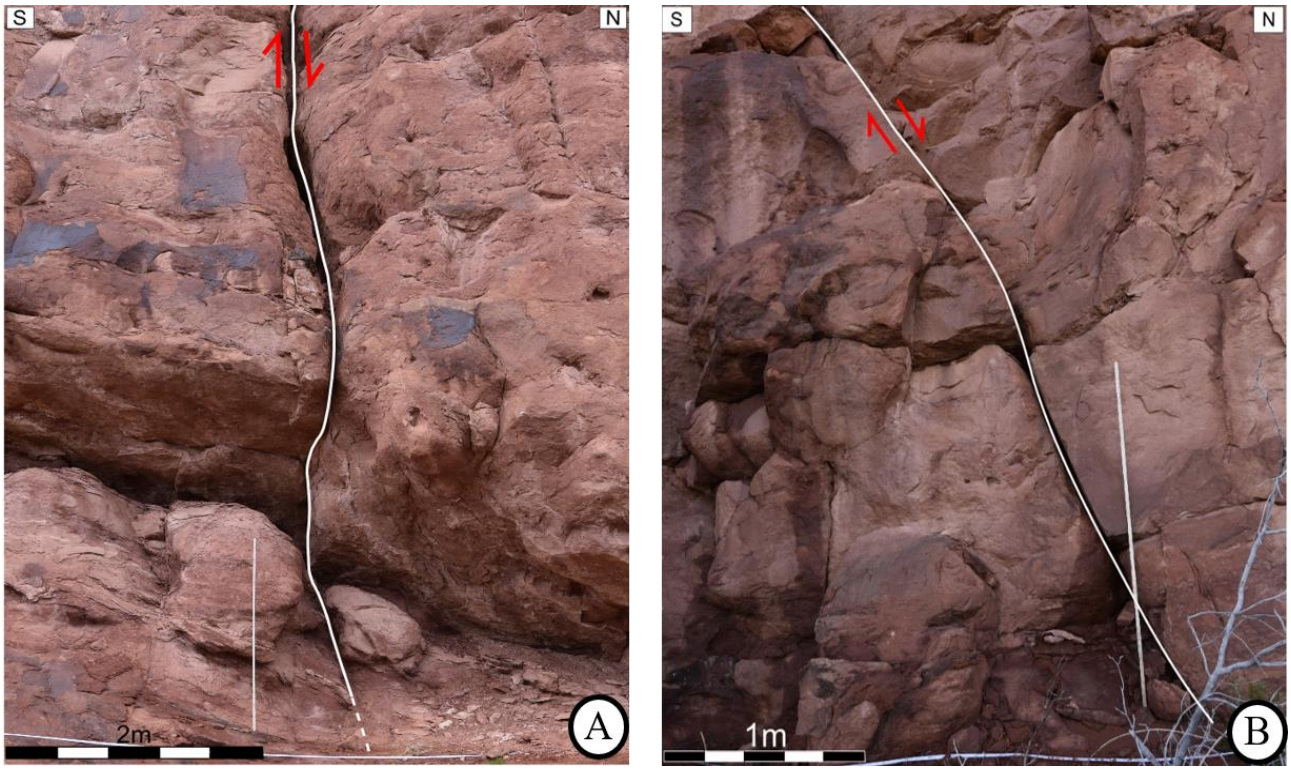

***Figure 3.4.5**: Interpretation of the minor subsidiary normal faults, Fault 3 (A) and Fault 6 (B), located in the hanging wall of the main fault situated at the Cache Valley locality.*

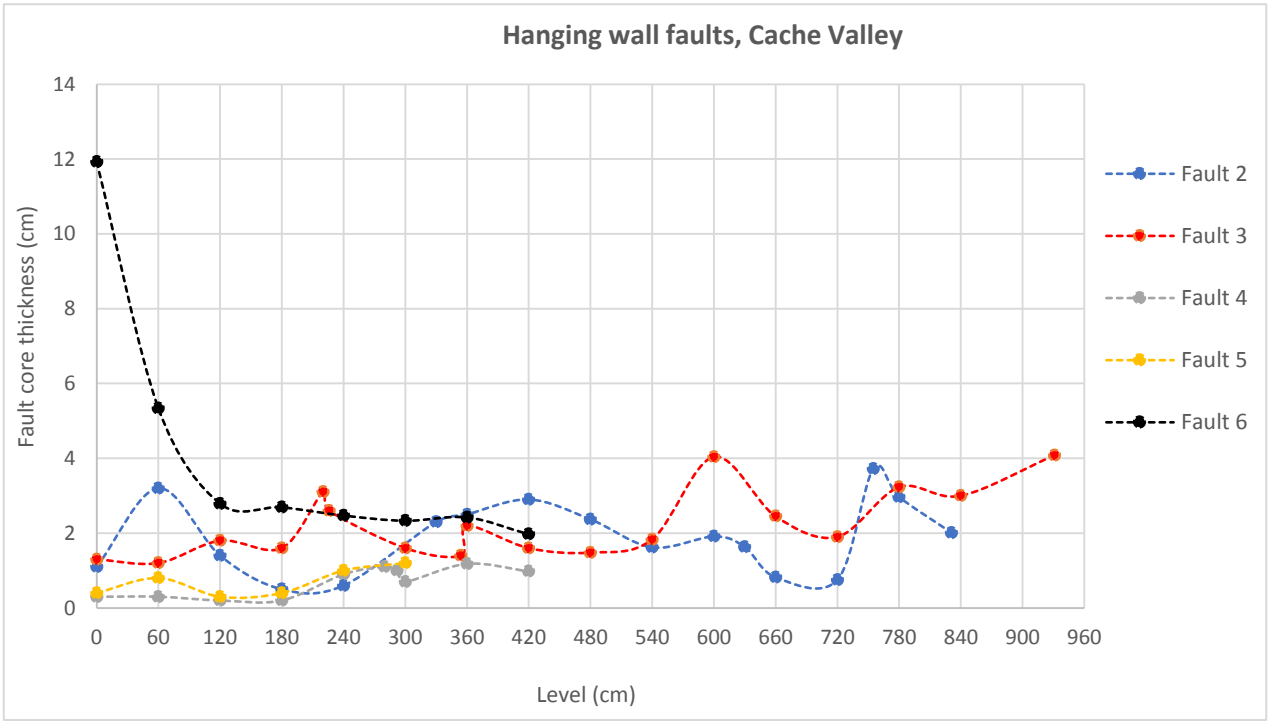

***Figure 3.4.6:** Plot of the measured fault core thickness at different levels along Fault 2-6. The plot illustrates how the fault core thickness of the five faults varies relative to each other, and how the thickness varies within each of the faults.*

The subsidiary normal fault situated in the footwall of the main fault is present at 99.10 m on the 100 m scanline running parallel to the base of the footwall. The displacement of the fault has been measured to 6.6 m. The fault is situated in both the bleached and unbleached sequence of the Navajo Sandstone (Figure 3.4.7). The fault core thickness was measured every 1.2 m along the fault core for a total height of 14.40 m in the field. The fault rocks present in the fault core are primarily dominated by a beige cataclasite, mixed with some scattered areas where fault gouge can be observed.

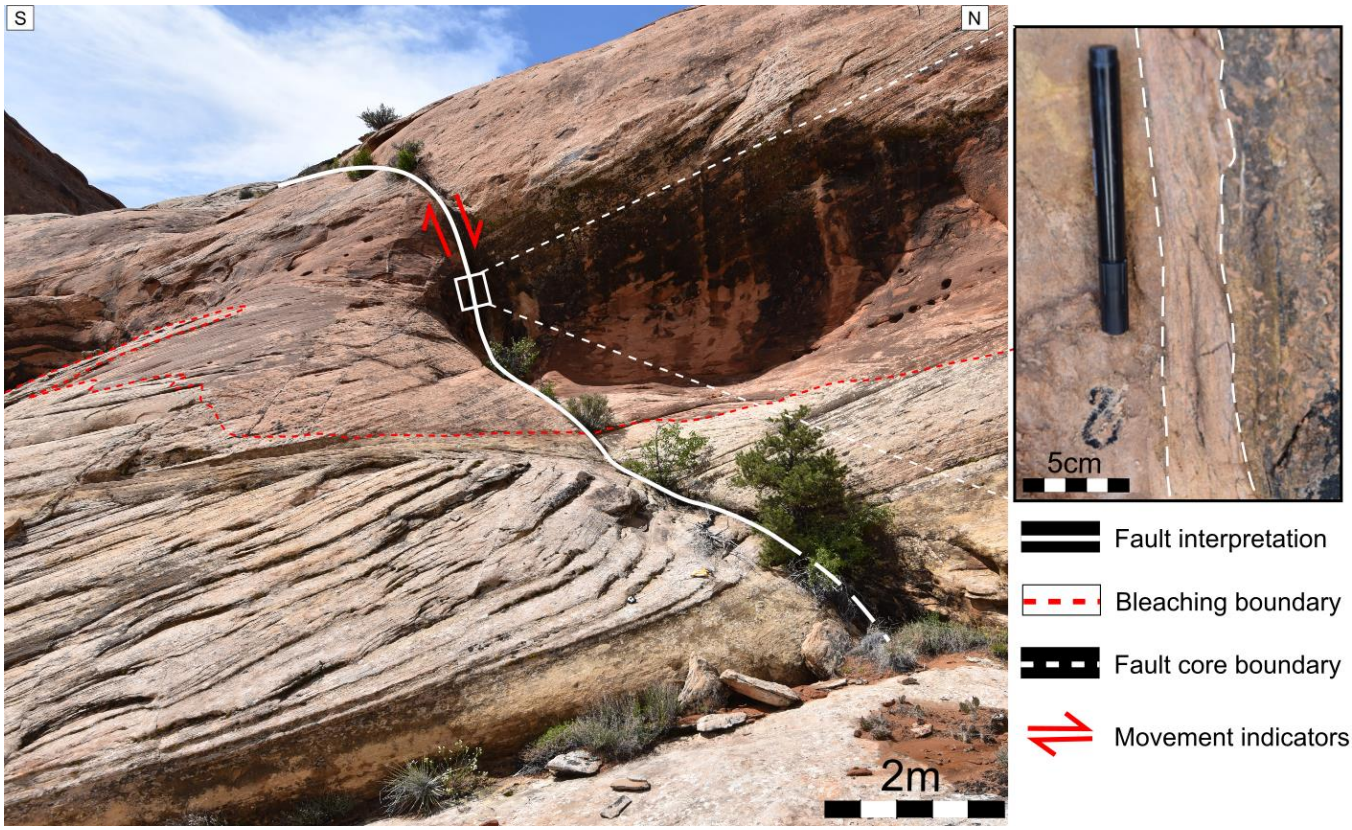

Figure 3.4.7: *Interpretation of the normal fault situated in the Navajo Sandstone within the footwall of the main fault. A bleaching boundary has been interpreted and shows where the fault is situated in the bleached interval. The picture on the right show a close up of the cataclasite observed in the fault core.*

Comparing the measured fault core thickness in the bleached and unbleached sequences, the thickness in the bleached interval show an overall wider fault core. The fault is located in the bleached interval at heights 0-480 cm, where the average fault core thickness are measured to 18.66 cm. While from height 480-1440 cm, the fault is located in the unbleached interval and the average core thickness are measured to 4.20 cm. This variation in thickness may be related to secondary porosity within the unit, with the removal of grain coating hematite in the bleached interval. The hematite around the grains increases the rheological strength of the interval and the removal of hematite would increase the pore space between the grains, resulting in a strain weakening of the bleached interval. A plot of the measured fault core thickness is presented in Figure 3.4.8, illustrating the thickness variations observed between the bleached- and unbleached interval.

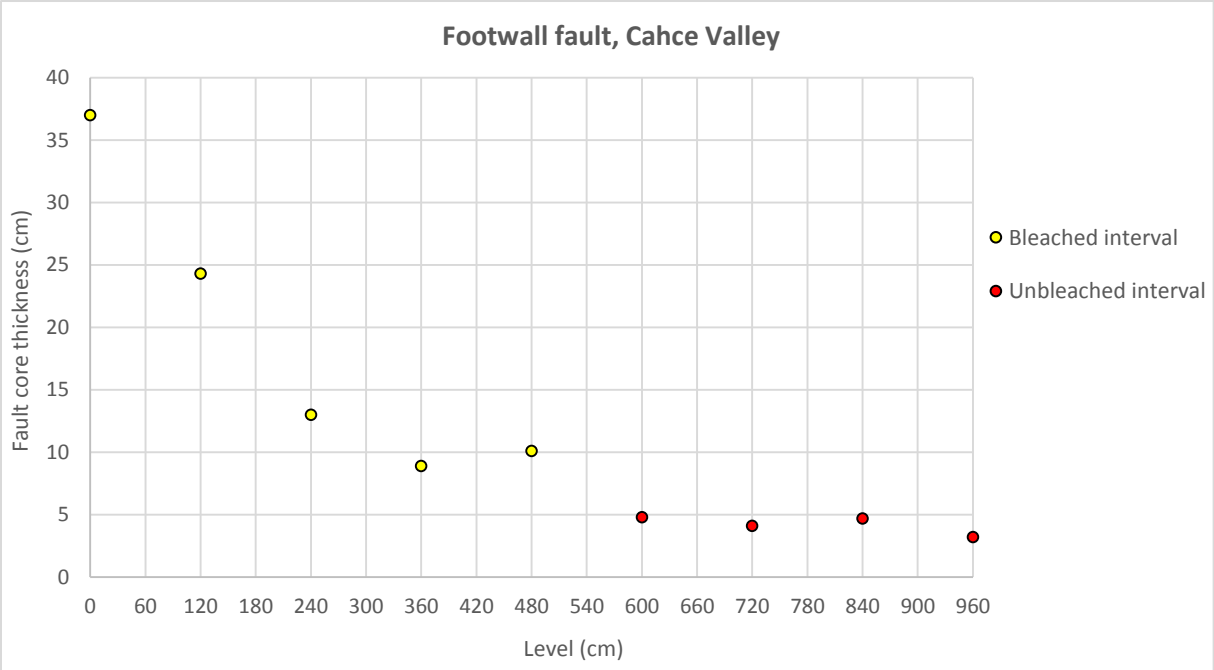

Figure 3.4.7: *Plot is illustrating the measured fault core thickness at the different levels along the fault core. The plot shows how the thickness vary within the bleached (yellow dots) and unbleached (red dots) interval.*

3.4.3. Statistical analysis of data

The fault core thickness measurements, from the main fault and the subsidiary faults situated in the wall rocks, have been used for univariate analysis and to create EF-plots, to recognize the distribution trend of the measurements.

The EF-plots regarding the main fault are illustrated on Figure 3.4.8 A-B. When the fault core thickness measurements of the main fault are plotted into an EF-plot, the thickness measurements can be divided into two segments. The general distribution follows a power-law- or log-normal distribution for both the log-thickness and linear-thickness plots. However, a changing point located at thickness values around 0.35 m, divides the measurements into two segments, where both segments follows a characteristic power-law trend. This trend is easily observed on the log EF- log thickness plot on Figure 3.4.8 B, where both segments show an approximately straight line up to the changing point. For all measurements, including the "tails" (black dashed circles on the figure), a log-normal distribution has been correlated to be the best fit for all data points. However, if divided into two segments and remove the "tail" members, a power-law distribution can be recognized as the best fit, with strong regression of fit values. Based on the form of the EF-plots and correlated trend lines, two power-law distribution trends for each segment appears to be the best fit for the data points.

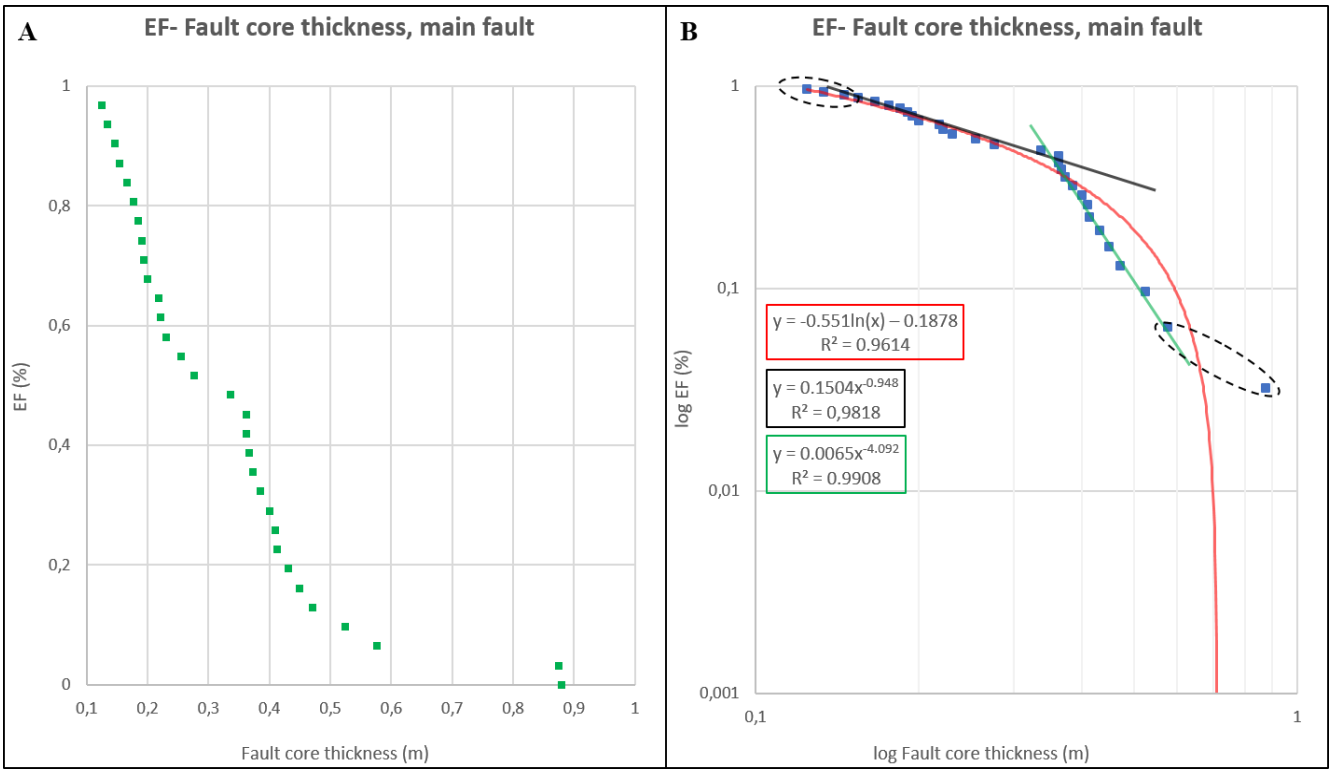

Figure 3.4.8: *EF-plots of the measured fault core thickness for the main fault at Cache Valley. (**A**) Shows the EF in linear scale in relation to fault core thickness, also in linear scale. (**B**) Show the EF in logarithmic scale in relation to fault core thickness, also in logarithmic scale. The different lines represent the trend lines correlated to best fit the measurements. The correlated functions and R^2 values are presented in the squares on the figure, following the same color code as the trend lines.*

All the fault core thickness measurements completed on the minor subsidiary faults have been plotted in one EF-plot sequence, presented in Figure 3.4.9 A-B. No distribution trend could be recognized in EF-plots for the measurements in the footwall fault due to sparse data-set, so these measurements have been included on the EF-plots on Figure 3.4.9 A-B. The overall trend on the EF-plots appear to follow a power-law distribution, with the characteristic hyperbolic curve on Figure 3.4.9 A. On the log EF-log thickness plot (Figure 3.4.9 B), the plot shows a concave down pattern, which fits better with a log-normal distribution. For all measurements, including the "tail" members (black dashed circles on the figure), a log-normal distribution has been correlated to be the best fit of the dataset. If the endmembers are removed, the plot forms a straight line, characteristic for a power-law distribution. The trend line has a solid regression of fit value of 0.9468, indicating a power-law distribution.

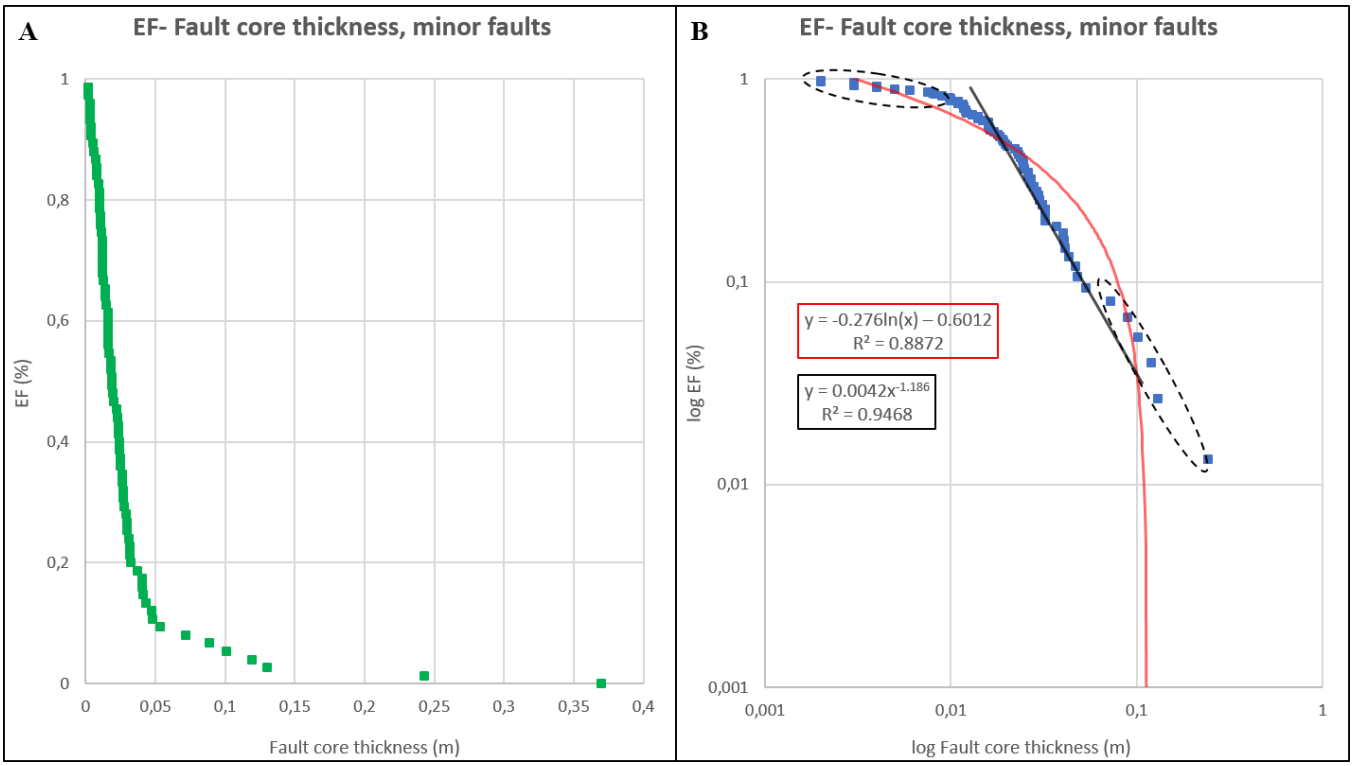

Figure 3.4.9: *EF-plots of the measured fault core thickness for the minor subsidiary faults in the hanging wall and footwall of the main fault at Cache Valley. (**A**) Shows the EF in linear scale in relation to fault core thickness, also in linear scale. (**B**) Show the EF in logarithmic scale in relation to fault core thickness, also in logarithmic scale. The different lines represent the trend lines correlated to best fit the measurements. The correlated functions and R^2 values are presented in the squares on the figure, following the same color code as the trend lines.*

3.5. Humbug Flats, Utah

3.5.1. Structures and stratigraphic units

The Humbug Flats locality is located ~50 km west of the town of Green River, on the northwestern corner of the Colorado Plateau, close to the northern edge of the dome-shaped, asymmetric San Rafael Swell anticline (Loc. 5 on Figure 2.1.4). Contrary to the other studied localities in Utah, the Humbug Flats is situated outside the Paradox Basin and has not been similarly affected by salt tectonics related to the basin. A set of normal fault arrays and horst segments trending E-W are located around the San Rafael Swell anticline, and the formation of these structures are suggested to be related to the formation and uplift of the San Rafael Swell during the Laramide orogeny (Shipton and Cowie, 2001; Davatzes et al., 2003). Furthermore, a subordinate set of normal fault lineaments trending NW-SE and minor WNW-ESE trending normal faults have also been reported by Ogata et al. (2014). The development of these faults is related to the same mechanisms.

A main fault trending NW-SE have been observed at the studied outcrop, and the estimated displacement of the fault is approximately 40 m. The studied and measured faults at the locality are minor subsidiary faults located in the footwall of the main fault. These faults were documented along a 60 m scanline, running from the main fault along the base of the footwall. An additional antithetic fault has been measured close to the main fault, but this fault was not recorded along the scanline, this fault is elevated 45.22 m above the studied scanline. Orientation measurements of the studied and measured faults are presented in Figure 3.5.1.

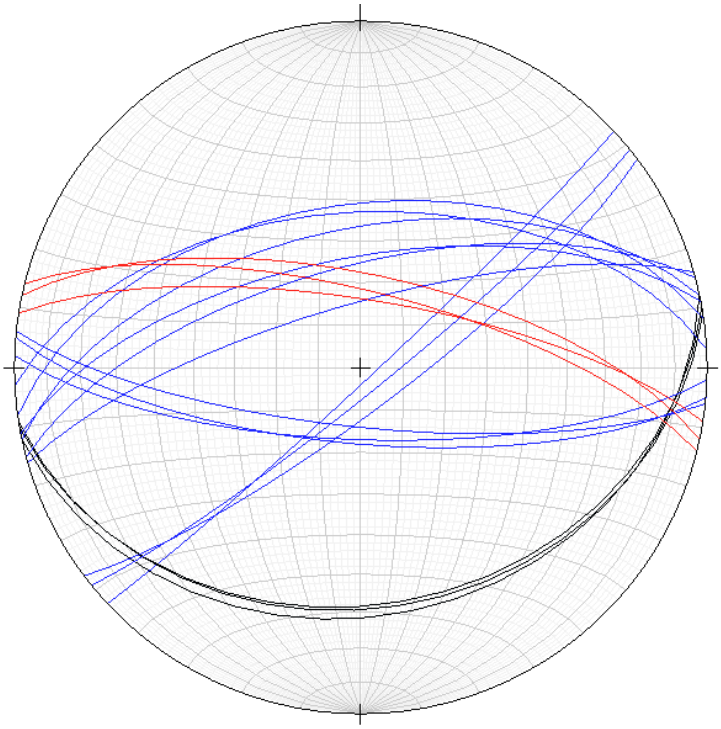

Figure 3.5.1: *Illustration of the orientation on the studied faults. The red lines represent the main fault, the blue lines the minor faults located in the footwall and the black lines represent the antithetic fault.*

The stratigraphic units located at the outcrop are the Navajo Sandstone, which is underlying the Carmel Formation, which is equal to the Dewey Bridge Member in the southeast. A bleached interval is observed at the top of the sandstone unit in Navajo Sandstone, and the bleaching can be traced throughout the valley. The bleached zone observed at the outcrop show similar features and properties compared to the bleached interval observed in Cache Valley. Above the bleached zone, a lot of debris and vegetation makes it difficult to trace the fault and perform fault core thickness measurements on pictures. A total of four minor subsidiary normal faults have been documented in the Navajo Sandstone, and the top bleached zone has been used as a marker for displacement measurements at the outcrop. The Carmel Formation is located above the debris, and this formation consists of different facies of sandstone and shale-siltstones. Within this formation, the elevated antithetic fault has been observed and measured.

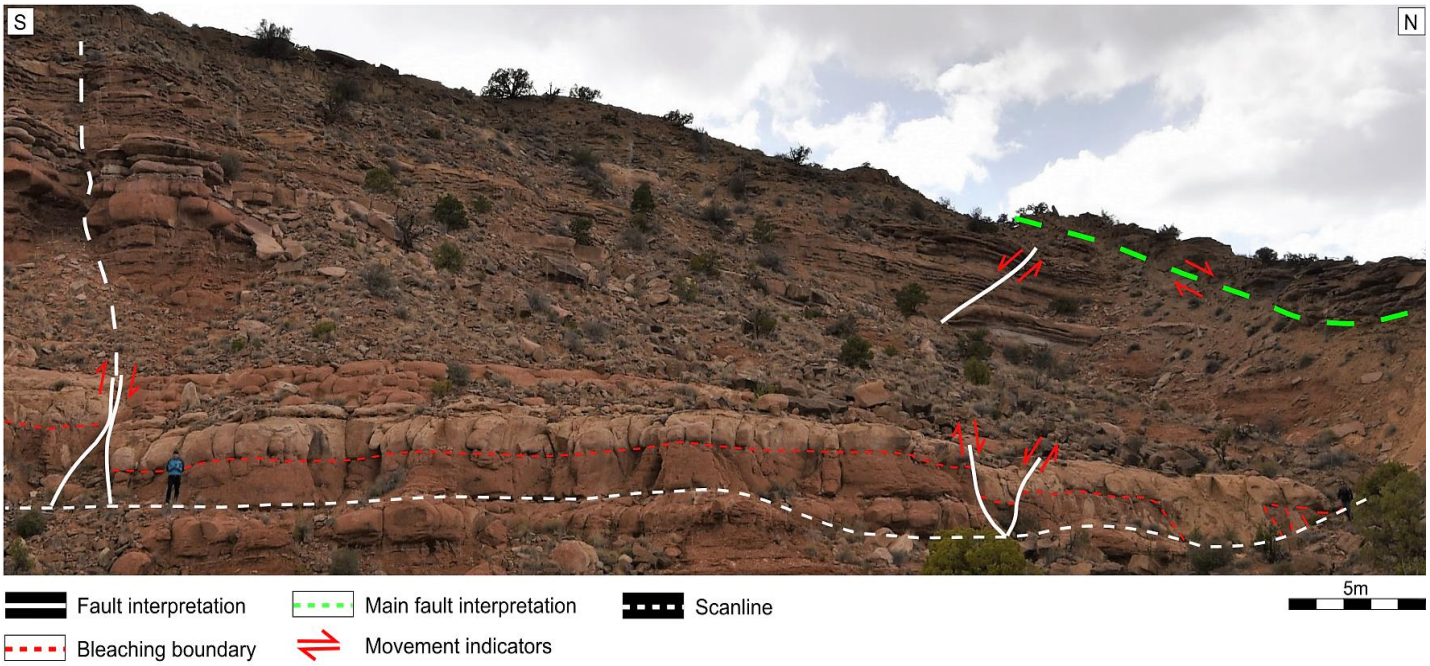

Figure 3.5.2: *Outcrop picture of the studied locality at Humbug Flats with fault interpretation. The antithetic fault is located close to the main fault (green dashed line), but no linkage between them could be observed in the field, due to debris material covering the fault trace. This fault is located in the Carmel Formation, while the other measured faults at the outcrop are located in the Navajo Sandstone. The boundary of the bleaching has been interpreted in the Navajo Sandstone.*

3.5.2. Fault core and fault description

The two first normal faults located along the scanline are positioned close to each other, at 14.0 m (F1) and 14.7 m (F2) on the scanline. The orientation measurements on the two faults show opposite orientations, where F1 is WNW-ESE trending with a dip of 54°NW, and F2 is trending NE-SW with a dip of 84°SE. The faults juxtapose the Navajo Sandstone at the outcrop and develop a minor graben

structure, observed by the downfaulted bleached zone (Figure 3.5.3). Fault displacement measurements have been carried out in the field for both faults, where F2 have a displacement of 87.1 cm and F1 a displacement of 46.2 cm, respectively. The fault rocks observed in the fault core in both faults are beige-brown cataclasite and some beige fault gouge. A minor elongated sandstone lens is incorporated in the fault core of F1 at level or height 132-205 cm.

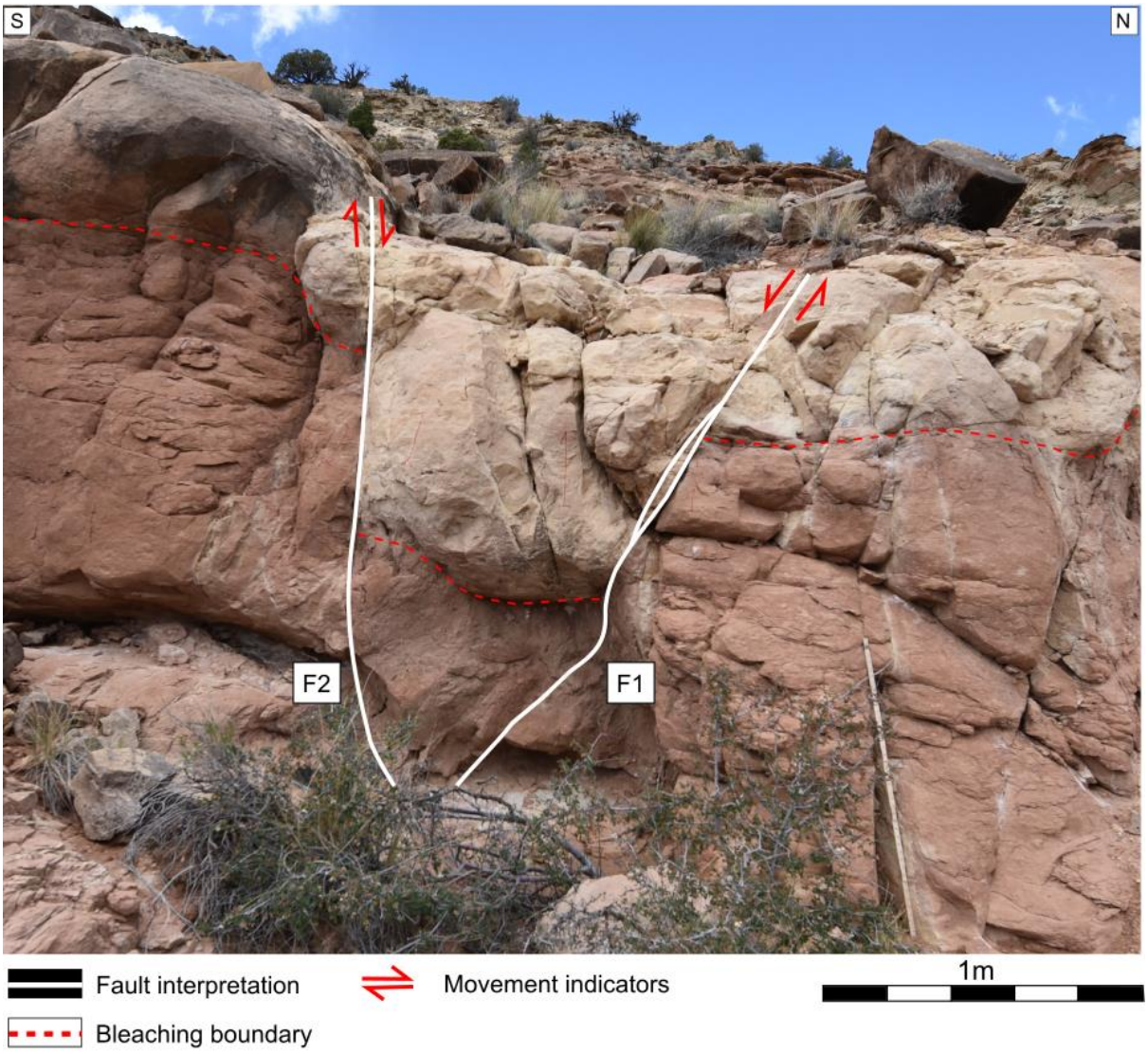

Figure 3.5.3: *Interpretation of fault F1 and F2 at the outcrop. The faults create a minor graben structure, as illustrated in the figure, where the bleached zone are downfaulted. This movement has been used to determine the displacement of the faults. Note the debris material located above the bleached layer, making it difficult to trace the faults.*

Fault core thickness measurements conducted on the two faults have only been possible in the field. Due to the debris and vegetation overlying the Navajo Sandstone, the accessible parts of the faults have been covered by field measurements. A total measured height of 3.0 m has been completed on each fault, resulting in a total of 17 fault core thickness measurements. Figure 3.5.4 illustrates a plot of the measured fault core thickness at different levels of the two fault at the outcrop.

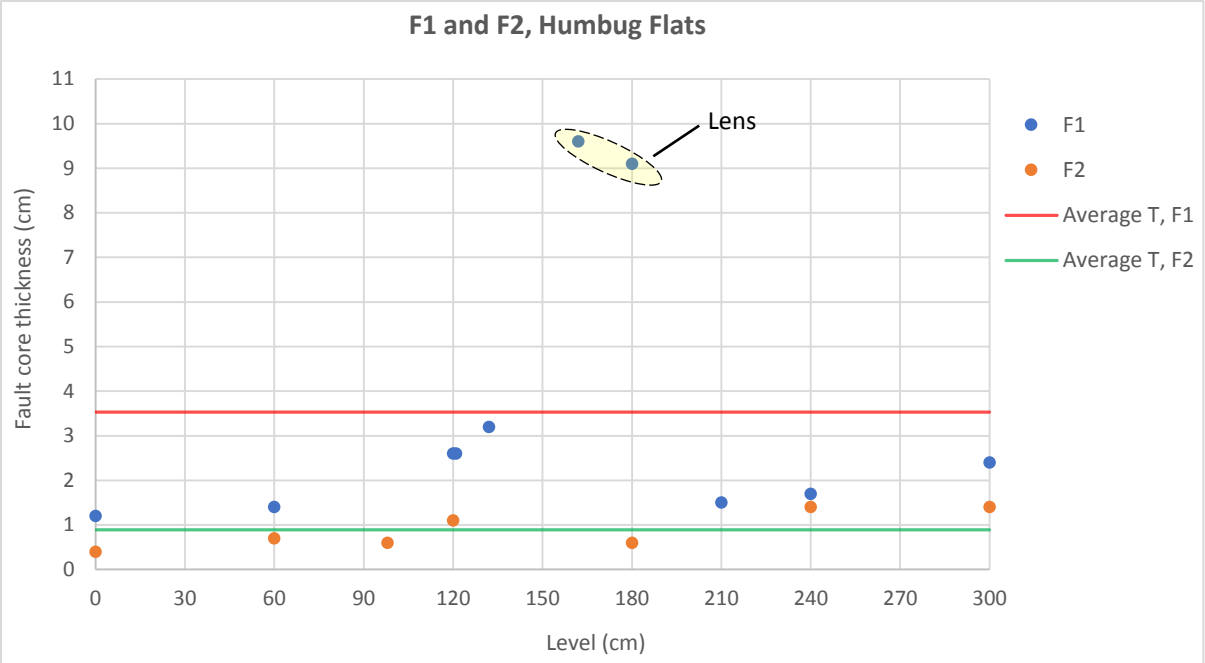

Figure 3.5.4: *Plot of the measured fault core thickness (T) completed on fault F1 and F2. The sudden increase in fault core thickness of F1 on level 132-205 cm is related to the presence of a fault lens.*

The antithetic normal fault is the only measured fault situated in the Carmel Formation and is elevated 45.22 m above the studied scanline. The fault is trending ENE-WSW with a gentle dip of 31°SE. Two displacement measurements were completed in the field at different levels along the fault core, displaying a displacement of 187.29 cm and 117.36 cm, respectively. The displacement measurements were completed using different sub-layers within the Carmel Formation as marker beds. Different types of fault rocks have been observed within the fault core. Including both beige cataclasite, greenish-grey fault or shale gouge and sandstone lenses of different sizes. This inclusion of different fault rocks is most likely related to the combination of interchanging lithology and different competency of the faulted rocks. The position of different fault rocks in the fault core also results in great lateral variation in fault core thickness, illustrated in Figure 3.5.6. This variation in core thickness shows how variation in lithology along the fault is a factor which controls the fault core thickness. Another feature observed in the fault core are calcite mineralization, which is interpreted to be the result of fluid migration and calcite precipitation along the fault slip surface. The localization of calcite is illustrated on the close-up picture on Figure 3.5.5. Calcite mineralization was also observed in fractures located in the footwall of this fault.

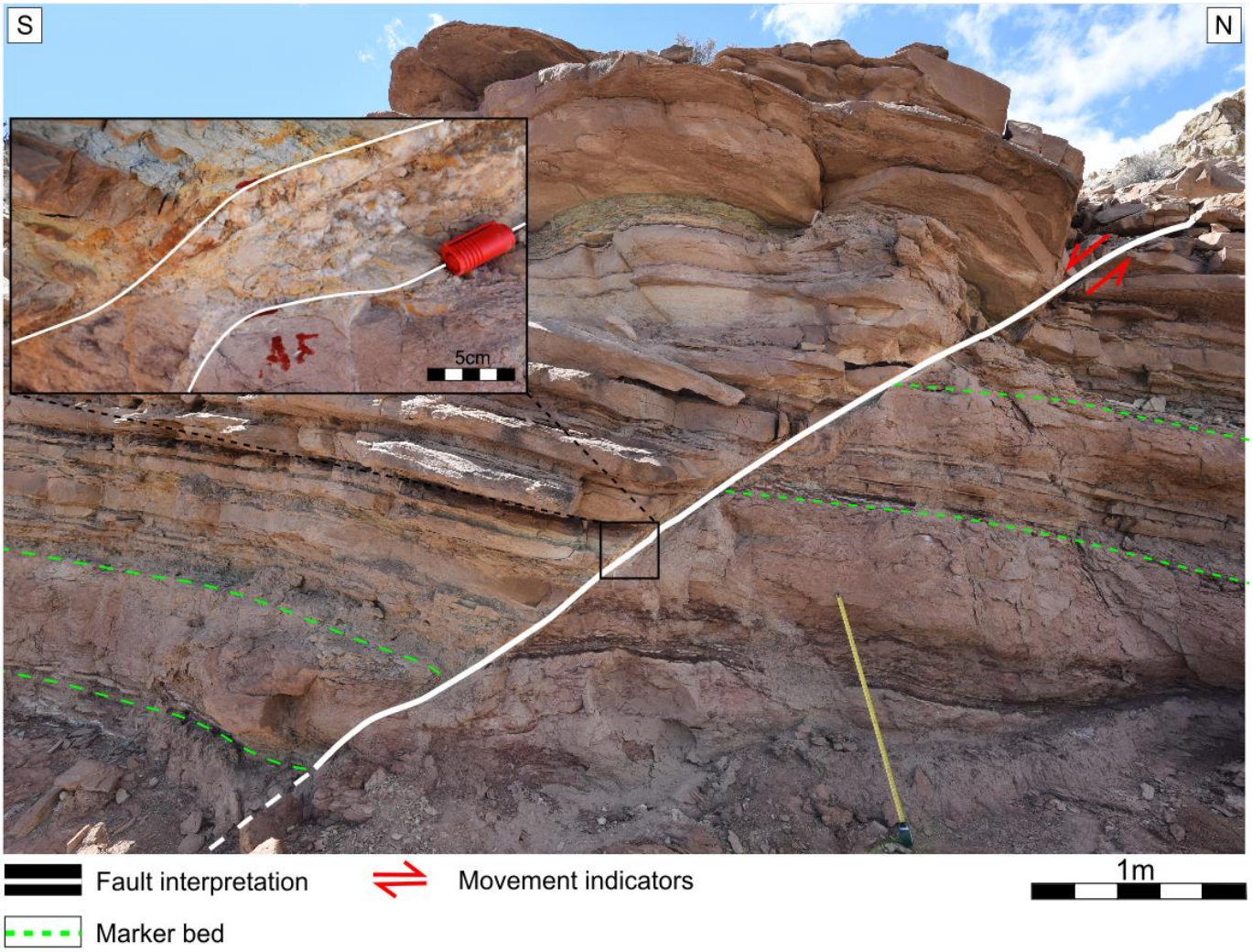

Figure 3.5.5: *Interpretation of the antithetic fault. The figure illustrates the interchanging lithologies and the different facies of sandstone and shale-siltstones in the Carmel Formation. This variation in lithology results in different fault rocks situated in the fault core. The close-up picture shows the calcite mineralization observed within the fault core.*

The fault core thickness was measured for 5.3 m along the fault in the field, giving a total of 14 thickness measurements and an average fault core thickness of 5.86 cm. However, the fault core shows great variations in thickness, ranging from a maximum of 18.6 cm and a minimum of 1.2 cm. This thickness variation can be observed in Figure 3.5.6, which shows a plot of the measured fault core thickness at different levels along the fault core. The mentioned sandstone lenses situated in the fault core can be observed on the plot from level 189-358 cm, where the thickness increases rapidly, and great variations can be observed.

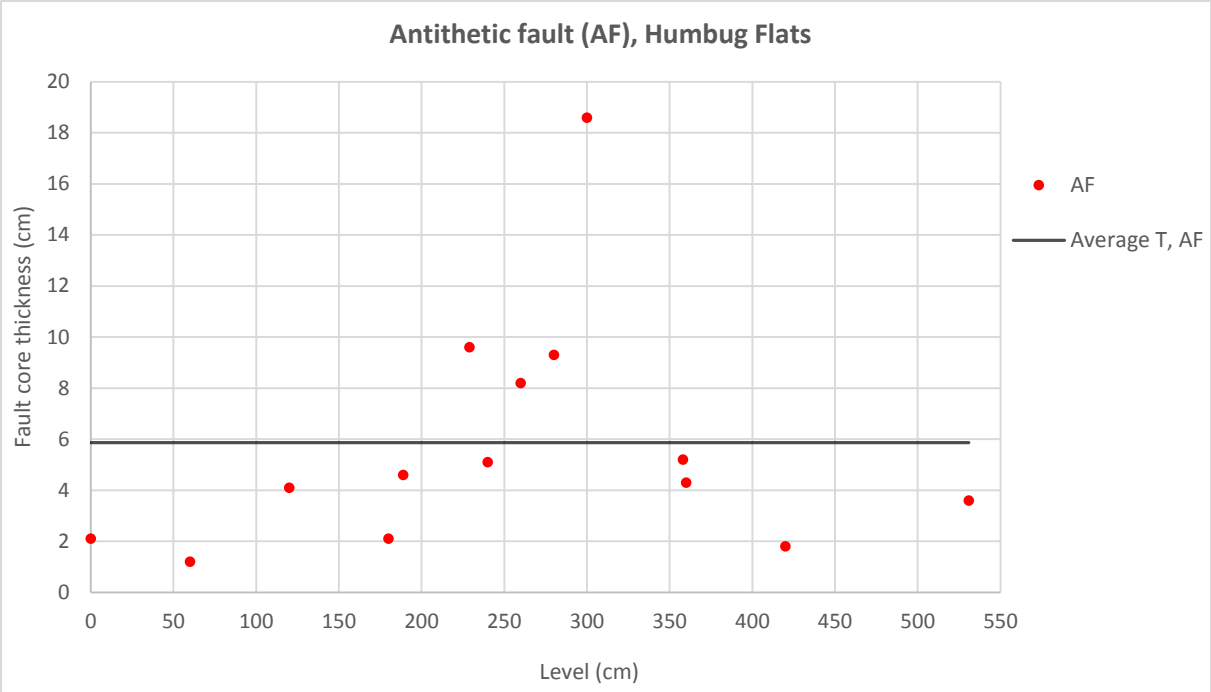

Figure 3.5.6: *Plot of the measured fault core thickness (T) completed at the different levels along the fault core. The great variations in thickness documented may be explained by the different and changing fault rocks in the fault core.*

The last faults located along the scanline are two minor normal faults, F3.1 and F3.2, located at 53.1 m and 55.4 m, respectively. Both of these faults are interpreted to be splay faults, splaying from a larger normal fault (F3), at level 296 cm, where the fault encounters a unbleached interval in the Navajo Sandstone. The orientation measurements completed on the faults show that the orientation of F3 and F3.1 are approximately equal, trending ENE-WSW with a dip of 59°NW. F3.2 are oriented an antithetic direction, trending WNW-ESE with a dip of 74°SE.

Displacement measurements have been completed on fault F3, using the bleached zone in the Navajo Sandstone as a marker, showing a measurable displacement of 247 cm. Displacement was only completed on fault F3 because no clear marker beds could be observed for F3.1 and F3.2. The same fault rocks have been observed in the fault core of the faults, consisting of beige cataclasite. Calcite mineralization is observed within the fault core of F3.2, illustrated on the close-up picture B in Figure 3.5.7.

Figure 3.5.7: *Outcrop picture and interpretation of the measured faults at the outcrop. The faults of F3.1 and F3.2 splay from the bigger normal fault F3, when the fault encounters a massive, unbleached interval of the Navajo Sandstone. Close-up picture* ***A****, illustrates the cataclasite observed in the fault core of F3.1, and* ***B*** *shows calcite mineralization in F3.2. The calcite forms small crystals that are attached to the fault core boundary and have grown into the fault core.*

Fault core thickness measurements have been completed on both F3.1, F3.2, and F3. For the F3.1 and F3.2 faults, measurements have been completed in till level 291 cm, where the faults connect to F3, developing one single fault. F3 have been measured until level 420 cm, where overburden debris and vegetation buries the fault trace. An interpretation of the fault trace of F3 can be observed in Figure 3.5.2, connecting the fault trace to a fault observed in the overlying Carmel Formation.

The two fault splay of F3.1 and F3.2 show an expected smaller fault core when comparing the thickness to F3. Where the average thickness of F1 is 2.30 cm and F2 is 1.56 cm, while the average thickness of F3 is measured to 11.76 cm. A plot illustrating the fault core thickness is illustrated in Figure 3.5.8. The plot shows the individual fault core thickness of fault F3.1 and F3.2 at level (height) 0-291 cm, followed by the thickness of F3.

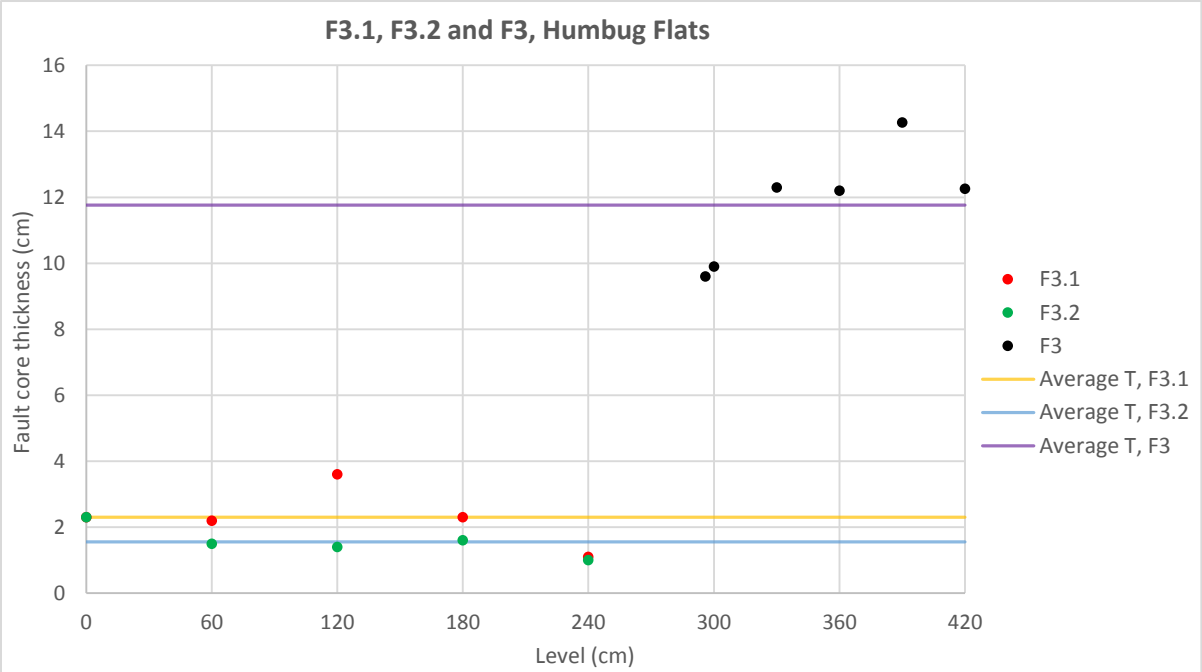

Figure 3.5.8: *Plot of the measured fault core thickness (T) at the studied faults. The fault splays have a thinner fault core, as expected when compared to the larger fault F3. The fault core of F3.2 shows a more or less table thickness throughout the measured levels, while F3.1 have smaller variations in thickness. For fault F3 some lateral variations in thickness can be observed after connecting with the splays at level 291 cm.*

3.5.2. Statistical analysis of data

The collected fault core thickness measurements from the minor normal faults situated in the footwall of the main fault at Humbug Flats have been used to construct EF-plots. The EF-plot for the fault core thickness is presented in Figure 3.5.9 A-B. The EF-thickness plot (Figure 3.5.9 A), shows an overall concave up trend, but around a thickness value of 0.05 m, a concave down trend can be observed. This pattern could indicate a hyperbolic curve, characteristic for a power-law distribution. As for the other suggested power-law distributed EF-plots (e.g. ANP, Cache Valley), if all measurements are included, including the "tail" members (black dashed circles on Figure 3.5.9 B), a log-normal distribution have been correlated to best fit the dataset. If the endmembers are removed, a strong power-law distribution can be observed, with an R^2 of 0.9673. This robust regression of fit, combined with the hyperbolic shape on the EF-thickness plot, supports a power-law distribution of the fault core thickness measurements.

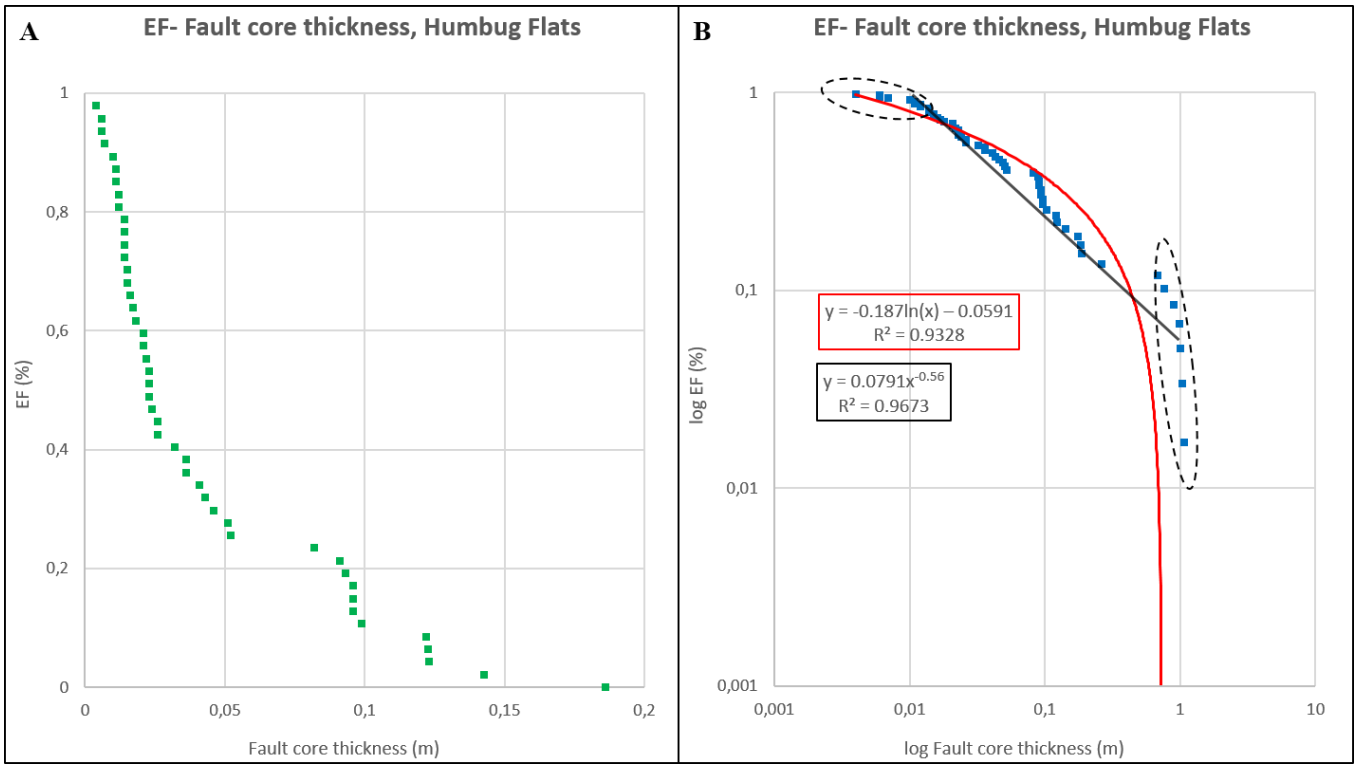

Figure 3.5.9: *EF-plots of the measured fault core thickness for the minor subsidiary faults in the footwall of the main fault at Humbug Flats. (**A**) Shows the EF in linear scale in relation to fault core thickness, also in linear scale. (**B**) Show the EF in logarithmic scale in relation to fault core thickness, also in logarithmic scale. The different lines represent the trend lines correlated to best fit the measurements. The correlated functions and R^2 values are presented in the squares on the figure, following the same color code as the trend lines.*

3.6. Vallone di Santo Spirito, Majella Mountain, Italy

3.6.1. Structures and stratigraphic units

The study area is located within Vallone di Santo Spirito on the eastern forelimb of the Majella anticline, about 3 km east of the town Fara San Martino, Abruzzo region. The valley continuous E-W for several kilometers through the Majella anticline and ends at the trail up to Mount Amaro.

Measurements of the fault core thickness and displacement were carried out for the different fault types located in the valley. A total of 12 scanlines running perpendicular to the fault strikes were studied, where the scanlines were located either on the northern or southern side of the valley. The location of each scanline is illustrated in Figure 3.6.1. The scanlines start from outside the valley (scanline 1) and continue about 2 km upwards the valley (scanline 12). Scanline length and fault types measured and documented along them are presented in Table 4. Challenges encountered at the outcrops were dense vegetation, steep outcrops and lack of marker beds. At each of the scanlines, fault position and fault type was documented, and fault core thickness measurements were conducted every 60 or 30 cm along the fault core. Fault displacement measurements were done in the field and complemented with measurements from pictures.

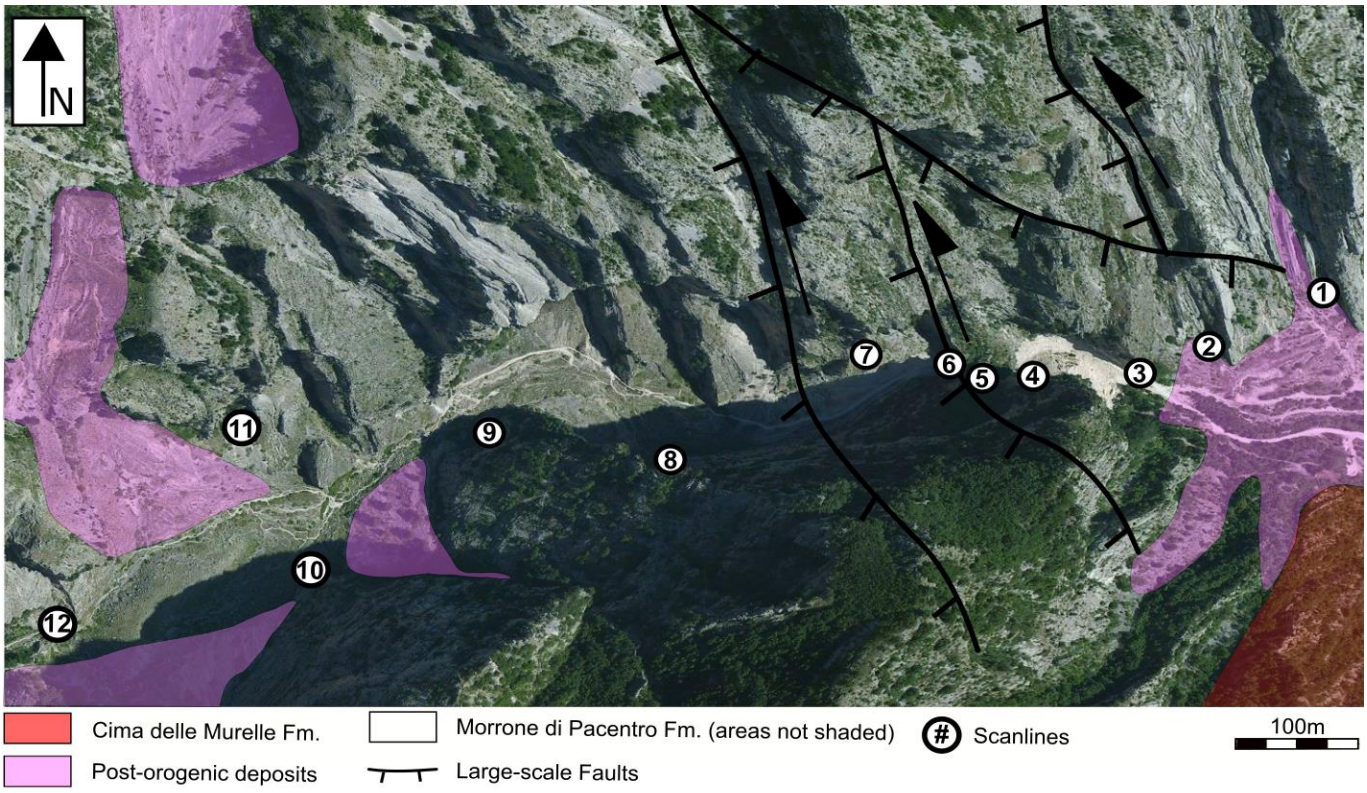

Figure 3.6.1: *Area picture of Vallone di Santo Spirito, with geological features interpreted. The geographical location of the study area can be observed on Figure 2.2.1 A and B in chapter 2. The geological interpretations are based on geological mapping done by Festa et al. (2014) and geological maps from the Geological Survey of Italy and Accotto et al. (2014). Area picture acquired from Michelin maps website.*

Table 4: *Summary of the studied scanlines, presenting the total scanline lengths at the different outcrops, the number of faults and the fault types measured.*

Scanline number	Scanline length (m)	Number of faults	Fault type (-s)
1	10.0	1	Reverse (1)
2	23.0	2	Pre-tilted normal (2)
3	123.5	9	Normal (6), right-lateral strike-slip (3)
4	40.0	3	Right-lateral strike-slip (3)
5	62.0	7	Normal (2), reverse (4), left-lateral strike-slip (1)
6	100.0	7	Reverse (2), left-lateral strike-slip (5)
7	40.0	2	Left-lateral strike-slip (2)
8	30.0	1	Normal (1)
9	62.0	4	Normal (3), reverse (1)
10	34.0	2	Pre-tilted normal (1), reverse (1)
11	50.0	4	Normal (1), reverse (2), left-lateral strike-slip (1)
12	33.3	3	Pre-tilted normal (2), right-lateral strike-slip (1)

The stratigraphic unit located in the study area is the Early Cretaceous carbonate platform unit of Morrone di Pacentro Formation, composed of a massive, white-beige micritic limestone. The Late Cretaceous carbonate platform unit of Cima delle Murelle Formation can be observed on a steep cliff towards the entrance into the valley but is not located in the study area. Post-orogenic talus deposits are scattered around the valley, consisting of well-sorted sediments with sizes ranging from cm to dm rock fragments. The location of the stratigraphic units can be observed in Figure 3.6.1.

The Morrone di Pacentro Formation has been exposed to intense weathering and erosion, evidenced by several karsts and collapsed karst structures observed throughout the study area. Intense karstification is observed around some of the major faults, with both major and minor karst located in proximity to the faults. Some of the karsts are probably related to dissolution features within different layers, where the karsts are following the bedding orientation, while others are located in the fault core and follows the fault orientation. When karst is located in the fault core, following the fault orientation, they have been complemented in the fault core thickness measurements. Weathering on the rocks gives a grey-brownish surface color, compared to the original white-beige limestones, and dark-grey precipitations are often observed around weathered rocks. These weathered rocks have a more massive texture, and carbonate cementation within the rocks have been observed in thin-sections from collected rocks samples.

Ten orientation measurements of the bedding were collected at different points along each of the studied scanlines. Figure 3.6.2 illustrates the bedding orientation collected at each scanline on an area picture of Vallone di Santo Spirito.

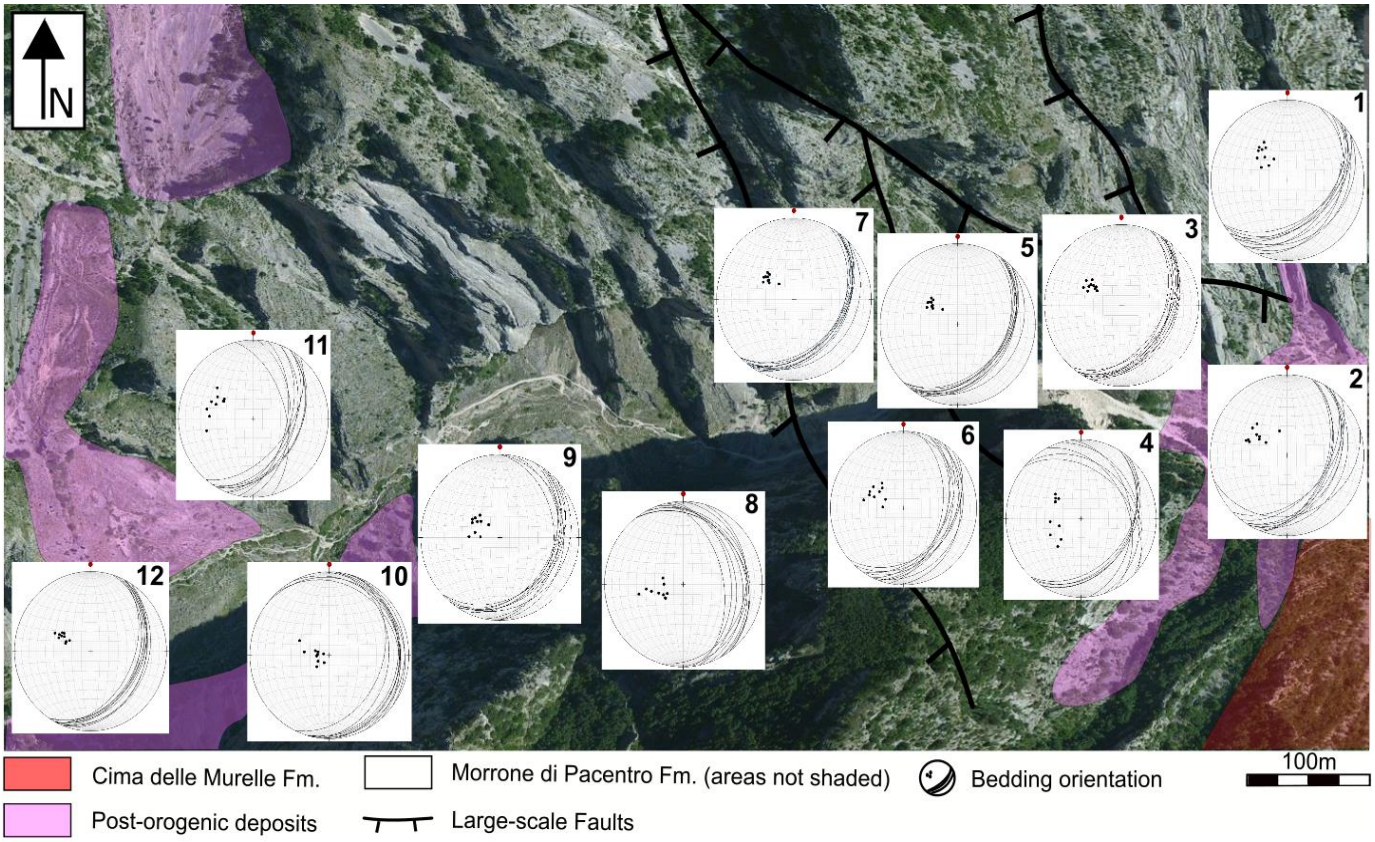

Figure 3.6.2: *Illustration of the collected bedding orientation at each of studied scanlines. The area picture on this figure is equal to Figure 3.6.1.*

These orientation measurements were used to observe if the bedding orientation changed upwards in the valley, and to observe where each scanline was situated relative to the Majella anticline. All scanlines have been interpreted to be located within the eastern forelimb of the Majella anticline, trending NE-SW with a dip ranging from 6°-54° towards the SE-E. Some of the orientation measurements were completed in between faults, and on these measurements the orientation show some anomalies, caused by the faulting effect on the layering. The observed bedding in between the studied faults at scanline 10 shows an almost horizontal orientation, compared to the eastward dipping layers located outside the faulted area.

3.6.2. Fault description

A total of 45 faults were measured and documented along the 12 scanlines in the study area (Table 4), 18 which are normal faults (4 pre-tilted normal faults), 11 reverse faults and 16 strike-slip faults (7 right-lateral and 9 left-lateral). Fault core thickness measurements have been conducted for all faults. Fault type classification was mainly done from field observations and orientation data. The orientation measurements were used to support the fault classification completed in the field. The orientation data

was also compared to Aydin et al. (2010) orientation data on the different fault types found along the eastern forelimb of the Majella anticline. The general orientation trend found for each of the fault types is illustrated in Figure 3.6.3.

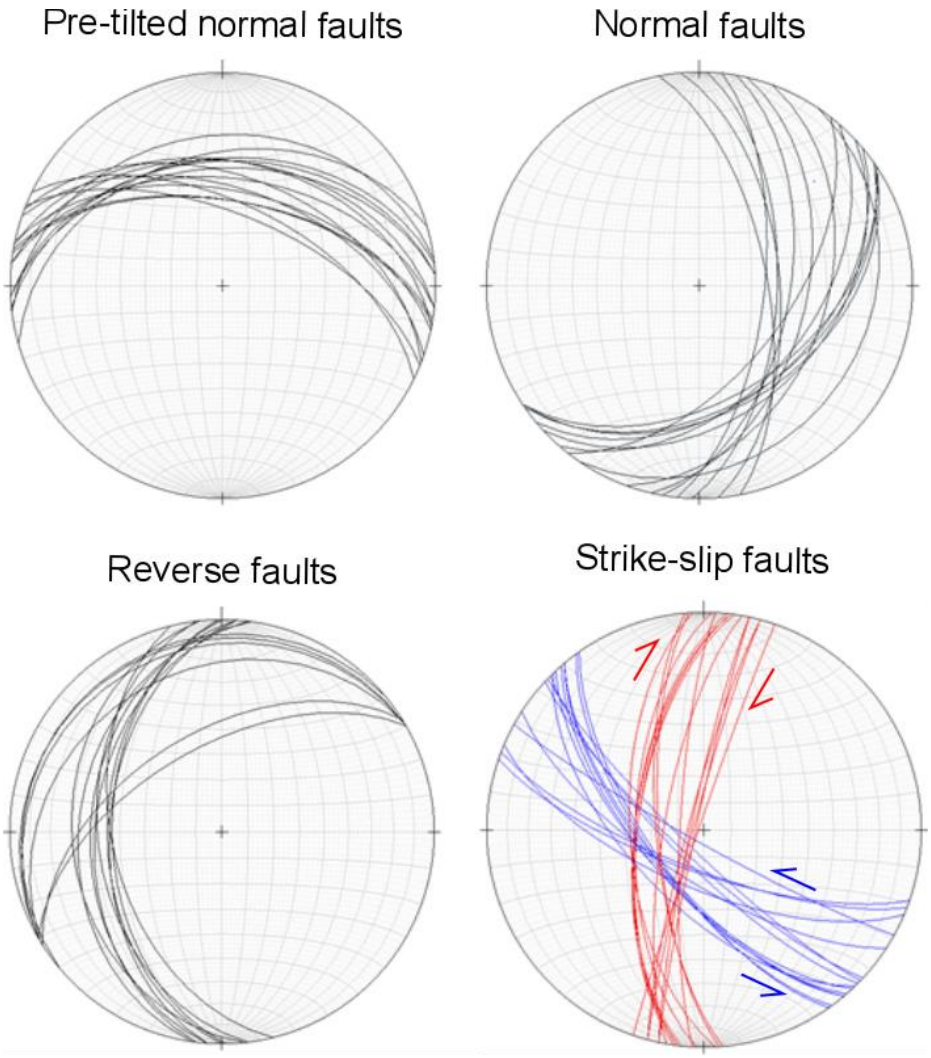

Figure 3.6.3: *Illustration of the different orientation trends for each fault types located in the study area.*

The normal faults observed in the study area have fault traces approximately parallel to the strike of the bedding (Figure 3.6.4) and are generally dipping downslope. The mechanisms related to the initiation and growth of the normal faults have been suggested to be related to shearing of bed-parallel pressure solution seams (PSSs) located within the layers (Graham et al., 2003; Aydin et al., 2010). The bed-parallel PSSs fragmented the rocks and developed weakness zones within each mechanical layering. Fault growth was initiated by linkage of the weakness zones, developing the approximate bed-parallel orientation of the normal faults. Normal faults were classified in the field based on the approximately bed-parallel orientation and a distinct fault core structure.

Pre-tilted normal faults observed in the study area are dip-slip faults which do not fit the general normal fault characterization (bed-parallel). Aydin et al. (2010) suggest that the pre-tilted normal faults are the oldest structures present, and formed before the folding and thrusting of the Majella anticline in the Oligocene-Pliocene. The pre-tilted normal faults may be related to the ENE-WSW extensional tectonics in the Tethys Ocean, which lasted until Late Cretaceous, creating NNW-SSE striking normal faults. The faults rotated towards the east, during the eastward compression of the Apennenic fold-and-thrust belt, creating the WNW-ESE trending faults. The observed and measured pre-tilted normal faults are often minor faults with a narrow fault core and have a more sub-vertical appearance in the outcrop, compared to the other normal faults.

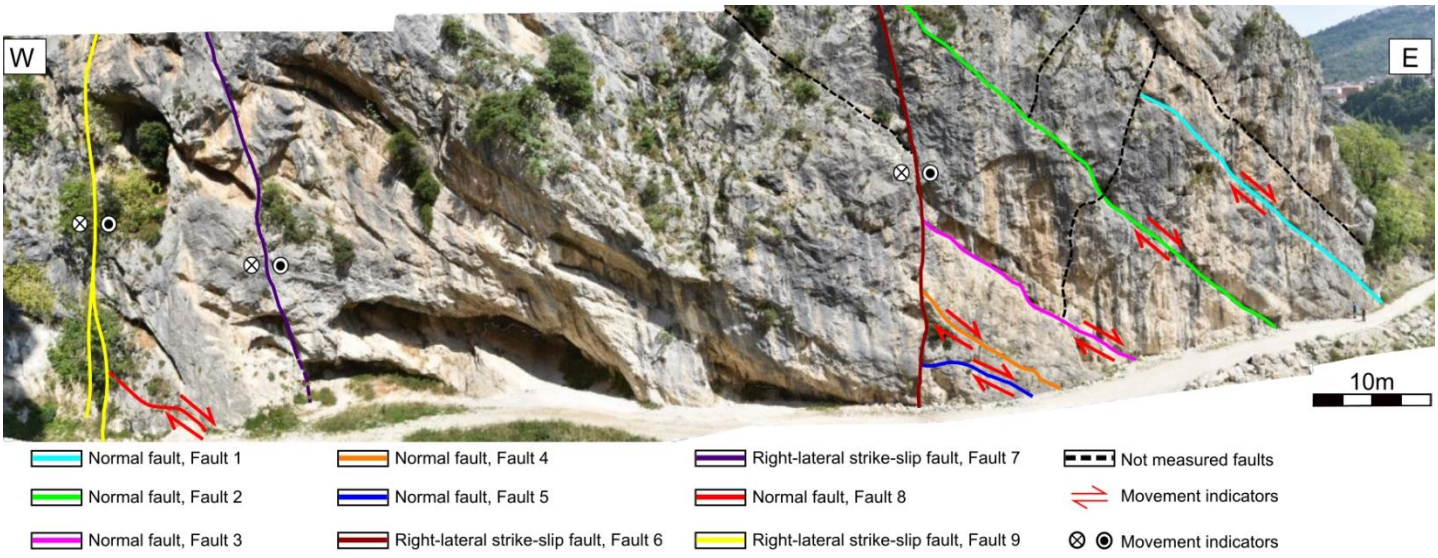

Figure 3.6.4: *Photomosaic of the outcrop where scanline was located, showing the fault interpretation. The normal faults interpreted on the figure illustrates the approximate bed parallel orientation, while the right-lateral strike-slip faults have a high cutoff angle. Note the major and minor faults located around Fault 7 in the middle of the photo. These karsts are probably related to dissolution mechanisms within the layers. The major karst at the base, to the right of fault 7, is approximately 30 m long and 8 m high.*

The reverse faults observed in the study area are oriented antithetic compared to the normal faults and the bedding orientation. The reverse faults at the outcrop have a low cutoff angle to the bedding. The mechanisms behind the initiation of the reverse faults are suggested by Aydin et al. (2010) to be related to the linkage of oblique PSSs located within the bedding. On Figure 3.6.5 two reverse faults have been interpreted along scanline 6 in the study area and illustrates the antithetic orientation compared to the bedding. The faults on the figure show also a listric texture as they approach the base of the outcrop.

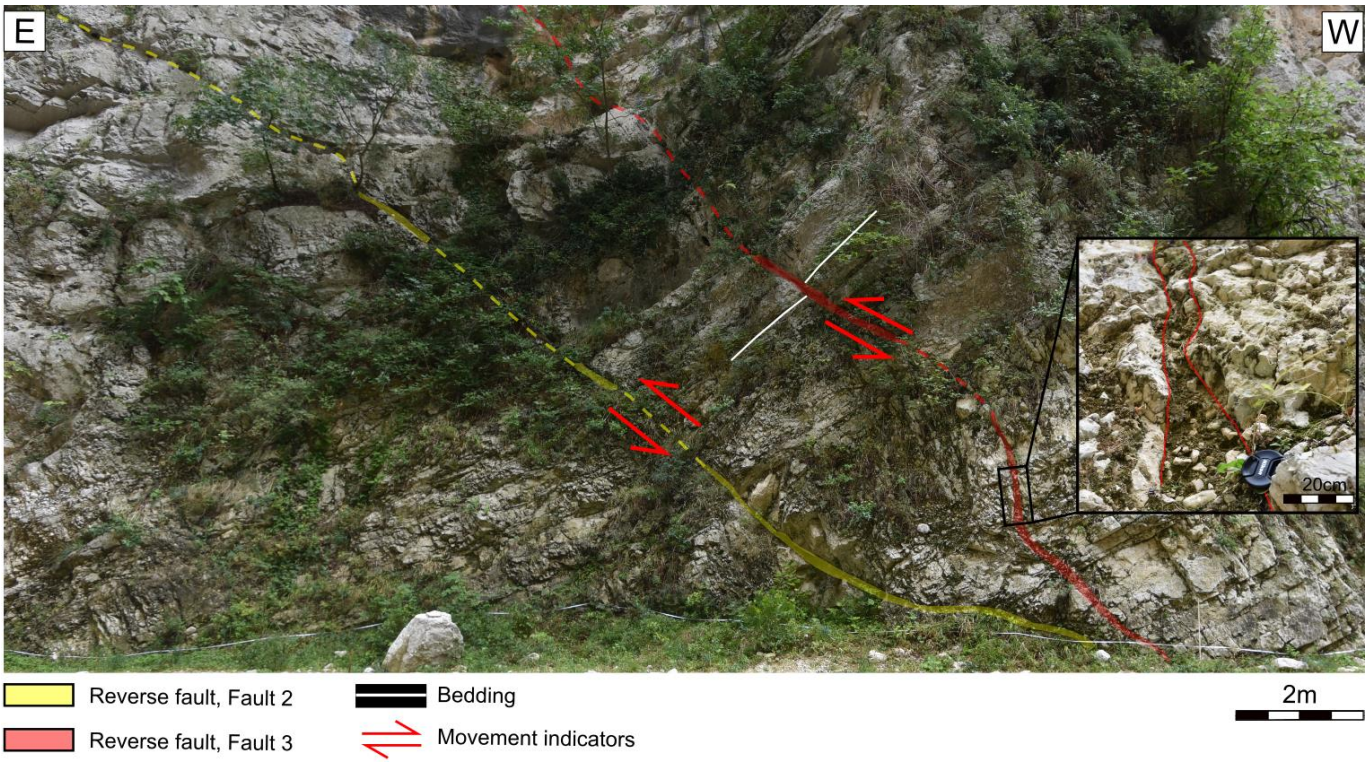

Figure 3.6.5: *Two reverse faults located along scanline 6 in the study area. The faults have a low cutoff angle to the bedding, compared to the strike-slip faults (Figure 3.6.6). Note the deformed and brecciated rocks surrounding the faults at the outcrop.*

The observed strike-slip faults have a vertical appearance and a high cutoff angle at the outcrops, which was used to separate the strike-slip faults from the reverse faults in the field. Some of the measured strike-slip faults have a distinct slip surface and slicken-lines, which made identification of slip direction easily. Orientation measurements were used to separate the right- and left-lateral strike-slip fault that did not have a distinct slip surface. The observed left-lateral strike-slip are trending NW-SE, while the right-lateral faults are trending N-S. Aydin et al. (2010) suggest from field observations and geological maps that the strike-slip faults occur in a hierarchical order, where the left-lateral faults appear to determine the location of the right-lateral faults. Figure 3.6.4, 3.6.6 and 3.6.7 illustrates the vertical strike-slip faults observed in the study area. The high cutoff angle can be observed in both figures.

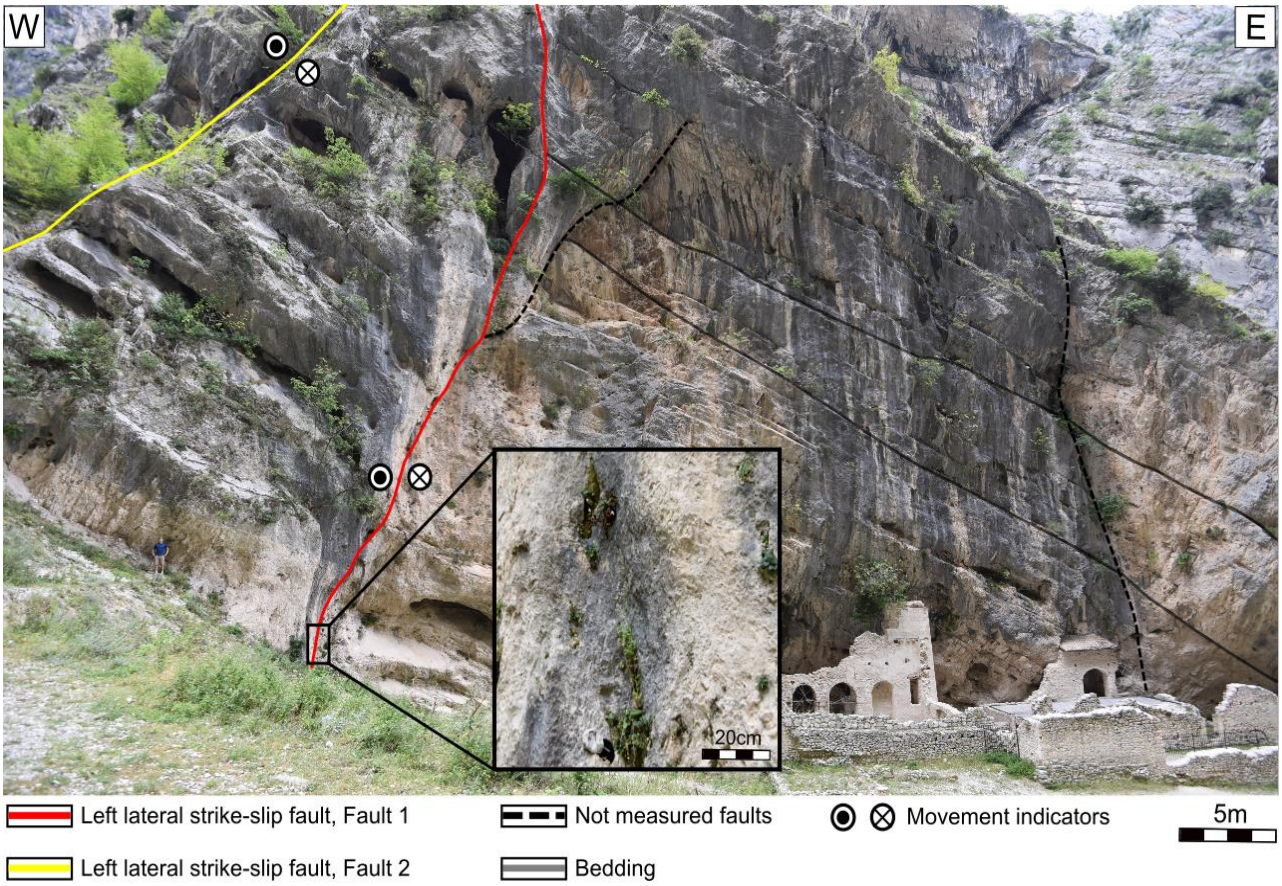

Figure 3.6.6: *Outcrop picture, with fault interpretation of two left-lateral strike-slip faults located along scanline 7. The close-up picture illustrates the cemented fault core observed in Fault 1, no fault core thickness measurements on this fault, because of the lack of a clear fault core boundary. The buildings located at the base of the outcrop are the Monastery of di Santo Martino in Valle, dated back to year 832.*

3.6.3. Fault core thickness and fault core descriptions

A total of 693 fault core thickness measurements has been completed on the 45 faults. Picture measurements of the fault core thickness have been performed on higher levels of the faults not accessible in the field. The measured fault core thickness completed on pictures was compared to the field measurements to verify the accuracy, which is illustrated in Figure 1.6.2 A and B. Fault core thickness measurements were performed at different levels or heights along the fault core in the field and on pictures. Table 5 presents a summary of the completed fault core thickness measurements, both in the field and on pictures. The average fault core thickness measurements from pictures and field show some variations related to the fact that the measurable accessible height is much greater on pictures, compared to the field measurements. A good example is Fault 1 located on scanline 4 (Figure 3.6.7), where the measured height in the field was 2.40 m, while on pictures the fault core could be measured for 27.60 m and a total of 48 thickness measurements were carried out.

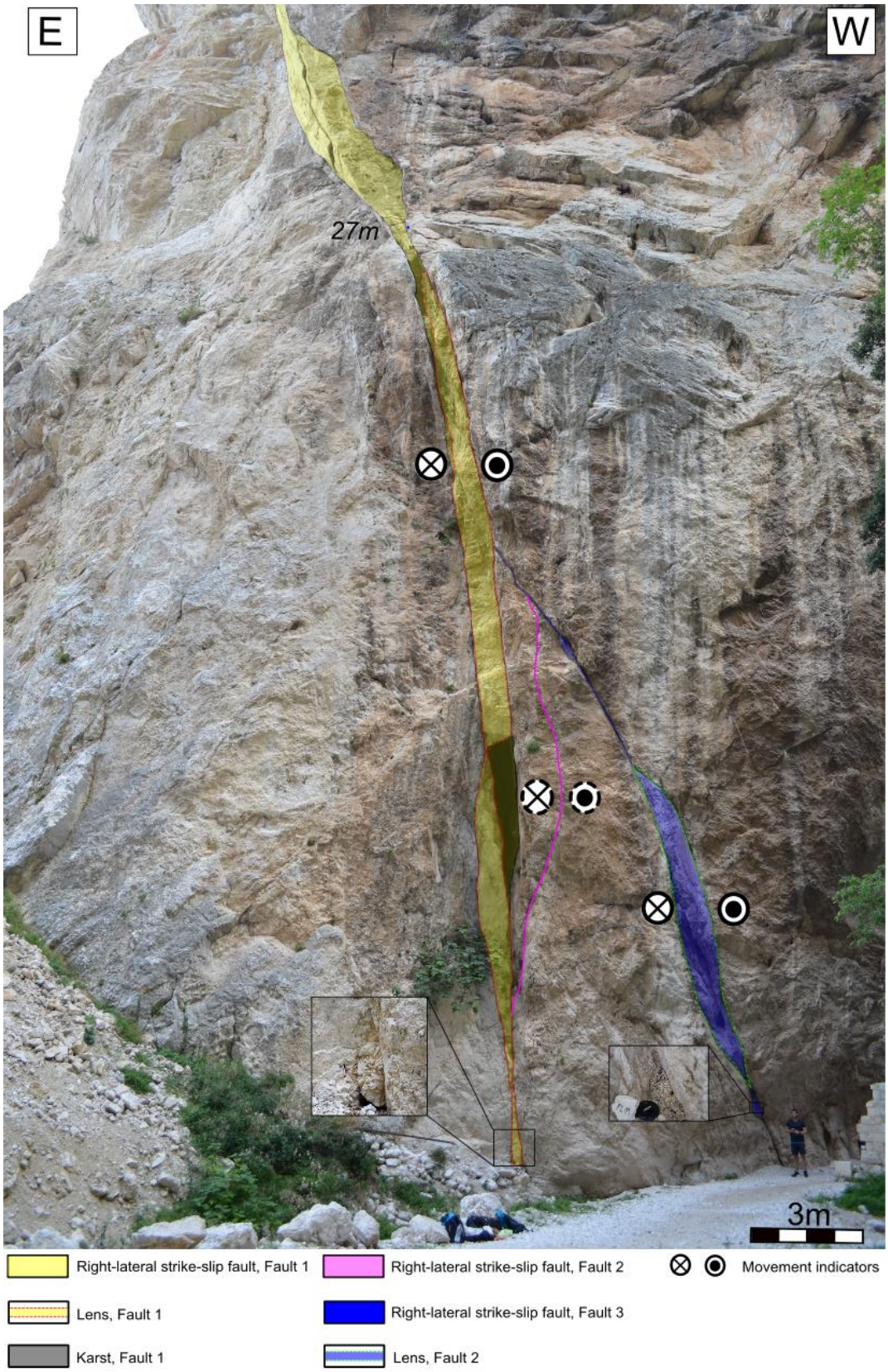

Figure 3.6.7: *Interpretation of the faults located along scanline 4 at the study area. A total measured height of 59 m and 103 fault core thickness measurements was completed on the three faults using picture measurements, compared to 6 m and 13 measurements conducted in the field. Fault 2 interpreted on the figure was not accessible in the field, but have been interpreted to be a right-lateral strike-slip fault.*

Table 5: *Summary of the fault measurements completed on the 45 faults located along the 12 scanlines at Vallone di Santo Spirito. H; height (or elevation), T; fault core thickness, R.L; right-lateral, L.L; left-lateral, Pic; measurements only possible or completed on pictures, X; no measurements, Cmtd; cemented fault core.*

Fault nr	Scanline number	Fault type	Position on scanline (m)	Orientation	Measured *H* field (m)	Measured *H* picture (m)	Average *T* field (cm)	Average *T* picture (cm)
Fault 1	1	Reverse fault	5.6	173/45	2.4	13.2	3.17	5.10
Fault 1	2	Pre-tilted normal fault	12.9	261/38	2.6	12.8	0.60	1.49
Fault 2	2	Pre-tilted normal fault	15.3	260/38	1.4	13.9	0.40	3.48
Fault 1	3	Normal fault	0.7	002/49	3.6	6.0	25.29	21.82
Fault 2	3	Normal fault	19.2	057/42	3.8	6.6	16.63	9.34
Fault 3	3	Normal fault	35.2	052/43	3.6	6.9	18.37	12.97
Fault 4	3	Normal fault	45.0	041/45	1.8	4.8	0.60	1.57
Fault 5	3	Normal fault	48.8	032/35	2.4	4.8	1.15	1.33
Fault 6	3	R.L. Strike-slip fault	55.5	193/84	2.4	4.2	1.58	1.46
Fault 7	3	R.L. Strike-slip fault	106.5	182/76	Pic	16.8	Pic	28.11
Fault 8	3	Normal fault	112.5	030/33	3.0	4.2	11.99	9.67
Fault 9	3	R.L. Strike-slip fault	122.0	186/66	2.4	3.6	144.20	137.06
Fault 1	4	R.L. Strike-slip fault	4.2	152/74	2.4	27.6	17.32	66.90
Fault 2	4	R.L. Strike-slip fault	4.4	X	Pic	11.9	Pic	4.10
Fault 3	4	R.L. Strike-slip fault	12.8	177/69	3.6	19.5	11.54	32.27
Fault 1	5	Normal fault	1.8	009/75	Pic	0.6	Pic	1.05
Fault 2	5	Normal fault	3.2	009/52	2.4	3.0	7.84	6.96

Fault 3	5	Reverse fault	32.5	175/27	3.0	7.3	7.33	7.23
Fault 4	5	Reverse fault	29.0	176/30	4.4	6.0	11.23	7.08
Fault 5	5	Reverse fault	33.0	109/62	8.4	15.9	2.84	5.91
Fault 6	5	Reverse fault	51.0	198/27	3.0	4.2	0.88	1.28
Fault 7	5	L.L. Strike-slip fault	57.7	135/70	3.6	9.0	7.46	10.08
Fault 1	6	L.L. Strike-slip fault	5.6	130/80	3.0	4.5	5.07	6.53
Fault 2	6	Reverse fault	42.0	177/23	6.6	8.8	16.41	14.12
Fault 3	6	Reverse fault	43.1	184/48	3.0	8.7	7.58	7.69
Fault 4	6	L.L. Strike-slip fault	79.0	140/67	2.4	5.4	22.24	18.35
Fault 5	6	L.L. Strike-slip fault	82.1	162/64	3.0	6.9	3.80	7.36
Fault 6	6	L.L. Strike-slip fault	85.9	121/72	1.8	2.8	2.75	3.36
Fault 7	6	L.L. Strike-slip fault	88.3	148/63	2.7	6.9	7.36	8.52
Fault 1	7	L.L. Strike-slip fault	3.6	128/82	Cmtd	Cmtd	Cmtd	Cmtd
Fault 2	7	L.L. Strike-slip fault	31.4	157/67	2.4	3.0	4.94	4.71
Fault 1	8	Normal fault	3.3	357/62	X	X	X	X
Fault 1	9	Reverse fault	22.0	188/37	10.8	X	13.13	X
Fault 2	9	Normal fault	30.7	343/45	1.2	4.9	9.03	6.82
Fault 3	9	Normal fault	36.5	346/37	1.2	4.8	2.93	2.73
Fault 4	9	Normal fault	37.3	352/43	1.2	5.7	2.80	6.01
Fault 1	10	Reverse fault	7.3	117/36	6.6	19.2	22.45	16.63
Fault 2	10	Pre-tilted normal fault	23.6	284/39	4.8	X	4.59	X
Fault 1	11	L.L. Strike-slip fault	3.3	149/78	2.1	X	6.55	X

Fault 2	11	Reverse fault	25.9	173/48	1.8	3.3	93.25	89.08
Fault 3	11	Reverse fault	38.8	164/67	1.8	5.2	17.00	24.56
Fault 4	11	Normal fault	45.1	351/62	2.4	10.2	4.56	4.57
Fault 1	12	Pre-tilted normal fault	4.3	289/55	3.0	3.6	1.58	2.09
Fault 2	12	Pre-tilted normal fault	9.2	288/57	4.2	4.8	2.68	2.54
Fault 3	12	R.L Strike-slip fault	30.0	195/84	1.8	3.6	4.38	5.60

On Figure 3.6.8 A-D different fault rocks observed in the fault core of the studied faults are illustrated. Carbonate fault gouge (Figure 3.6.8 A and B) have been observed in the fault core of all the different fault types in the study area. The carbonate gouge is non-cohesive and consists of very fine-grained beige-grey carbonate grains with carbonate clasts ranging in size from mm to dm. Figure 3.6.8 D illustrates carbonate gouge which has been chemically altered and cemented. The gouge located in the fault core are cohesive and massive, which could indicate cementation. Fault breccia (Figure 3.6.8 C) have been observed in some of the fault cores, and often located in the fault core of the major strike-slip faults observed. This fault rock is often cohesive, but non-cohesive breccia have also been documented, and they are often observed in breccia pockets within the fault core. The presence of these pockets increase the thickness of the fault cores.

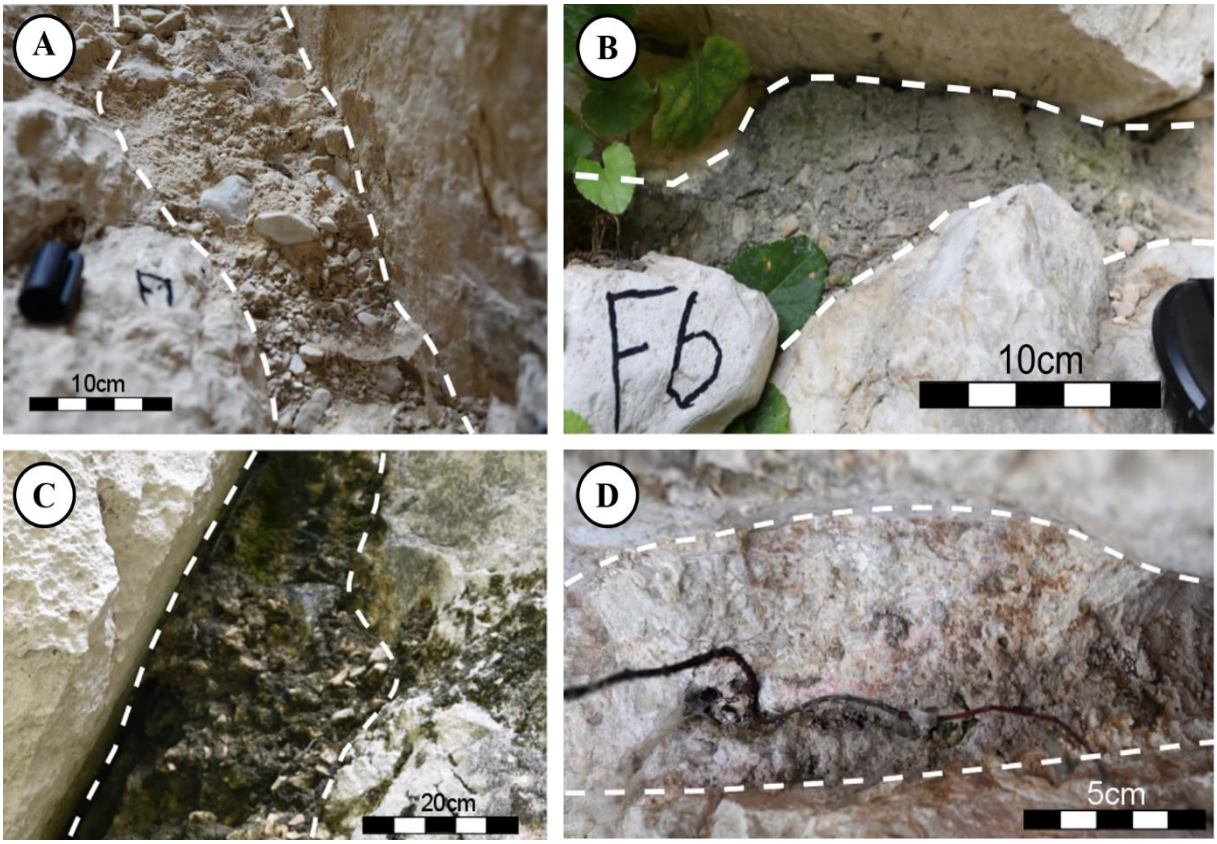

Figure 3.6.8: *Illustration of the different fault rocks observed in the study area. (**A**) Beige carbonate gouge observed in the fault core of a right-lateral strike-slip fault. Some carbonate clasts are incorporated in the gouge. (**B**) Grey carbonate gouge observed in the fault core of a reverse fault in the study area. (**C**) A major, cohesive breccia pocket observed in the fault core of a left-lateral strike-slip fault. (**D**) White-brownish, cohesive cemented fault gouge located in the fault core of a right-lateral strike-slip fault.*

3.6.4. Statistical analysis of data

The data collection of 694 fault core thickness measurements from Vallone di Santo Spirito, have been used to complete univariate analysis and to construct EF-plots. The EF-plots for the fault core thickness measurements are illustrated in Figure 3.6.9 A-B. On the EF-thickness plot (Figure 3.6.9 A), a characteristic hyperbolic shaped, concave-up trend can be observed. The hyperbolic shaped trend is typical for a power-law- or log-normal distribution trend. The log EF-log thickness plot (Figure 3.6.9 B), show a concave down trend of the data points. For all measurements, the best fit correlated to the data points supports a log-normal distribution, with a robust regression of fit of 0.9591. If 10 % of the measurements are removed, resulting in removal of the endmembers (black dashed circles on figure), the dataset forms an approximately straight line. This straight line is characteristic for a power-law distribution and gives a regression of fit equal to 0.9653. Since both correlated distribution trends show a solid regression of fit, the fault core thickness measurements show either a power-law- or log-normal distribution trend.

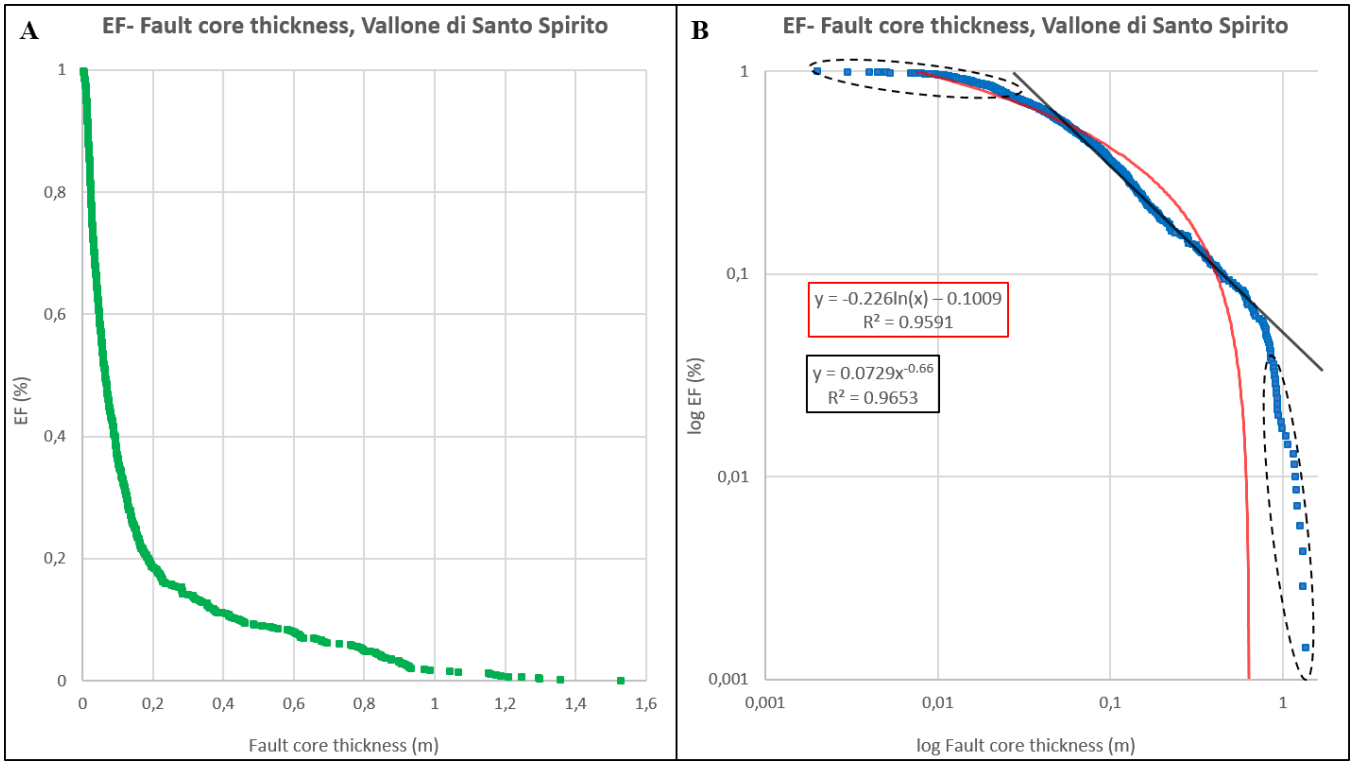

Figure 3.6.9: *EF-plots of the measured fault core thickness in the different fault types located in the Vallone di Santo Spirito. (**A**) Shows the EF in linear scale in relation to fault core thickness, also in linear scale. (**B**) Show the EF in logarithmic scale in relation to fault core thickness, also in logarithmic scale. The different lines represent the trend lines correlated to best fit the measurements. The correlated functions and R^2 values are presented in the squares on the figure, following the same color code as the trend lines.*

4. Discussion

The fault core thickness measurements show changes and variations at different levels along the faults and are affected by lithology and displacement. In this chapter, the results presented in the preceding chapter are interpreted and discussed to shed light on i) factors affecting the fault core thickness, ii) the relationship between the fault core thickness and displacement, and iii) the implications and applications of the results for different fault scales, lithologies, and tectonic settings.

4.1. Variation in fault core thickness

4.1.1. Variation caused by lithology

The dataset collected in this project includes fault core thickness and fault displacement measurements from 99 faults situated in siliciclastic rocks and carbonates. The fault core thickness data show variations that are related to lithology and the resulting fault rocks incorporated into the fault core. To examine the fault core thickness dataset, the measurements has been sorted into six different bins or groups, covering: 0.1-1 cm, 1-5 cm, 10-20 cm, 20-50 cm and 50-250 cm. In the siliciclastic rock measurements from Utah, an additional bin covering the thickness of 250-2500 cm is included, related to the wide fault core (including fault lenses) measured at the Hidden Canyon Fault. The average thickness (harmonic and arithmetric), average displacement, and the maximum and minimum displacement, were calculated for each thickness bin. The calculations and thickness bins are presented in Table 6. For the carbonate dataset from Vallone di Santo Spirito, a lack of sufficient displacement measurements is presented in the table, related to the lack of marker beds within the massive Morrone di Pacentro Formation, also addressed by Aydin et al., (2010).

From the data presented in Table 6, two histograms illustrating the average fault core thickness and displacement, within every thickness bin for both lithologies are shown in Figure 4.1.1. The histogram includes two Y-axis, where one shows the average fault core thickness in a logarithmic scale and the other shows the average displacement in a linear scale. In both lithologies, a general trend can be observed, as fault displacement increases the fault core thickness also increases. This indicates that displacement, within both of the studied lithologies, is a controlling factor affecting the fault core thickness. Comparing the average displacement within each bin, only the 1-5 cm bin shows similar values for the different lithologies, otherwise the siliciclastic data shows higher average displacements, than the carbonate data. The histograms show approximately similar average thickness values for the lowermost bins, while the upper 50-250 cm bin in the siliciclastic data shows higher average values, compared to the carbonate data. However, when considering the data separately, the carbonate data display a much higher core thickness-displacement ratio, compared to the siliciclastic data. This indicates a much wider fault core is located in the carbonates for a lower displacement, compared to siliciclastic rocks.

Table 6: *Distribution and sorting of the 1556 fault core thickness- and 128 displacement measurements. The fault core thickness measurements have been sorted and divided into bins. X; no measurements.*

Fault core thickness (T)	***T* samples**	**Average *T***		**Displacement (*D*)**			
Range (cm)		**Arithmetric**	**Harmonic**	***D* samples**	**Average**	**D_{min}**	**D_{max}**
Siliciclastic rocks							
0.1-1	106	0.56	0.48	13	18.91	2.00	87.10
1-5	326	2.44	2.05	55	32.16	4.11	183.38
5-10	97	7.06	6.75	19	91.02	8.27	334.03
10-20	85	14.39	13.79	10	102.15	35.27	350.99
20-50	106	31.82	29.59	7	391.15	140.30	813.81
50-250	124	144.67	120.78	8	434.85	159.72	879.90
250-2500	27	1673.31	1643.24	1	200.00	200.00	200.00
Carbonates							
0.1-1	23	0.66	0.56	X	X	X	X
1-5	268	2.72	2.25	9	30.12	14.55	42.96
5-10	150	7.27	6.97	3	48.97	22.60	100.00
10-20	122	13.98	13.50	2	79.81	62.79	96.82
20-50	66	31.57	29.48	1	117.28	117.28	117.28
50-250	64	84.52	78.99	X	X	X	X

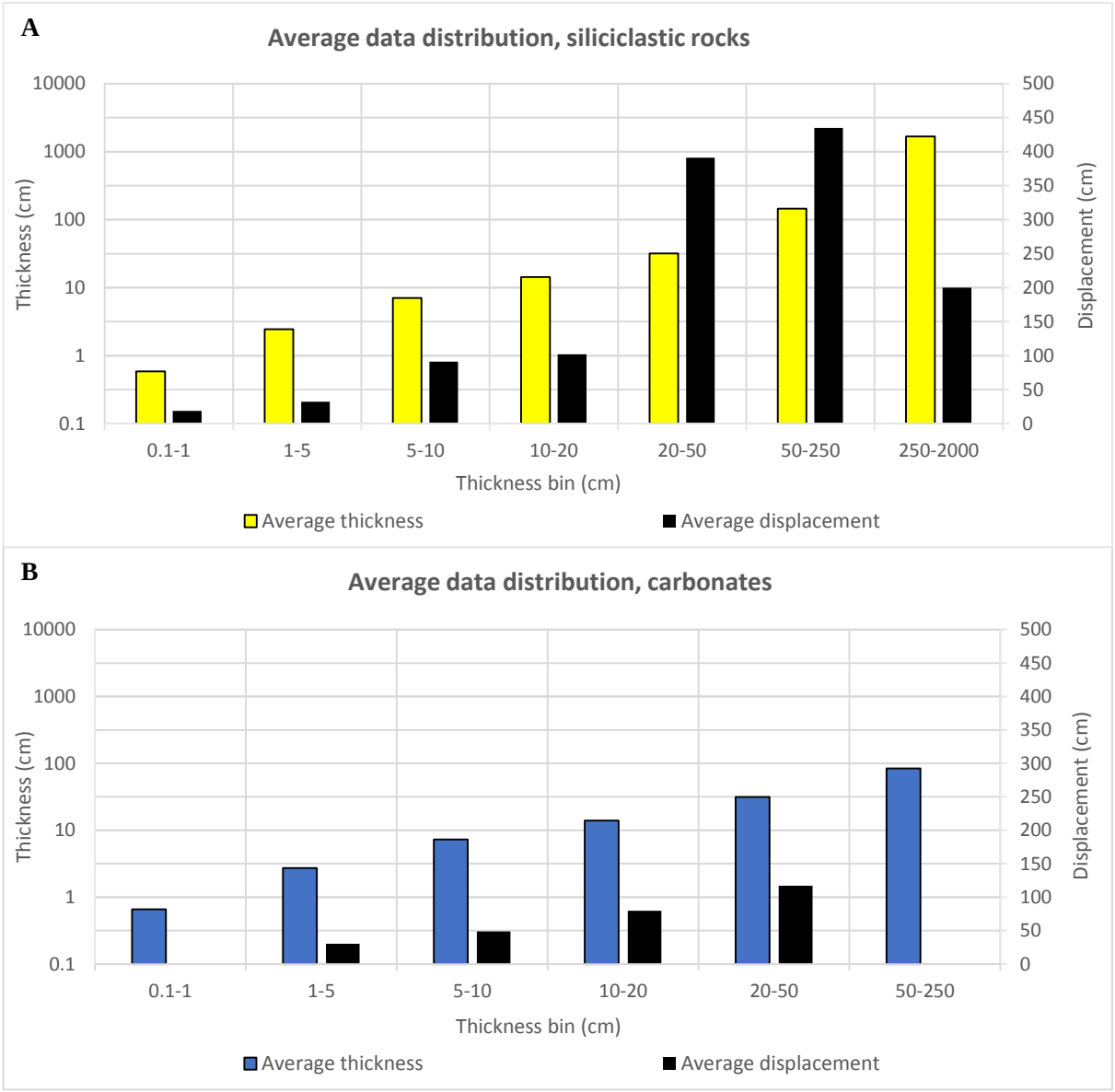

Figure 4.1.1: *Histogram illustrating the average fault core thickness and displacement, within each of the thickness bins for the siliciclastic rocks (**A**), and carbonates (**B**). The histograms are based on the average arithmetic data on Table 6, collected from all the measured and studied faults, in both study areas. A general trend can be observed, where the increase in fault core thickness corresponds with an increase in displacement.*

The fault core thickness data from both lithologies was compared, and two circle diagrams are covering the distribution of thickness measurements/samples within each of the bins are illustrated in Figure 4.1.2. A total of 871 measurements were completed in the siliciclastic data, and 693 measurements in the carbonate data. The majority of fault core thicknesses fall within the 1-5 cm bin, covering 38 % of the siliciclastic data, and 39 % of the carbonate data, respectively. The distribution of measurements is also approximately similar when increasing the range of the core thickness to 0.1-10 cm, representing 64 % of the carbonate data and 61 % of the siliciclastic data. A change in

distribution can be observed between the lithologies for thicknesses > 20 cm, for the siliciclastic measurements 29 % of the measurements are over 20 cm, while only 18 % of the carbonate measurements fall within this range.

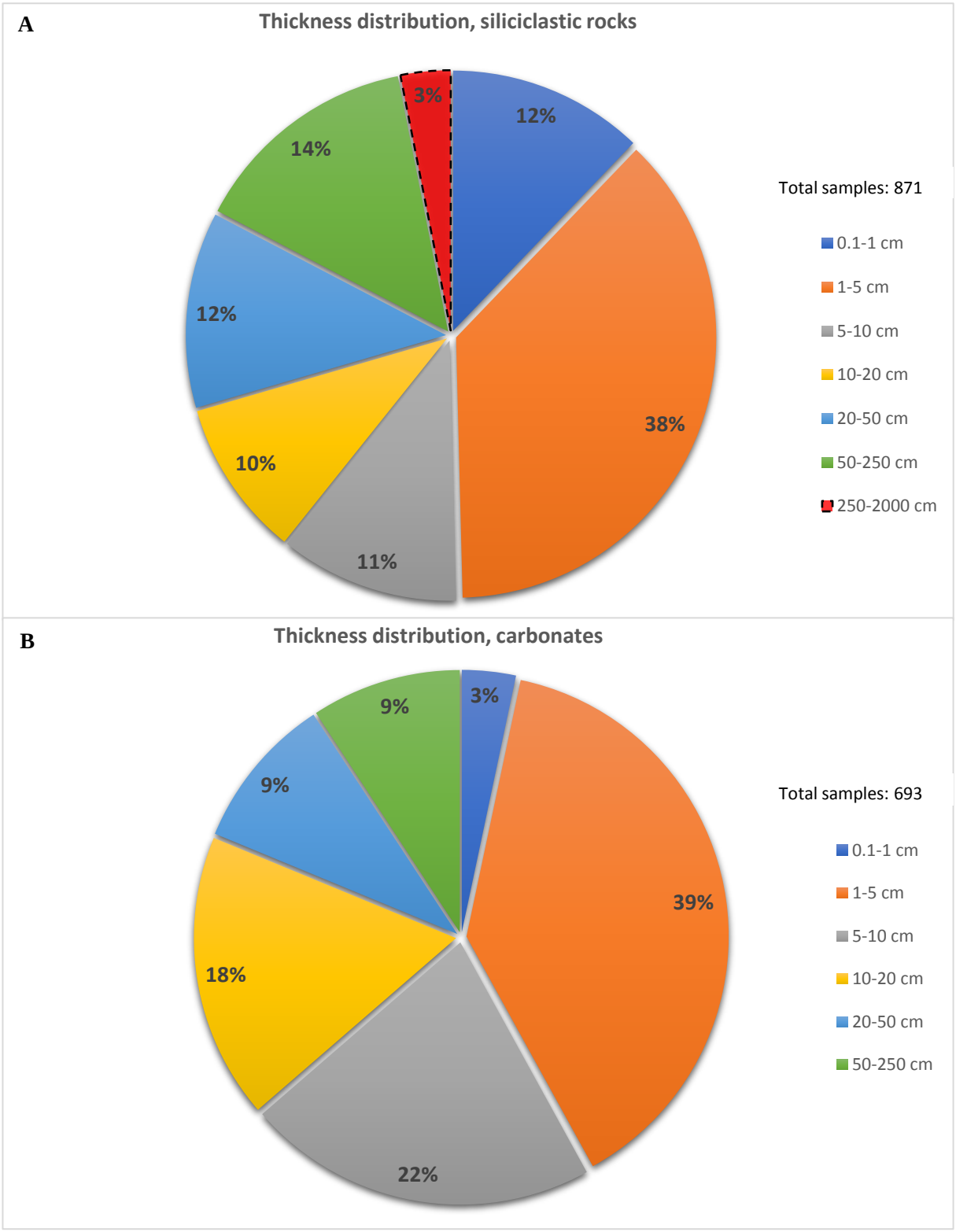

Figure 4.1.2: *Circle diagrams illustrating the fault core thickness distribution in sandstones and siliciclastic rocks (**A**), and in carbonates (**B**). The circle diagrams are based on data presented in Table 6 and represents the percentage or total measurements completed within each of the thickness bins.*

Comparing the fault core thickness between the two study areas includes some uncertainties related to the size and displacement of the faults measured in the carbonate study area. Few displacement measurements were performed, and the size of several of the faults are therefore unknown. The displacement measurements in the carbonates have been divided into four different displacement bins covering: 0-20 cm, 20-50 cm, 50-100 cm, and 100-150 cm, to enable comparison with the siliciclastic data. For each of the bins, the average displacement, the average fault core thickness and maximum- and minimum thickness, were calculated. The displacement bins and calculations are presented in Table 7.

Table 7: *Comparison of fault displacement and fault core thickness from the two study areas.*

Displacement (*D*)	***D* samples**	**Average *D***	**Fault core thickness (*T*)**		
Range (cm)			**Average**	**T_{min}**	**T_{max}**
Siliciclastic rocks					
0-20	37	10.34	1.72	0.40	4.70
20-50	23	33.60	4.08	1.00	12.58
50-100	9	77.85	7.13	2.51	16.00
100-150	11	123.62	9.02	3.60	23.84
Carbonates					
0-20	2	16.82	1.98	1.91	2.04
20-50	9	31.59	4.17	1.60	7.63
50-100	3	86.54	14.30	5.91	19.45
100-150	1	117.28	28.46	28.46	28.46

Although fewer displacement measurements are presented for the carbonate data in Table 7, the average thickness data support that fault cores in carbonates are wider than fault cores in siliciclastic rocks, for all the given displacement bins, which supports the observations on Figure 4.1.1, and the findings of Bastesen et al. (2013). The faults examined in Table 7 are minor faults, and the fault core thickness in both lithologies show great variations, supported by the maximum and minimum thickness values. Bastesen et al. (2013) suggest that minor faults have a larger core thickness-displacement relationship, than faults with > 10 m displacement in both lithologies, and the fault core complexity and thickness variations becomes more stable when the displacement exceeds 10 m. This theory is also supported by Torabi and Berg (2011), which suggest that the general power-law relationship is higher for medium-large faults than for minor faults and further propose that the variations stabilize when faults approach ~ 1 m of displacement.

The fault core thickness measurements completed in this project, support a fault model where the increase in core thickness, with respect to displacement, is greater for minor faults compared to major faults (e.g. Braathen et al., 2009; Torabi and Berg, 2011; Bastesen et al., 2013).

Other studies in the literature on lithological effects on the fault core thickness have suggested that faults juxtaposing sandstone-shale generally have significantly lower thickness-displacement relationship (Knott et al., 1996; Fossen and Hesthammer, 2000), and display on average a third of the thickness displayed by faults juxtaposing sandstone-sandstone or shale-shale of similar displacement (Sperrevik et al., 2002). The latter lithology relationship, regarding the narrow fault cores in sandstone-shale, compared to homogeneous lithologies, was not observed in this project. On the contrary, the studied and measured faults in this project displacing sandstone-shale display a significant wider fault core compared to faults which are mainly displacing sandstone-sandstone of similar displacement (Figure 3.3.3). The normal fault illustrated in Figure 3.3.3 is both juxtaposing a sandstone-sandstone sequence and a sandstone-shale sequence. The measured core thickness varies by a factor of 27 when comparing the sandstone-shale and the sandstone-sandstone sequence. The factor is found by dividing the average fault core thickness when displacing shale-sandstone, with the average fault core thickness when juxtaposing sandstone-sandstone. Other fault core thickness measurements from this project show that fault displacing a sandstone-shale sequence increase the core thickness by a factor of 4-15 when comparing the thickness with sandstone-sandstone sequences. This increase in core thickness could be related to ductile smearing and drag of shale sequences into the fault core, related to the competency and rheology of the shale, and compared to sandstone a competency contrast develops.

A study by Peacock and Sanderson (1992) on lithological and layering effects on fault geometry, show that normal faults that juxtapose heterogeneous sequences of siliciclastic rocks with competency contrasts (e.g. sandstone and shale), would generally develop a steeper dip in the bed with a high frictional angle (competent beds), compared to a shallower dip in layers with a lower frictional angle (less competent beds). It has also been reported by van der Zee et al. (2008) that faults juxtaposing sandstone-shale will contribute to fault splaying at fault asperities in less competent shale layers. These splay faults will generally reconnect with the principal slip surface, as the fault segments propagate and incorporate host rock lenses or shale smears in the fault core. This type of fault dip linkage between fault segments will develop a fault geometry where the shallow dipping fault segment may act as relay zone to the steeper dipping segments (Childs et al., 2009). The fault segments will continue to propagate and modify the dip contrast, which will eventually lead to breaching of the relay zone and incorporation of host rock lenses in the fault core (Childs et al., 2009). This process implies that faults situated in heterolithic-layered sequences promote a wider fault core thickness, compared to faults in homogeneous sequences.

Several outcrop studies have suggested that incorporation of host rock lenses in the fault core increases the thickness of the fault core and the internal core complexity (e.g. Lindanger et al., 2007; Childs et al., 2009; Bastesen and Braathen, 2010; Bastesen et al., 2013; Gabrielsen et al., 2016). A total of 53 minor and major fault core lenses have been documented and measured through this project. Some major fault core lenses increasing the fault core thickness have been measured at the Hidden Canyon Fault (Figure 3.2.2), ANP locality (Figure 3.3.4) and in two major right-lateral strike-slip faults located in Vallone di Santo Spirito (Figure 3.6.7). Bastesen and Braathen (2010) suggests that fault core lenses become more common with increasing displacement and that the lens formation causes a great increase in core thickness and complexity. The data in this project show an increase by a factor ranging between 2-16 for the siliciclastic data, and 2-10 for the carbonate data, respectively. This lens-factor have been found through calculations of the average core thickness from levels where fault core lenses are present and dividing it by the average thickness from levels which lack lenses.

The major Moab Member sandstone lens at the R-191 Canyon locality, which is juxtaposed in between the faults F1 and F2, is considered a fault core lens. The lens exposes a lozenge-shaped geometry and is situated in between two slip surfaces, with fault gouge located on both sides (Figure 3.1.3 and 3.1.5). This normal fault at the outcrop would expose a complex fault core structure, including six slip surfaces and a sandstone lens (Figure 3.1.2). Foxford et al. (1998) observed that the minimum number of major slip surfaces located in any of their studied Moab Fault transects was two, and internal slip surfaces within the fault cores are common. This would result in a fault core thickness of 2322.68 cm at level 0 at the locality if all fault core structures were included. However, different displacement on the two normal faults F1 and F2 has been suggested by Foxford et al. (1998). From orientation measurements on F1, the fault fits the characteristics of a splay- or branch fault to the Moab Fault (Foxford et al., 1998). This could indicate that fault F1 was a minor splay- or linked fault segment to fault F2 and that the Moab Member lens developed as a relay ramp juxtaposed in between the faults. During fault propagation and modification of the fault architecture and geometry, the fault segments continued breaching and breakdown the relay zone. Eventually, the relay ramp breached, and the residual of the Moab Member relay ramp is now represented as the lens exposed at the outcrop. This modification and breakdown of asperities have led to the absence of a lens structure on the northern outcrop of the fault, where the residual of the lens have subsequently been comminuted to fault rock during intense shearing and linkage of slip surfaces (Lindanger et al., 2007; Childs et al., 2009; Gabrielsen et al., 2016). The different displacement of the normal faults could be related to displacement transfer between the two fault segments, during the breakdown of the assumed relay ramp structure (Peacock and Sanderson, 1991; Foxford et al., 1998). This hypothesis of breaching and breakdown of relay ramp structures could also be one of the deformation mechanisms related to the incorporation of the two Moab Member sandstone lenses in the fault core of the Hidden Canyon Fault. Fault displacement transfer between the fault segments situated in the adjacent canyons could explain

the suggested difference in displacements of the faults (Peacock and Sanderson, 1991; Foxford et al., 1998). The lenses are situated approximately at the interpreted fault core boundary towards the hanging wall and footwall on Figure 3.2.2, respectively. Internal deformation of the lenses has been observed. It is thought that this deformation may be related to the impact on the lenses as the fault reactivates and propagates, and the internal deformation initiates shearing and breakdown of the lens- or relay ramp structures (Braathen et al., 2009; Childs et al., 2009). During the shearing and breakdown process, the connection between the lenses got cutoff by internal slip surfaces and fault surface asperities bypassed, and each of the two lenses became incorporated in the core as fault rocks (Lindanger et al., 2007; Childs et al., 2009).

4.1.2. Variation caused by fault type

Fault core thickness measurements were performed on different fault types in the study area of Vallone di Santo Spirito, and variations in core thickness between the different fault types have been documented. Table 8 presents an overview of the fault core thickness measurements carried out for the different fault types. The table shows the core thickness differences, and the overall thickness variations for each of the fault types, illustrated by the maximum and minimum thickness values. The variations in thickness for each of the fault types can be observed in the boxplot in Figure 4.1.3. In cases where the median value is not located in the middle of the box, it indicates that the fault core thickness is skewed.

The complex fault system observed in Vallone di Santo Spirito, and the different scales and variations of core thickness within each of the fault types could imply a hierarchical ordering of the fault system (Torabi and Berg, 2011). A hierarchical order between the strike-slip faults has been suggested by Aydin et al. (2010), where the left-lateral faults appear to determine the location of the right-lateral faults, on a large scale. However, in this project, the widest fault cores have been documented and measured within the right-lateral faults. At the studied scanlines in Vallone di Santo Spirito, left-lateral- and right-lateral faults were never located on the same scanlines (Table 4), so their spatial relationship could not be determined, compared to the observations done by Aydin et al. (2010). Furthermore, no displacement measurements were performed on any of the strike-slip faults, that could help determine the size and magnitude of the faults.

Table 8: *Summary of the completed fault core thickness measurements on the different fault types in Vallone di Santo Spirito. T; fault core thickness, R.L; right-lateral, L.L; left-lateral, Dev; deviation.*

Fault type	*T* samples	Average *T* (cm)	T_{min}	T_{max}	Dev. 25 %	Dev. 75 %	Median
R.L. Strike-slip faults	151	40.23	0.73	152.90	8.00	79.36	39.74
L.L. Strike-slip faults	128	8.56	0.84	39.53	2.99	11.50	5.55
Reverse faults	191	10.74	0.71	87.62	3.50	12.66	7.00
Normal faults	78	2.32	0.20	14,00	1.28	2.36	1.99
Pre-tilted normal faults	166	9.41	0.45	48.61	3.10	13.45	6.66

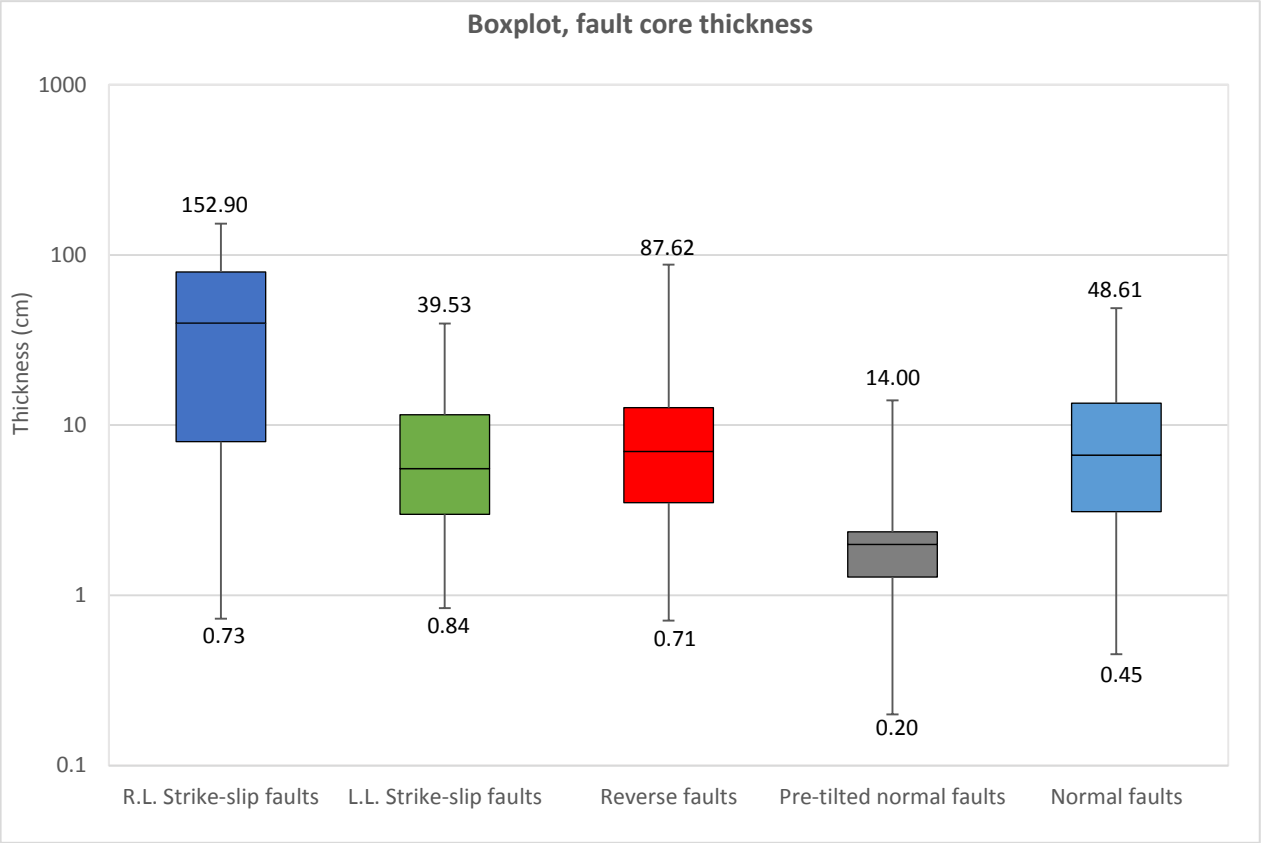

Figure 4.1.3: *The boxplot is illustrating the variations in fault core thickness related to fault type in Vallone di Santo Spirito. The plot is based on data presented in Table 8. R.L; right-lateral, L.L; left-lateral.*

Another observation, related to the different fault types in the study area, suggests that certain fault types develop relatively to one another (Table 4). Where right-lateral strike-slip faults are located, generally normal faults are situated on the same scanline (Figure 3.6.4). The same relationship can be observed for the left-lateral strike-slip faults and the reverse faults. Since the different fault types (except the pre-tilted normal faults) in the study area have been suggested to have formed during the Apennenic fold-and-thrust belt (Graham et al., 2003; Aydin et al., 2005; Aydin et al., 2010), this could indicate that fault initiation and propagation for the different fault types are connected and would

imply for a relatively simultaneously faulting process. The faulting process have been reported to be related to linkage of bed-parallel-, oblique-, and bed-perpendicular PSS structures (e.g. Graham et al., 2003; Aydin et al., 2005; Agosta et al., 2010b; Aydin et al., 2010), and the simultaneous faulting would indicate that linkage of one of the PSS structures would induce linkage of surrounding PSS structures. However, this hypothesis of simultaneous faulting promotes an issue and uncertainty related to the stress states and the Andersonian theory of faulting, based on the Coulomb slip criterion. The Andersonian theory is based on certain stress states and principal stress directions need to be in place to form certain fault types. A possible explanation for the simultaneously faulting process could indicate a fluctuating stress field, related to the presence of pre-existing weakness zones (PSSs) combined with an unstable and elevated pore fluid pressure. The linkage of one PSS structure could trigger an inversion of the stress field, due to stress release, which could further induce the linkage of PSS structures in another principal stress direction. The stress field could also be fluctuating and unstable under compression and relaxation stages occurred during the Apennenic fold-and-thrust belt.

4.2. Displacement changes along faults

Faults are characterized by displacement changes along the fault strike and dip. The maximum displacement of an isolated, blind fault is theoretically located at the center of the fault, and are progressively decreasing towards the fault tips, creating a triangular or C-shaped displacement profile (Barnett et al., 1987; Walsh and Watterson, 1989). In nature, idealized, isolated faults and perfect bell shaped displacement profiles are uncommon. Asymmetric, skewed and complex fault displacement profiles are often observed and might be explained by interactions and/or linkage of fault segments, changes in fault orientations and lithological variations. Fault development and propagation can be assumed to initiate by an accumulation of fault displacement during a series of slip events of different magnitude (Cartwright et al., 1995; Peacock and Sanderson, 1996). The magnitude of these slip events along the fault plane may be related to the lithological competency, determining the amount of slip, as well as the interaction and connection of surrounding fault segments. The faults studied and measured for this project show variation in displacement along the fault heights, and a large dataset of displacement measurements was conducted at the ANP locality. The faults located at the ANP outcrop expose complex fault geometries and networks, indicating interactions of the surrounding faults (Figure 3.3.2 and 3.3.5). Furthermore, the outcrop includes a variety of lithologies with different competency along the fault heights, and variations in displacement have been measured and observed between changing lithologies (Figure 4.2.1).

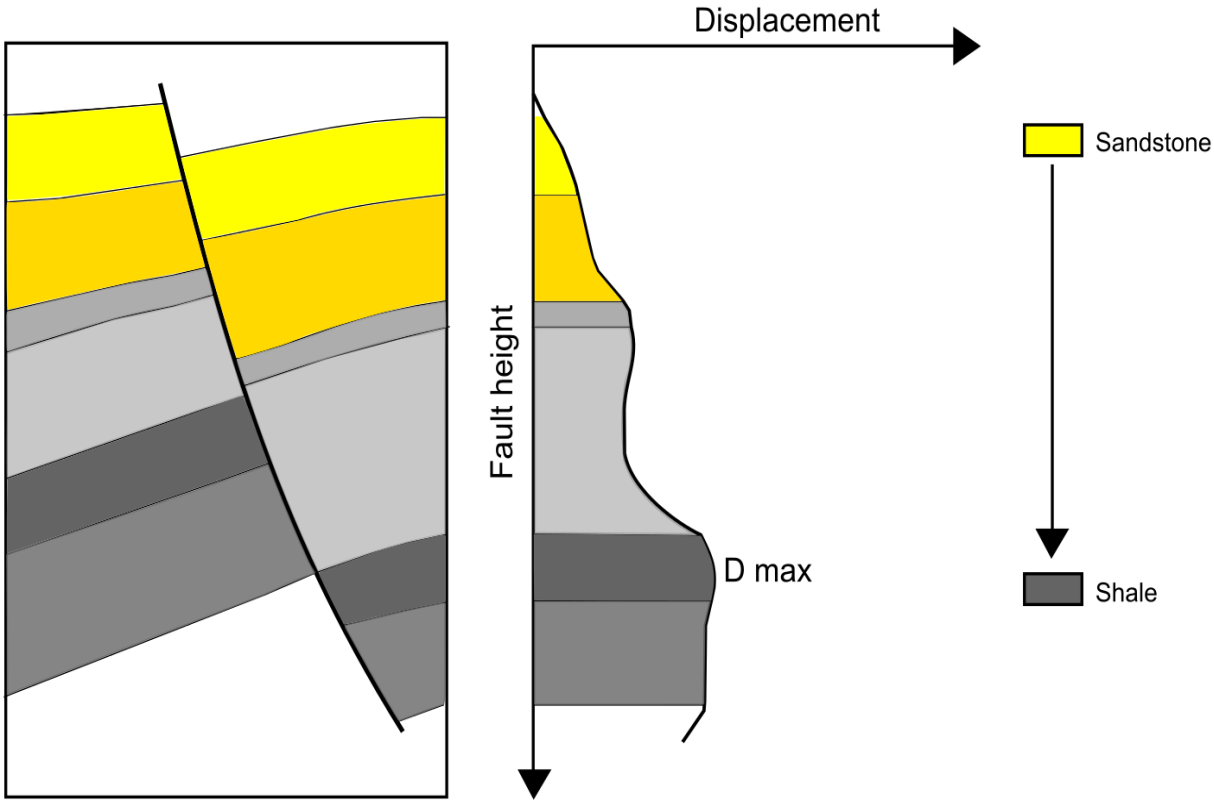

Figure 4.2.1: *Schematic illustration of a normal fault displacing different sedimentary layers and the resulting displacement profile. The profile shows the variations in displacement along the fault height, due to competency contrasts between the layers.*

Interactions between fault segments often lead to complex displacement profiles and overlapping segments. When linkage occurs, the resulting displacement profile is modified and is related to the relative size of the fault segments and the location of the maximum- and minimum displacement points along the fault segments. The minimum displacement point is often located at the segments linkage point, and this point separates the two maximum displacement point of the fault segments (Ellis and Dunlap, 1988; Peacock and Sanderson, 1991; Tvedt et al., 2013). However, if fault segments of different size link, the maximum displacement point is located near the center of the larger segment (Peacock and Sanderson, 1991). Ellis and Dunlap (1988) suggests that the maximum displacement point marks the points where fault propagation and linkage to other fault segments are initiated. For the variations in displacement along the fault heights, this linkage process would result in major variations in displacement. Figure 4.2.2 presents a displacement profile from a minor normal fault located at the ANP locality. Based on the maximum- and minimum displacement points related to fault segment linkage, this profile might represent the linkage of three fault segments.

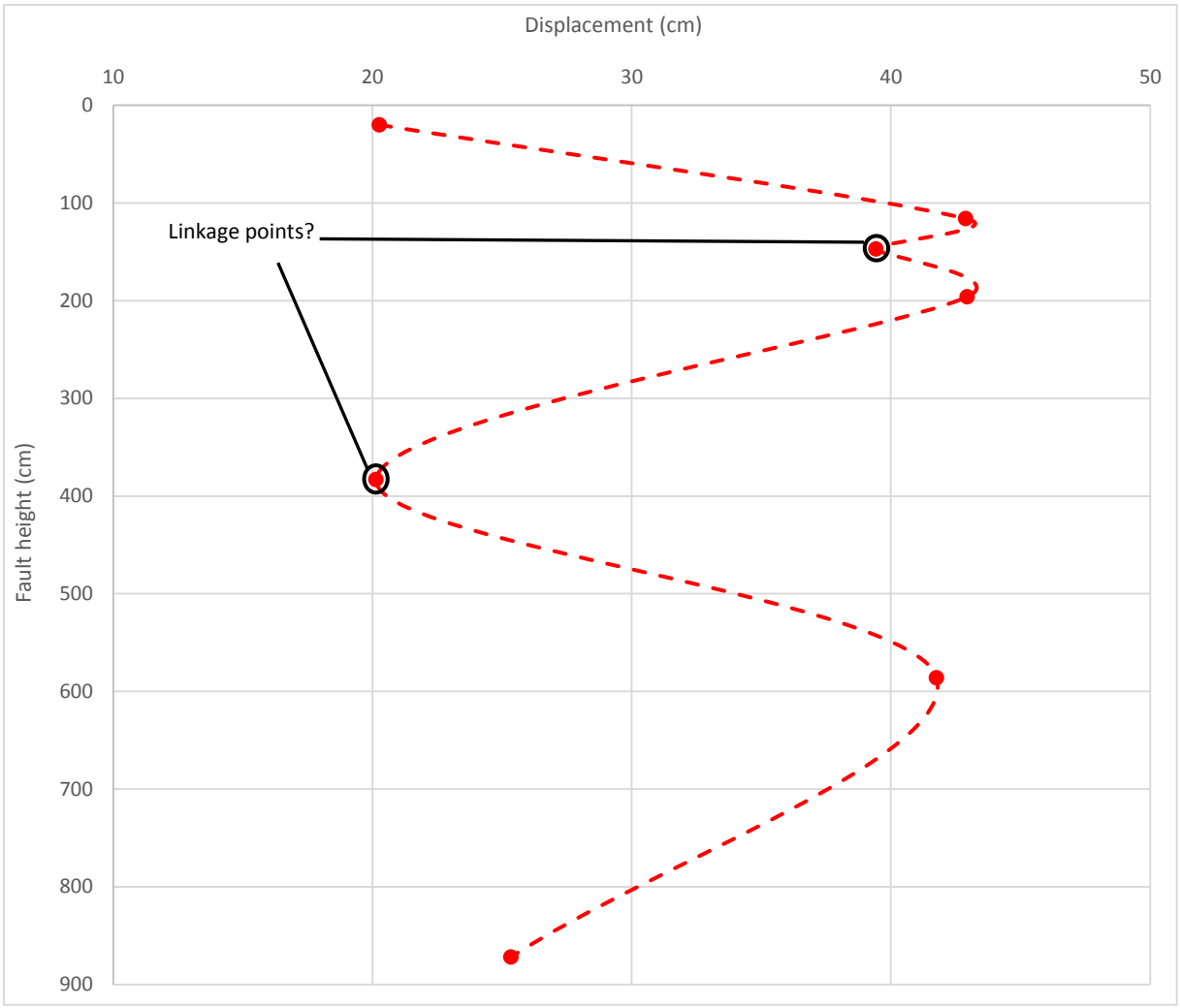

Figure 4.2.2: *Displacement profile from a minor normal fault at ANP. Three maximum displacement points are measured along the fault height, and separating these points are lower displacement points.*

4.3. Discussion on statistical analysis of data

4.3.1. Univariate distributions of fault core and displacement data

The relationship between the fault core thickness and fault displacement is widely accepted in the literature to follow a power-law relationship (Knott et al., 1996; Shipton et al., 2006; Bastesen and Braathen, 2010; Torabi and Berg, 2011; among others). In this project, the univariate distribution trend of the fault core thickness has been examined using EF-plots. From these plots, the general distribution trend is suggested to follow a power-law- or log-normal distribution trends, which coincides with the global dataset (Figure 4.3.1 A-B). However, a distinct power-law distribution in univariate plots can be challenging to determine with confidence (Clauset et al., 2009; Sornette, 2009). A problem related to the analysis is the truncation effect, which results in "tails" forming at one or both ends of the examined dataset, and then deviates from a typical power-law trend (Sornette, 2009;

Torabi and Berg, 2011). The truncation effect results in underestimation of the frequency of minor faults and is related to the resolution limitation of the sampling methods applied (Torabi and Berg, 2011). A log-normal distribution trend has often been determined when all measurements are analyzed, but if the "tail" members are removed, a power-law distribution could be characterized with a straight line forming in the log EF-log thickness plots (e.g. Figure 3.3.7 B and D, 3.4.8 B, 3.4.9 B, 3.5.9 B). The easiest approach to this problem might be to state that a power-law distribution of the dataset is plausible and to rule out the other hypotheses (Clauset et al., 2009).

A dataset of 1133 average fault core thickness and fault displacement measurements from previously published results have been compiled in this project by Torabi and Berg (2011) (Table 9). To recognize the distribution trend of this dataset, univariate analysis was performed and EF-plots were created. Due to great scatter in the measurements, only two EF-plots concerning the log EF-log thickness and log EF-log displacement was plotted. All fault core thickness and displacement measurements from this project have been plotted on EF-plots, for comparison with the published results. The EF-plots regarding the fault core thickness are illustrated in Figure 4.3.1 A-B, while the displacement plots are illustrated in Figure 4.3.2 A-B.

The EF-plots of the fault core thickness measurements on Figure 4.3.1 A-B appear to follow similar distribution trends, with the characteristic concave-down trend observed. Considering all measurements, including the "tail" members (black dashed circles on figure), a log-normal distribution has been correlated to best fit both plots. However, on both of the plots, two distinct straight segments can be observed within the data points, indicating two power-law trends can be suggested for both segments. If the "tails" are removed, two power-law distribution trend can be interpreted on each of the plots, displaying a strong coefficient of determination of $R^2 > 0.95$.

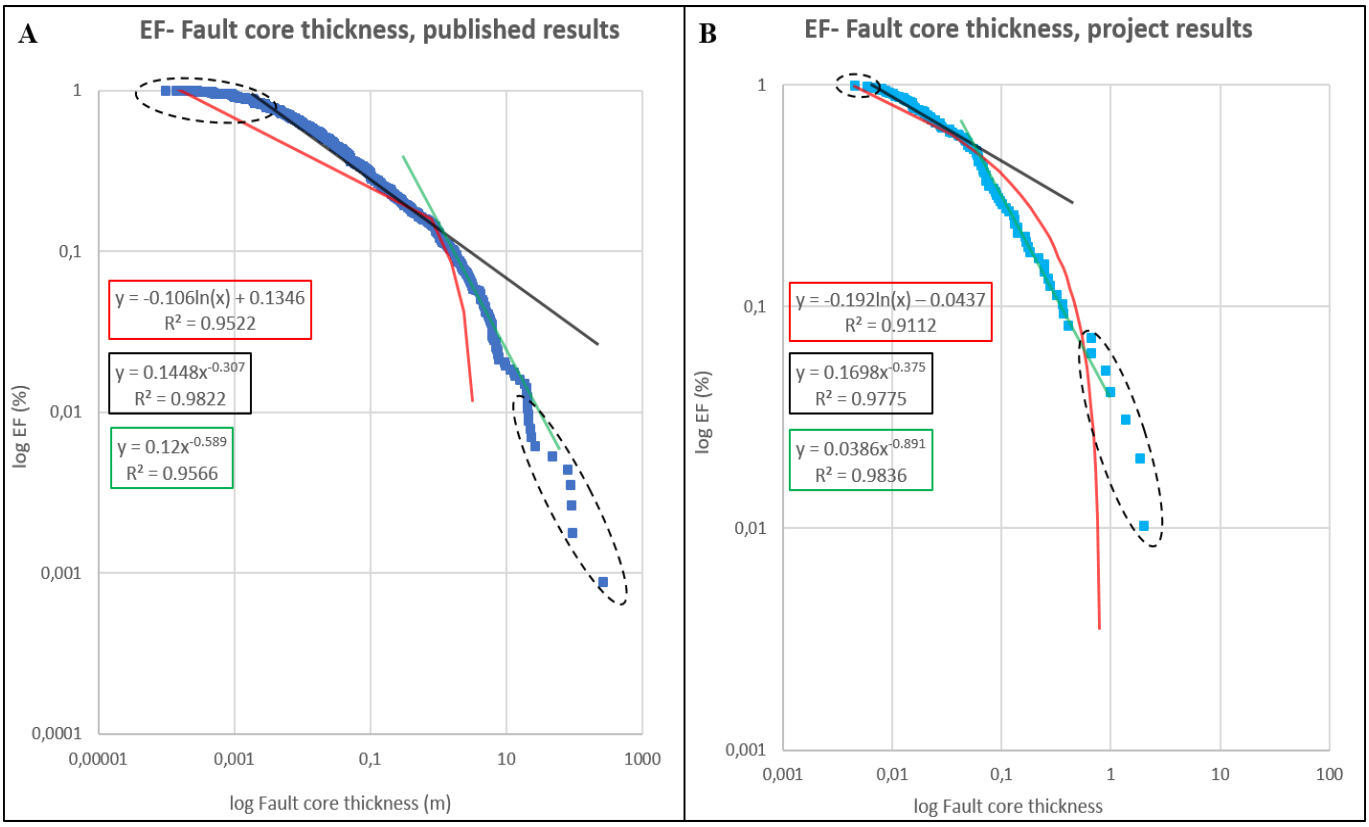

Figure 4.3.1: *EF-plots of the average fault core thickness from previously published results (**A**) and from this project (**B**). Both of the EF-plots have been correlated to best fit a log-normal- or two power-law distribution trends. The correlated functions and R^2 values are presented in the squares on the figure, following the same color code as the trend lines. The black dashed circles represents the endmembers or "tails".*

For the displacement measurements on Figure 4.3.2 A-B, similar distribution trends can also here be observed, with characteristic concave-down trends. For the measurements from this project, the concave-down trend is straighter compared to the published measurements. Considering all the measurements, including the "tail" members, a log-normal distribution has been correlated as the best fit of the data points. A lower R^2 is presented for the log-normal distribution in the project dataset, related to the straighter segment located. However, if the "tail" members are removed, a power-law distribution trend can be correlated for both of the plots. For the published dataset, two distinct straight segments can be observed, suggesting two power-law distribution trends within the data points. While for the project dataset, only one power-law distribution trend can be correlated for the straight segment, with a robust coefficient of determination of 0.9535. The differences in total number of power-law distribution trends, can be related to the amount and magnitude of data analyzed. For the published dataset a total of 1133 measurements has been analyzed, compared to the 55 measurements in this project dataset.

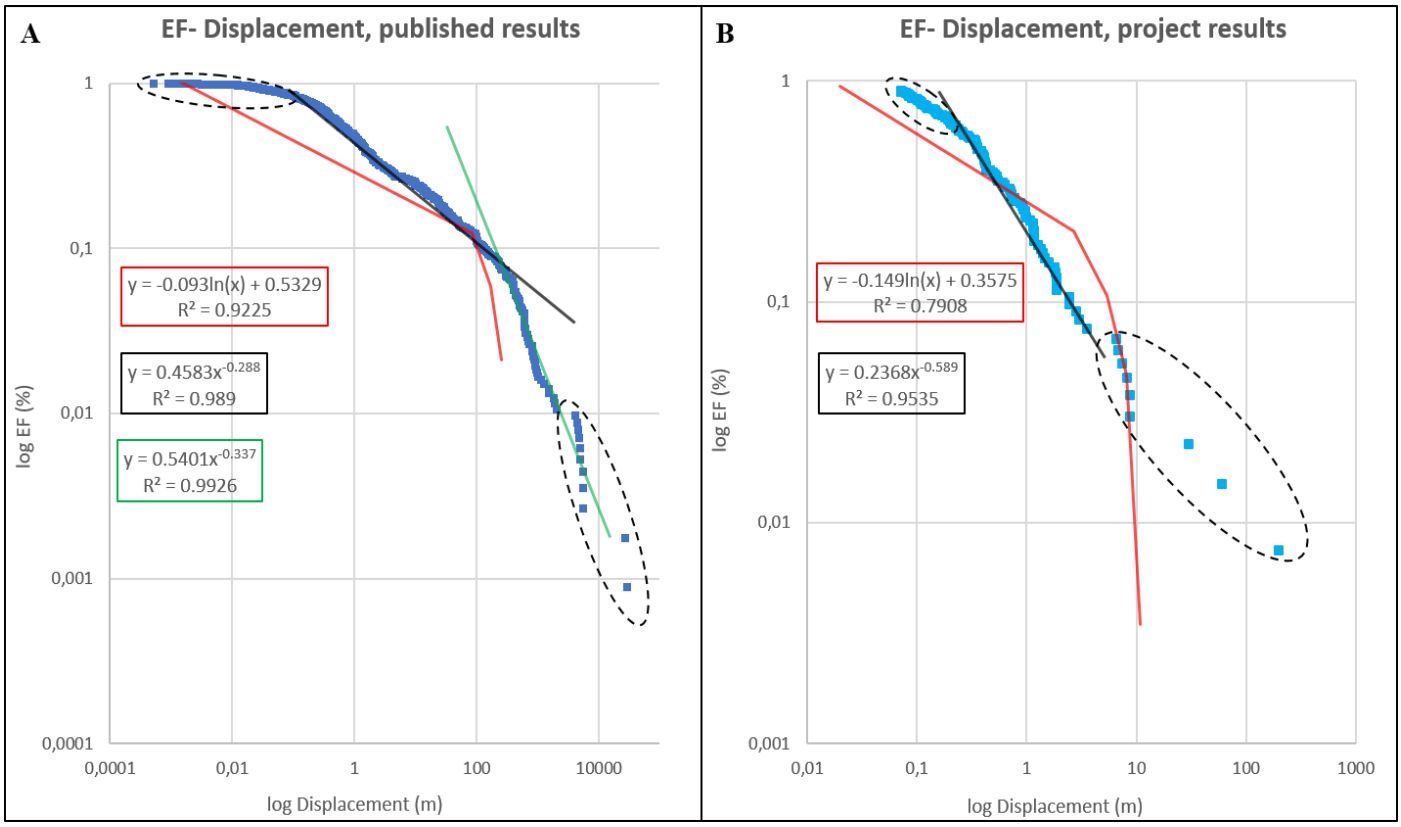

Figure 4.3.2: *EF-plots of the average displacement from previously published results (**A**) and from this project (**B**). For the published measurements the data points have been to best fit a log-normal or two power-law distribution trends. While the project measurements have been correlated to best fit a log-normal or one power-law distribution trend. The correlated functions and R^2 values are presented in the squares on the figure, following the same color code as the trend lines. The black dashed circles represents the endmembers or "tails".*

4.3.2. Fault core thickness versus fault displacement

The fault core thickness-displacement relationship in the literature has often been investigated using average measurements and the plots presenting the relationship show average data points. In this project, the relationship has been investigated using exact measurements of the core thickness and displacement from the same levels along the fault heights. This method was chosen to capture the variations in fault core thickness and displacement along the fault height. Some of the plotted data are based on average fault core thickness measurements, and these data points represents faults where the displacement data are based on previous studies in the literature (R-191 Canyon (Foxford et al., 1996; Foxford et al., 1998), Hidden Canyon Fault (Berg and Skar, 2005; Johansen and Fossen, 2008) and Cache Valley main fault (Braathen et al., 2012; Alikarami et al., 2013)). This method has resulted in a dataset of 133 measurements of fault core thickness with a known displacement, in both siliciclastic rocks and carbonates. A log-log plot of the measurements is illustrated in Figure 4.3.3. Previously

plots illustrating the relationship, have been plotted with the fault core thickness on the X-axis (e.g. Evans, 1990; Knott et al., 1996; van der Zee et al., 2008; Torabi and Berg, 2011), but from field observations and completed measurements in this project, the core thickness is likely to be affected by fault displacement (Figure 3.3.6 and 4.1.1). Hence, in this project, the relationship is presented with the fault core thickness on the Y-axis and the displacement on the X-axis. The range of data covers seven orders of magnitude for the displacement measurements, and six orders for the fault core thickness measurements, respectively. The core thickness-displacement relationship has been correlated to a power-law best fit ($T = 0.0839D^{0.7275}$), with a correlation coefficient of 0.6411.

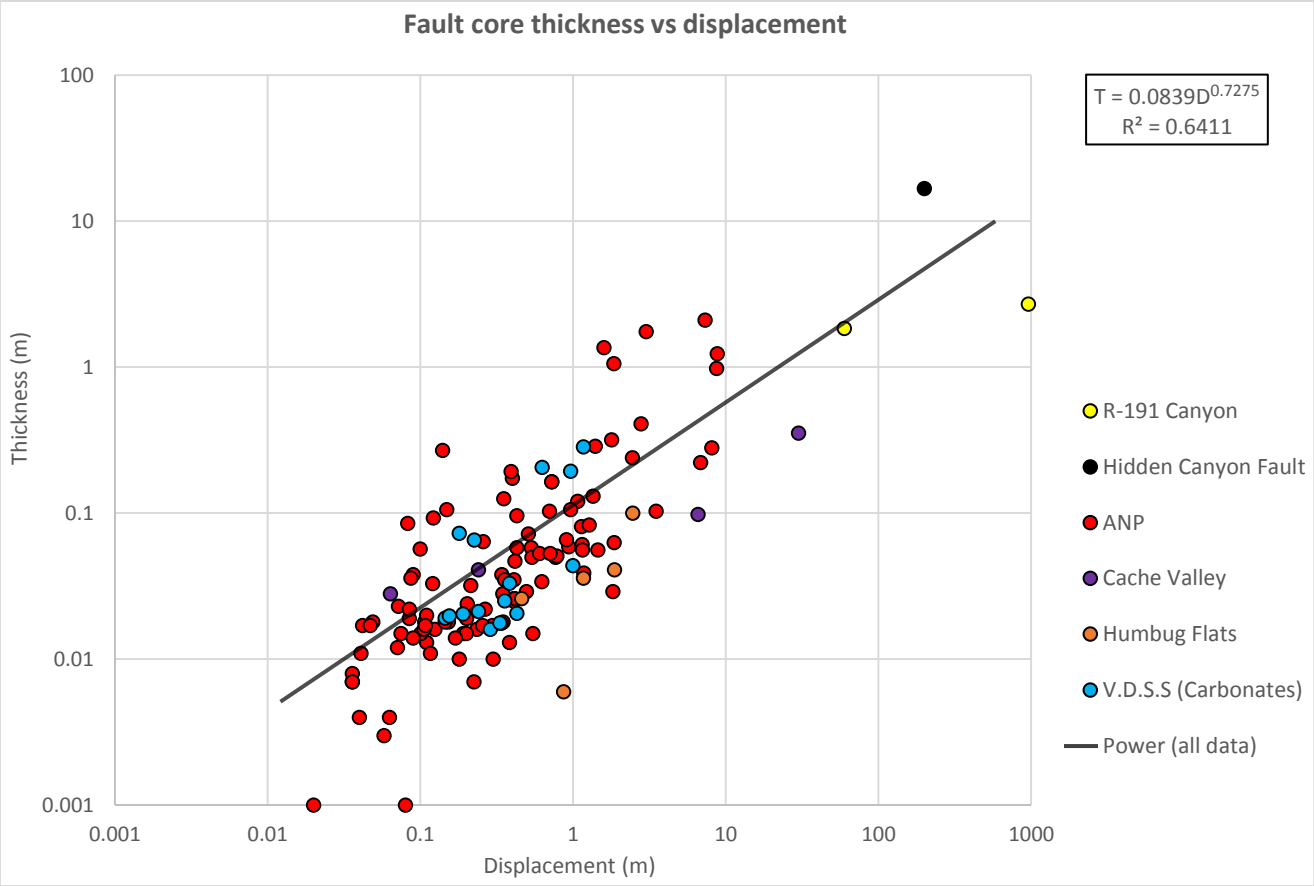

Figure 4.3.3: *Log-log plot of the 133 fault core thickness-displacement measurements from all the studied localities. The relationship shows a positive correlation with a power-law function and a R^2 value of 0.6411. V.D.S.S; Vallone di Santo Spirito.*

Since the fault core thickness-displacement relationship in the literature is examined using average measurements, a plot of the average measurements is illustrated in Figure 4.3.4. This plot has also been correlated to best fit a power-law function of $T = 0.0758D^{0.7321}$, with an associated regression of fit (R^2) of 0.7411. When comparing the two plots, the average plot improves the regression of fit for the relationship with exactly 0.1. This could indicate that the best approach to describe and examine the relationship is to use average measurements, instead of exact measurements. An uncertainty related to the average measurements are the variations in fault core thickness and displacement at the different

levels along the fault heights. Where the exact dataset captures these variations with multiple data points on the plot, the average dataset only computes one data point for the same values. This leads to examination and correlation of fewer data points on the average measurements and the variations are not captured, compared to the exact dataset. For comparison, the power-law function and trend line from Figure 4.3.3 are illustrated in Figure 4.3.4.

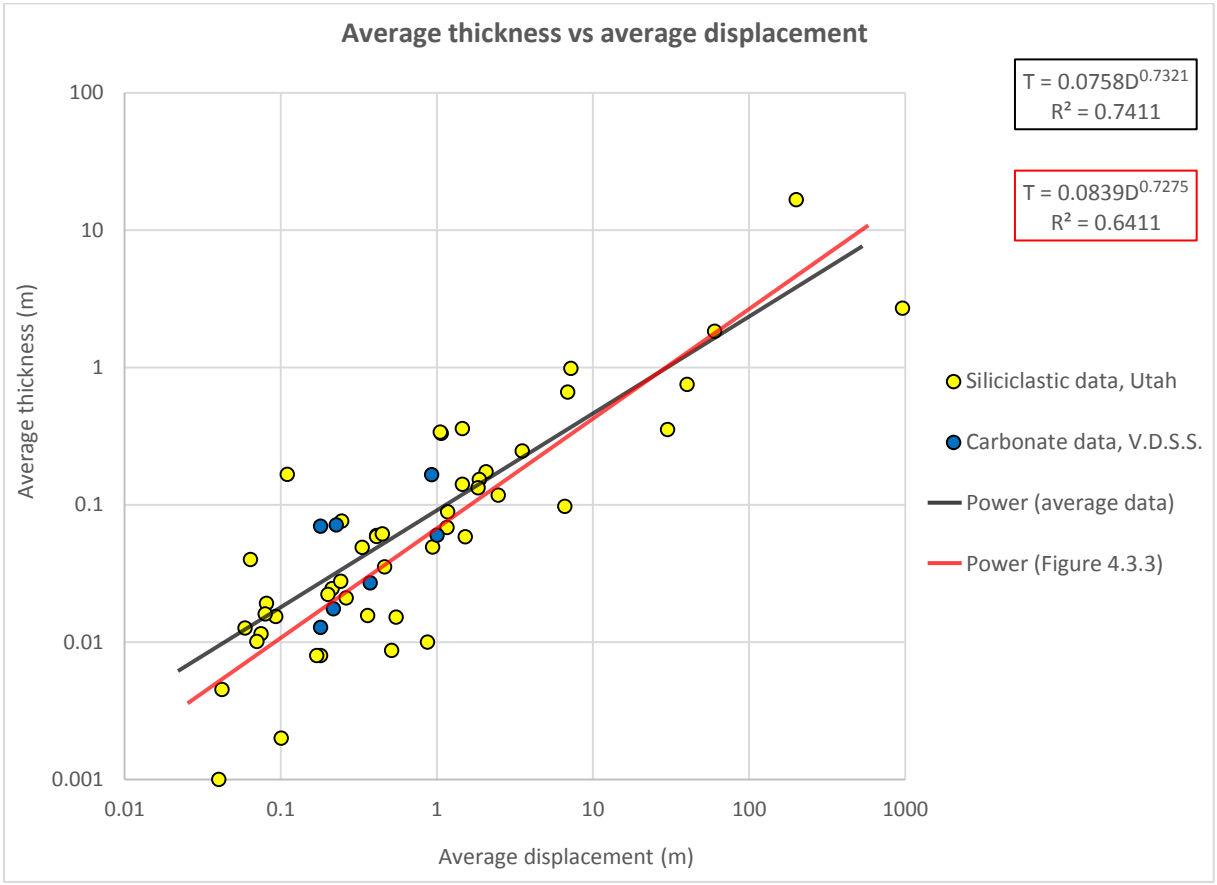

Figure 4.3.4: *Log-log plot illustrating the fault core thickness-fault displacement relationship using the average measurements. The power-law function of this plot displays a better fit to the relationship when comparing the R^2 value of the two power-law functions. V.D.S.S: Vallone di Santo Spirito.*

4.3.3. Comparison with previously published results

In the review paper on scaling relationship between fault attributes by Torabi and Berg (2011), a collection of different fault attribute datasets from previously published articles was examined and analyzed. The dataset regarding the fault core thickness and fault displacement have been compiled in this project. The dataset consists of measurements conducted in different lithologies and tectonic regimes. On Table 9 an overview of the compiled datasets is presented, showing which authors the measurements are collected by, their study areas and the examined faulted lithology.

Table 9: *Overview of previously published data, their study areas, and examined lithology. These datasets of fault core thickness and displacement have been compiled by Torabi and Berg (2011). Sst; sandstone*

Authors	Study area (-s)	Lithology
Bastesen and Braathen (2010)	Western Sinai, central Oman and Svalbard	Carbonates
Childs et al. (2009)	Taranaki, New Zealand and Lancashire, U.K	Poorly lithified sandstone
Childs et al. (2009)	West Asturian-Leonese zone, northern Spain	Crystalline rocks
Di Toro and Pennacchioni (2005)	Adamello batholith, southern Alps	Granite
Foxford et al. (1998)	Moab Fault transects, Utah	Sst and siliciclastic rocks
Shipton et al. (2005)	Big Hole Fault, San Rafael Swell, Utah	Sandstone
Shipton et al. (2006)	Mount Abbot, Sierra Nevada, California	Granite
Sperrevik et al. (2002)	Western Sinai	Sandstone-sandstone
Sperrevik et al. (2002)	Western Sinai	Sandstone-shale
Sperrevik et al. (2002)	Western Sinai	Shale-shale
Sperrevik et al. (2002)	Northumberland, U.K	Sandstone-sandstone
Sperrevik et al. (2002)	Northumberland, U.K	Sandstone-shale
Wibberley et al. (2008)	Pelvoux Massif, western Alps	Granite
Wibberley et al. (2008)	Median Tectonic Line, Japan	Mylonite
Wibberley et al. (2008)	Moine Thrust Belt, Scotland	Siliciclastic rocks
van der Zee and Urai (2005)	Miri, Sarawak, Malaysia	Sandstone-shale
van der Zee et al. (2008): Evans (1990)	Bismark Fault, southwestern Montana	Siliciclastic rocks
van der Zee et al. (2008)	Lodève Basin, France	Sandstone-shale
van der Zee et al. (2008)	Lodève Basin, France	Sandstone-shale

All measurements in the compiled dataset (Table 9), combined with this projects dataset, have been analyzed to examine the fault core thickness-displacement relationship on a large, global dataset. On Figure 4.3.5 a log-log plot presenting the compiled dataset and this project dataset are illustrated. The plot has been correlated to best fit a power-law relationship ($T = 0.026D^{0.7558}$), with a robust R^2 value of 0.7390 for the global dataset. The datasets analyzed covers different lithologies and tectonic setting, and the dataset displays a solid relationship for measurements of several individual data sets. However, a global dataset involving several datasets and one power-law function would have several advantages and disadvantages, compared to individual datasets. A global dataset would contain data from a range of tectonic settings and regimes, composed of different fault geometries, architecture and

different biases related to the measurements (Shipton et al., 2006). Another disadvantage with a global dataset is the lack of a common and clear definition of the fault core thickness and its boundaries (Shipton et al., 2006; Childs et al., 2009; Torabi and Berg, 2011). This may lead to measurements completed in one study, could differ from another study, resulting in variations due to the subjectivity of the measurements. Additionally, not all components of a given definition may be present at all localities (Shipton et al., 2006). Advantages of combining several individual datasets into one global dataset are the range of data, covering several orders of magnitude, both for fault core thickness and displacement data. This range of data and the multiple data points reduces the influence of scattering in the data.

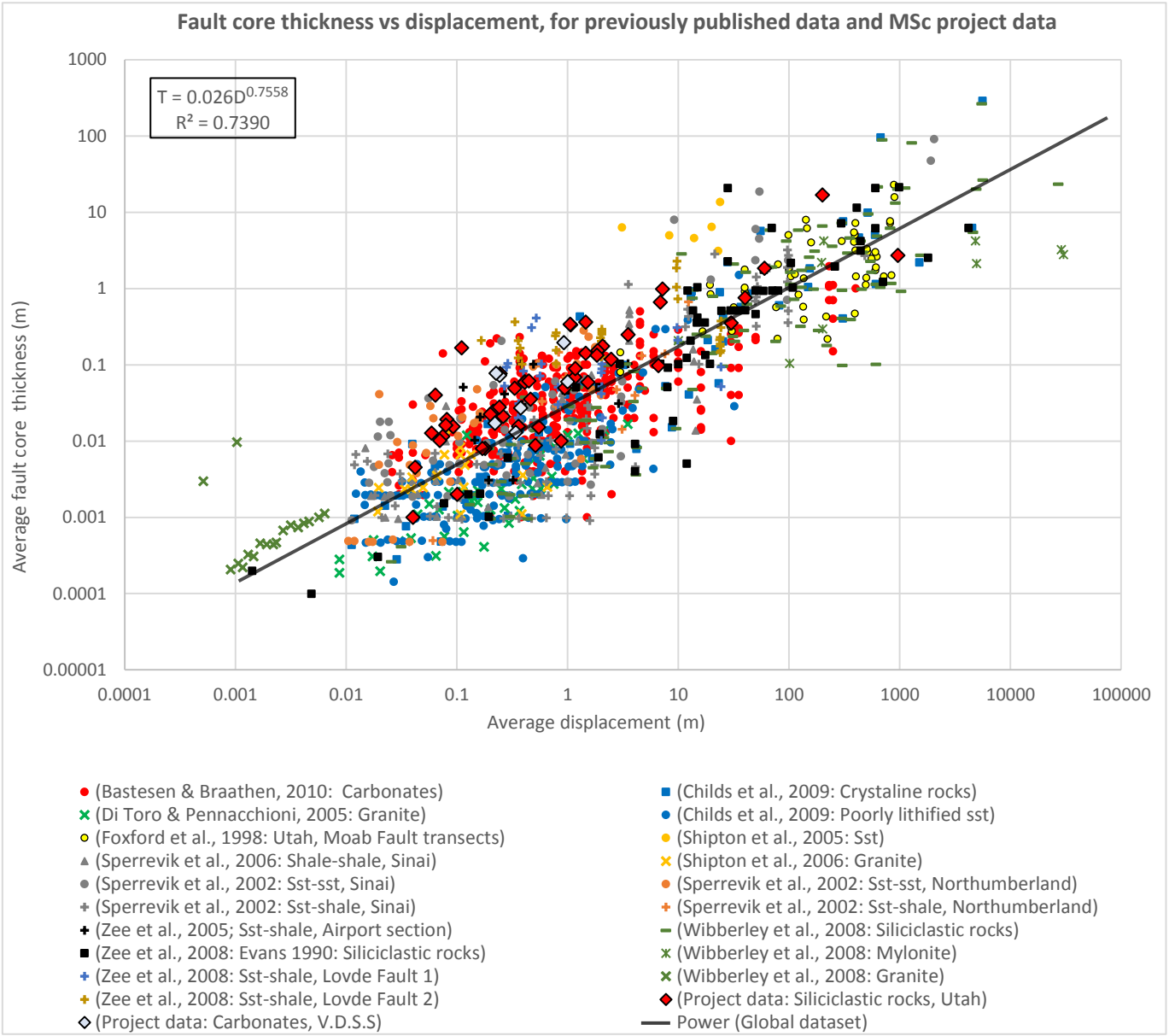

Figure 4.3.5: *Log-log plot of the average fault core thickness and displacement measurements from previously published- and the project results. The dataset has been correlated to best fit a power-law relationship, and a strong correlation (R^2 of 0.7390) have been found for the relationship.*
V.D.S.S; Vallone di Santo Spirito

Another approach in gathering a global dataset may be to sort the individual datasets based on the studied, faulted lithology. This implies that one single power-law function does not fit a global dataset, and the relationship could vary based on lithology and tectonic setting (Wibberley et al., 2008; Kolyukhin and Torabi, 2012). The plot on Figure 4.3.6 A, shows the fault core thickness-displacement relationship of the compiled datasets, based on the faulted lithology. The different datasets are all correlated to best fit power-law functions. The relationship between the fault core thickness and displacement for the siliciclastic based measurements have been correlated to best fit the power law function of $T = 0.0232D^{0.838}$, with a regression of fit of 0.7643 (black trend line on Figure 4.3.6 A). The crystalline measurements cover the greatest orders of magnitude, but also show the best regression of fit, $R^2 = 0.8218$, with a core thickness-displacement relationship following a power-law function of $T = 0.0163D^{0.7188}$ (green trend line of Figure 4.3.6 A). A great scatter in the data points are observed within the carbonate measurements, and the fault core thickness-displacement relationship have been correlated to best fit a power-law function of $T = 0.0306D^{0.4822}$, with an associated goodness of regression fit of 0.4148 (red trend line of Figure 4.3.6 A). The carbonate dataset consists of only one set of published data, all recorded by Bastesen and Braathen (2010), and provides no diversity to the global dataset which would be beneficial. However, on Figure 4.3.6 B, the results from this project is included in the lithological based datasets. For the carbonate dataset the addition of another dataset, show little influence on the global dataset. The added dataset from this project consists of few measurements but improves the slope and regression by 0.0002. The addition of another dataset gives a more diverse dataset to be examined, and the combined datasets show a positive correlation to the core thickness-displacement relationship. The inclusion of the dataset from this project in the siliciclastic dataset also shows a marginal influence on the global dataset. The dataset improves the slope and regression by 0.0049. The small positive impact of the additional datasets suggests that given a large dataset covering a great range of magnitudes, the correlation between the fault core thickness and displacement for a given study area might improve. The lithological based dataset also indicates that one power-law function does not fit a global dataset, where lithological differences are not emphasized. This shows that the fault core thickness-displacement relationship is affected by the faulted lithology and a stronger positive regression can be found when sorting the different datasets based on lithology.

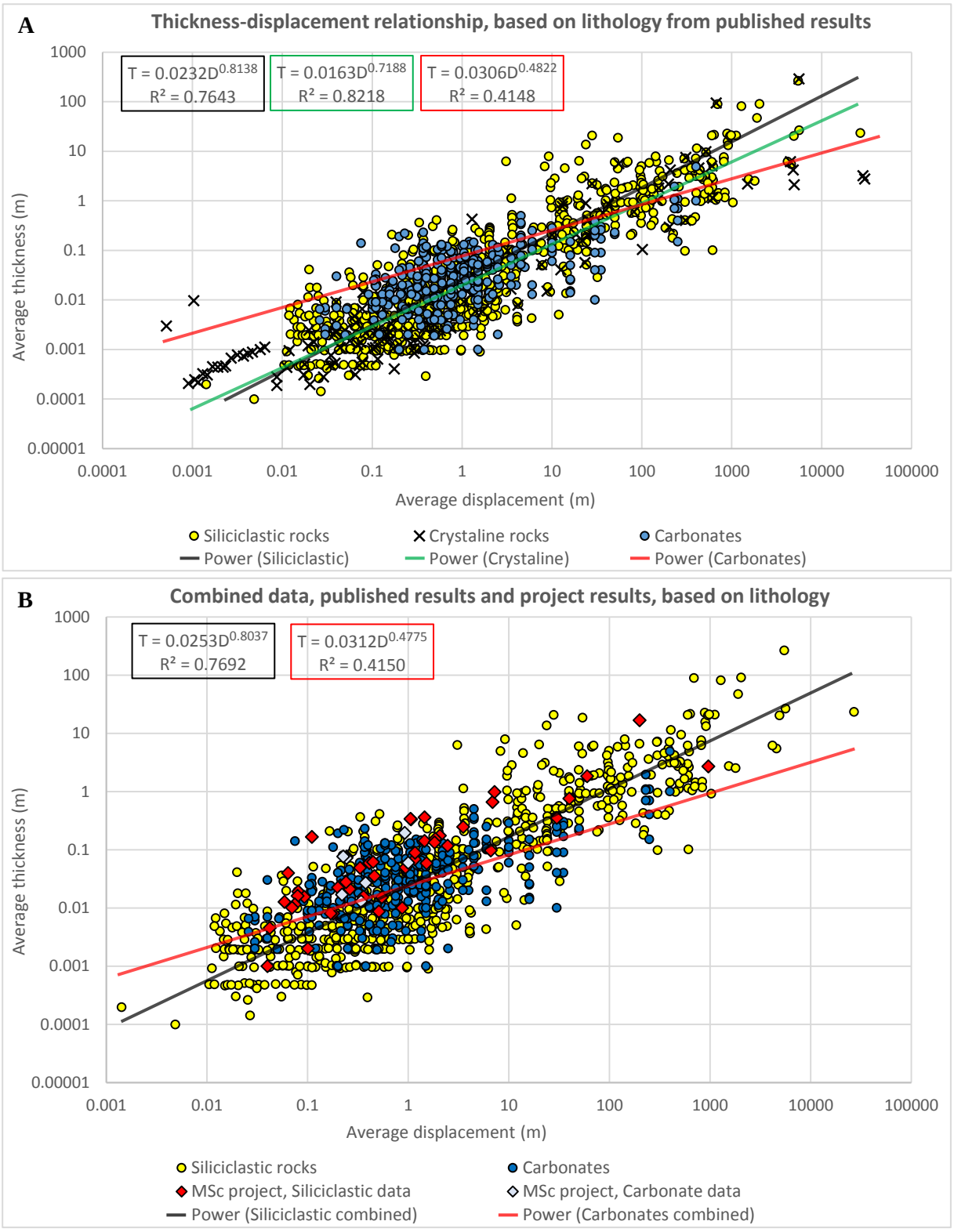

Figure 4.3.6: *(**A**) Log-log plot illustrating the fault core thickness-displacement relationship of the published results which have been sorted based on lithology. The plot exhibits similar scaling relationships between the two fault attributes. (**B**) When the measurements from this project are included in the siliciclastic and carbonate datasets, the regression value of the core thickness-displacement relationship is slightly improved with 0.0049 and 0.0002, respectively. This indicates that the collected measurements from this project fit the global dataset, and are improving the dataset when included.*

4.4. Implications for fault architecture and fault core structures

Faults in reservoir modeling have commonly been regarded as 2D planes with transmissibility multipliers, but should rather be handled as 3D fault zones with a complex architecture and geometry (Fredman et al., 2007; Braathen et al., 2009). Assuming faults as 3D rock volumes, with different petrophysical properties located within the fault zone, a potentially more realistic structural and fluid flow model can be developed, which would be beneficial in reservoir characterization and well-planning. In a faulted reservoir, the largest faults are usually detected and interpreted on seismic data, but minor faults and fractures are not detected due to the sub-seismic scale of the structures, and can only be detected in well- or core plugs. However, these samples only represent a small fraction of the entire fault and fracture system. The connectivity of faults and fractures plays a major role in the vertical and horizontal fluid flow within the reservoir. Hence, detailed studies on field analogs of faulted reservoirs are necessary to collect additional information about the fault and fracture distribution at the sub-seismic scale and to improve flow models.

In reservoir modeling, the width and petrophysical properties of fault zones are necessary in order to run fluid flow simulations (Sperrevik et al., 2002; Fredman et al., 2007; Braathen et al., 2009). The fault core is regarded as the key for estimating the sealing potential of a fault zone, but great lateral variations in core thickness and different fault rocks in the core affect the estimation of input parameters in the reservoir model. Different fault rocks in the fault core have different effects on the permeability of the fault, where fault gouge and shale smear have been reported to reduce cross fault permeability (Færseth et al., 2007). While undeformed host rock lenses incorporated in the fault core represents an uncertainty in the sealing potential of faults and could constitute a flow path across the faults (Fredman et al., 2007; Lindanger et al., 2007; Bastesen et al., 2013). However, the thickness of the fault core could vary by a factor of 27 over relatively short distances along the fault height, and these variations are affected by several factors, such as displacement and lithology. The power-law relationship of the core thickness and displacement examined in this project for different lithologies, it could be possible to develop a method to improve the evaluation of the maximum and minimum core thickness for faults in different lithologies for a given displacement value. Furthermore, the core thickness-displacement relationship investigated on Figure 4.3.3, where exact fault height measurements were examined, could be a start developing a model or method to estimate exact fault core thickness for a given displacement. This would be beneficial in understanding fault evolution and fault architecture, and to better estimate the major variations in core thickness and complexity observed in this thesis.

5. Conclusions and further work

5.1. Conclusions

The main aim of this project has been to gain further understanding of fault core geometry and structures, as well as the variations in fault core thickness in both siliciclastic and carbonate rocks. Furthermore, the datasets collected created a unique opportunity to statistically analyze both univariate distributions of fault core thickness and displacement and their relationship. These aims were reached through field-based investigations in Utah and the Majella Mountain, using field- and picture measurements. A total of 1564 fault core thickness- and 128 displacement measurements have been gathered in this project, documenting the variations in core thickness and displacement along the fault height. The data from this project were then compared with data from previously published articles to examine the relationship on a bigger scale. From the results and discussion presented, the following conclusions are drawn:

- Univariate analysis completed using EF-plots on the fault core thickness and displacement measurements fit best to a power-law distribution trend if the endmembers or "tail" members on the log-normal distributed EF-plots are removed.
- The minor faults measured in this project shows great lateral variations in core thickness, and they also display a relatively greater core thickness compared to larger faults.
- Fault core complexity observed (i.e. lenses, changing fault rocks, linkage or splay faults) also influence the variations in core thickness, compared to planar or isolated faults.
- Lithological effects on the fault core thickness have been observed and documented in this project. The collected data supports that average fault core thickness in carbonates are generally wider within similar displacement scales when compared with siliciclastic rocks.
- The fault core thickness is suggested to be controlled by several interconnected factors, such as the fault geometry, interactions and/or connection with surrounding faults, displacement, lithology and the competency contrasts between faulted layers and the tectonic regime.
- Variations in fault core thickness have been documented between different fault types in Vallone di Santo Spirito. These variations could be related to the size relationship between the fault types or the overall stress field responsible for the initiation and propagation of the faults.
- Analyzing the fault core thickness-displacement relationship, two different approaches have been conducted to investigate the relationship. The first method uses exact fault height measurements of the fault core thickness and displacement, and the relationship has been correlated to best fit the power-law function of $T = 0.0839D^{0.7275}$, with a R^2 value of 0.6411. While the second method uses average measurements, and the power-law relationship

$T = 0.0758D^{0.7321}$ have been correlated to best describe the relationship, with a R^2 value of 0.7411.

- Examining average measurements, a stronger regression of fit have been calculated, but an issue related to average data is the variations in core thickness and displacement along the fault height, investigated in this project.
- Analyzing a global dataset, composed of compiled datasets of previously published results and the project datasets, the core thickness-displacement relationship has been correlated to best fit the power-law function of $T = 0.026D^{0.7558}$, with a strong R^2 of 0.7390. The global dataset includes data collected from different tectonic regimes and lithologies.
- Sorting the global dataset based on lithology, an improved core thickness-displacement relationship has been documented. These lithological based relationships show that a more robust relationship can be found sorting the dataset based on lithology and that one power-law function does not fit a global dataset, where lithological differences are not emphasized.
- The fault core thickness measurements completed in this project, support a fault model where the increase in core thickness, with respect to displacement, is greater for minor faults compared to major faults.

5.2. Suggestions for further work

This study has mainly focused on variations in fault core thickness along fault height, and the relationship between core thickness and displacement in siliciclastic and carbonate rocks. The methods used in this project, give an opportunity to investigate the vertical variations in fault core thickness along fault height and examine different factors affecting the thickness. There are several questions and aspects related to fault attributes, fault core structures, and fault architecture, which could be further studied. A start may be to collect a carbonate dataset, where displacement is easily observed and measurable. When comparing the fault core thickness-displacement relationship for different lithologies, a large dataset from each lithology is required to better examine the differences. These measurements could further be compared to previously published results, to increase the global database and to examine the relationship on a larger scale. Additionally, it would be interesting to collect fault core thickness and displacement data from crystalline/basement rocks, to increase the diversity of the studied dataset. It would also be interesting to collect fault core thickness and displacement measurements from a variety of tectonic regimes (e.g. rift settings, salt-related deformation, fold-and-thrust belts) to compare the relationship in these regimes and to examine the connection with deformation history and the geometry of the fault attributes.

Another interesting aspect, not related to scaling relationships, would be to measure and analyze petrophysical properties of fault rocks situated in the fault core for different faulted lithologies and to

connect these properties to the thickness variations along the fault core, as found in this study. This would be interesting considering fault sealing analysis and reservoir modeling, where the sealing capacity is related to the impermeability of the fault core. This could further be investigated by measuring the minimum core thickness properties and correlating them with displacement. Understanding the petrophysical properties of the minimum core thickness and how it's related to displacement and faulted lithology, could be a better indicator of the fault sealing capacity.

6. References

Accotto, C., Coscarelli, F., Malerba, E., Palazzin, G., and Festa, A., 2014, Geological map of the Aventino river valley (Eastern Majella, Central Italy) Universita' Di Torino, Dipartimento di Scienze della Terra

Agosta, F., Alessandroni, M., Antonellini, M., Tondi, E., and Giorgioni, M., 2010a, From fractures to flow: A field-based quantitative analysis of an outcropping carbonate reservoir: Tectonophysics, v. 490, p. 197-213.

Agosta, F., Alessandroni, M., Tondi, E., and Aydin, A., 2010b, Oblique normal faulting along the northern edge of the Majella anticline, central Italy: Inferences on hydrocarbon migration and accumulation: Journal of Structural Geology, v. 32, p. 1317-1333.

Agosta, F., and Aydin, A., 2006, Architecture and deformation mechanism of a basin-bounding normal fault in Mesozoic platform carbonates, central Italy: Journal of Structural Geology, v. 28, p. 1445-1467.

Alikarami, R., Torabi, A., Kolyukhin, D., and Skurtveit, E., 2013, Geostatistical relationships between mechanical and petrophysical properties of deformed sandstone: International Journal of Rock Mechanics and Mining Sciences, v. 63, p. 27-38.

Antonellini, M., Tondi, E., Agosta, F., Aydin, A., and Cello, G., 2008, Failure modes in deep-water carbonates and their impact for fault development: Majella Mountain, Central Apennines, Italy: Marine and Petroleum Geology, v. 25, p. 1074-1096.

Aydin, A., Agosta, F., and Tondi, E., 2005, Types, mechanisms and distribution of the faults in platform carbonate along the leading edge of the Maiella thrust sheet around Fara San Martino, central Italy: Stanford Rock Fracture Project 2005, v. 16B.

Aydin, A., Antonellini, M., Tondi, E., and Agosta, F., 2010, Deformation along the leading edge of the Maiella thrust sheet in central Italy: Journal of Structural Geology, v. 32, p. 1291-1304.

Aydin, A., Borja, R. I., and Eichhubl, P., 2006, Geological and mathematical framework for failure modes in granular rock: Journal of Structural Geology, v. 28, p. 83-98.

Aydin, A., and Johnson, A. M., 1978, Development of faults as zones of deformation bands and as slip surfaces in sandstone, Rock Friction and Earthquake Prediction, Springer, p. 931-942.

Barbeau, D., 2003, A flexural model for the Paradox Basin: implications for the tectonics of the Ancestral Rocky Mountains: Basin Research, v. 15, p. 97-115.

Barnett, J. A., Mortimer, J., Rippon, J. H., Walsh, J. J., and Watterson, J., 1987, Displacement geometry in the volume containing a single normal fault: AAPG Bulletin, v. 71, p. 925-937.

Bastesen, E., and Braathen, A., 2010, Extensional faults in fine grained carbonates–analysis of fault core lithology and thickness–displacement relationships: Journal of Structural Geology, v. 32, p. 1609-1628.

Bastesen, E., Braathen, A., and Skar, T., 2013, Comparison of scaling relationships of extensional fault cores in tight carbonate and porous sandstone reservoirs: Petroleum Geoscience, v. 19, p. 385-398.

Berg, S. S., and Skar, T., 2005, Controls on damage zone asymmetry of a normal fault zone: outcrop analyses of a segment of the Moab fault, SE Utah: Journal of Structural Geology, v. 27, p. 1803-1822.

Billi, A., Salvini, F., and Storti, F., 2003, The damage zone-fault core transition in carbonate rocks: implications for fault growth, structure and permeability: Journal of Structural geology, v. 25, p. 1779-1794.

Bird, P., 2002, Stress direction history of the western United States and Mexico since 85 Ma: Tectonics, v. 21, p. 1014.

Bjørlykke, K., Høeg, K., Faleide, J. I., and Jahren, J., 2005, When do faults in sedimentary basins leak? Stress and deformation in sedimentary basins; examples from the North Sea and Haltenbanken, offshore Norway: AAPG bulletin, v. 89, p. 1019-1031.

Braathen, A., Ogata, K., Bastesen, E., and Gabrielsen, R., Fractures and structural elements of extensional faults; importance for seal bypass systems in sandstone reservoir successions, *in* Proceedings Proceedings of the 3rd international conference on fault and top seals—from characterization to modelling, Montepellier, France, 2012.

Braathen, A., Tveranger, J., Fossen, H., Skar, T., Cardozo, N., Semshaug, S., Bastesen, E., and Sverdrup, E., 2009, Fault facies and its application to sandstone reservoirs: AAPG Bulletin, v. 93, p. 891-917.

Bump, A. P., and Davis, G. H., 2003, Late Cretaceous–early Tertiary Laramide deformation of the northern Colorado Plateau, Utah and Colorado: Journal of Structural Geology, v. 25, p. 421-440.

Byerlee, J., and Summers, R., A note on the effect of fault gouge thickness on fault stability, *in* Proceedings International Journal of Rock Mechanics and Mining Sciences & Geomechanics Abstracts1976, Volume 13, Elsevier, p. 35-36.

Caine, J. S., Evans, J. P., and Forster, C. B., 1996, Fault zone architecture and permeability structure: Geology, v. 24, p. 1025-1028.

Cartwright, J. A., Trudgill, B. D., and Mansfield, C. S., 1995, Fault growth by segment linkage: an explanation for scatter in maximum displacement and trace length data from the Canyonlands Grabens of SE Utah: Journal of Structural Geology, v. 17, p. 1319-1326.

Casabianca, D., Bosence, D., and Beckett, D., 2002, Reservoir potential of Cretaceous platform-margin breccias, central Italian Appenines Journal of Petroleum Geology, v. 25, p. 179-202.

Childs, C., Manzocchi, T., Walsh, J. J., Bonson, C. G., Nicol, A., and Schöpfer, M. P., 2009, A geometric model of fault zone and fault rock thickness variations: Journal of Structural Geology, v. 31, p. 117-127.

Choi, J.-H., Edwards, P., Ko, K., and Kim, Y.-S., 2016, Definition and classification of fault damage zones: a review and a new methodological approach: Earth-Science Reviews, v. 152, p. 70-87.

Clark, R., and Cox, S., 1996, A modern regression approach to determining fault displacement-length scaling relationships: Journal of Structural Geology, v. 18, p. 147-152.

Clark, R., Cox, S., and Laslett, G., 1999, Generalizations of power-law distributions applicable to sampled fault-trace lengths: model choice, parameter estimation and caveats: Geophysical Journal International, v. 136, p. 357-372.

Clauset, A., Shalizi, C. R., and Newman, M. E., 2009, Power-law distributions in empirical data: SIAM review, v. 51, p. 661-703.

Cowie, P. A., and Shipton, Z. K., 1998, Fault tip displacement gradients and process zone dimensions: Journal of Structural Geology, v. 20, p. 983-997.

Davatzes, N., and Aydin, A., 2003, Overprinting faulting mechanisms in high porosity sandstones of SE Utah: Journal of Structural Geology, v. 25, p. 1795-1813.

Davatzes, N. C., Aydin, A., and Eichhubl, P., 2003, Overprinting faulting mechanisms during the development of multiple fault sets in sandstone, Chimney Rock fault array, Utah, USA: Tectonophysics, v. 363, p. 1-18.

Davatzes, N. C., Eichhubl, P., and Aydin, A., 2005, Structural evolution of fault zones in sandstone by multiple deformation mechanisms: Moab fault, southeast Utah: Geological Society of America Bulletin, v. 117, p. 135-148.

DeCelles, P. G., 2004, Late Jurassic to Eocene evolution of the Cordilleran thrust belt and foreland basin system, western USA: American Journal of Science, v. 304, p. 105-168.

Di Cuia, R., Shakerley, A., Masini, M., and Casabianca, D., 2009, Integrating outcrop data at different scales to describe fractured carbonate reservoirs: example of the Maiella carbonates, Italy: First Break, v. 27, p. 45-55.

Di Luzio, E., Saroli, M., Esposito, C., Bianchi-Fasani, G., Cavinato, G., and Scarascia-Mugnozza, G., 2004, Influence of structural framework on mountain slope deformation in the Maiella anticline (Central Apennines, Italy): Geomorphology, no. 3, p. 417-432.

Di Toro, G., and Pennacchioni, G., 2005, Fault plane processes and mesoscopic structure of a strong-type seismogenic fault in tonalites (Adamello batholith, Southern Alps): Tectonophysics, v. 402, p. 55-80.

Doelling, H. H., 1985, Geology of Arches National Park (Utah), Utah Geological & Mineral Survey, Salt Lake City UT.

Doelling, H. H., 1988, Geology of Salt Valley Anticline and Arches National Park, Grand County, Utah. *In: Salt deformation in the Paradox Region*. (Doelling, H.H., Oviatt, C.G. & Huntoon, P.W. (Eds.)), Utah Geological and Mineral Survey, Salt Lake City UT, 58 p.:

Eberli, G. P., Bernoulli, D., Sanders, D., and Vecsei, A., 1993, From Aggradation to Progradation: The Maiella Platform, Abruzzi, Italy. In: Simo, T., Scott, R.W., Masse, J.P. (Eds.), Atlas of Cretaceous Carbonate Platforms: AAPG Memoir, p. 213-232.

Ellis, M. A., and Dunlap, W. J., 1988, Displacement variation along thrust faults: Implications for the development of large faults: Journal of Structural Geology, v. 10, p. 183-192.

Engelder, J. T., 1974, Cataclasis and the generation of fault gouge: Geological Society of America Bulletin, v. 85, p. 1515-1522.

English, J. M., and Johnston, S. T., 2004, The Laramide orogeny: what were the driving forces?: International Geology Review, v. 46, p. 833-838.

Evans, J. P., 1990, Thickness-displacement relationships for fault zones: Journal of Structural Geology, v. 12, p. 1061-1065.

Evans, J. P., Forster, C. B., and Goddard, J. V., 1997, Permeability of fault-related rocks, and implications for hydraulic structure of fault zones: Journal of Structural Geology, v. 19, p. 1393-1404.

Faulkner, D., Mitchell, T., Jensen, E., and Cembrano, J., 2011, Scaling of fault damage zones with displacement and the implications for fault growth processes: Journal of Geophysical Research: Solid Earth, v. 116.

Festa, A., Accotto, C., Coscarelli, F., Malerba, E., and Palazzin, G., 2014, Geology of the Aventino River Valley (eastern Majella, central Italy): Journal of Maps, v. 10, p. 584-599.

Fisher, Q., and Knipe, R. J., 1998, Fault sealing processes in siliciclastic sediments: Geological Society, London, Special Publications, v. 147, p. 117-134.

Foos, A., 1999, Geology of the Colorado Plateau: Geology Field Trip Guides by Anabelle Foos, University of Akron. Available online at: http://www2. nature. nps. gov/geology/education.

Fossen, H., and Bale, A., 2007, Deformation bands and their influence on fluid flow: AAPG Bulletin, v. 91, p. 1685-1700.

Fossen, H., and Hesthammer, J., 2000, Possible absence of small faults in the Gullfaks Field, northern North Sea: implications for downscaling of faults in some porous sandstones: Journal of Structural Geology, v. 22, p. 851-863.

Fossen, H., Schultz, R. A., Shipton, Z. K., and Mair, K., 2007, Deformation bands in sandstone: a review: Journal of the Geological Society, v. 164, p. 755-769.

Foxford, K., Garden, I., Guscott, S., Burley, S., Lewis, J., Walsh, J., and Watterson, J., 1996, The field geology of the Moab Fault: Geology and Resources of the Paradox Basin, Utah Geological Association Publication 25, p. 265-283.

Foxford, K., Walsh, J., Watterson, J., Garden, I., Guscott, S., and Burley, S., 1998, Structure and content of the Moab fault zone, Utah, USA, and its implications for fault seal prediction: Geological Society, London, Special Publications, v. 147, p. 87-103.

Fredman, N., Tveranger, J., Semshaug, S., Braathen, A., and Sverdrup, E., 2007, Sensitivity of fluid flow to fault core architecture and petrophysical properties of fault rocks in siliciclastic reservoirs: a synthetic fault model study: Petroleum Geoscience, v. 13, p. 305-320.

Færseth, R. B., 2006, Shale smear along large faults: continuity of smear and the fault seal capacity: Journal of the Geological Society, v. 163, p. 741-751.

Færseth, R. B., Johnsen, E., and Sperrevik, S., 2007, Methodology for risking fault seal capacity: Implications of fault zone architecture: AAPG Bulletin, v. 91, p. 1231-1246.

Gabrielsen, R. H., Braathen, A., Kjemperud, M., and Valdresbråten, M. L. R., 2016, The geometry and dimensions of fault-core lenses: Geological Society, London, Special Publications, v. 439.

Ghisetti, F., and Vezzani, L., 2002, Normal faulting, extension and uplift in the outer thrust belt of the central Apennines (Italy): role of the Caramanico Fault: Basin Research, v. 14, p. 225-236.

Graham, B., Antonellini, M., and Aydin, A., 2003, Formation and growth of normal faults in carbonates within a compressive environment: Geology, v. 31, p. 11-14.

Hampson, G. J., 2010, Sediment dispersal and quantitative stratigraphic architecture across an ancient shelf: Sedimentology, v. 57, p. 96-141.

Hintze, L., and Kowallis, B., 2009, Geologic history of Utah: Brigham Young University Geology Studies Special Publication 9, Tech. rept. Brigham Young University, Salt Lake City, UT.

Hite, R. J., and Lohman, S. W., 1973, Geologic appraisal of Paradox basin salt deposits for water emplacement: US Geological Survey Open-File Report 2331-1258.

Johansen, T. E. S., and Fossen, H., 2008, Internal geometry of fault damage zones in interbedded siliciclastic sediments: Geological Society, London, Special Publications, v. 299, p. 35-56.

Johansen, T. E. S., Fossen, H., and Kluge, R., 2005, The impact of syn-faulting porosity reduction on damage zone architecture in porous sandstone: an outcrop example from the Moab Fault, Utah: Journal of Structural Geology, v. 27, p. 1469-1485.

Kim, Y.-S., Peacock, D. C., and Sanderson, D. J., 2004, Fault damage zones: Journal of Structural Geology, v. 26, p. 503-517.

Knipe, R. J., Jones, G., and Fisher, Q., 1998, Faulting, fault sealing and fluid flow in hydrocarbon reservoirs: an introduction: Geological Society, London, Special Publications, v. 147, p. 7-21.

Knott, S., 1994, Fault zone thickness versus displacement in the Permo-Triassic sandstones of NW England: Journal of the Geological Society, v. 151, p. 17-25.

Knott, S. D., Beach, A., Brockbank, P. J., Brown, J. L., McCallum, J. E., and Welbon, A. I., 1996, Spatial and mechanical controls on normal fault populations: Journal of Structural Geology, v. 18, p. 359-372.

Kolyukhin, D., and Torabi, A., 2012, Statistical analysis of the relationships between faults attributes: Journal of Geophysical Research: Solid Earth, v. 117 (B5).

Levander, A., Schmandt, B., Miller, M., Liu, K., Karlstrom, K., Crow, R., Lee, C.-T., and Humphreys, E., 2011, Continuing Colorado plateau uplift by delamination-style convective lithospheric downwelling: Nature, v. 472, p. 461-465.

Lindanger, M., Gabrielsen, R. H., and Braathen, A., 2007, Analysis of rock lenses in extensional faults: Norwegian Journal of Geology, v. 87, p. 361-372.

Lindsay, N., Murphy, F., Walsh, J., and Watterson, J., 1993, Outcrop studies of shale smears on fault surfaces: International Association of Sedimentologists Special Publication v. 15, p. 113-123.

Mandl, G., De Jong, L., and Maltha, A., 1977, Shear zones in granular material: Rock Mechanics, v. 9, p. 95-144.

Marchegiani, L., Van Dijk, J., Gillespie, P., Tondi, E., and Cello, G., 2006, Scaling properties of the dimensional and spatial characteristics of fault and fracture systems in the Majella Mountain, central Italy: Geological Society, London, Special Publications, v. 261, p. 113-131.

Masini, M., Bigi, S., Poblet, J., Bulnes, M., Di Cuia, R., and Casabianca, D., 2011, Kinematic evolution and strain simulation, based on cross-section restoration, of the Maiella Mountain: an analogue for oil fields in the Apennines (Italy): Geological Society, London, Special Publications, v. 349, p. 25-44.

Matheron, G., 1963, Principles of geostatistics: Economic Geology, v. 58, p. 1246-1266.

Meike, A., and Wenk, H.-R., 1988, A TEM study of microstructures associated with solution cleavage in limestone: Tectonophysics, v. 154, p. 137-148.

Morsilli, M., Rusciadelli, G., and Bosellini, A., 2002, Large-scale gravity-driven structures: control on margin architecture and related deposits of a Cretaceous Carbonate Platform (Montagna della Maiella, Central Apennines, Italy): Bollettino Società Geologica Italiana, Volume Speciale, p. 619-628.

Mutti, M., Bernoulli, D., Eberli, G. P., and Vecsei, A., 1996, Depositional geometries and facies associations in an Upper Cretaceous prograding carbonate platform margin (Orfento Supersequence, Maiella, Italy): Journal of Sedimentary Research, v. 66, p. 749-765.

Nemec, W., 2011, Geostatistics, Lecture notes: University of Bergen, Department of Earth Science p. 179.

Nenna, F., and Aydin, A., 2011, The formation and growth of pressure solution seams in clastic rocks: A field and analytical study: Journal of Structural Geology, v. 33, p. 633-643.

Nuccio, V. F., and Condon, S. M., 1996, Burial and thermal history of the Paradox Basin, Utah and Colorado, and petroleum potential of the Middle Pennsylvanian Paradox Formation: U.S. Geological Survey Bulletin 2000-O, p. 1-41.

Ogata, K., Senger, K., Braathen, A., and Tveranger, J., 2014, Fracture corridors as seal-bypass systems in siliciclastic reservoir-cap rock successions: Field-based insights from the Jurassic Entrada Formation (SE Utah, USA): Journal of Structural Geology, v. 66, p. 162-187.

Olig, S. S., Fenton, C. H., McCleary, J., and Wong, I. G., 1996, The earthquake potential of the Moab Fault and its relation to salt tectonics in the Paradox Basin, Utah: Huffman Jr., A.C., Lund, W.R., Godwin, L.H. (Eds), Geology and Resources of the Paradox Basin Utah Geological Association Guidebook, 25, p. 246-251.

Otsuki, K., 1978, On the relationship between the width of shear zone and the displacement along fault: Journal of the Geological Society of Japan v. 84, p. 661-669.

Peacock, D., Fisher, Q., Willemse, E., and Aydin, A., 1998, The relationship between faults and pressure solution seams in carbonate rocks and the implications for fluid flow: Geological Society, London, Special Publications, v. 147, p. 105-115.

Peacock, D., Knipe, R., and Sanderson, D., 2000, Glossary of normal faults: Journal of Structural Geology, v. 22, p. 291-305.

Peacock, D., and Sanderson, D., 1991, Displacements, segment linkage and relay ramps in normal fault zones: Journal of Structural Geology, v. 13, p. 721-733.

Peacock, D., and Sanderson, D. J., 1996, Effects of propagation rate on displacement variations along faults: Journal of Structural Geology, v. 18, p. 311-320.

Peacock, D. C., and Sanderson, D. J., 1992, Effects of layering and anisotropy on fault geometry: Journal of the Geological Society, v. 149, p. 793-802.

Pederson, J. L., Mackley, R. D., and Eddleman, J. L., 2002, Colorado Plateau uplift and erosion evaluated using GIS: GSA TODAY, v. 12, p. 4-10.

Pizzi, A., Falcucci, E., Gori, S., Galadini, F., Messina, P., Di Vincenzo, M., Esestime, P., Giaccio, B., Pomposo, G., and Sposato, A., 2010, Active faulting in the Maiella Massif (central Apennines, Italy): Geoacta, p. 57-73.

Robertson, E., 1983, Relationship of fault displacement to gouge and breccia thickness: Mining Engineering, v. 35, p. 1426-1432.

Rotevatn, A., and Fossen, H., 2012, Soft faults with hard tips: magnitude-order displacement gradient variations controlled by strain softening versus hardening; implications for fault scaling: Journal of the Geological Society, v. 169, p. 123-126.

Rustichelli, A., Torrieri, S., Tondi, E., Laurita, S., Strauss, C., Agosta, F., and Balsamo, F., 2016, Fracture characteristics in Cretaceous platform and overlying ramp carbonates: An outcrop study from Maiella Mountain (central Italy): Marine and Petroleum Geology, v. 76, p. 68-87.

Santantonio, M., Scrocca, D., and Lipparini, L., 2013, The Ombrina-Rospo Plateau (Apulian Platform): Evolution of a carbonate platform and its margins during the Jurassic and Cretaceous: Marine and Petroleum Geology, v. 42, p. 4-29.

Schultz, R. A., and Fossen, H., 2008, Terminology for structural discontinuities: AAPG Bulletin, v. 92, p. 853-867.

Schultz, R. A., Soliva, R., Fossen, H., Okubo, C. H., and Reeves, D. M., 2008, Dependence of displacement–length scaling relations for fractures and deformation bands on the volumetric changes across them: Journal of Structural Geology, v. 30, p. 1405-1411.

Scisciani, V., Tavarnelli, E., and Calamita, F., 2002, The interaction of extensional and contractional deformations in the outer zones of the Central Apennines, Italy: Journal of Structural Geology, v. 24, p. 1647-1658.

Seifried, D. T., 2012, Faults architecture and their scaling relationships: Insights into fault core thickness and fault displacement: MSc. Thesis, University of Bergen, 79 p.

Shipton, Z., and Cowie, P., 2001, Analysis of three-dimensional damage zone development over a micron to km scale range in the high-porosity Navajo sandstone, Utah: Journal of Structural Geology, v. 23, p. 1825-1844.

Shipton, Z., Evans, J., and Thompson, L., 2005, The geometry and thickness of deformation-band fault core and its influence on sealing characteristics of deformation-band fault zones: AAPG Memoir v. 85, p. 181-195.

Shipton, Z. K., and Cowie, P. A., 2003, A conceptual model for the origin of fault damage zone structures in high-porosity sandstone: Journal of Structural Geology, v. 25, p. 333-344.

Shipton, Z. K., Soden, A. M., Kirkpatrick, J. D., Bright, A. M., and Lunn, R. J., 2006, How thick is a fault? Fault displacement- thickness scaling revisited: Earthquakes: Radiated energy and the physics of faulting, p. 193-198.

Sibson, R., 1977, Fault rocks and fault mechanisms: Journal of the Geological Society, v. 133, p. 191-213.

Smith, D. L., and Miller, E. L., 1990, Late Paleozoic extension in the Great Basin, western United States: Geology, v. 18, p. 712-715.

Solum, J. G., Davatzes, N. C., and Lockner, D. A., 2010, Fault-related clay authigenesis along the Moab Fault: Implications for calculations of fault rock composition and mechanical and hydrologic fault zone properties: Journal of Structural Geology, v. 32, p. 1899-1911.

Sornette, D., 2009, Probability distributions in complex systems, Encyclopedia of Complexity and Systems Science, Springer, New York, p. 7009-7024.

Sperrevik, S., Gillespie, P. A., Fisher, Q. J., Halvorsen, T., and Knipe, R. J., 2002, Empirical estimation of fault rock properties: Norwegian Petroleum Society Special Publications, v. 11, p. 109-125.

Stokes, W., 1986, Geology of Utah: Utah Museum of Natural History and Utah Geological and Mineral Survey.

Sverdrup, E., and Bjørlykke, K., 1997, Fault properties and the development of cemented fault zones in sedimentary basins: field examples and predictive models: Norwegian Petroleum Society Special Publications, v. 7, p. 91-106.

Torabi, A., 2014, Cataclastic bands in immature and poorly lithified sandstone, examples from Corsica, France: Tectonophysics, v. 630, p. 91-102.

Torabi, A., and Berg, S. S., 2011, Scaling of fault attributes: A review: Marine and Petroleum Geology, v. 28, p. 1444-1460.

Torabi, A., and Fossen, H., 2009, Spatial variation of microstructure and petrophysical properties along deformation bands in reservoir sandstones: AAPG Bulletin, v. 93, p. 919-938.

Torabi, A., Fossen, H., and Braathen, A., 2013, Insight into petrophysical properties of deformed sandstone reservoirs: AAPG Bulletin, v. 97, p. 619-637.

Trudgill, B., 2011, Evolution of salt structures in the northern Paradox Basin: Controls on evaporite deposition, salt wall growth and supra- salt stratigraphic architecture: Basin Research, v. 23, p. 208-238.

Tvedt, A. B., Rotevatn, A., Jackson, C. A.-L., Fossen, H., and Gawthorpe, R. L., 2013, Growth of normal faults in multilayer sequences: a 3D seismic case study from the Egersund Basin, Norwegian North Sea: Journal of Structural Geology, v. 55, p. 1-20.

van der Zee, W., and Urai, J. L., 2005, Processes of normal fault evolution in a siliciclastic sequence: a case study from Miri, Sarawak, Malaysia: Journal of Structural Geology, v. 27, p. 2281-2300.

van der Zee, W., Wibberley, C. A., and Urai, J. L., 2008, The influence of layering and pre-existing joints on the development of internal structure in normal fault zones: The Lodève basin, France: Geological Society, London, Special Publications, v. 299, p. 57-74.

Viti, C., Collettini, C., and Tesei, T., 2014, Pressure solution seams in carbonatic fault rocks: mineralogy, micro/nanostructures and deformation mechanism: Contributions to Mineralogy and Petrology, v. 167, p. 1-15.

Walsh, J. J., and Watterson, J., 1988, Analysis of the relationship between displacements and dimensions of faults: Journal of Structural Geology, v. 10, p. 239-247.

Walsh, J. J., and Watterson, J., 1989, Displacement gradients on fault surfaces: Journal of Structural Geology, v. 11, p. 307-316.

Wibberley, C. A., Yielding, G., and Di Toro, G., 2008, Recent advances in the understanding of fault zone internal structure: a review: Geological Society, London, Special Publications, v. 299, no. 1, p. 5-33.

Willemse, E. J., Peacock, D. C., and Aydin, A., 1997, Nucleation and growth of strike-slip faults in limestones from Somerset, UK: Journal of Structural Geology, v. 19, p. 1461-1477.

Woodcock, N., and Mort, K., 2008, Classification of fault breccias and related fault rocks: Geological Magazine, v. 145, p. 435-440.

Yielding, G., Needham, T., and Jones, H., 1996, Sampling of fault populations using sub-surface data: a review: Journal of Structural Geology, v. 18, p. 135-146.